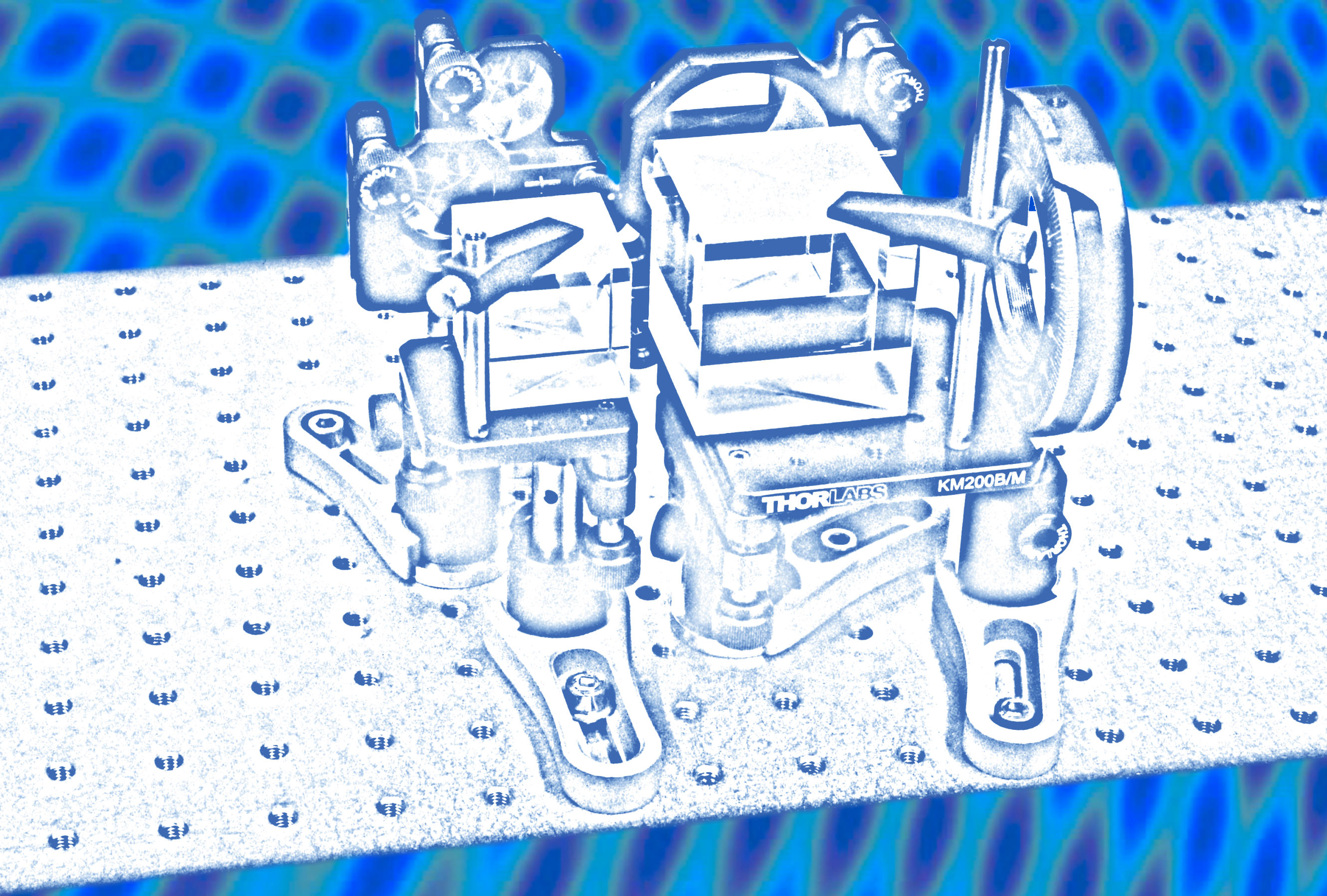

On the improvement of heterodyne displacement interferometry

Enhancing measurement linearity and system modularity

Arjan J.H. Meskers

On the improvement of heterodyne displacement interferometry

Enhancing measurement linearity and system modularity

PROEFSCHRIFT

ter verkrijging van de graad van doctor
aan de Technische Universiteit Delft,
op gezag van de Rector Magnificus prof. ir. K.C.A.M. Luyben,
voorzitter van het College voor Promoties,
in het openbaar te verdedigen
op vrijdag 7 november 2014 om 10:00 uur

door

Adrianus Johannes Hendricus MESKERS

werktuigbouwkundig ingenieur
geboren te Voorhout

Dit proefschrift is goedgekeurd door de promotor:
Prof. ir. R.H. Munnig Schmidt

Copromotor:
Ir. J.W. Spronck

Samenstelling promotiecommissie:

Rector Magnificus	voorzitter
Prof. ir. R.H. Munnig Schmidt	Technische Universiteit Delft, promotor
Ir. J.W. Spronck	Technische Universiteit Delft, co-promotor
Prof. dr. U. Staufer	Technische Universiteit Delft
Prof. dr. H.P. Urbach	Technische Universiteit Delft
Prof. dr. ir. P.P.L. Regtien	Technische Universiteit Twente
Dr. H. Haitjema	Mitutoyo
Ir. B. van der Pasch	ASML
Prof. dr. ir. J.L. Herder	Technische Universiteit Delft, reservelid

ABOUT THE COVER

FRONT PAGE: a picture showing the basic optical setup of a non-monolithic Delft interferometer for displacement measurement with $\lambda/8$ resolution of a plane target mirror, see also page 32, Fig.4.4.

BACKGROUND: simulation of interference between waves that originate from two separated point sources, located at the upper left and lower right, see also page 13, Fig.2.4.

This research was financed and supported by *Innovatiegerichte Onderzoekspogramma (IOP),* project nr. IPT04001, the Netherlands.

ISBN 978-94-6203-674-1

An electronic version of this thesis is available at: *http://repository.tudelft.nl*

Author email: arjanmeskers@gmail.com

Printed by Wöhrmann Print Service, Zutphen.

Voorwoord

(An English transcript of this text can be found at page 143, 'Preface')

In mijn tijd aan de TU Delft heb ik ontzettend veel dingen gedaan en geleerd, zowel op het gebied van kennis als karaktervorming. Mijn leukste studietijd begon bij de start van de werktuigbouwkunde master Mechatronic System Design (MSD), eindelijk vakken volgen die ik écht wilde. In die tijd had ik ook mijn eerste kennismaking met Rob en Jo, op dat moment nog voor mij professor Munnig Schmidt en professor Spronck. De vakken werden op een geheel Delftse wijze gedoceerd waardoor het volgen van ervan erg leuk was. Ik heb toen besloten om parallel een tweede master te gaan volgen aan dezelfde faculteit, de biomedische master Tissue Biomechanics and Implants (TBI).

In plaats van een literatuuropdracht voor TBI heb ik via Rob in 2009 een plek verkregen op het lab van de Precision Engineering Research Group aan het Massachusetts Institute of Technology (MIT) onder leiding van professor Alexander Slocum; dat was een geweldige ervaring. Rob, voor deze kans ben ik je nog steeds zeer erkentelijk! Alex, thank you for this magnificent experience and this memorable period, you are an incredible, enthusiastic and motivating professor. I also would like to thank Nevan Hanumara for making my stay at the MIT even more memorable. Nevan, since that period we have met several times, either in the United States or here in Delft, it's always a pleasure meeting and I hope we can help each other out many more times through our network of connections. Na mijn periode aan het MIT was ik er stellig van overtuigd dat ik aan die universiteit wilde gaan promoveren en geen andere, totdat ik bij Jo langs ging...

Tijdens mijn afstuderen voor TBI adviseerde Rob mij om bij Jo langs te gaan voor een leuke afstudeeropdracht voor mijn MSD master. Ik werd echter gevraagd voor een promotie onderzoek en ging al snel akkoord (aangestoken door Jo's enthousiasme), ik had op dat moment nog geen idee hoe omvangrijk en complex het onderwerp was. Nu, minder dan vier jaar na dat moment kan ik terug kijken op een plezierige, leerzame, en drukke periode die erg snel voorbij is gegaan. Het was een periode waarin mijn denkwijzen aanmerkelijk zijn veranderd. Persoonlijke ontwikkeling heeft bij mij een grote rol gespeeld, met name het minder gejaagd zijn tijdens het overleggen en weerleggen van ideeën bleek een opgave. De meetings met Jo en Rob en de halfjaarlijkse vergaderingen met de gebruikerscommissie waren hiervoor goede oefeningen. Het inbouwen van rust op de juiste momenten is een inzicht waar ik nog elke dag profijt van heb.

Op geen enkel moment heb ik getwijfeld aan dit promotietraject, alles vormde een uitdaging die ik graag aanging en waar ik ook plezier in had. Voornamelijk het schrijven van publicaties vond ik enerverend en vormde steeds weer opnieuw een uitdaging, vooral ook omdat dit intensief en tijdrovend was. Ik heb veel geleerd bij

het uitvoeren van de afgebakende stukken onderzoek die nodig waren om bepaalde aspecten wetenschappelijk te valideren. Het gaf veel voldoening als mijn resultaten na kritische analyse door ervaren onderzoekers werden erkend en dat deze door mede wetenschapers gebruikt konden worden. Echter, zoals veel afgestudeerde promovendi met mij zullen beamen, het schrijven van een proefschrift is een uitdaging van een andere ordegrootte. Dit proefschrift heeft veel van mijn doorzettingsvermogen gevraagd, maar, zoals op ieder moment tijdens deze periode, ik stond niet alleen.
Rob, Jo, dank voor deze mooie tijd, met jullie aan het roer van de groep 'mechatronici' was het een erg aangename leeromgeving met een breed bereik in kennis.
Rob, dank voor je inzet en de gesprekken die ik met je heb mogen hebben over het onderzoek, je werkervaring bij ASML en hoe het er in de industrie aan toe gaat. Je hebt in de jaren dat ik aan de TU Delft studeerde een mooi, maar vooral educatief, boek geschreven, waarvan ik nu pas kan inschatten hoeveel tijd en energie het moet hebben gekost om te schrijven. We hebben weliswaar geen wekelijkse meetings gehad, maar van de overleggen die we hadden ben ik altijd wijzer geworden. Ik heb veel van je geleerd, bedankt.
Jo, het heeft mij altijd verbaast hoe scherp je bent in je denkwijzen, dag in dag uit, bewonderingswaardig. Van je fysische achtergrond heb ik dankbaar gebruik mogen maken tijdens dit onderzoek. Ook heeft je creatieve en multidisciplinaire karakter en je betrokkenheid (ook met alle andere studenten en promovendi) naast het onderzoek een grote en positieve invloed op mij gehad, bedankt.
Waar ik jullie beiden dankbaar voor ben is dat jullie mij veel vrijheid hebben gegeven om ook dingen te doen die niet direct gerelateerd waren aan mijn promotie onderzoek, zoals deelname aan de Alpbach en Post-Alpbach Summerschools en het opstarten van een eigen stuk onderzoek (de elektro-optische faseplaat). Mits de argumentatie van mijn keuzes kloppend was, hebben jullie mij altijd jullie goedkeuring gegeven. Ik ben mij ervan bewust dat de vrijheid die jullie mij hebben geboden geen vanzelfsprekendheid was. Ook ben ik er achter gekomen dat de manier van samenwerking en het op gelijk niveau met elkaar communiceren een zeldzaamheid was die niet iedere promovendus met zijn begeleiders mag ervaren. Jullie open karakter, inzet en advies hebben mij een stevige basis gegeven om een succesvolle carrière in de wetenschap tegemoet te gaan.
Another person who I wish to thank is Jonathan Ellis. Jon, thank you for helping me getting up to speed (i.e. high speed) at the start of the project. During your last four months in the Netherlands you were an unlimited source of information about optical interferometry, thank you for answering every question I had. With your help, I had the opportunity to give presentations at two conferences and to publish, together with you, my first journal publication, all in the first year of my PhD.
Daarnaast wil ik graag mijn gebruikerscommissie bedanken[1], Han Haitjema *(Mitutoyo)*, Dirk Voigt *(VSL)*, Arthur van Nes *(VSL)*, Rob Bergmans *(VSL)*, Bert van der Pasch *(ASML)*, Suzanne Cosijns *(ASML)*, Kees Bos *(Keysight, voorheen Agilent Technologies)*, Lex Uittenbogaard *(Keysight)*, Ad Verlaan *(TNO)*, Machteld de Kroon *(TNO)*, Henny Spaan *(IBS Precision engineering)*, Guido Florussen *(IBS Precision engineering)*, Pleun Dona *(FEI Company)*, Annette Steggerda *(Rijksdienst voor Ondernemend Nederland, voorheen Agentschap NL)* en Eddy Schippers *(Rijksdienst voor Ondernemend Nederland)*. Velen van jullie namen ieder half jaar de moeite

[1]Bij het lezen van mijn proefschrift zal niet iedereen weten wie ik bedoel wanneer ik alleen voornamen noem, daarom heb ik gekozen om voor én achternaam te gebruiken, zodat er geen onduidelijk over kan bestaan wie mij heeft geholpen tijdens mijn promotieonderzoek.

om naar de TU te komen en advies te geven over het onderzoek, dank jullie wel.
Han, je kritische blik op het onderzoek tijdens de meetings heeft gaandeweg steeds meer mijn waardering gekregen. Wanneer ik dacht dat ik een goed afgebakend stuk onderzoek had kon jij altijd wel een paar punten aanwijzen waar ik nog eens beter naar kon kijken. Vooral in het begin waren dit goede momenten voor mij om te leren meer rust in te bouwen bij het geven van tegenargumentatie. Han, jouw inzichten hebben tot betere resultaten geleid en boden mij een extra stimulans om mijn denkwijze onder de loep te nemen, bedankt.
Kees en Lex, de meetings met jullie heb ik altijd als erg prettig en informatief ervaren. Jullie kennis van de laser interferometrie systemen van *Agilent Technologies* en jullie hulp bij het beschikbaar stellen van meetapparatuur van *Agilent Technologies* hebben het project zeer geholpen, ontzettend bedankt hiervoor. I also would like to thank two other people from *Keysight*, Larry Zurbrick and Greg Felix. Larry and Greg, thank you for your willingness to visit the university, and for your interest in the research. Your viewpoints and advice regarding the Delft interferometry concept were much appreciated. During the research I became acquainted with your company's high-end interferometric measurement systems/equipment and after completing my work I fully appreciate the challenges that are involved in reaching sub-nm measurement uncertainty. Therefore, I find it astonishing and a great accomplishment what's already commercially achieved. With this research, I hope that I have contributed to a further reduction of measurement uncertainty for these magnificent optical measurement tools that your company realizes.
Suzanne, dank voor je bezoeken aan de TU Delft en voor de informatieve discussies die ik met je bij *ASML* heb mogen hebben. Jouw praktische kijk op de vele fouten bronnen heeft er onder andere in geresulteerd dat het onderzoek dicht bij de praktijk bleef. Daarbij wil ik ook Bert van der Pasch, Robbert van Leeuwen en Hans Vermeulen van *ASML* bedanken voor het ontvangen van Jo en mij bij *ASML*, voor hun interesse in het onderzoek en voor het geven van advies.
Van het *Van Swinden Laboratorium* (*VSL*) wil ik Arthur, Dirk en Rob, bedanken voor hun adviezen met de wat diepere natuurkundige achtergrond en voor het gebruik van apparatuur van het *VSL*. Daarnaast, Dirk, ik heb onze tussentijdse email correspondentie erg gewaardeerd en ook je tijd voor het pre-reviewen van mijn publicaties. Je hebt mij geholpen bepaalde aspecten van optica inzichtelijk te maken en we hebben een mooie gezamenlijke publicatie geschreven, bedankt.
Ad, je bent een ervaren wetenschapper, tijdens onze gesprekken ging je echter met mij om als een collega, dat heb ik zeer gewaardeerd. Ook vond ik het erg leuk dat je mij in het tweede jaar hebt betrokken bij het voorbereiden van de 'HPOM-2' [1, 2] thermische vacuüm tests in de cleanrooms van *TNO*, dit was een leerzame ervaring. Related to these tests I would also like to thank Thilo Schuldt *(University of Konstanz)* and Dmitry Ityaksov *(TNO)* for their time and enthusiasm teaching me new aspects regarding frequency stabilization and laser operation.
Natuurkunde heeft mij altijd gefascineerd, echter, door mijn werktuigbouwkundige studies waren een aantal fundamentele aspecten gerelateerd aan optica achter gebleven. Hiervoor kon ik gelukkig terecht bij de vakgroep optica van Technische Natuurwetenschappen. De vakken 'optical waveguiding' en 'theoretical optics' gegeven door Paul Urbach, Jaap Caro en Omar El Gawhary behoorden tot de interessantste vakken die ik gevolgd heb. Paul, Jaap en Omar, bedankt voor het beantwoorden van de vele vragen die voor een fysicus misschien weleens voor de hand lagen. I would also like to thank two other members of the optics group: Nandini Bhattacharya and

Jeffrey Meisner. Nandini, thank you for your interest in the electro-optic wave plate, and for our discussions about the design of a new instrument for measuring magnetic fields of space-based plasmas using radio waves (related to the Post-Alpbach summerschool). Jeff, your experience with radio waves helped a lot during the elaboration of the fundamentals of this instrument and gave me a new perspective on electromagnetic waves, thank you.
Natuurlijk mag ik mijn mede promovendi niet vergeten, Oscar van de Ven, Johan Vogel, Ruijun Deng, Phuc (Foppe) Vuong, Patrice Lambert, Teun Hoevenaars, Rudolf Saathof, Takeshi Morishima, Guido Delhaes, Jan Shutte, Jasper Wesselingh, Jeroen van Schieveen, Chris Valentin, Evert Hooijkamp en Pablo Estevez Castillo. Dank voor de vele brainstorm sessies en de (informatieve) koffie pauzes en lunches.
Johan, Oscar en Rudolf, bedankt voor de overpeinzingen met betrekking tot Fourier transformaties. Johan, dank voor je hulp bij de numerieke simulatie van een interferentiegolffront afkomstig van een single-mode optische fiber.
Naast promovendi bestond de MSD groep ook uit masterstudenten, Bart Festen, Luuk Ursem, Martijn Wansink, Max Café, Robert Valk, Simon van Veen, Charlie van der Schoor, Gihin Mok, Paul Ouwehand, Arnold Zondervan, Stefan van der Kleij, Jeroen Karregat en Rens Berkhof. Het was leuk om te zien hoe jullie projecten gaandeweg vorm kregen. Arnold, dank voor je hulp met de elektro-optische faseplaat.
Daarnaast, dank aan de TU medewerkers die mij hebben geholpen tijdens mijn promotie, Harry Jansen, Patrick van Holst en Rob Luttjeboer. Bedankt voor jullie hulp en advies wanneer er dingen gebouwd moesten worden en voor jullie accuraatheid en bereidheid om 'even snel tussendoor' hulp te bieden, dit heb ik erg gewaardeerd.
Tot slot wil ik Corinne du Burck, Birgit Rademakers, Marli Guffens, Gaby Offermans en Marianne Stolker bedanken voor het verrichten van een hoop regelwerk, zonder jullie zou een promovendus heel wat minder tijd aan onderzoek kunnen besteden.
Hoezeer ik iedereen die ik genoemd heb ook waardeer, mijn grootste waardering gaat uit naar mijn ouders. Ik heb veel respect voor de manier waarop jullie mijn broer en mij hebben opgevoed, jullie betrokkenheid en advies bij de vele keuzes in het leven hebben er toch maar mooi toe geleidt dat jullie twee werktuigbouwkundige ingenieurs als kinderen hebben waarvan er één ook nog eens vliegenier is geworden en de ander een doctorstitel in de wetenschap heeft verkregen. En niet te vergeten, dat hebben jullie allemaal gedaan naast een drukke bedrijfsvoering die een eigen bedrijf, een snijbloemen kwekerij, met zich meebrengt. Sander, mijn 'grote broer', ook jij hebt eraan bijgedragen dat ik ben geworden wie ik vandaag de dag ben, bedankt voor je technische enthousiasme, je ondernemendheid en de wil om uitdagingen aan te gaan. Jullie drie zijn mijn ideale voorbeeld van doorzettingsvermogen.
Met het bedanken van de belangrijkste persoon heb ik gewacht tot het laatst: lieve Janneke, dank voor je steun en vrolijke gezelschap tijdens mijn promotie. Ik weet heel goed dat het voor jou niet altijd even gemakkelijk was om met iemand samen te leven die naast zijn promotieonderzoek ook nog eens met heel veel andere dingen bezig was; een klein nadeel van iemand die alles leuk vindt wat technisch/wetenschappelijk is. Het afgelopen jaar stond erg in het teken van het afronden van mijn onderzoek en minder in het teken van samen dingen doen. Echter, samen met jou dingen ondernemen is het leukste wat er is! Ik hoop daarom dat we nog vele avonturen samen mogen beleven, waarbij ik beloof te leren wat de term 'vakantie houden' daadwerkelijk inhoudt.

Arjan Meskers
Delft, September 2014

Summary

Lithographic exposure equipment for integrated circuit manufacturing requires ever more accurate position measurement systems, which is currently led by the advent of Extreme UltraViolet (EUV)-lithography machines. This work describes an interferometric displacement measurement system that possess the potential to foresee in the need for measurement accuracy in lithography systems far into this century. Not only the measurement accuracies in these machines are demanding, also the size extension of the silicon substrates from 300 mm to 450 mm presents a challenge. The progress of these aspects promotes the improvement or development of new measurement tools for lithographic exposure equipment.

The aim of this research was to design a "*compact heterodyne displacement interferometer for a measurement range of 450 mm that achieves sub-nm measurement uncertainty, while allowing for a modular system buildup that has a flexible optical layout and is robust enough for fast module replacement to reduce downtime*".

This work was a continuation of the research done by Dr. Ki-Nam Joo (who cooperated with Dr. Jonathan Ellis), who used an interferometer concept that originated from the field of astronomy. That research described how the measurement linearity of a heterodyne displacement interferometer was increased by reduction of a significant periodic and nonlinear source of error by using two separated optical beams (each carrying one source frequency) that are kept separated until detection [3, 4].
The aim of this research extended further than only improvements at component level, improvements at system level were made as well, centralized around enhancement of measurement linearity and system modularity. These two aspects have been subdivided into separated topics of which each was theoretically analyzed and also experimentally validated when relevant to the interferometer concept.
Every result, theoretically or experimentally, was compared to the performance of a benchmark system. That system consisted of a state-of-the-art heterodyne displacement interferometer system from Agilent Technologies, which used free-space coaxial beams for source frequency delivery and fiber coupled optical detection (located away from the interferometers). This system was set to operate in an EUV-lithography machine which acted as a host-system. This host-system contained a near-vacuum environment enclosing one reticle stage and two wafer stages, where every stage was monitored in six Degrees of Freedom (DoF) by two interferometers that each measured five-DoF; comprising a total of 30 measurement axes. Using two five-DoF interferometers for each stage ensured e.g. measurement redundancy.

When operating in a vacuum (or near-vacuum) environment, periodic nonlinearity (PNL) is the main factor that limits the measurement linearity of a heterodyne interferometer that is supplied by a coaxial optical beam (i.e. a coaxial interferometer).

Such a coaxial beam contains two linearly polarized frequencies that are orthogonally oriented, these frequencies may mix due to 'frequency leakage' which originates from polarization based separation of the two frequencies. This leakage results in a nonlinear error that is superimposed on the obtained displacement data and it repeats itself each fraction of a wavelength displacement, hence 'periodic' nonlinearity. It was shown that surpassing the need for polarization based frequency separation eliminated one primary source of PNL and thereby increased measurement linearity [3, 4].
The research described in this work used the basic interferometer layouts from Dr. Joo's research as a starting point for performing measurements with two types of interferometers using the same operating principle (two separated optical beams, each carrying a frequency). One used a cube corner reflector as target, and one used a plane mirror as target. The emphasis of this work is on the latter one, since the benchmark interferometer also measured a plane mirror target. The heterodyne source from Dr. Joo's research [4] was for practical reasons replaced by a 2-mode frequency stabilized helium neon (HeNe) laser source. Experiments and frequency domain analysis confirmed that this 'alternative' heterodyne frequency source provided the necessary output for this research: two separated and non-mixed source frequencies (with a frequency offset of ~2 MHz). The improved interferometer design and alternative heterodyne source together constituted the demonstrator setup of the 'Delft interferometer system'.
Because coaxial interferometers show enlarged levels of PNL upon polarization misalignment and polarization imperfections, one of the first measurements performed in this research investigated the influence of source frequency polarization on the presence of PNL. Experiments validated that the measurement output from the Delft interferometer did not contain PNL higher than the first fringe-order[2] and achieved an average PNL-error of less than 4 pm, irrespective of the polarization manipulation. The benchmark system on the other hand, showed for equal manipulation up to eighth fringe-orders PNL, with the first fringe-order PNL exceeding 10 nm, and eventually seized operation due to too large nonlinearity. This research was published and showed the robustness of the Delft interferometer concept for input polarization and its increased measurement linearity with respect to the benchmark system [5].
Although the Delft interferometer showed picometer sized PNL, still, the interference signals contained unwanted frequency content upon detection, which forms the origin of PNL. An observed source of PNL consisted of back-reflections (i.e. ghosting), and another potential source was formed by cube corner polarization rotation in combination with a polarizing beam splitter. No sources of PNL other than these two were observed or are expected to meaningfully influence measurement performance. Further experimentation investigated the separated source frequency transport to the interferometer, because separated optical beams allow for optical pathlength differences that potentially affect measurement uncertainty. The benefit of the Delft interferometer concept is that each interferometer has its own reference which makes it theoretically possible to account for phase differences due to pathlength inequalities. This was confirmed by experiments, showing phase disturbance reduction ratios in the order of 6000. These ratios, however, were limited by the experimental setup itself and are expected to be exceeded under normal operating conditions [6]. This

[2] A 'fringe-order' can be expressed in the frequency domain by $(k \cdot N \cdot v) / \lambda_{HeNe}$, where k = a positive integer expressing the n^{th} order, v = target velocity, N = interferometer fold factor, and λ_{HeNe}= 633 nm.

demonstrator setup indicated that the Delft interferometer concept can operate with separated source frequency delivery while maintaining its measurement linearity.
A minor downside for having a reference at each interferometer is that for the mentioned 30 measurement axes the Delft interferometer system requires five additional detector channels compared to the benchmark system, which is fortunately well compensated by the benefit of enabling fiber optic delivery. Employment of optical fibers for source frequency delivery improved both the optical layout flexibility and system modularity, because only the location of the fiber-ends required attention; unlike the line-of-sight of free-space coaxial beams. In addition, optical fibers provide an opportunity to achieve plug-and-play connections between modules.
Theoretical and experimental analyzes including multi-mode optical fibers indicated that the multi-mode type of optical fiber was not suitable for frequency delivery, due to the presence of multiple individual optical pathways, i.e. 'modes'. These modes prevented proper collimation over the aimed measurement range and resulted in too low irradiance levels upon detection. More importantly, each mode carried its individual phase which showed to be highly susceptible to environmental influences, which decreased the measurement linearity [7]. Despite the many types of optical fibers only single-mode optical fibers provided the optical quality required for achieving the aimed measurement performance.
With the use of single-mode polarization-maintaining optical fibers a fully fiber coupled Delft interferometer was realized. This setup demonstrated the feasibility of using optical fibers for constructing an optically flexible interferometer system with undetectable levels of PNL. These results were presented at a conference as well as accepted for publication [8, 9]. Related work demonstrated that the Delft interferometer concept is significantly insensitive for irradiance fluctuations, indicating that also non polarization-maintaining single-mode fibers are an option, and that mechanical vibrations at fiber connections are potentially not critical [6].
In another analysis the influence of optical wavefronts on measurement linearity was studied. In 'traditional' interferometer systems the source frequencies are carried by a coaxial beam, the source frequencies in such a beam are equally affected by disturbances like refractive index differences, because they have common optical pathways that prevent relative phase differences between the two frequencies; resulting in identical wavefront shapes. In contrast, two separated beams (each carrying one source frequency) are individually disturbed and have therefore individually shaped wavefronts. Interference between the wavefronts of the source frequencies creates an 'interference wavefront', whose shape consists of the relative phase differences between the two interfering wavefronts. During target rotation and movement the overlap between the two interfering wavefronts varies and alters the interference signal's strength and wavefront shape, both affect measurement linearity.
A new measurement method was designed for investigating the shape of interference wavefronts. The method enabled assessment of an interference wavefront its shape with sub-nm accuracy (even in open air) and showed that already at the exit of a laser source the interference wavefront of a coaxial beam was deformed several tens of nanometers, i.e. ±20 to ±50 nm. In contrast, it was indirectly shown that the optical wavefront at the exit of a single-mode optical fiber was spherically shaped and significantly less deformed, measurements showed deformation of less than 2 nm. This new measurement method and its findings were published as well as presented at a conference [10, 11].

Further analysis regarding the influence of optical wavefront shapes in combination with beam walkoff indicated that the Delft interferometer is potentially less affected by beam walkoff than the benchmark system. The analysis showed that upon beam walkoff it is better to have two individually shaped but relatively flat (and not tilted) wavefronts delivered to an interferometer, rather than using two identical but significantly more deformed wavefronts (caused by the free-space transport system) as used in the benchmark system.
Moreover, by means of theoretical analysis also a number of other aspects have been studied, such as data-age, and thermal influence; exemplifying *internal* and *external error* sources respectively. *Internal error* sources consisted of sources of error that were due to the design of the interferometer. In this category the Delft interferometer performed equally or better than the benchmark interferometer. *External error sources* concerned the influence from the measurement environment and system installation, also here the Delft concept showed equal or better performance; except for thermal influence. The use of individual optical pathways in combination with several cube corner reflectors make the Delft interferometer sensitive for inhomogeneous heating, which is expected to be this concept's principal error source.
Additional research concerning heterodyne frequency generation methods resulted in the development of an electro-optical wave plate as a new addition to heterodyne frequency generation. Experiments demonstrated that the rotational direction of the wave plate's refractive index determined the frequency shift to be up or down, and that the index's rotational rate was proportional to the magnitude of the frequency shift. Other experiments, where the device was placed in an optical cavity, demonstrated that also single and double-sided frequency combs were generated.
This optical frequency modulation method possesses much potential for the field of metrology, and allows for new measurement approaches in e.g. heterodyne displacement interferometry, such as phase-locked displacement measurement.

The research described in this work has resulted in four peer reviewed journal publications, one non-journal publication, three conference talks with accompanying publications, new methods for optical wavefront detection and heterodyne frequency generation, and a comprehensive error analysis for heterodyne displacement interferometers. These works together discussed a new heterodyne interferometer concept with improved measurement linearity compared to a state-of-the-art benchmark interferometer system. The initial interferometer design of Dr. Joo has been improved regarding alignment performance, and achieved together with a new optical layout similar compactness as the benchmark interferometer. The Delft interferometer system ensures sub-nm measurement uncertainty over a measurement range of 450 mm, while having a flexible optical layout between the heterodyne source, the interferometers, and the phase measurement equipment. The use of optical fibers aids host-system integration and provides a modular system buildup, where its modules can be connected on a potentially plug-and-play basis, reducing both commissioning time and downtime.

To make the presented interferometer concept ready for commercial applicability future work should cover experiments with a prototype of a five-DoF monolithic interferometer as proposed in *Chapters 4* and *9*, including passive thermal shielding of the interferometer optics. Moreover, when a true plug-and-play interferometer system is desired, a study regarding fiber connectors should be performed, with special attention to the mechanical stability and wavefront quality of the fiber-to-free-space out-coupling at the interferometer.

Contents

Part I

Project introduction

The first chapter, *Chapter 1*, addresses the motivation and the aim of the research. *Chapter 2* provides a brief introduction to optical interferometry for displacement measurement, containing information that aids interpreting the results described in this work.

Chapter 1

Motivation and research aim

This thesis deals with the design of a 'heterodyne displacement interferometer', a measurement instrument that measures displacements with light and plays an important role in the fields of precision engineering and metrology (i.e. the science of measuring). One of its main advantages is that it allows for non-contact measurements, and therefore, does not affect the dynamics of the measurement target by e.g. adding weight or stiffness. The instrument is also known for its high accuracy: the ratio between measured displacement versus the measurement uncertainty can well exceed a factor of a billion for an interferometer as discussed in this thesis (i.e. less than a nanometer uncertainty over one meter displacement).

Heterodyne interferometers know a large field of application but they are primarily employed in applications that require high measurement accuracy. One of the most demanding measurement tasks can be found within a lithography machine from the semiconductor industry (e.g. ASML's NXE system, using EUV-light, Fig.1.1a). Such machines perform the optical transfer of the layout of a chip layer from a mask onto a layer of photosensitive material that is deposited on a silicon substrate. Such substrates are called 'wafers' (Fig.1.1b), and act as carriers of many identical chips (i.e. integrated circuits) during the fabrication process. Upon completion, the wafers are cut into separate individual chips, known as 'dies', see Fig.1.1c.

Integrated circuits consist of multiple mutually interconnected layers, similar to the interconnecting infrastructure between successive floors of a sky-scraper. Such structures are achieved by chemically processing the silicon substrate, re-coating it with photosensitive material, and again exposing it; repetition of these steps results in a stacked arrangement of interconnecting layers of sub-micrometer structures, illustrated in Fig.1.1d. This process is repeated until the chip is finished, resulting in a 3D micro-structure.
A finalized integrated circuit only operates properly when the successive layers successfully interconnect, this depends on how well one layer 'overlays' with the layer underneath, deviations from the ideal overlay are expressed in terms of 'overlay-error'. The size of the allowed error depends on the size of the smallest patterned structures, depicted in Fig.1.1e. When using Extreme UltraViolet light (EUV), features as small as 13.5 nm can be obtained, allowing a maximum overlay error of approximately 3 nm[1] depending on the applied process.

[1]For comparison, human hairs and nails grow per second on average 4.8 nm and 1.1 nm, respectively.

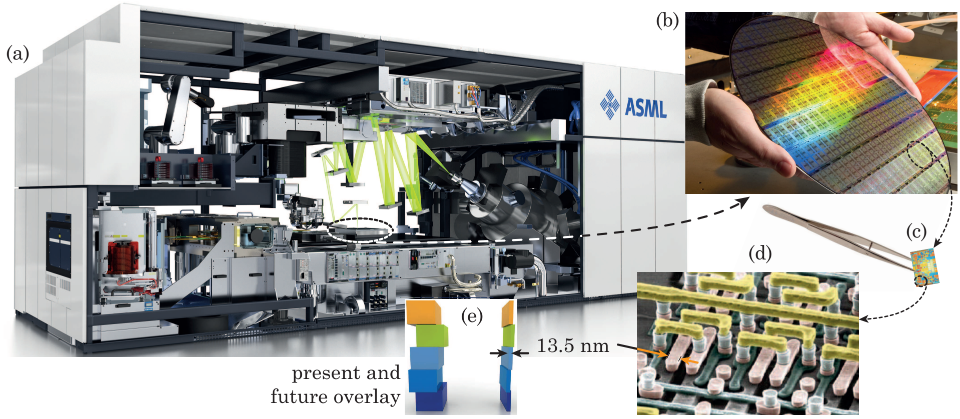

Figure 1.1: A lithography machine (a) transfers the layout of an integrated circuit onto a silicon substrate, i.e. wafer (b), by means of projecting a pattern onto a photo-sensitive material layer deposited on the wafer. This wafer carries many identical chips and is split after completion into individual chips (c). Each chip has a 3D architecture consisting out of several interconnected layers that are built on top of each other (d). Stacking the micro structures becomes more difficult as they get smaller (e).

Accurate positioning of a wafer inside the lithography machine is achieved by tracking the position of a 'wafer stage' that carries the wafer (encircled in Fig.1.1a). This stage moves with accelerations of about 50-60 m/s^2 and reaches velocities of several meters per second, which present a challenge for meeting the overlay requirements. The eventual overlay error is a summation of several error sources, including the measurement error of the instrument that measures the position of the stage; whose measurement error must be much smaller than the allowed overlay error.

A method currently applied to trace the position of a wafer stage, consists of short range interferometers (i.e. optical encoders) that are located on top of the stage (they use optical interferometry in a different way as the interferometers discussed in this work). These optical encoders track their own position, and thereby the wafer stage, with respect to a reference grid that is located about 15 mm above the wafer stage [12]. The grid is attached to the 'metrology frame[2]' and acts as an absolute position reference. The main reason for using encoders is that their short optical pathway allows them to cope with refractive index fluctuations due to (air)turbulence, whereas long range interferometers (addressed in this work) would not meet the required measurement accuracy in the same environment.

However, in near-vacuum environments, as used by ASML's NXE systems, the refractive index fluctuations are reduced, re-enabling the used of long range interferometers, which are more preferred because they can be located off the stage. This decreases system complexity since taking out the encoders leads to clearing e.g. weight, heat sources, and electrical connections from the stage; moreover, the large and heavy reference grid above the movement area of the wafer stage can also be removed. Unfortunately, the measurement accuracy of the current generation of long range interferometers is limited due to frequency mixing that leads to periodic nonlinear errors (PNL), see Fig.1.2a.

[2]The metrology frame is a framework within the lithography machine on which no forces are exerted, thereby, it provides a vibration reduced, long term stationary, and 'absolute' reference for several measurement instruments.

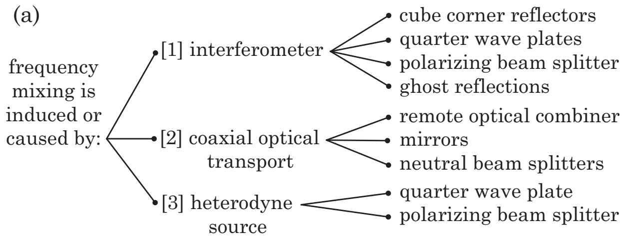

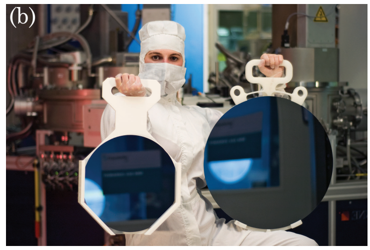

Figure 1.2: (a) PNL related measurement error originates in current interferometer systems from processes at several locations; indicated with respect to their influence on the measurement error (i.e. [1] represents much influence). (b) Ø300 mm wafer versus Ø450 mm wafer, the future standard wafer size.

Two aspects that are key for the end users of chips, are the unit price, and the continuous strive to have more functionality packed in each new chip. These two aspects drive the chip manufacturing processes towards higher production rates and smaller feature sizes; reducing cost and enhancing chip-performance respectively. The combination of these key aspects leads to costly machines, one lithography machine, e.g. an ASML TWINSCAN, costs about 30 million Euros [13]. Such cost makes clear that once commissioned the machine ideally operates 24/7 without downtime[3], handling many wafers per hour (230 wafers per hour in 2014 [14]). Thus, besides accurate positioning also the high production rate poses a challenge.

Increasing production speed to foresee in the market's need for chips is reaching its limits in the near future, the next step is to increase the wafer size. The industrial standard wafer size of Ø300 mm is to be extended to Ø450 mm, see Fig.1.2b.

All these continuous advancements in this industry have led to the following statement that was submitted to the Dutch IOP:

"There is an industrial need for a compact displacement interferometer system that can measure with sub-nanometer accuracy for a measurement range of 450 mm."

However, this aim could be expanded a little further by looking at trend such as: precision manufacturing of nanometer sized parts at high production rates leads to complex machines. Increasing system complexity enlarges the number of parts, which raises the chances of failure and making these systems more prone to downtime. One way to solve this is by means of reliable design (i.e. high design costs and expensive components), the use of modular systems that allow for fast replacement, or a combination of these two.

The initial aim has been supplemented with *robustness* and *modularity*, two aspects that have gradually received more attention over the past four years; leading to the overall aim:

"Design a compact heterodyne displacement interferometer for a measurement range of 450 mm that achieves sub-nm measurement uncertainty, while allowing for a modular system buildup that has a flexible optical layout and is robust enough for fast module replacement to reduce downtime."

The research was therefore concentrated on the enhancement of two main aspects: measurement linearity and system modularity.

[3]Downtime refers to the period of time that a system is unavailable and fails to perform its primary function.

About this thesis

This work consists of five parts that together address the aim of this research:

"*Design a compact heterodyne displacement interferometer for a measurement range of 450 mm that achieves sub-nm measurement uncertainty, while allowing for a modular system buildup that has a flexible optical layout and is robust enough for fast module replacement to reduce downtime*."

Part I, *Project introduction*
Chapter 1 addresses the motivation and the aim of the research. *Chapter 2* provides an introduction to optical interferometry for displacement measurement, containing information that helps interpreting the results described in this work.

Part II, *Interferometer system design*:
This part is focused on the design process where the measurement linearity and system modularity of a benchmark system are analyzed, which will eventually result in an improved heterodyne displacement interferometer: the 'Delft interferometer'. In *Chapter 3* a benchmark interferometer system is sketched as it is currently used in lithography machines. This system serves as the starting point of this research and is used as a state-of-the-art technology reference throughout this work.

The following chapter, *Chapter 4*, addresses one of the benchmark system's fundamental error sources, 'periodic nonlinearity', i.e. PNL, this error source requires reduction to comply with the research aim: *'a measurement range of 450 mm with sub-nm measurement uncertainty'*. It is in this chapter that the Delft interferometer is introduced, accompanied by an 'alternative' heterodyne frequency generation method that differs from the benchmark system.

Chapter 5 clarifies what the term 'modularity' implies and how it results in a new system architecture that allows *for a modular system buildup that has a flexible optical layout and is robust enough for fast module replacement*, without compromising measurement accuracy.

All elements for an enhanced interferometer system are put together in *Chapter 6*, which sketches the Delft interferometer system's overall layout.

Part III, *Error source analysis: Delft vs. benchmark*
In this part all internal and external error sources (except PNL) are addressed for both the benchmark and Delft interferometer, in *Chapter 7* and *Chapter 8* respectively. These chapters give insight in the improvement achieved with the new interferometer design.

Part IV, *Industrial implementation*
This fourth part only consists of *Chapter 9*, which treats the implementation of the new interferometer into industry. This chapter describes two practical configurations of a 5-DoF Delft interferometer, and it describes how the Delft interferometer concept can best be introduced into industry.

The last part, **Part V, *Closing*** covers *Chapter 10*, which summarizes the most important results and implications of the described research, together with recommendations covering potential improvements or aspects that could/need to be further investigated before the Delft interferometer reaches commercial maturity.

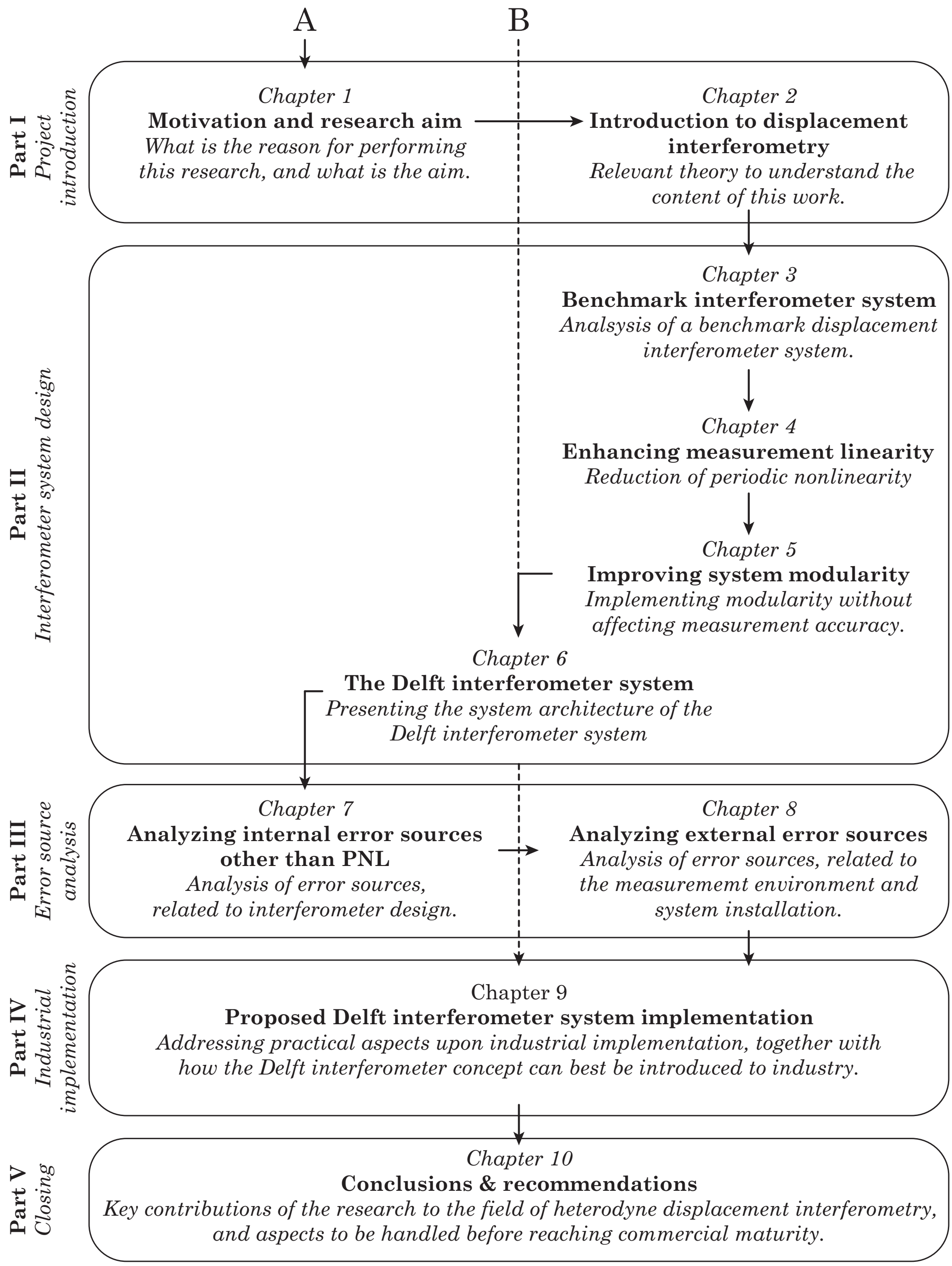

Figure 1.3: Illustration of the thesis outline with two reading orders: A is for who is unfamiliar / and B is for who is familiar with high-end heterodyne displacement interferometer systems for lithography machines.

Chapter 2

Introduction to displacement interferometry

The previous chapter presented the aim of this research and clarified that the research focuses on the improvement of a heterodyne displacement interferometer.
Measuring light that is reflected off a target and thereby determining its displacement, has many advantages. This chapter addresses the use of optical interferometry of light to measure displacement of a target.
At the basis of interferometry lies the behavior of waves, this work deals with waves in the optical range[1] *(to be more specific, wavelengths of ~633 nm, which is determined by the emission line of a Helium Neon laser). At the start, a brief introduction to the mathematical description of electromagnetic waves is given in Section 2.1, followed by Jones calculus in Section 2.1.1, which enables the mathematical implementation of wave properties, e.g. phase, and polarization. Section 2.1.2 clarifies how the Jones formulation can be used to calculate and predict outcomes of two waves that 'interfere' upon detection. In the last section, Section 2.2, the operating principles of a 'homodyne' and a 'heterodyne' displacement interferometer are exemplified, of which the latter is key to this research.*

2.1 Waves

In physics a wave can be described by *'a disturbance traveling through a medium by which energy is transferred from one particle of the medium to another without causing any permanent displacement of the medium itself'*. There are waves that require a medium to propagate through by locally deforming it, e.g. 'mechanical' or 'acoustic' waves, and there are waves that do not require a propagation medium, e.g. 'electromagnetic' waves. Such waves can travel through a vacuum because they consist of periodic oscillations of electrical and magnetic fields.

A wave can be either transversal, i.e. perpendicular to the direction of propagation, or longitudinal, i.e. normal to the direction of propagation. Mechanical waves

[1] *Describing wavelengths between 480 nm to 780 nm*

can be both transversal or longitudinal, whereas electromagnetic waves can only be transversal, which can be expressed mathematically using the *complex wave notation*, represented by:

$$\text{complex wave notation} : \psi(x,t) = Ae^{i(kx \pm \omega t \pm \delta)}. \tag{2.1}$$

Applying Eulers formula, $e^{i\varphi} = \cos\varphi + i\sin\varphi$ to Eq.2.1, results in

$$\psi(x,t) = A \cdot [\cos\,(kx \pm \omega t \pm \delta) + i \sin\,(kx \pm \omega t \pm \delta)]\,. \tag{2.2}$$

Both equations differ in notation but concern the same wave, $\psi(x,t)$, depicting the amplitude of the wave at a given point in space and time. The initial amplitude of the wave is expressed by A. The wave its angular frequency, i.e. temporal frequency, is represented by $\omega = 2\pi f$ [rad/s], t [s] is time, and $f = c_v/n\lambda$ [Hz]; in which c_v [m/s] is the speed of light in vacuum, n is the [dimensionless] refractive index of the propagation medium, and λ [m] is the wave's wavelength. The wave factor $k = 2\pi/\lambda$ [rad/m] gives the number of radians per unit distance, i.e. spatial frequency, and the variable x [m] relates to the wave's displacement, which can range from $-\infty$ to $+\infty$ (for an ideal wave of infinite extent); δ [rad] represents the wave its initial phase.

The displacement interferometers addressed in this research are relative measurement instruments, therefore, the stationary and absolute value kx is not relevant and is left out; resulting in the following wave notation:

$$\psi(t) = Ae^{i(\omega t \pm \delta)}. \tag{2.3}$$

This notation gives all what is required for this research, it includes the wave its amplitude, wavelength, and starting phase, which gives a description of the wave's amplitude over time.

2.1.1 Polarization

Before discussing how waves interfere, *polarization* needs to be addressed, which proves fundamental to the superposition of waves. Although there is much to tell about polarization of optical waves, only a few aspects have to be taken into account to understand the role of optical polarization for this research.

An electromagnetic wave can be described by a quantum of energy, i.e. a photon, (given by $E = hc_v/\lambda$, with h being Planck's constant) that alternates between an electric and a magnetic state – hence electromagnetic –, illustrated in Fig.2.1. These two

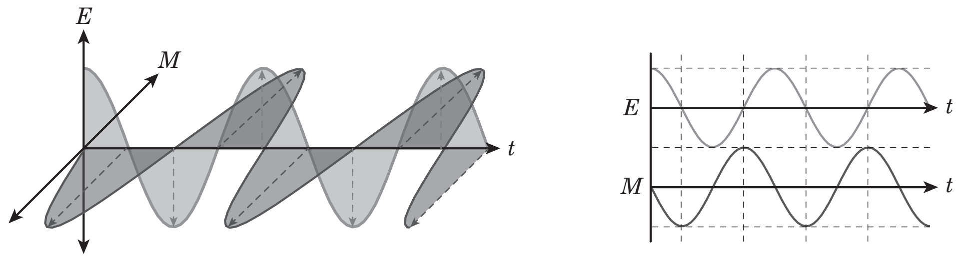

Figure 2.1: The energy of a photon alternates between an electric field, E and a magnetic field, M over time; constituting an electromagnetic wave. When the electric field energy is at maximum, the magnetic field energy is zero, and vice versa.

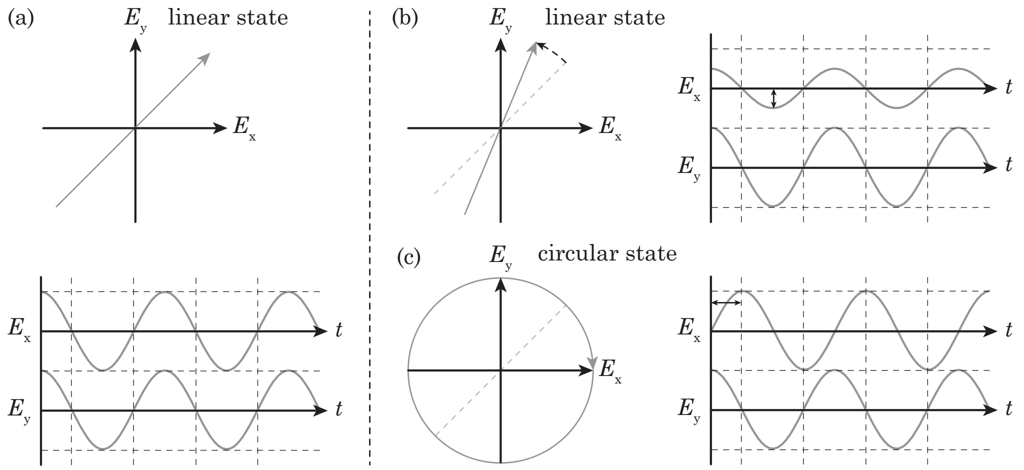

Figure 2.2: (a) Illustration of a linearly polarized wave, whose orientation and linearity are described by a vector consisting of E_x and E_y. (b) The polarization orientation is determined by the relative amplitude or the vector of its components, whereas the polarization state (c) depends on the relative phase between the vector's orthogonal components.

states, called 'fields', are orthogonally oriented and have both a relative orientation and an absolute orientation. The absolute orientation can be described by taking e.g. the electric field and describing the orientation of this field relative to its surroundings. It is most meaningful to involve the electric field orientation in calculations since propagation media interact with the photon's electric field.

The electric field can be assumed to be comprised of two independent sinusoids, which is still in agreement with the 'electro-magnetic' description (i.e. every quarter a wavelength E goes from maximum to zero). These two sinusoids together make up the electric-field vector that determines the polarization properties of the wave (Fig.2.2a). The resultant of the amplitudes of the two axes determines the polarization orientation of a wave (Fig.2.2b) while the relative phase offset between the two waves determines the polarization state of the wave, see Fig.2.2c.

The polarization of a wave is not included in the wave notation as shown in Eq.2.3, one can do so by making use of Jones calculus. Jones calculus uses matrix formulation to describe polarized light. It uses 2x1 Jones vectors for describing the electric field components, and 2x2 Jones matrices to describe polarizing components. It is important to note that the Jones formulation is limited to treating completely polarized light and cannot describe unpolarized or partially polarized light.

Mueller matrices on the other hand, can describe any polarization based on Stokes vectors and consist of 4x4 matrices. Although Mueller matrices approach reality more closely, it is not used in this work because the Jones formulation is well capable of describing interference phenomena and situations where field amplitudes must be superimposed, which suffices for this research.

A linearly polarized wave is described by the following Jones vector:

$$\text{Jones vector} : J_{\text{linear}} = \begin{bmatrix} E_x \\ E_y \end{bmatrix} e^{i(\omega t \pm \delta)}. \tag{2.4}$$

Where E_x and E_y together determine the orientation and amplitude of the wave's electric field. In an equal way, a circularly polarized wave is described by:

$$J_{\text{circular}} = \frac{1}{\sqrt{2}} \begin{bmatrix} E_{\text{x}} \\ \pm iE_{\text{y}} \end{bmatrix} e^{i(\omega t \pm \delta)}. \tag{2.5}$$

Here, $\pm i$ denotes the rotational direction of the circularly polarized wave.

Information about the polarization of a wave is important because waves only interact, i.e. interfere, via common polarization components. In other words, the E_{x} component of wave a, only interacts with the E_{x} component of wave b. Perpendicular oriented components such as the E_{x} component of wave a and the E_{y} component of wave b do not interact with each other. Thus, for calculation of the interference result between waves (i.e. superpositioning) the polarization state and orientation of the two interfering waves is required.

2.1.2 Interference and detection

In the previous section it was stated that interference is actually the superposition of waves and only takes place when both have common polarization components; this can mathematically be shown using Jones calculus. Interference between two waves can be expressed as following, where the $\propto$ denotes 'proportional to':

$$\text{interference} : I \propto E_{\text{a}}^{\dagger} \cdot E_{\text{b}}. \tag{2.6}$$

Here, '†' denotes that the vector is transposed upon superpositioning the two vectors, which consist throughout this work of $E_{\text{a}} = E_0 \cos(\omega_{\text{a}} t \pm \delta_{\text{a}})$ and $E_{\text{b}} = E_0 \cos(\omega_{\text{b}} t \pm \delta_{\text{b}})$. Its result can be written as (omitting the complex wave notation Eq.2.3, for clarity):

$$I \propto E_{\text{a,x}} E_{\text{b,x}} + E_{\text{a,y}}^{*} E_{\text{b,y}}^{*}. \tag{2.7}$$

This shows that the irradiance, I, of the two superimposed waves consists of the summation of E_{x}^2 and E_{y}^2.

When considering interference between two linearly but *perpendicularly* polarized waves, where we have $E_{\text{a,x}} = 1$, $E_{\text{a,y}} = 0$, $E_{\text{b,x}} = 0$, and $E_{\text{b,y}} = 1$, having equal frequency $\omega_{\text{a}} = \omega_{\text{b}}$ and starting phase $\delta_{\text{a}} = \delta_{\text{b}}$:

$$J_{\text{linear a}} = \begin{bmatrix} E_{\text{a,x}} \\ E_{\text{a,y}} \end{bmatrix} e^{i(\omega_{\text{a}} t \pm \delta_{\text{a}})}, \; J_{\text{linear b}} = \begin{bmatrix} E_{\text{b,x}} \\ E_{\text{b,y}} \end{bmatrix} e^{i(\omega_{\text{b}} t \pm \delta_{\text{b}})}. \tag{2.8}$$

Substituting these vectors in Eq.2.7, the result is zero. It can thus be stated that upon successful superposition of two waves one requires to have non-orthogonal electromagnetic fields. When having such vectors, their result can be either 'constructive' interference or 'destructive' interference, illustrated in Fig.2.3 (where only the real part is used since the real valued equation represents an actual plane wave.).

The signal that is eventually measured by a photodetector differs from the superimposed electric fields sketched in Fig.2.3. Photodetectors contain photosensitive-material in which absorbed photons create an electrical current that eventually is measured. During this process the electric current is proportional to the number and energy (related to wavelength) of the absorbed photons. The number of incident photons is termed *irradiance*, which is expressed in terms of energy: [Watt/surface

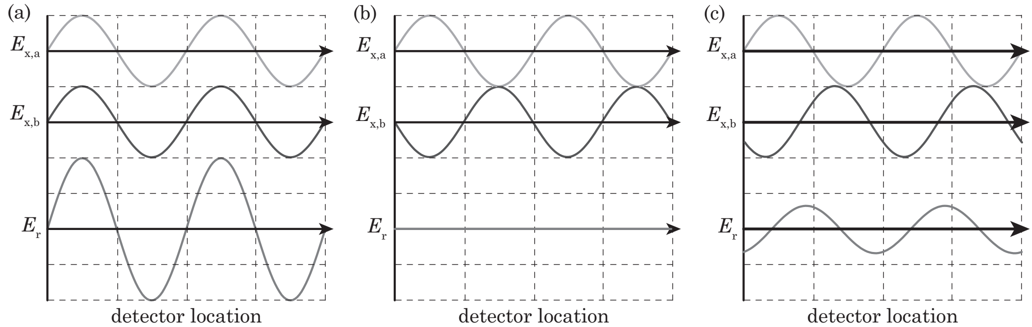

Figure 2.3: Superposition of the x-components of two standing electromagnetic waves, a and b, of equal frequency and amplitude. Depending on the relative phase offset between the two waves, one obtains constructive interference (a), destructive interference (b), or a situation in between (c). When the relative phase between the two waves is constant over time (as shown), the amplitude of the resultant superimposed electromagnetic fields, E_r, is detector location dependent.

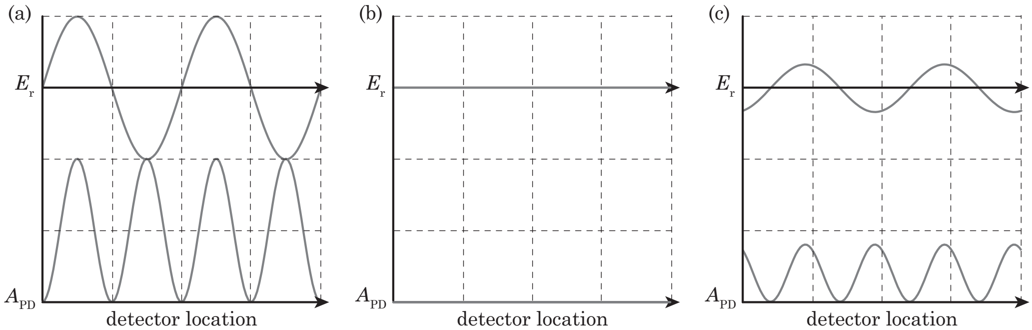

Figure 2.4: *Continuing with Fig.2.3*: as E_r enters the photodetector the optical energy is converted into an electric current, A_{PD}. Since irradiance cannot be negative, the frequency doubles with respect to the incident electromagnetic wave; moreover, the resulting signal will have an amplitude equaling E_r^2, Eq.2.7.

area]. The photodetector current resulting from interference is depicted in Fig.2.4. When the relative phase between the two waves and their frequency are invariant over time, one obtains an amount of irradiance that depends on the *location* where the photodetector measures (i.e. DC-signal); this relates to homodyne displacement interferometry.

Our interest concerns interference between two linearly vertically polarized waves, having unequal frequencies (i.e. $\omega_\mathrm{a} < \omega_\mathrm{b}$). Upon superposition of two of such waves and assuming an equal starting phase (i.e. $\delta_\mathrm{a} = \delta_\mathrm{b}$), one obtains:

$$I \propto \begin{bmatrix} E_\mathrm{a,x} \\ E_\mathrm{a,y} \end{bmatrix} e^{i(\omega_\mathrm{a} t \pm \delta)} \cdot \begin{bmatrix} E_\mathrm{b,x} \\ E_\mathrm{b,y} \end{bmatrix} e^{i(\omega_\mathrm{b} t \pm \delta)} = \left(E_\mathrm{a,y} E_\mathrm{b,y}\right) e^{i(\omega_\mathrm{a} - \omega_\mathrm{b})t}. \tag{2.9}$$

The result is illustrated in Fig.2.5, from (a) can be seen that the two waves create a so called 'beat' frequency, i.e. f_beat, indicated by the black line in E_r. The frequency of f_beat equals the frequency difference between the two frequencies, in this case frequency a is 9 Hz and frequency b is 10 Hz, their relative frequency difference of 1 Hz can be seen from the black line in E_r. This means that every second, the two waves go from 'in phase' to 'out of phase' and again 'in phase' (Fig.2.5a). It can also be noted

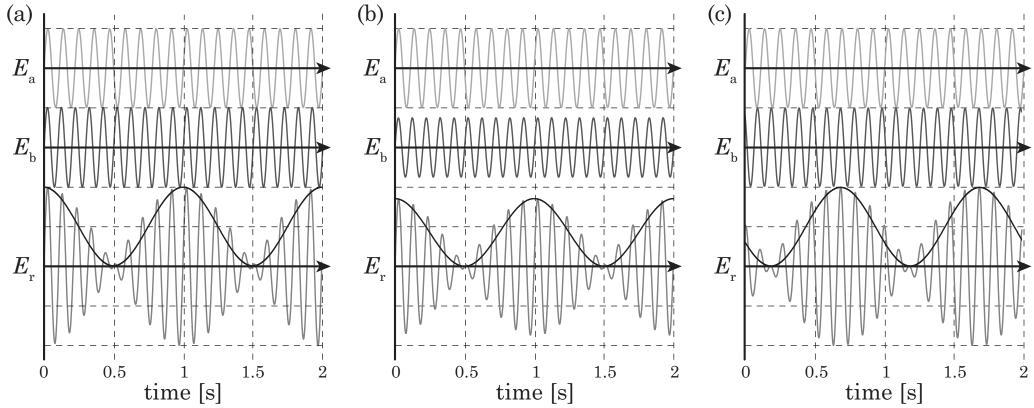

Figure 2.5: Superposition between two electromagnetic waves of unequal frequency result in a beat-frequency , f_{beat}, black line in E_r, which is in fact an AC-signal instead of a DC signal. (b) Interference between two waves of unequal amplitude shows that the amplitude of the AC-component of the interference signal is determined by the smallest electric field component, i.e. E_b. (c) A change in phase of one of the frequencies does not result in a decreased signal amplitude but rather in a corresponding phase change of the AC-signal.

from Fig.2.5b that although interference is the superposition of a and b, the amplitude of the AC-component (i.e. the component that makes the beating frequency) is only as large as the smallest electric field component. Therefore, the smallest electric field component determines the eventually measured signal amplitude. The concept of monitoring the interference result from two offset frequencies (i.e. heterodyne) that are individually too fast to detect with the intention of extracting information from their interaction forms the basis of heterodyne displacement interferometry.

2.2 Interference in displacement measurement

The superposition of two waves depends on the relative phase between the two waves, as this phase changes their superimposed result changes. This change in phase, φ, of a wave is depicted in Fig.2.6. When the incoming and reflected wave are made to interfere, constructive and destructive interference takes place as depicted in Fig.2.3. In this case, the irradiance at the detector is directly coupled to the displacement of the target mirror. This example illustrates what happens in homodyne displacement interferometry (i.e. displacement measurement using a single input frequency).

2.2.1 Homodyne displacement interferometry

A homodyne displacement interferometer works according the principle illustrated in Fig.2.6. A Michelson interferometer system sketched in Fig.2.7a, uses a laser source for generating an electromagnetic wave of a specific wavelength; in displacement interferometry this is most often a Helium Neon laser (i.e. HeNe) having a well defined wavelength of 633 nm. A neutral beam splitter (nbs, which can also be a polarizing beam splitter) transmits half of the wave towards a moving cube corner

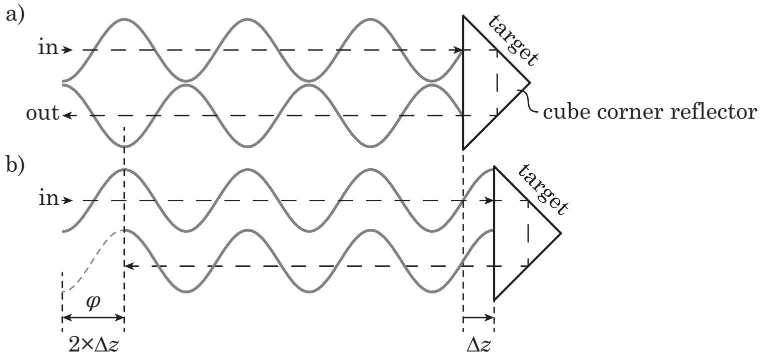

Figure 2.6: (a) A wave comes in from the left, reflects off a target mirror and continues propagation to the left. In (b), the same situation is illustrated but with a mirror moved by distance $\triangle z$, resulting in a phase shift, φ, of the reflected wave, which equals two times the displacement.

reflector (cc_t, which is the measurement target), and reflects the other half towards a stationary reference cube corner reflector (cc_r). After reflection both beams are made to interfere with each other by means of a polarizer (pol) placed in front of the photodetector (PD). The detection performed is based upon the irradiance level at the detector, also known as DC-detection, see Fig.2.4.

2.2.2 Heterodyne displacement interferometry

An almost equal interferometer configuration can also operate using two offset frequencies (i.e. split frequency, which is a fixed value), illustrated in Fig.2.7b. This interferometer uses two frequencies that are carried by a coaxial beam; the waves are orthogonally linearly polarized to prevent instant interference between the two waves (i.e. frequencies). Before entering the actual interferometer optics, a reference signal is created by means of a neutral beam splitter (nbs) (reflecting only a

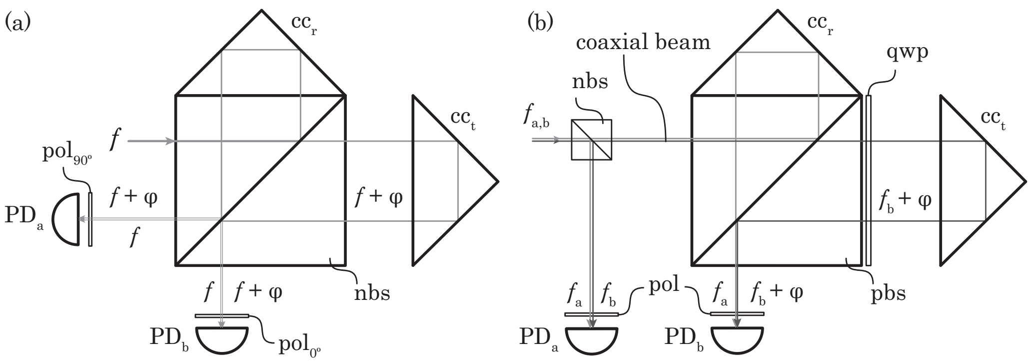

Figure 2.7: (a) Homodyne displacement interferometer using a single input frequency, its detection is based upon *irradiance* measurement (i.e. DC-detection). Here, direction sensing is enabled using two photodetectors with polarizers that are relatively 90° rotated. (b) Heterodyne interferometer, where two frequencies are used and *phase* measurement is used (i.e. AC-detection). Legend: f_x, source frequency; nbs, neutral beam splitter; pbs, polarizing beam splitter; pol, polarizer; qwp, quarter wave plate; cc_r, reference cube corner reflector; cc_t, target cube corner reflector; PD_x, photodetector.

few percent, leaving most of the irradiance for the measurement) and a polarizer that induces interference and creates a beating signal at the detector (PD_a); this beat-frequency is equal to the split frequency. The frequencies carried by the coaxial beam are subsequently separated by a polarizing beam splitter which reflects frequency a and transmits frequency b, to a stationary reference reflector (cc_r) and a moving target reflector (cc_t), respectively. This second beating signal will be detected using again a photodetector with a polarizer in front of it. When the target reflector moves, the frequency measured by PD_b will deviate from its stationary value due to a Doppler shift caused by target motion (i.e. phase shift, φ; the accumulation of phase over time presents itself upon detection as a change in frequency). The phase corresponding with target displacement is then obtained via a differential measurement between the reference signal and the measurement signal.

The main difference between *homodyne* and *heterodyne* detection, is the frequency content of their detected signals:

Homodyne displacement interferometry: when the target is stationary, the detector measures a DC-signal; when the target moves, the detector measures an AC-signal.

Heterodyne displacement interferometry: even with a stationary target an AC-signal is measured, consisting of the beat-frequency, f_{beat}, see Fig.2.5.

The advantage of AC-signals over DC-signals is that they allow for much better noise filtering, this gives heterodyne interferometers a higher signal-to-noise ratio (SNR) than homodyne interferometers, which eventually results in better measurement accuracy. Due to this reason this method is the preferred method for measuring displacement in systems that require the best performance, like lithography machines.

2.3 Conclusions

Optical waves can be described mathematically using Jones calculus (2x2 matrices), describing only fully polarized waves and using the more complex Mueller calculus (4x4 matrices), which can describe any polarization. Although Mueller matrices approach reality more closely they are not used in this work since the less complex Jones calculus already suffices for this research.

It was shown that only common polarization components of two waves interact with each other and that this interaction can be described by superposition of the two waves. It was furthermore shown that the superposition of the relative phase and the amplitude of two interfering waves determine the interference result, i.e. interference signal.

Two methods of optical displacement interferometry were addressed: homodyne, using one input frequency, and heterodyne, using two input frequencies. The main advantage of heterodyne displacement interferometry is the measurement of a beat-frequency even when the target is stationary. The all-time measurement of the beat-frequency results in a better signal-to-noise ratio, which achieves better measurement accuracy compared to homodyne interferometers. Therefore, heterodyne interferometry is the preferred displacement measurement method for EUV-lithography machines (i.e. with the interferometers operating in near-vacuum); and it presents the method where this research focused on.

Part II

Interferometer system design

The following part addresses the design process that shows how measurement linearity and system modularity of a heterodyne displacement interferometer system are increased, which eventually leads to the *Delft interferometer*.

In *Chapter 3* a benchmark system is sketched, representing a commercial state-of-the art displacement interferometry system as it is employed in lithography machines. This chapter shows how this interferometer system achieves target displacement, and it indicates a fundamental error source, PNL, that limits its measurement performance.

In the next chapter, *Chapter 4*, the origins of PNL in the benchmark system are discussed. This chapter reviews where this error source originates from and how it can be reduced with the intention to increase measurement linearity. It is in this chapter where the Delft interferometer is introduced, accompanied by an alternative heterodyne frequency generation method which is required for this research.

***Chapter 5* clarifies the implication of the term 'modularity' and how this results in a new interferometer layout that allows for a modular system buildup that has a flexible optical layout and is robust enough for fast component replacement; without compromising the measurement accuracy.**

In *Chapter 6* all elements for the Delft interferometer system are put together and an overall system layout is sketched.

Chapter 3

Benchmark interferometer system

This chapter continues with the heterodyne displacement interferometer described in the previous chapter, and shows how the concept is applied in a commercially available measurement system that is employed within a lithography machine (i.e. host-system).
The site where the host-system is situated and where the interferometers perform their measurements are set out in Section 3.1, giving insight into the overall measurement environment. Section 3.2 addresses the targets inside the host-system that are measured by an interferometer and shows the layout of a state-of-the-art heterodyne interferometer system as it is currently applied in industry, the 'benchmark system', which acts as a technology-reference throughout this work. The final section, Section 3.3, clarifies how target displacement is measured, and indicates a fundamental error source that limits the benchmark interferometer's measurement performance: periodic nonlinearity.

3.1 Measurement environment

The environment wherein the interferometers are situated is illustrated in Fig.3.1. Environment A consists of a clean-room environment with a floor that consists of a steel construction on which tiles are laid with an open matrix structure, comprising a work floor that allows for the passing of down-flowing 'clean' air – hence clean-room. The steel construction supports also multiple 'pedestals' (large massive concrete blocks), on each is a lithography machine B (i.e. host-system) located. Such a machine generally contains two separated frames, a *base* frame and a vibration reduced *metrology* frame. The base frame supports actuators and balancing masses that continuously exert forces on the frame. In contrast to the metrology frame that is kept as stationary as possible. It supports several measurement instruments – hence 'metrology' frame – and acts as an overall position reference, i.e. the motion between subsystems inside the machine are all coordinated relative to this framework. *(for a well documented and more detailed description, see Chapter 9 of [15])*

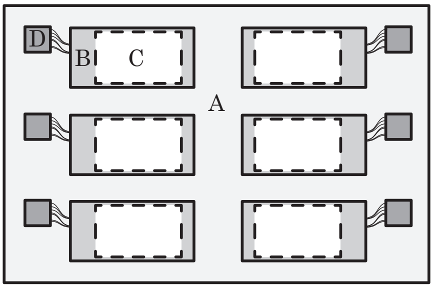

Figure 3.1: Schematic representation of the several environments wherein the interferometers operate: A, factory building; B, host-system; C, near-vacuum environment; and D, sources of heat of the interferometry system, which are located externally and flexibly connected to the host-system.

The photo-lithography process takes place within environment C, which is the location where the displacement interferometers perform their measurements. This environment is highly controlled with regard to temperature, gas pressure, and gas purity (to regulate e.g. gas composition and particle contamination). The gas pressure within this environment is near-vacuum (i.e. ~10 kPa [16]), which helps reducing the impact of refractive index fluctuations (due to e.g. turbulence) on the interferometric measurement; and improves thereby the measurement accuracy. The system is also purged with hydrogen gas [16] to e.g. clean optical components during operation. On one hand this helps when compensating for refractive index fluctuations due to specifically knowing the properties of the gaseous media, but on the other hand, adding and removing gas causes temperature differences and turbulence within this environment which are both error sources for interferometers.

Sources of heat are preferably kept outside of a precision positioning system such as a lithography machine, since heat causes thermal expansion that affects many components differently; and is thus difficult to compensate for. The laser source and electronic readout are therefore placed outside the host-system in an external cabinet, D. The connection between the host-system and this cabinet consists of optical fibers and electrical cables, enabling flexible placement of the two with respect to each other.

3.2 Monitoring precision stages

An ASML NXE system as illustrated in Fig.1.1, contains three 'targets' whose displacement is monitored with heterodyne displacement interferometers; all located inside environment C from the previous section. These three targets are a calibration stage, a reticle stage, and an exposure stage, see Fig.3.2.

The calibration stage is used for wafer positioning during a calibration process, where the wafer profile is mapped prior to the exposure process. The exposure stage is subsequently used for wafer positioning during the exposure process, during which the layout from a photo-mask (i.e. reticle) is transferred by means of projection into the photosensitive material layer on the wafer. The reticle contains the layout for one chip-layer and is held by a stage located above the two wafer stages, see Fig.3.2. When the chip layout is projected onto the photosensitive material it is optically

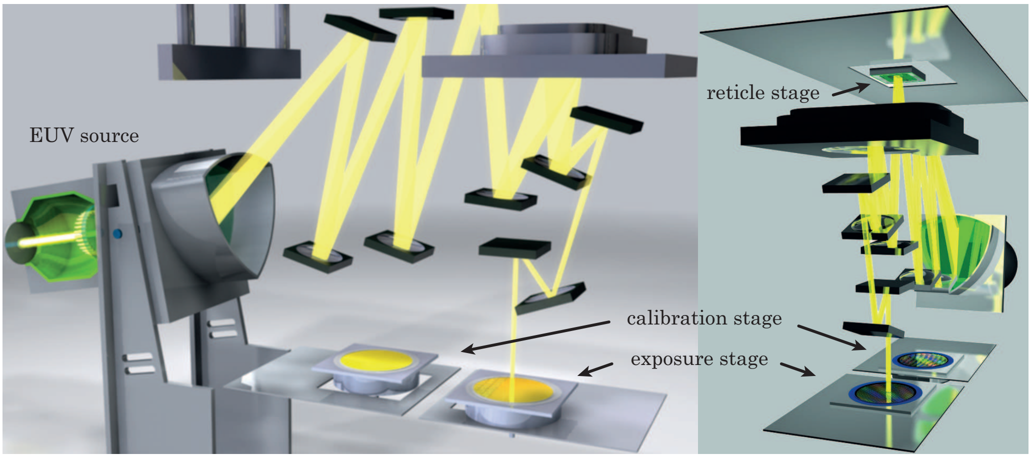

Figure 3.2: Artist impression of the interior of a lithography machine, illustrating how photo-resistive material on top of a wafer is exposed by EUV light that propagates via mirrors and a reticle. Between the reticle stage and the exposure stage the image is scaled down by a factor of four, resulting in a four fold reduction of the accelerations and velocities required for the exposure stage. The position of the stages is monitored by heterodyne displacement interferometers *(not shown)*. (modified from www.3dit.de)

scaled down by a factor of four, which results for the reticle stage in accelerations in the order of 400 m/s^2, while reaching velocities of ~4 m/s. The calibration and exposure processes take place in parallel to maximize the system's throughput.

During the calibration process the wafer's geometrical properties are mapped with respect to the wafer's individual calibration marks that are located on its top surface, the resulting data is stored and used during the exposure process. Drift in the position measurement of the interferometers or wafer deformation that occurs after the calibration and during the exposure process cannot be accounted for. Such drift deteriorates the exposure quality and leads to e.g. increased overlay error or out of focus projection. In other words, both the wafer and (especially) the interferometer system must be stable over the time frame in between the calibration process and the end of exposure.

The time required for exposing the wafer governs the machine's throughput. To indicate, an ASML TWINSCAN system has a wafer throughput of about 230 wafers per hour, that is one wafer (300 mm) every ~16 s [14]. Over this time span the interferometers must show high measurement stability to meet the overlay requirements.

Each stage is monitored in six Degrees of Freedom (DoFs) using two, five-DoF displacement measuring interferometers (ensuring measurement redundancy), illustrated in Fig.3.3, leading to a total of 30 measurement axes. The movement area of a wafer stage is many times larger than that of the reticle stage, therefore, the design of the interferometer system is governed by the specifications of the wafer stages.

The optical pathlength required for a 450 mm wafer stage is initially estimated (in collaboration with ASML) to have in the x and y-direction a deadpath of max. 0.5 m, and a stroke of 0.45 m with an additional extension of 0.05 m for flexibility, together with a stroke of max. 0.01 m in the z-direction. The three rotational DoFs are in the order of 1 mrad each, which includes both initial rotation (applied at the start of exposure) and dynamic rotation (applied during exposure).

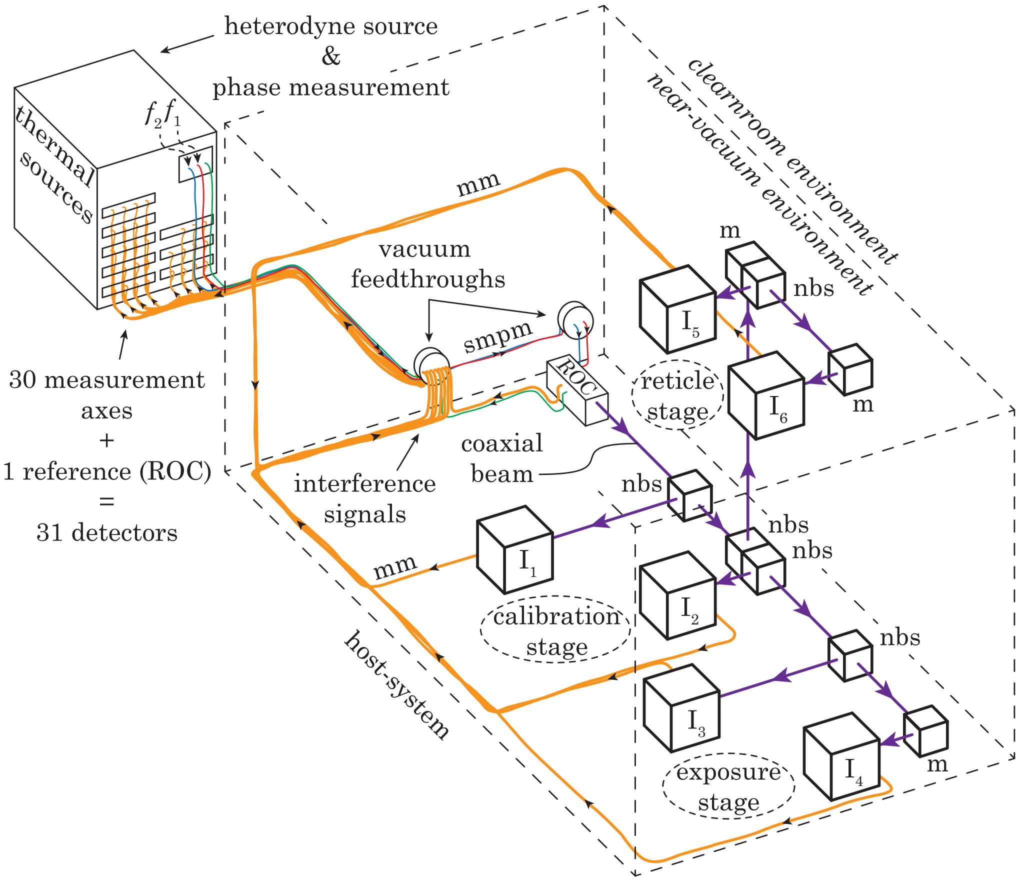

Figure 3.3: Impression of a commercial interferometer system employed in a lithography machine (the actual situation might differ from the illustration). The green feedback line from the remote optical combiner (ROC), represents electrical feedback for irradiance balancing of the source light[1]. Legend: I_x, five-DoF measuring monolithic interferometer; f_x, source frequency; mm, multi-mode optical fiber; smpm, single-mode polarization-maintaining optical fiber; nbs, neutral beam splitter; and m, mirror.

The depicted benchmark system consists of heterodyne interferometers which are fed by coaxial optical beams that carry the two *source frequencies*[1]. These beams propagate free through space (i.e. free-space) and are guided via several mirrors and beam splitters, which makes the beams sensitive for environmental disturbances. These mirrors and beam splitters require placement at specific locations that are controlled for vibrations and thermal fluctuations, as these could affect the geometry and orientation of the components and lead to measurement error (see *Chapter 7*). Moreover, free-space beams require free 'lines of sight' between the optical guiding components, which makes this means of optical transport inflexible and not easy to implement into a complex and tight spaced host-system such as a lithography machine.

[1]A displacement measuring interferometer system obtains displacement information by measuring the beat-frequency of several interference signals, see *Chapter 4*. Therefore, since the actual measurand is frequency, the expression *source frequency* is used throughout this work. The term *source* refers to a frequency that is generated by the heterodyne frequency source and is used as input for an interferometer.

The free-space coaxial beams originate from a 'remote optical combiner' (i.e. ROC) that is located within the vacuum environment. A heterodyne frequency source located outside the host-system, uses a stabilized helium neon (i.e. HeNe) laser and provides the input for the single-mode polarization-maintaining optical fibers that are attached to the ROC. This heterodyne frequency source outputs two frequencies with a fixed frequency offset at a wavelength of 633 nm (i.e. HeNe emission).

The ROC combines the optical output of the two fibers into a collimated coaxial beam whose polarizations are oriented orthogonally. The reason for using a single-mode fiber for each source frequency, is that they cannot be transported both through one single-mode fiber simultaneously due to frequency mixing, which induces PNL in the displacement measurement [17] (thoroughly addressed in the next chapter). A part of the coaxial beams is sampled within the ROC for creating a reference signal (consisting of the split-frequency), this reference signal is a common reference signal that is used in conjunction with the interference signals from the six interferometers.

Each optically monolithic interferometer (Fig.3.4 shows an example of an optically monolithic 5-DoF interferometer from *Agilent Technologies*) measures five-DoFs, resulting in five interference signals at the interferometer its output. These interference signals are coupled into multi-mode optical fibers that transport the signals from within the vacuum environment to the externally located phase measurement equipment. Note that the two frequencies that exit the interferometer are already made to interfere before entering the optical fibers, by means of a polarizer in front of each fiber. Optical fiber transport of these interference signals is less stringent than the delivery of source frequencies to each interferometer, and can therefore be carried out by multi-mode optical fibers that are more robust and practical to use than single-mode fibers as shown in *Chapter 5*. The output of the phase measurement equipment is subsequently used as position-feedback for the three stages.

** The sketched benchmark system might deviate at some points from reality, however, it presents a realistic case that enables addressing all aspects that are relevant for this research.*

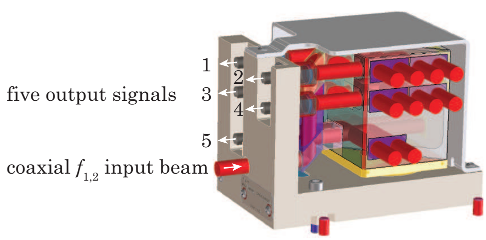

Figure 3.4: Example of an optically monolithic interferometer, which shows similarity to an interferometer as used by the benchmark system.

3.3 Displacement measurement in the benchmark system

The previous section stated very briefly that PNL in the measurement is caused by interference between more than two frequencies at the photo detector, rather than only having interference between the reference and measurement frequency that make up a single beat-frequency (thoroughly addressed in *Chapter 4*). To understand why this is a problem and where these different frequencies originate from, it is important to know how a displacement measurement is performed with a coaxial heterodyne displacement interferometer.

In the benchmark system a common reference frequency is generated by sampling both frequencies at the remote optical combiner, ROC, measured by PD_a, see Fig.3.5. The location of the ROC, and thereby the location of the common reference signal, can be as far as 1 to 5 m away from the interferometers. A second detector, PD_b, is located at the interferometer and measures a beat-frequency that varies (through the Doppler shift affecting f_2) as the target mirror displaces.

The following example clarifies how displacement is measured using a benchmark interferometer, consider the following parameters:

1. $f_1 = c / \lambda_1$, where c is the speed of light in m/s, and λ_1 equals 633 nm.

2. $f_2 = f_1 + f_s$, with f_s Hz being the fixed frequency offset, i.e. split frequency.

3. $\lambda_2 = c / f_2$.

4. v, is the target velocity in m/s.

5. N, representsthe interferometer's fold factor.

6. f_D, is the Doppler frequency.

7. n, being the refractive index.

During the measurement both detectors measure a beat-frequency, which is equal for both detectors when the target is stationary. As the target moves towards the interferometer the beat-frequency measured by PD_b increases, whereas it decreases as the target moves away. In accordance with Fig.3.5, one obtains:

$$\text{interference signal at } PD_a: \; I_{PD_a} \propto f_2 - f_1, \tag{3.1}$$

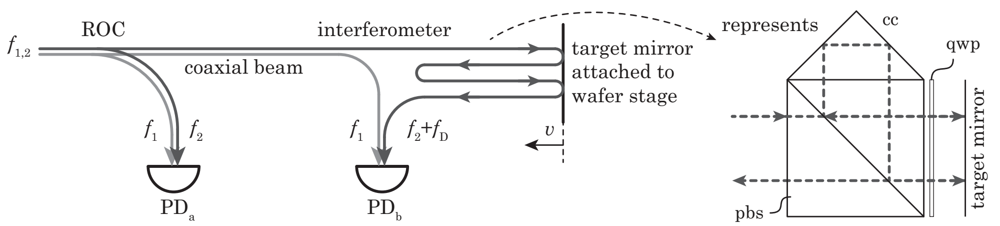

Figure 3.5: In the benchmark system the phase difference between the common reference signal of PD_a and the interference signal of PD_bdetermines target displacement; here, f_1 acts as reference frequency. The beam traverses four times between the target mirror and interferometer, which results in an interferometer fold factor of four (coupled to optical resolution, see Fig.2.6). Throughout this thesis this schematic representation is used, which more clearly shows the optical beam pathways, compared to the overlapping beams of the figure at the right.

$$I_{\mathrm{PD_b}} \propto (f_2 + f_{\mathrm{D}}) - f_1, \tag{3.2}$$

$$f_{\mathrm{D}} = \frac{N \cdot n \cdot v}{\lambda_2}. \tag{3.3}$$

Equation 3.2 indicates that when the target is moving away from the interferometer the beat frequency of interference signal I_{PD_b} becomes zero for $(v/\lambda_2) > f_s$ (in the other direction there is no limitation). When the beat-frequency becomes zero the measurement system loses its sense of direction and can no longer continue measuring, which is the reason that this situation typically is avoided. Therefore, the minimum split frequency is always larger than the maximum expected Doppler frequency caused by target speed.

The phase measurement equipment actually records phase as being an integration of a frequency difference over time t, as in

$$\theta_{\mathrm{PD_a}} \propto 2\pi \cdot \int (f_2 - f_1)\,\mathrm{d}t, \tag{3.4}$$

$$\theta_{\mathrm{PD_b}} \propto 2\pi \cdot \int [(f_2 + f_{\mathrm{D}}) - f_1]\,\mathrm{d}t. \tag{3.5}$$

The phase difference between the two detectors consists of the target's displacement (including measurement uncertainty)

$$\theta_{\mathrm{ab}} = \theta_{\mathrm{PD_b}} - \theta_{\mathrm{PD_a}} \Longrightarrow \theta_{\mathrm{ab}} = \left(\frac{N \cdot n \cdot v}{\lambda_2}\right) \cdot 2\pi t. \tag{3.6}$$

By substitution of $v = s/t$, one obtains target displacement s, as in

$$s = \frac{\lambda_2 \cdot \theta_{\mathrm{ab}}}{2\pi N n}. \tag{3.7}$$

Equation 3.7 shows that target displacement s consists of an integration over time of the relative phase difference θ_{ab} between the two photo detectors. Any disturbance that causes a change in the measured phase adds measurement uncertainty, since it is interpreted as target displacement.

When the two coaxial frequencies are not perfectly separated by the interferometer's polarizing beam splitter, f_1 leaks into the optical path where only f_2 is supposed to be present (and vice versa). This results in the measurement of *multiple* superimposed beat-frequencies by $\mathrm{PD_b}$ that eventually lead to a periodic nonlinear error (i.e. PNL), which can only partially be solved by digital compensation using the error its deterministic/systematic character. Although this error can be reduced significantly it is inevitably present in this system due to the optical layout, and therefore, it presents the primary performance limiting source of error when operating in vacuum.

3.4 Conclusions

This chapter sketched a commercial state-of-the-art heterodyne interferometer system that is used as benchmark for this research. This benchmark system contains six monolithic interferometers that measure each five DoFs, and are attached to the metrology frame. These interferometers monitor three positioning stages within a near-vacuum environment, a wafer calibration stage, a wafer exposure stage and a reticle stage; each is measured by two 5-DoF interferometers, resulting in a total of 30 measurement axes.

The six 5-DoF interferometers receive their source frequencies via free-space coaxial beams that are guided via mirrors and neutral beam splitters, which are attached to the metrology frame as well. The coaxial beam originates from a remote optical combiner (ROC), which is an optical system that receives input from a heterodyne laser source via two separated single-mode polarization-maintaining optical fibers; the ROC combines these fiber outputs into a free-space coaxial beam. The transport of the interference signals away from the interferometer subsequently takes place via multi-mode optical fibers.

Comparing the free-space delivery of the coaxial beams with the transport of the fiber-coupled interference signals, it is shown that free-space propagation is a demanding means of optical transport: it has an inflexible layout and it is sensitive for environmental disturbances (e.g. vibrations and turbulence).

The final section of this chapter, Section 3.3, illustrated how displacement is measurement with the benchmark interferometer system. This section also indicated that an error source called *periodic nonlinearity* is fundamentally linked with this system due to the use of coaxial heterodyne beams.

Chapter 4

Enhancing measurement linearity

The previous chapter introduced a benchmark interferometer system that was set to operate in an EUV-lithography machine, this system functions as a technology-reference throughout this work. This chapter focuses on an inherent source of measurement error of that system: periodic nonlinearity (PNL), which is inextricably linked to the use of the coaxial beams. The origins of PNL and their result are discussed, together with a solution for reducing this error source; with the intention to improve measurement linearity.

The first section of this chapter defines what 'error sources' there are and how they affect 'measurement' uncertainty. The next section, Section 4.2, gives insight in the several origins of PNL.
In Section 4.3 it is shown that PNL can be reduced by optical redesign of the interferometer layout; it is in this section that the 'Delft' interferometer is introduced. The following section, Section 4.4, addresses the operational concept of the Delft interferometer and introduces a five-DoF monolithic interferometer design.
Testing the new interferometer design for the presence of PNL required the development of an alternative heterodyne frequency source, which ensures feeding the interferometer with two non-mixed source frequencies. The design and operation of this source are addressed in Section 4.5. With the use this alternative frequency source the Delft interferometer concept its operation is validated in Section 4.6. In the next section, Section 4.7, the interferometer its sensitivity for PNL versus input polarization is investigated. Section 4.8 discusses remaining and potential sources of PNL in the Delft interferometer design.

At final, Section 4.9 concludes that the interferometer and alternative frequency source have led to a heterodyne displacement interferometer system that shows substantially reduced levels of PNL with respect to the benchmark system; this indicates the enhancement of the measurement linearity.

This chapter contains work from a publication by the author, published in Optics Letters, titled: *Heterodyne displacement interferometer, insensitive for input polarization* [5].

4.1 Error sources and measurement linearity

An 'error source' is an unwanted input in a measurement system that adds uncertainty to the measurement outcome. There are in general two types of error sources, those that are systematic and those that are random (i.e. stochastic). Systematic error sources are said to be fully repeatable with respect to time and amplitude; these can be both static or dynamic. The influence of this type of error can be accounted for due to its predictable behavior.

The relation between the measured value and the true physical state that is being measured is proportional when there are no error sources present, or when the error sources are systematic. The proportional relation between the measured value and the measurand results in a 'linear' measurement system, which relates to *measurement linearity*.

However, an error source can also be simultaneously systematic and random as well, periodic nonlinearity (PNL) is such an error source. PNL is primarily present in heterodyne displacement interferometers that use coaxial heterodyne beams. The period of such an error can repeat itself - hence systematic in periodicity - but its starting phase, its shape, and its amplitude can be random, see Fig.4.1.

The starting phase of this error (Fig.4.1a) is related to e.g. the geometry/layout of the optics and the location of the target mirror, whereas the amplitude and shape are determined by e.g. polarization alignment and ghost-reflections, see Fig.4.1b.

PNL can (partially) be accounted for by means of calibration. Performing a 'calibration stroke', as described by [18], allows for characterization of the error with the intention to predict its influence for a specific system configuration. It is important to note that this calibration is only viable as long as the system is unchanged, a change in e.g. temperature or target rotation already reduces the accuracy of the calibration.

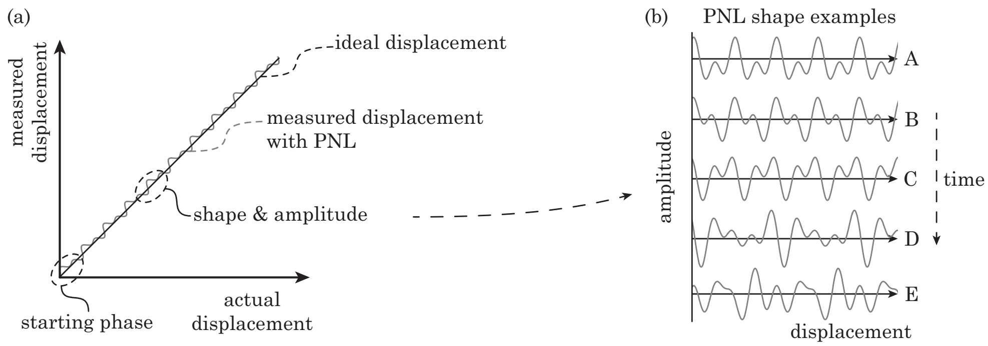

Figure 4.1: (a) PNL is an error that has a systematic repetition but a random starting phase, a random shape, and a random amplitude; these make the error nonlinear. (b) The shape of PNL is determined by the number of sinusoids that interfere with each other upon detection; this includes their relative phase, and their amplitude. As the target displaces PNL can change shape, A to E, due to varying impact of e.g. ghosting. PNL thus consists of at least two (un)related interference signals and can manifest in complex shapes.

4.2 The origins of periodic nonlinearity (PNL)

PNL manifests itself with traditional heterodyne interferometers that use coaxial heterodyne beams, see Fig.4.2. These beams carry two linearly polarized source frequencies that are separated using polarizing optics, such as a polarizing beam splitter as illustrated in Fig.4.2b. During this separation process the frequencies may mix due to *frequency leakage* (briefly described at the end of Section 3.3), which eventually results in periodic errors that are superimposed on the obtained displacement data. This frequency leakage is caused amongst others by imperfect polarization orthogonality and linearity of the source frequencies combined with imperfect polarizing optics and non-ideal alignment [19]. In other words, due to polarization related imperfections encountered in reality, polarization based frequency splitting of coaxially placed source frequencies results inevitably in frequency leakage.

Another source of PNL is formed by back-reflections (i.e. ghost-reflections) in the interferometer system [20]. These are internal reflections that cause unwanted optical pathways both inside the interferometer optics as well as between the interferometer and the target mirror. To exemplify, in the ideal case f_2 travels between the interferometer and target two times, see Fig.4.2b, there are however situations possible where this frequency traverses this distance more or less often than the usual two times before it reaches detector $\mathrm{PD_b}$; leading to the presence of PNL in the measurement output. The systematic part of PNL is correlated to target movement and is determined by:

$$f_{\mathrm{PNL}} = (k \cdot N \cdot v)/\lambda. \tag{4.1}$$

This relation indicates the *fringe-order* when visualizing the displacement measurement data in the frequency-domain; v [m/s] represents the target's displacement velocity, k expresses the n^{th} fringe-order, N represents the interferometer's fold-factor

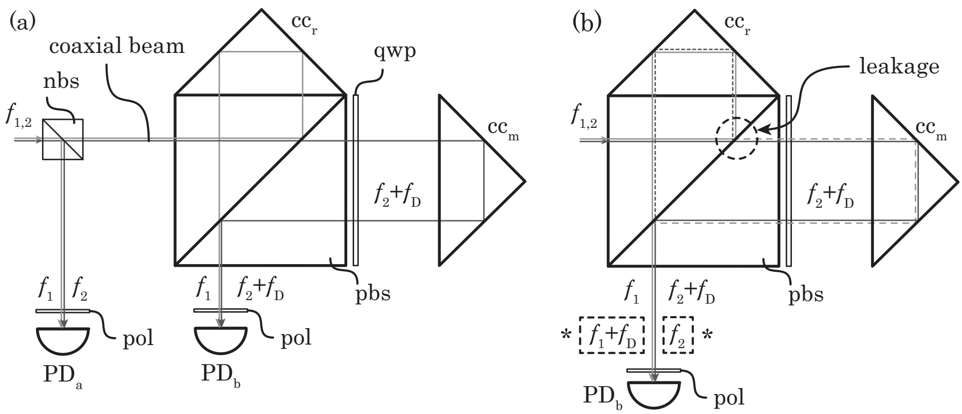

Figure 4.2: (a) A heterodyne displacement interferometer showing *ideal* polarization based frequency splitting of the coaxial beams. (b) Illustration of *imperfect* frequency splitting due to e.g. misalignment or imperfect polarization properties of the coaxial beam or beam splitter; leading to frequency leakage. This results in two additional interference components, denoted by an *; leading to the detection at $\mathrm{PD_b}$ of five superimposed interference signals: (I) f_1 with f_1+f_D, (II) f_1 with f_2+f_D, (III) f_1 with f_2, (IV) f_2 with f_1+f_D, and (V) f_2 with f_2+ f_D. Legend: f_x, source frequency; f_D, Doppler frequency; nbs, neutral beam splitter; pbs, polarizing beam splitter; pol, polarizer; qwp, quarter wave plate; $\mathrm{cc_r}$, reference cube corner reflector; $\mathrm{cc_m}$, measured cube corner reflector; and $\mathrm{PD_x}$, photodetector.

(N = 2 in the case of Fig.4.2, i.e. the frequency traverses two times between the interferometer and the measurement target), and λ being the used wavelength. The reason for calculating a frequency, f_{PNL}, is related to the method of PNL visualization by means of Fourier Transformations, which is explained in Section 4.7.2.

PNL that originates from frequency leakage caused by imperfect polarization splitting shows up at different frequency locations than PNL that originates from ghost-reflections. PNL resulting from frequency leakage shows up at fringe-orders given by $k = i$, where i is a positive integer value; whereas ghost-reflections result in PNL at locations that are given by $k = i \cdot \frac{1}{j}$, where j = 2 at minimum (PNL from ghost-reflections is further addressed in Section 4.8.1.). Experience has shown that the presence of PNL due to frequency leakage is significantly larger than PNL caused by ghost-reflections.

There are several approaches for reducing PNL in coaxial interferometer systems. Physically reducing PNL is one of the most costly methods since it involves expensive high quality optics and routinely based individual system alignment. This reduction approach is based upon the source frequency orthogonality quality of the coaxial beams together with the quality of their linear polarizations. If these are of high quality it is also essential that high quality polarizing optics are applied for beam splitting, combined with accurate alignment [19,21–24]. The ideal result is a perfect split of the two coaxial frequencies into a measurement frequency and a reference frequency, as illustrated in Fig.4.2. The result is that the beat-frequency detected by $\mathrm{PD_b}$ only consists of the interference between an unmodified reference frequency, f_1, and a Doppler shifted measurement frequency, f_2.

A less expensive approach is to digitally compensate for PNL by analytical modeling [19,24–26]. The advantage of this method is that it typically ensures PNL below 1 nm for small system imperfections without changing the interferometer configuration. However, some of these methods require (periodic) calibration, a minimum displacement per time frame, and additional calculation time compared to uncompensated systems. These drawbacks make PNL compensation algorithms difficult or unsuitable to apply to (quasi) static and small stroke systems, or systems that require near real time operation, depending on the applied algorithm.

The stages in the lithography machine move sufficiently fast and with large enough strokes to perform intermediate calibrations during wafer handling. Still, the calibration stroke requires a small stroke at start, which consumes a part of the overall stroke, as well as time (although the calibration stroke is negligibly small compared to the required 500 mm measurement stroke). Furthermore, after the calibration stroke, all obtained displacement data requires to be digitally compensated, which consumes time and affects the data-age of the displacement information. It is important to realize that data handling is critical due to the relatively high stage velocities, 1 to 2 m/s at 50-60 m/s^2 for the wafer stages, and 4 m/s at 400 m/s^2 for the reticle stage. Therefore, the data-age is ideally kept as small and constant as possible (further addressed in Section 7.3).

The ideal solution would be to have no PNL in the first place, so that compensation is not needed. This can be obtained by spatial separation of the two beams that carry the different source frequencies, and keeping them separated throughout the interferometer until detection takes place [3, 4, 9, 27–31]. This spatial separation cancels the need for polarization based splitting and prevents frequency leakage to occur, and thereby, it eliminates a primary source of PNL.

4.3 Reducing PNL

The previous section proposed a solution to substantially reduce PNL: using two separated optical beams (each containing one source frequency) and keeping these beam separated throughout the interferometer until detection. Transporting the source frequencies separately instead of using one coaxial beam eliminates the need to separate the two frequencies at the interferometer using polarizing optics, this prevents frequency leakage and removes the need for PNL compensation.

Unfortunately, immediate implementation of the 'separated source frequency transport' concept into the benchmark system (compare Figs.4.3a and b) would not operate as wanted. In the case of a coaxial beam both source frequencies propagate along the same optical pathway and are thereby influenced equally when disturbed (e.g. mirror vibration). In contrast, separated optical beams (each transporting one source frequency) can be affected unequally when exposed to external disturbances, which is especially problematic after generating the common reference signal at PD_a (i.e. at the ROC). One could assume that having two of such optical beams propagating closely together approaches the operation of a coaxial beam (Fig.4.3b, addressed in a patent from *Agilent Technologies* [32]); this may, however, not be assumed that easily when aiming for sub-nm measurement uncertainty. In that specific situation PNL is reduced at the cost of additional measurement uncertainty due to e.g. turbulence, which potentially leads to an even larger amount of measurement uncertainty.

Using two separated optical beams for source frequency delivery while aiming for sub-nm uncertainty necessitates placement of a reference signal at the interferometer (see Fig.4.3c and d). In the two sketches each detector receives both frequencies, which is a prerequisite for excluding influences from disturbances that act upon the optical transport of the separated source frequencies (see next Section).

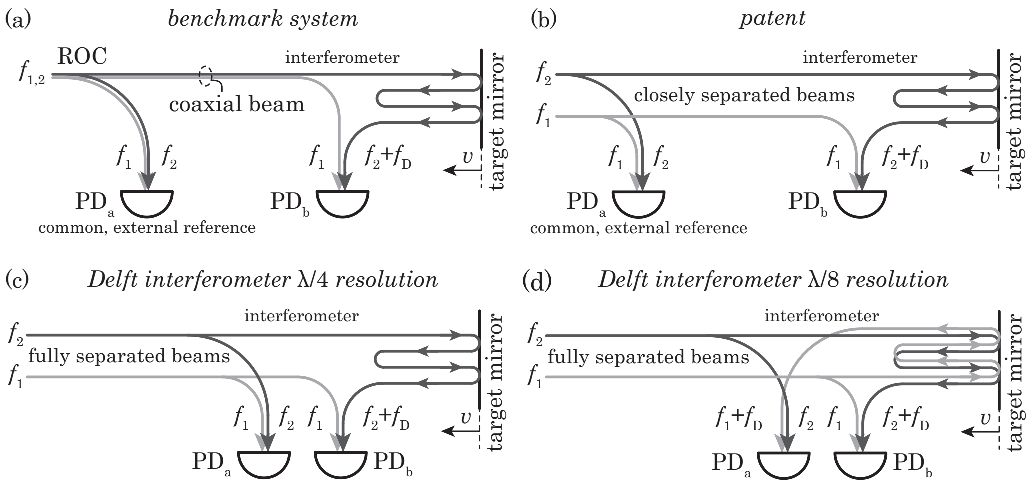

Figure 4.3: (a) Coaxial beam optical transport in the benchmark system. (b) Employment of separated source frequency delivery while using the original photodetector locations; described in a patent from *Agilent Technologies* [32]. Illustrations (c) and (d) are related to the Delft interferometer concept, both show the generation of a reference signal at the interferometer, instead of using an external reference. The optical layout depicted in (d) results in twice the displacement resolution compared to (c), see also Section 4.4.

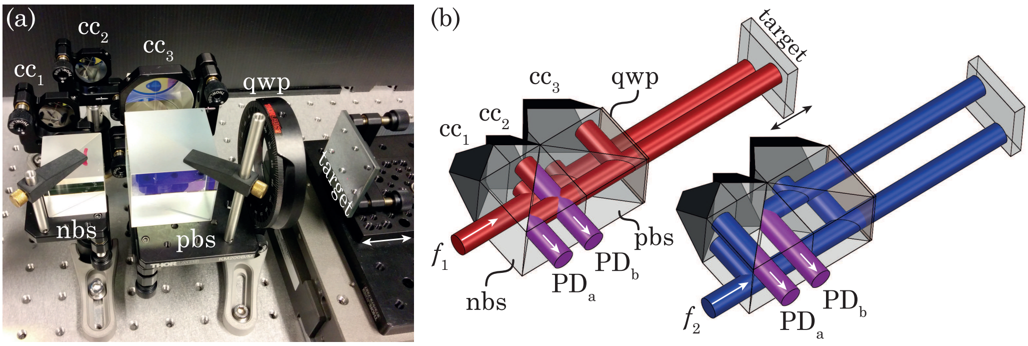

Figure 4.4: (a) The illustration shows a laboratory setup of the Delft interferometer with a λ/8 resolution, using cuber corner reflectors that aid in alignment (improved with respect to preceding research). (b) 3D overview of the same setup, indicating the optical pathways of the two frequencies through the interferometer. Legend: cc_x, cube corner reflectors; f_x, source frequency; PD_x, photodetector; nbs, non-polarizing beam splitter; pbs, polarizing beam splitter; and qwp, quarter wave plate.

The optical layout sketched in Fig.4.3d was used for building an experimental setup, shown in Fig.4.4. This setup was used for investigating the sensitivity of the interferometer regarding polarization related misalignment and the presence of PNL in the measurement.

Although the laboratory setup was well suited for testing the concept of the Delft interferometer, for practical reasons it is important to decrease the size of its optics; minimizing instrument volume is beneficial in view of host-system implementation. As illustrated in Fig.4.4a, the polarizing beam splitter can actually be used twice and removes the need for the neutral beam splitter, resulting in an interferometer having almost half the optical volume.

Another improvement is the placement of the optical pathways in a single plane as shown in Fig.4.5b, which also allows for 'stacking' when creating a multiple DoF interferometer (see Section 4.4.3).

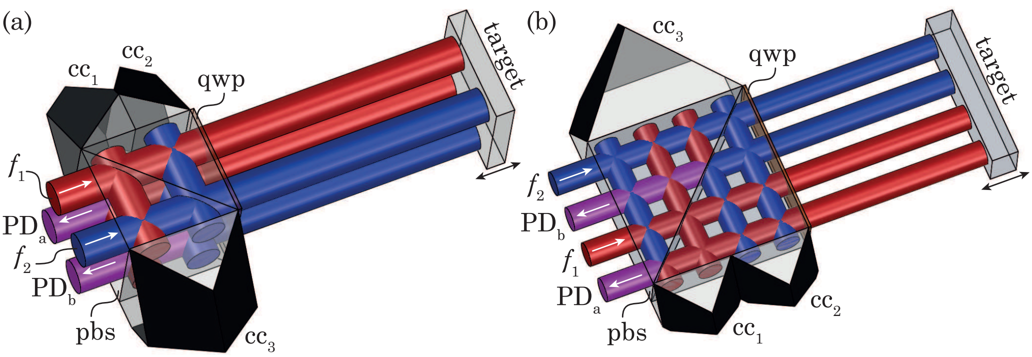

Figure 4.5: Two new single DoF Delft interferometers using plane mirror targets that have minimized optical volume, and can be stacked for measurement of multiple DoFs.

4.4 Operational concept of a Delft interferometer

Chapter 3 clarified how displacement is measured with the benchmark system, the same is described in this section for two types of Delft interferometers that both measure a single DoF. This analysis uses the conditions mentioned in Section 3.3.

4.4.1 Single DoF, reference mirror concept

The primary design of the Delft interferometer shows much resemblance with the benchmark system. In this case the Delft interferometer uses frequency f_1 for measuring target displacement while frequency f_2 reflects off a mirror attached to the optically monolithic interferometer itself. The following equations are similar to those of the benchmark system from Section 3.3, and are repeated for comparison with the Delft interferometer's *doubled resolution* concept in the following section.

In accordance to Fig.4.6, the interference signals at the photodetectors are proportional to

$$I_{\mathrm{PD_a}} \propto f_2 - (f_1 + f_{\mathrm{D}\lambda 1}) \,, \text{ and } \; I_{\mathrm{PD_b}} \propto (f_2 + f_{\mathrm{D}\lambda 2}) - f_1, \tag{4.2}$$

where $f_{\mathrm{D}\lambda 1} = \frac{N \cdot n \cdot v}{\lambda_1}$, which is nonzero, and $f_{\mathrm{D}\lambda 2} = \frac{N \cdot n \cdot v}{\lambda_2}$, which is essentially zero. Obtaining the phase for the detectors, measured over a time t:

$$\theta_{\mathrm{PD_a}} \propto 2\pi \cdot \int [f_2 - (f_1 + f_{\mathrm{D}\lambda 1})]\, \mathrm{d}t, \text{ and } \; \theta_{\mathrm{PD_b}} \propto 2\pi \cdot \int (f_2 - f_1)\, \mathrm{d}t. \tag{4.3}$$

Target displacement is subsequently obtained via a differential operation between the phase obtained using these detectors

$$\theta_{\mathrm{ab}} = \theta_{\mathrm{PD_b}} - \theta_{\mathrm{PD_a}} \Longrightarrow \theta_{\mathrm{ab}} = \left(\frac{N \cdot n \cdot v}{\lambda_1}\right) \cdot 2\pi t. \tag{4.4}$$

Substitution of $v = s/t$, results in obtaining the target's displacement:

$$s = \frac{\lambda_1 \cdot \theta_{\mathrm{ab}}}{2\pi N n}. \tag{4.5}$$

This outcome is similar to the outcome obtained for a benchmark interferometer, with the difference in the location of the reference signal (compare Fig.3.5 and 4.6), and using separated optical pathways for the two frequencies. A Delft interferometer generates a reference signal at the interferometer, whereas the benchmark interferometer uses the common reference off the interferometer, i.e. at the ROC.

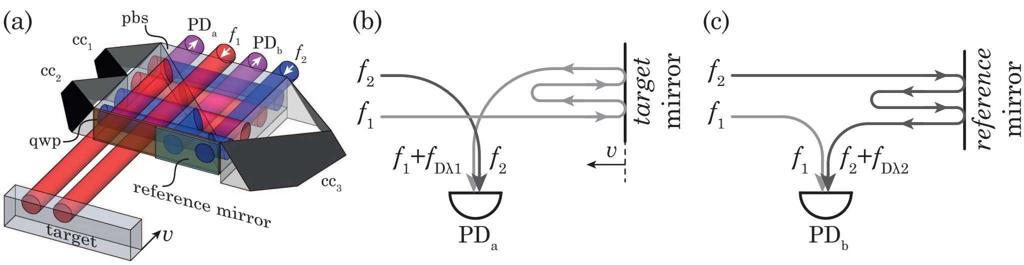

Figure 4.6: With a Delft interferometer target displacement is obtained by means of a differential phase measurement based on interference signals from photodetectors $\mathrm{PD_{a,b}}$, both located at the interferometer.

4.4.2 Single DoF, doubled resolution concept

The Delft interferometer concept shown in the previous section can be further extended by also using f_1 for measuring the target, illustrated in Fig.4.7, which results in a doubling of the measurement resolution as shown by the following analysis.

The beat-frequency at both detectors is equal when the target is stationary, which is in accordance with the benchmark system and the previous Delft interferometer. Additional observation showed that upon target movement the beat-frequency at one photodetector kept unaltered; see Fig.3.5 and Fig.4.6. However, for this interferometer, as the target moves the beat-frequency at both detectors is altered:

$$I_{\mathrm{PD_a}} \propto f_2 - (f_1 + f_{\mathrm{D}\lambda 1}), \text{ and } I_{\mathrm{PD_b}} \propto (f_2 + f_{\mathrm{D}\lambda 2}) - f_1, \tag{4.6}$$

where $f_{\mathrm{D}\lambda 1} = \frac{N \cdot n \cdot v}{\lambda_1}$ and $f_{\mathrm{D}\lambda 2} = \frac{N \cdot n \cdot v}{\lambda_2}$. From these equations can be seen that upon a movement in the positive direction the beat-frequency at $\mathrm{PD_a}$ increases while it decreases at $\mathrm{PD_b}$; and vice versa for a movement in the negative direction. This causes a relative difference between the two beat-frequencies that is proportional to two times the interferometer's fold factor, N. In contrast, for the benchmark interferometer or the Delft interferometer from the previous section, one measures with an optical resolution that equals N.

In a similar fashion to the previous section it can be derived that:

$$\theta_{\mathrm{PD_a}} \propto 2\pi \cdot \int [f_2 - (f_1 + f_{\mathrm{D}\lambda 1})]\,\mathrm{d}t, \text{ and } \theta_{\mathrm{PD_b}} \propto 2\pi \cdot \int [(f_2 + f_{\mathrm{D}\lambda 2}) - f_1]\,\mathrm{d}t. \tag{4.7}$$

Taking the difference:

$$\theta_{\mathrm{ab}} = \theta_{\mathrm{PD_b}} - \theta_{\mathrm{PD_a}} \Longrightarrow \theta_{\mathrm{ab}} = \left(\frac{N \cdot n \cdot v}{\lambda_2} + \frac{N \cdot n \cdot v}{\lambda_1}\right) \cdot 2\pi t. \tag{4.8}$$

Once more, substituting $v = s/t$, results in obtaining the target's displacement:

$$s = \frac{\lambda_1 \lambda_2 \cdot \theta_{\mathrm{ab}}}{2\pi N n \cdot (\lambda_1 + \lambda_2)}, \tag{4.9}$$

where θ_{ab} contains twice the target's displacement. This analysis shows that the Delft system obtains target displacement analogous to the benchmark system with the advantage of having twice the displacement resolution.

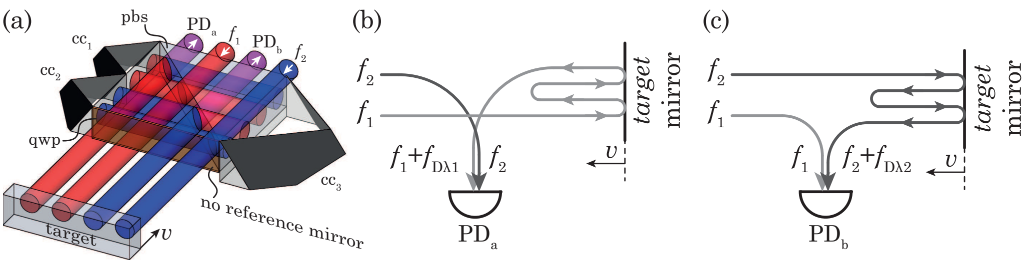

Figure 4.7: This version of the Delft interferometer equals the interferometer from Fig.4.6 with the difference that f_1 does not receive information of a mirror fixed to the interferometer but from the same target that also reflects f_2.

It is important to realize that this interferometer actually consists of two separate interferometers that both have an optical resolution of $\lambda/4$ (which is relevant when calculating the fringe-order locations in Section 4.7). Therefore, the $\lambda/8$ displacement resolution can be split into an *optical resolution* and a *digital resolution*. The optical resolution is related to the interferometer its fold factor (i.e. $N = 2 \rightarrow \lambda/2$ opt. res., $N = 4 \rightarrow \lambda/4$ opt. res.), next, the operation of the Delft interferometer causes this resolution to double upon digital processing – hence 'digital resolution'.

4.4.3 Measuring multiple DoFs

The two presented Delft interferometer configurations are limited to the measurement of only one DoF. By means of combining and stacking these configurations one obtains a 5-DoF interferometer, which can be manufactured as an optical monolith similar to the optically monolithic interferometers from the benchmark system. The interferometer illustrated in Fig.4.8 achieves 5-DoF measurement by measuring target displacement with several pairs of optical beams and combining their results. Each displacement (s) is comprised of a phase difference between two detectors:

1st DoF: $s_{\mathrm{x}} = \theta_{\mathrm{PD_a}} - \theta_{\mathrm{PD_b}}$

2nd DoF: $s_{\mathrm{z}} = s_{\mathrm{ef}} - s_{\mathrm{x}}$, where $s_{\mathrm{ef}} = \theta_{\mathrm{PD_e}} - \theta_{\mathrm{PD_f}}$

3rd DoF: $\mathrm{roll} = \arctan\left(\frac{s_{\mathrm{ec}} - s_{\mathrm{fc}}}{Y}\right)$, where $s_{\mathrm{ec}} = \theta_{\mathrm{PD_e}} - \theta_{\mathrm{PD_c}}$ and $s_{\mathrm{fc}} = \theta_{\mathrm{PD_f}} - \theta_{\mathrm{PD_c}}$

4th DoF: $\mathrm{pitch} = \arctan\left(\frac{s_{\mathrm{ac}} - s_{\mathrm{dc}}}{Z}\right)$, where $s_{\mathrm{ac}} = \theta_{\mathrm{PD_a}} - \theta_{\mathrm{PD_c}}$ and $s_{\mathrm{dc}} = \theta_{\mathrm{PD_d}} - \theta_{\mathrm{PD_c}}$

5th DoF: $\mathrm{yaw} = \arctan\left(\frac{s_{\mathrm{ac}} - s_{\mathrm{bc}}}{Y}\right)$, where $s_{\mathrm{ac}} = \theta_{\mathrm{PD_a}} - \theta_{\mathrm{PD_c}}$ and $s_{\mathrm{bc}} = \theta_{\mathrm{PD_b}} - \theta_{\mathrm{PD_c}}$

The displacement over the x- and z-axis are both determined with a resolution of $\lambda/8$, whereas the linear displacement used for the rotational DoFs has a resolution of $\lambda/4$ because these are determined with respect to the reference mirror. If necessary, the angular resolution can be increased by enlarging the distance between the optical measurement beams (denoted by Y and Z in Fig.4.8). However, this increases the size of the interferometer optics, resulting in an expanded instrument volume that is unwanted due to the limited space available in e.g. a lithography machine.

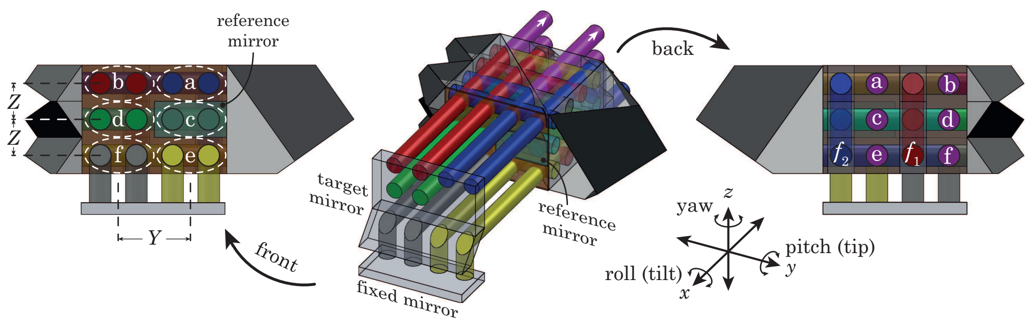

Figure 4.8: 3D representation of a monolithic Delft interferometer that measures 2 translational DoFs (i.e. x and z-displacement) and 3 rotational DoFs. The ingoing source frequencies are indicated by $f_{1,2}$, and the six outgoing interference signals to the photodetectors are given by **a** to **f**. The illustrated 'target mirror' and 'fixed mirror' represent only a part of the actual mirrors, the 'target mirror' continues in the y direction and the 'fixed mirror' covers a much larger surface area in the xy plane.

4.5 Alternative heterodyne frequency source

To test if the Delft interferometer concept achieves PNL reduction through the use of its separated optical pathways, it requires to be provided with non-mixed source frequencies. In this way it is ensured that when PNL is measured it originates from the interferometer and not from the heterodyne frequency source. This section explains how the frequency source of the benchmark system operates and why this research required an alternative frequency source.

The laser source of the benchmark system consists of a single-mode Helium Neon (HeNe) laser that produces two frequencies via the Zeeman effect (where a magnetic field splits the spectral line). This laser source outputs a coaxial beam that carries two different frequencies that are counter rotating circularly polarized. After exiting the laser cavity these beams propagate through a quarter wave plate (qwp) that converts the circular polarization states into two linear orthogonal polarization states.

This resulting coaxial beam is comprised of one beam (containing one source frequency) with a vertically aligned linear polarization state, and one beam (containing another source frequency) with a horizontally aligned linear polarization state. The two source frequencies are then separated by means of polarization based splitting of the coaxial beam (using a polarizing beam splitter) after which each beam propagates through an acousto optic modulator (AOM) to further increase their frequency offset (i.e. the 'split frequency'). The output of the two AOMs is then coupled into separate single-mode polarization-maintaining optical fibers, which transport the two beams to the ROC inside the host-system.

As shown in Section 3.3, the frequency difference between the two source frequencies limits the maximum target velocity in one direction (via the Doppler shift). It is thus preferred to have a split frequency that is substantially larger than the maximum expected Doppler frequency.

However, as the frequency split generated via the Zeeman effect increases, the optical output power of the laser source decreases. A solution to this is provided by the use of AOMs that extend the frequency split from the Zeeman effect. The combination of a small Zeeman split that is extended by AOMs results in a heterodyne frequency source that provides a large enough frequency offset, and delivers sufficient optical power to supply the many measurement axes.

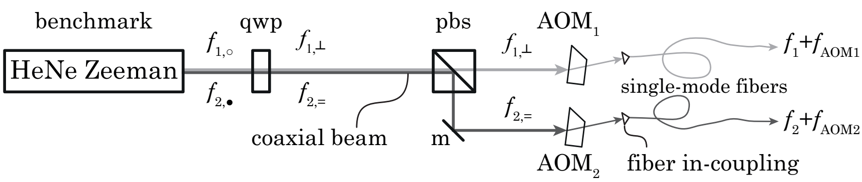

Figure 4.9: Schematic representation of the heterodyne frequency generation in the benchmark system, where the split frequency of the frequency output of a HeNe Zeeman is increased by two *(explained in the text)* acousto-optic modulators (AOMs). Legend: qwp, quarter wave plate; ●, left handed circular polarization; ○, right handed circular polarization; $\perp$, vertical linear polarization; =, horizontal linear polarization; f_x, optical frequency; AOM$_x$, acousto-optic frequency modulator; pbs, polarizing beam splitter; and m, mirror.

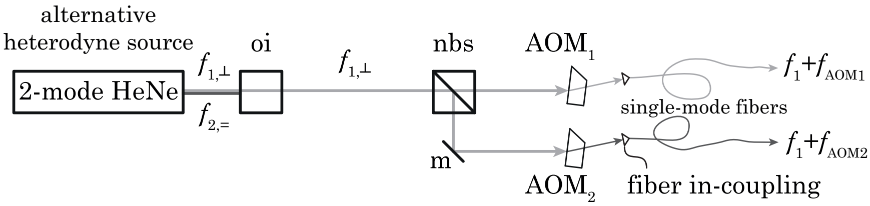

Figure 4.10: A two mode HeNe laser is used, where only one frequency passes an optical isolator (oi) and is frequency offset by two AOMs. Legend: $\perp$, vertical linear polarization; =, horizontal linear polarization; f_{X}. optical frequency; AOM$_{\mathrm{X}}$, acousto-optic frequency modulator; nbs, neutral beam splitter; and m, mirror.

**Instead of using two AOMs also a single AOM could be employed (modulating only one of the two beams after the polarizing beam splitter), unfortunately, this would result in a split frequency that is larger than the detection bandwidth of the phase measurement equipment. Most commercially available AOMs have a small sized crystal that operates at frequencies of several tens of MHz in order to obtain a sufficiently large mode separation, increasing the size of the crystal results in larger mode separation at lower operating frequencies, nevertheless, these are commercially limited available and expensive. A commercially more often applied concept that stays within the measurement bandwidth of the phase measurement equipment consists of two smaller AOMs that operate at frequencies that only differ a few MHz.*

Unfortunately, the use of a coaxial beam inherently results in mixed source frequencies that lead to PNL (even with the use of a Delft interferometer, as the frequency mixing occurs prior to the interferometer). As explained earlier, this is related to the polarization based frequency splitting of the linearly polarized beams. There are several parameters that affect the amount of frequency leakage, (indexed based on the likelihood/level of leakage, from high to low):

1. rotational alignment of the qwp relative to the polarizing beam splitter

2. purity of the polarization states before and after the qwp

3. orthogonality of the two polarizations

Optimization of the (polarization related) alignment between the qwp and the pbs minimizes frequency leakage, still, frequency leakage will be imminently present. Additionally, thermal fluctuations and vibrations influence the amount of frequency leakage via the relative alignment between the qwp and the pbs.

Fortunately there are other methods to stably produce two offset frequencies that are phase coupled (i.e. sharing the same source). The heterodyne frequency source employed throughout this research consisted of a two-mode HeNe laser (i.e. one mode is a frequency) that was frequency stabilized via thermal stabilization of the laser cavity length, which was based upon mode intensity balancing.

The two output frequencies of this laser are fundamental to its cavity-length, which supports two linearly orthogonally polarized modes separated by about 600 MHz. Upon exiting the laser cavity one of the beams is blocked (based upon its polarization[1]) by an optical isolator (using magnetic Faraday rotation), which in combination

[1]Note that also here the 'blocked' mode could 'leak' into the system upon imperfect polarization based splitting, however, due to the 600 MHz difference this leakage is much less detrimental to the measurement uncertainty than the leakage of a frequency that differs only a few MHz from the received beating signal.

with a linear polarizer also prevents back-reflections from reentering the laser cavity (avoiding destabilization of the lasing process). The transmitted beam (ideally containing only one frequency) is split using a neutral beam splitter (nbs) whose two exiting beams propagate to two AOMs that together apply a ~2 MHz frequency offset (i.e. one operated at 39 MHz and one at 41 MHz), resulting in two spatially separated beams of which each transports one frequency.

Besides providing non-mixed source frequencies, another advantage of this method is the available amount of optical power. The output power of the used stabilized two-mode HeNe laser is already ~2.5 mW *(Thorlabs, frequency stabilized HeNe laser, model HRS015, which was used throughout this research)* of which half is used (i.e. one mode), in contrast, the benchmark's laser source is more advanced but provides at maximum ~1 mW [33]. This higher output power enhances the signal-to-noise ratio and aids improving the measurement accuracy (see Section 7.4).

Additionally, instead of a 2-mode laser also a 3-mode laser could be used, whose center mode provides an amount of optical power that approaches 2 mW while its two (equally polarized) outer modes are blocked.

4.6 Validating the operational concept

To validate and study the operational concept of the Delft interferometer, an experimental setup was built using the Delft doubled resolution configuration, see Fig.4.11. The setup consisted of the interferometer illustrated in Fig.4.4, which received the source frequencies via free-space from the alternative frequency source. Three photo detectors as illustrated in Fig.4.11a, were used to visualize the individual interference signals received by PD_2 and PD_3, using PD_1 as a reference.

The source frequencies in this setup are exposed to unknown and uncontrollable disturbances (e.g. air turbulence, or motion of individual optical components) that affect the source beams of both source frequencies differently, denoted by θ and φ.

Figure 4.12a shows the target displacement over time using a mirror that was mounted on top of a linear stage *(Aerotech, model ABL10100LT)*, which was programmed to move away from the interferometer at a 'constant' velocity of 0.5 mm/s. The three

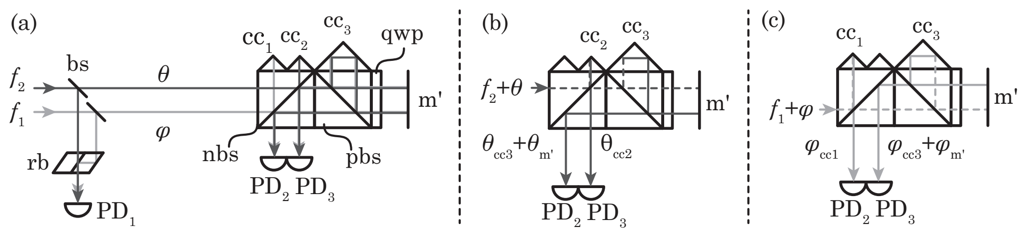

Figure 4.11: (a) Experimental setup for studying the measurement operation of a Delft doubled resolution interferometer. (b), (c) Illustrating the optical pathways of f_1 and f_2 respectively (dotted lines denote beams in the lower plane whereas solid lines are beams in the upper plane). Legend: f_x, source frequency; bs, beam sampler; rb, rhomboid; PD_x, photodetector; m, mirror; nbs, neutral beam splitter; pbs, polarizing beam splitter; cc_x, cube corner reflector; qwp, quarter wave plate; and m´, target mirror.

lines represent the displacement that was obtained through three differential measurements, $PD_{3\text{-}2}$, $PD_{2\text{-}1}$, and $PD_{3\text{-}1}$, where the indices indicate between which photodetectors the differential measurement was performed.

The combination of a target that was moving away from the interferometer, together

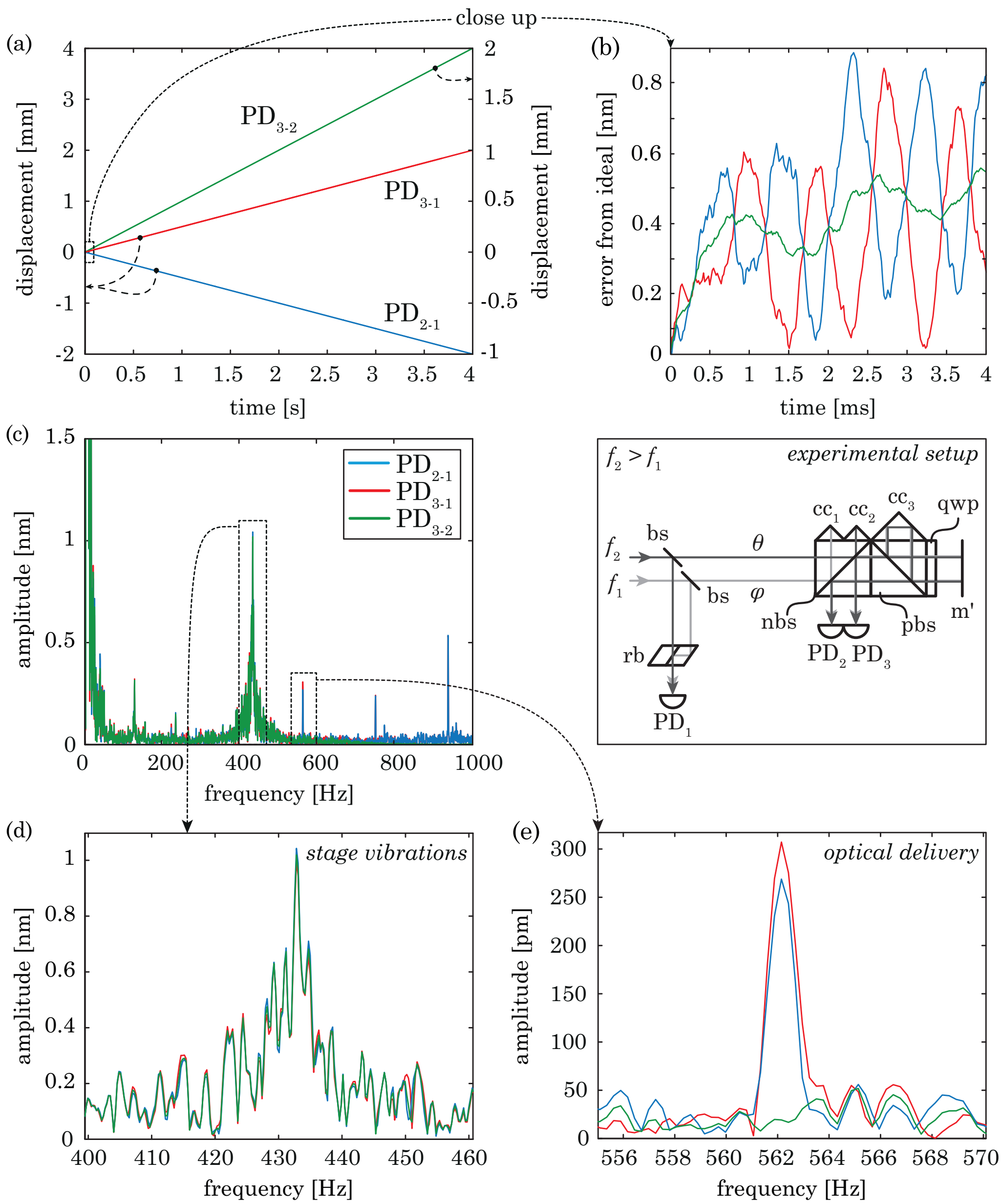

Figure 4.12: Results from a target moving with a constant velocity of 0.5 mm/s. (a) Displacement of $PD_{3\text{-}2}$ (i.e. PD_2 minus PD_3) is put on a secondary axis to indicate that it consists of the differential result of $PD_{3\text{-}1}$ minus $PD_{2\text{-}1}$. (b) A close up of (a), showing the error with respect to an ideal straight line; the mirrored peaks (red and blue) indicate disturbances in the optical delivery, see also Section 5.3. (c) to (e) By looking at the displacement in the frequency domain one can distinguish the origin of the disturbance.

with $f_2 > f_1$, resulted in a decrease of the beat-frequency at PD_2 with respect to the beat-frequency measured by PD_1; whereas the beat-frequency at PD_3 increased relative to PD_1. This led to the measurement of a *negative* displacement using a differential measurement between PD_2 and PD_1 (i.e. $PD_{2\text{-}1}$), whereas the differential result between the other two detectors pairs was positive, illustrated in Fig.4.12a. Due to this 'opposite displacement' the differential result from $PD_{3\text{-}2}$ contains twice the actual displacement. These results confirm that the two individual interferometers measure with an optical resolution of $\lambda/4$, while they together constitute an overall resolution of $\lambda/8$.

Figure 4.12b shows more detailed that the result from $PD_{3\text{-}2}$ originates from the differential operation: $PD_{3\text{-}1}$ minus $PD_{2\text{-}1}$. The output of the detector pairs $PD_{2\text{-}1}$ and $PD_{3\text{-}1}$ show deviations of a few tens of nm, which are primarily constituted by θ and φ. As shown, every disturbance arrives at PD_2 as well as at PD_3, therefore, a differential measurement between these detectors partially[2] resolves these deviations.

The frequency spectrum of the three differential signals is shown in Fig.4.12c, this spectrum is calculated from a Fast Fourier Transform (FFT) operation, applied to the data shown in Fig.4.12a. Visualization of the data in the frequency domain enables to distinguish between two different types of disturbance sources; achieved by using the reference signal from PD_1. The close-up shown in Fig.4.12d shows that the outputs of all three signals are overlapping, which indicates that the disturbances in this frequency region originate from stage vibrations since the displacement from the three differential signals coincides. Figure 4.12e on the other hand shows significant amplitudes for the differential signals from $PD_{1\text{-}2}$ and $PD_{1\text{-}3}$, while $PD_{2\text{-}3}$ almost shows no amplitude, indicating that the disturbance at this frequency is incurred during source frequency transport between PD_1 and the interferometer.

Taking into account these results and the interferometer's operation one can conclude that the output of the two interferometers (that together constitute the Delft interferometer) is allowed to include disturbances, provided that the influence of each disturbance is equal in amplitude for both interferometers, and that there is no phase difference between the detectors PD_2 and PD_3 (see Section 7.3). When these conditions are met, any disturbance other than target displacement will be excluded from the measurement due to the differential operation. This also holds for the presence of PNL in the Delft interferometer: the two individual interferometers may contain PNL, as long the PNL from PD_2 and PD_3 are mirror images, in which case any PNL will be canceled. This indicates the significance of optical symmetry between the two interferometers and emphasizes the importance of having an optically monolithic structure to optimize the symmetry as much as possible.

4.7 Validating PNL versus input polarization

The PNL of coaxial heterodyne interferometers is highly influenced by the polarization state and orientation of the source beams. In this section it is validated that the Delft interferometer used during this research shows very low levels of PNL regardless of the polarization state and/or polarization orientation of the free-space delivered source light. During the experiments manipulation of the polarization state and

[2]Only 'partially', since phase differences between PD_2 and PD_3 caused by asymmetry in the non-monolithic interferometer setup result in incomplete cancellation, see Section 7.3.

polarization orientation was achieved by means of manually rotated quarter-wave plates (qwps) and half-wave plates (hwps), respectively. The outcomes obtained with two Delft interferometers were compared with the results of a traditional coaxial system [34] that was subjected to equal polarization manipulation.

PNL was visualized by fitting an n^{th}-order polynomial through obtained displacement data that originated from target mirrors that were mounted on the linear *Aerotech* stage, which was programmed to move at 'constant' velocity. Using a target that moves at constant velocity helps visualizing periodic effects in the frequency domain, constant movement aids in the determination of the specific frequency and the amplitude of the disturbance.

The polynomial fit was subsequently subtracted from the displacement data themselves, thereby removing macro-scale motion and quasi-static effects (i.e. thermal deformation or source frequency drift). The resulting data set was then analyzed by means of fast Fourier transform, revealing the location (i.e. frequency, fringe-order) and the amplitude of any PNL [35–37]. The frequency locations of the PNL that is related to the operation of the interferometer were determined using Eq.4.1. For the FFT analysis a 'flat top' window has been applied, providing the best amplitude accuracy for determination of the PNL and noise level amplitudes. Processing the data as described combined with f_{PNL} in the kilohertz range makes the measurement method insensitive for long time constant effects, which helped in lowering the noise level.

4.7.1 Capacitive probe stage motion analysis

The FFT data analysis used for visualization of PNL also includes peaks caused by mechanical vibrations, and by (potential) PNL from the *Aerotech* stage. In order to draw correct conclusions from the frequency domain data it was important to know whether PNL from the interferometer coincided with these other phenomena, otherwise false PNL results were obtained. Therefore, stage motion was investigated with a capacitive probe [38], which has a low noise level and is inherently free of PNL. Measurements were performed at different stage locations (due to the capacitive probe's short measurement stroke of 100 μm), after which the obtained data were processed in the same way as previously described. Analysis showed no distinct peaks from vibrations or PNL from the stage itself at the frequencies where PNL of the interferometer manifests (i.e. 1^{st}, 2^{nd}, 3^{rd}, etc. fringe-order).

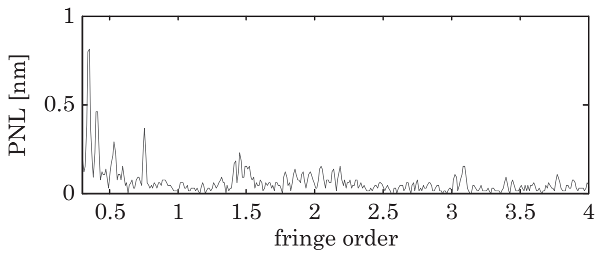

Figure 4.13: Capacitive probe measurements confirm that the single DoF *Aerotech* stage did not exhibit significant periodic nonlinearity at the frequencies/fringe-order of interest. *Note that for expressing the horizontal scale in 'fringe-order' the displacement data was divided by Eq.4.1.*

4.7.2 PNL versus input polarization state and orientation

Note that polarization 'state' refers to the state of the polarization, which can go from full linear to full circular. The polarization 'orientation' refers to the relative rotational orientation of the polarization 'state' with respect to either the environment or a polarized optical component. For example: a linear polarization state can be oriented vertically, horizontally or anything in between.

For the first measurement, the linear polarization states of the free-space coaxial beams entering the benchmark interferometer, were reoriented (i.e. misalignment) with respect to the polarizing axis of the interferometer optics. This was done using a half-wave plate (hwp) at wpl_1 (see Fig.4.14a).

Figure 4.15a shows the results when the hwp rotated the polarizations between about 15° clockwise and counterclockwise. At these maxima the commercial system ceased operating because the PNL became too large for the electronics to continue measuring. Noticeable is the V-shape (i.e. comprised of two nearly straight lines, indicating a somewhat proportional relation to first fringe-order PNL) of the first fringe-order and the bowl shape of the second- and higher fringe-orders of which the shape flattens as the fringe-order increased [35, 36].

Two different types of Delft interferometers were tested in an equal manner but supplied with two separated source frequencies rather than coaxially placed source frequencies. These interferometers concerned a *Delft-CC* type with a λ/4 optical resolution See Fig.4.14b), and a *Delft-PM* type with a λ/8 optical resolution [9], see Fig.4.14c. With these interferometers, a hwp was inserted into beam f_1 (i.e. wpl_2, Fig.4.14a) while f_2 was kept linearly (vertically) polarized. The results are shown in Figs.4.15c and d.

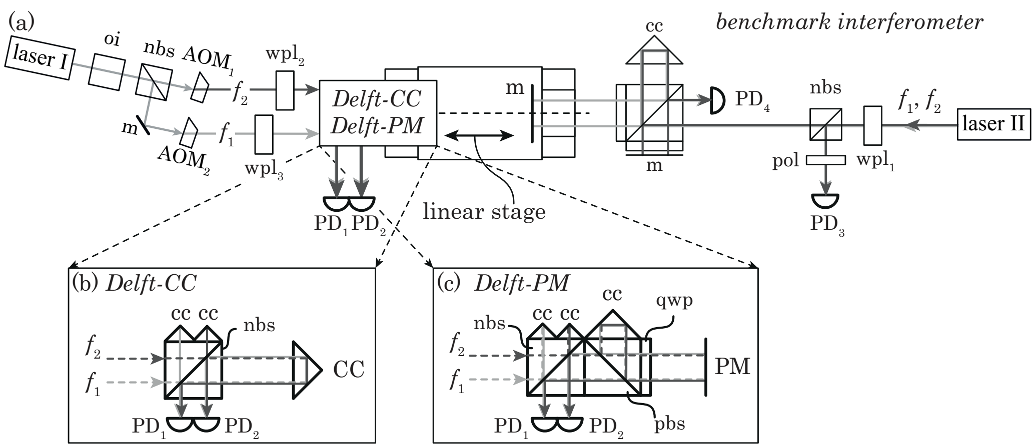

Figure 4.14: (a) Experimental setup where two interferometers measure target displacement simultaneously from opposite directions. At the left either the *Delft-CC* or *Delft-PM* interferometer is located, with at the right the benchmark interferometer system. (b), (c) Show the optical pathways of the *Delft-CC* and *Delft-PM* interferometer are shown respectively. Legend: laser I, 2-mode HeNe laser; laser II, Zeeman HeNe laser; f_x, source frequency; PD_x, photodetector; pol, polarizer; nbs, neutral beam splitter; pbs, polarizing beam splitter; qwp, quarter wave plate; cc, corner cube mirror; CC, corner cube target mirror; PM, plane target mirror; wpl_x, wave plate. *Note that the benchmark interferometer was comprised of an optical monolith, unlike the Delft interferometers.*

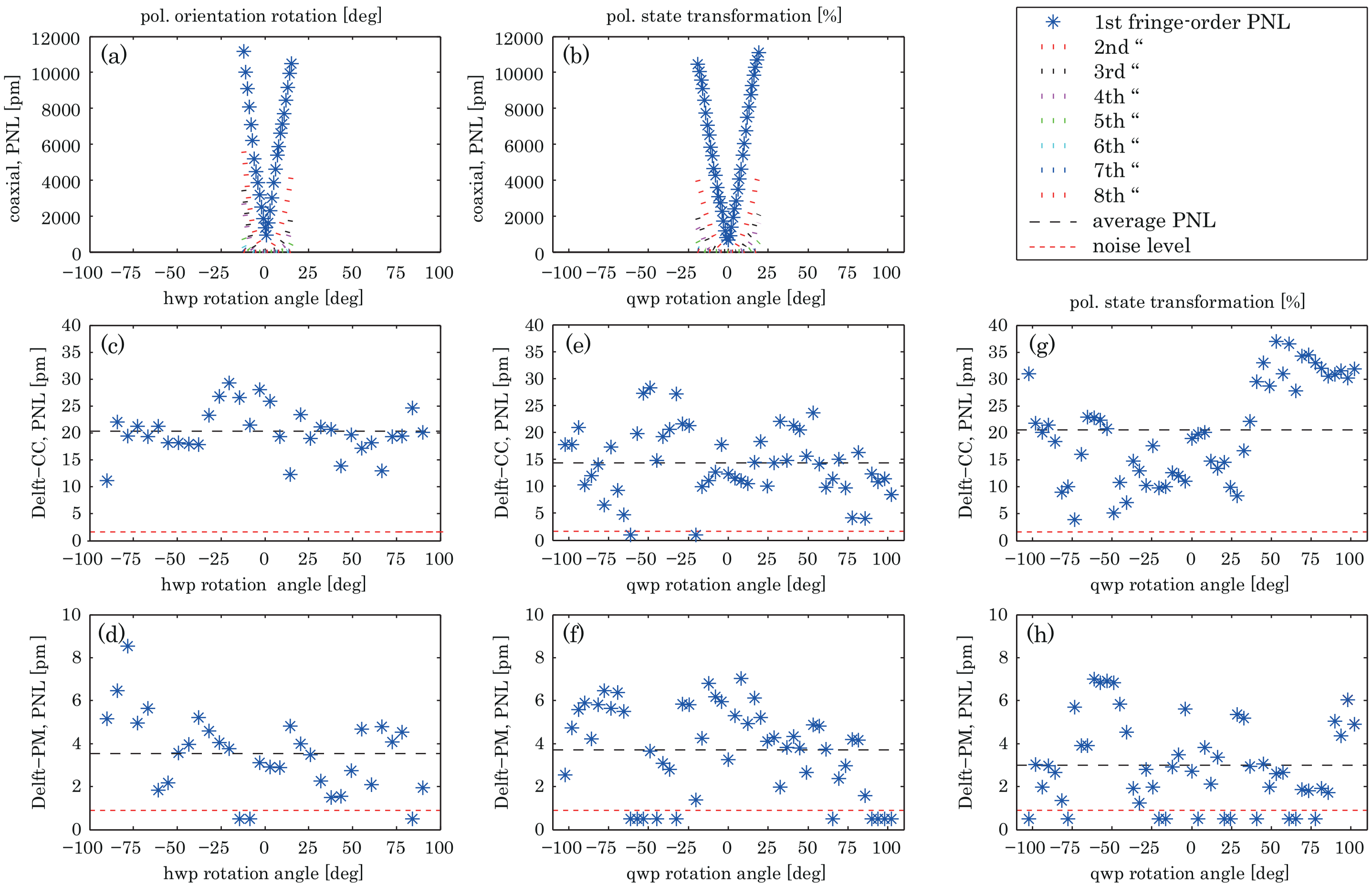

Figure 4.15: Measurement results showing PNL amplitudes of three interferometers. In (a), both source frequencies were rotated (coaxial beam) using a hwp; while in (c) and (d) only f_1 was rotated. In (b), both source frequencies their linear polarization states were transformed from linearly polarized toward left and right circularly polarized; in (e) and (f) this was only done for f_1 (i.e. f_2 remained linear). In (g) and (h), the polarization state of f_1 was manipulated again from linearly polarized to left and right circularly polarized, while f_2 was kept continuously circularly polarized. Note that below noise level indicates that no PNL was observed.

Neither of the Delft concepts showed a significant change in operational performance during polarization rotation of f_1. Both interferometers continued operation even at 90° relative rotation, where f_1's polarization is perpendicular to f_2's polarization (indicating that f_1 and/or f_2 was not 100% linearly polarized). Both Delft interferometers showed for all measurements only first fringe-order PNL without showing higher fringe-orders. With the *Delft-CC* interferometer an average first fringe-order PNL of ~20 pm was obtained, while *Delft-PM* interferometer obtained an average below 4 pm. This confirms that the polarization orientation of the source beams is of negligible influence on the measurement performance of the Delft interferometers.

The remaining levels of PNL depicted in Figs.4.15c to h, are attributed to secondary effects, such as ghost-reflections [20] (addressed in Section 4.8.1).

The sensitivity of the benchmark interferometer for PNL related to the input polarization states was tested using a quarter wave plate (qwp) at wpl_1, see Fig.4.14. Figure 4.15b shows the results of the polarization transformation of the coaxial beam, where rotation of the qwp transforms the linear polarization states into left and right circularly polarized states. At about 20° qwp rotation the benchmark system again ceased operation, for the same reason as with the hwp rotation test.

In a similar fashion, with each Delft interferometer two tests were performed using qwps for obtaining their PNL sensitivity versus polarization state. The first test involved insertion of a qwp in f_1 (wpl_2, see Fig.4.14) while keeping f_2 linearly (vertically) polarized. The results in Figs.4.15e and f again show no significant impact on the presence of PNL. The PNL magnitude for the *Delft-CC* improved to an average first fringe-order PNL of ~15 pm, while the *Delft-PM* design obtained a first fringe-order PNL average below 4 pm.

The second qwp test with the Delft interferometers involved insertion of one qwp into f_1 and one into f_2 (at wpl_2 and wpl_3, respectively, see Fig.4.14). The qwp in f_1 manipulated the polarization state again from linear toward full left- and right circularly polarized, while the qwp at wpl_3 kept f_2 fully circularly polarized. This resulted in an average first fringe-order PNL of ~20 pm for the *Delft-CC* design and an average first fringe-order PNL of ~3 pm for the *Delft-PM* design. This verifies that also the polarization state of the source beams is of negligible influence on the measurement performance of the Delft interferometers.

The repeatability of the measurements (shown in Fig.4.15), was tested by repeated measurements at the same wave plate angle. The average repeatability was about 4 pm for the *Delft-CC* and 2 pm for the *Delft-PM* interferometer.

4.7.3 Conclusions about PNL versus input polarization

In this section the presence of PNL was determined for a coaxial benchmark interferometer and two types of Delft interferometers. During experiments with these interferometers PNL was intentionally induced through polarization-manipulation of the source beams. For this manipulation wave plates were used for rotating the heterodyne frequencies their polarization orientation or transforming their polarization state.

Results showed for the benchmark interferometer up to eight fringe-order PNL of which the first fringe-order exceeded 10 nm when exposed to approximately ±15° hwp rotation or ±20° qwp rotation; at these limits the nonlinearity became too large for the electronics to continue measuring.

In contrast, the two Delft interferometers continued operation regardless of any polarization manipulation and performed without digital compensation; their measurement results only showed first fringe-order PNL with an average of less than 20 pm (*Delft-CC* configuration) and 4 pm (*Delft-PM* configuration).

The results indicated no significant relation between PNL and polarization imperfections for these Delft interferometers, therefore, it can be stated that they are insensitive to any imperfection in source beam polarization, at least within the 20 or 40 pm range (depending on the interferometer layout); in contrast to the benchmark interferometer.

4.8 Remaining and potential sources of PNL

Although PNL is significantly reduced using the Delft interferometer concept, it can never completely be eradicated (see also Section 4.1, and 4.2). The Delft interferometer concept has two sources that can lead to PNL: back-reflections (i.e. ghost-reflections), and polarization related leakage; both are addressed in this section.

4.8.1 Validated PNL due to leakage and ghost-reflections

Two different measurement cases were studied to confirm the presence and the effect of leakage and ghost-reflections for the interferometer illustrated in Fig.4.16a and c, respectively. The measurement target was again a mirror mounted on the linear *Aerotech* stage, which moved at constant velocity of 0.5 mm/s, and the data was processed as described in Section 4.7.2. The influence from ghost reflections in relation to PNL in heterodyne interferometers is also described by [20].

In the first case (Fig.4.16a) the birefringent axis of the quarter wave plate (qwp) was misaligned with respect to the linear polarization orientation of the beams that were propagating to the target mirror (m'). The leakage that resulted from the imperfect operation or imperfect alignment of the qwp is indicated in Fig.4.16b. Initially there was too little difference between the results before (Fig.4.17a) and after (Fig.4.17b) qwp misalignment, to conclude the effect of qwp misalignment on the measurements. Therefore, two pellicle beam samplers (8% reflective on both sides) were inserted at locations A and B, which induced re-injected the leakage into the interferometer. The re-injected leakage resulted in the presence of PNL at integer fringe-orders (i.e. 1, 2, 3,..); confirming the expectations from Section 4.2.

During the second case the qwp-alignment was optimized with respect to the linear polarization orientations of the beams that were traversing between interferometer and target mirror; and a pellicle beam sampler (p) was inserted between the qwp and the target mirror, see Fig.4.16c. This pellicle reflects 8% for every passing of the measurement beams, resulting primarily in the presence of PNL at a spacing of both a half and a full fringe-order. Similar to the first measurement case this effect was

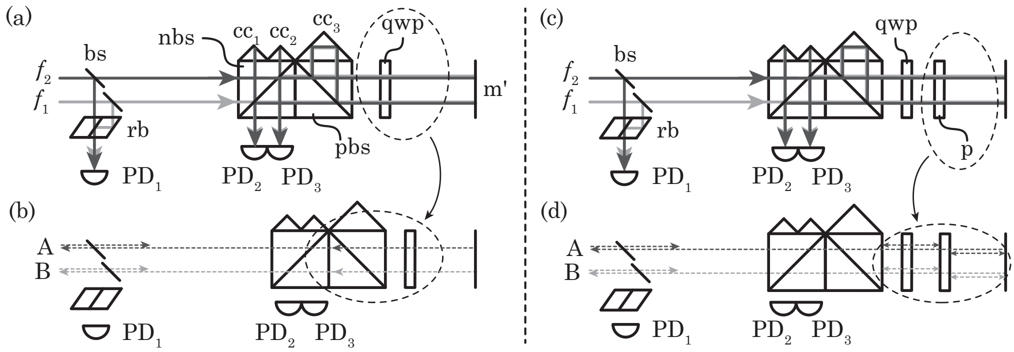

Figure 4.16: The depicted system is a schematic representation of the experimental setup shown in Fig.4.4, illustrating (un)intended optical pathways. The letters A and B denote the locations from where back-reflections were re-injected into the interferometer. (a), (b) Showing the setup used to confirm PNL from polarization misalignment of the quarter wave plate, qwp. (c), (d) Illustrating the setup for testing for ghost-reflections from a partially reflective pellicle, p. Legend: f_x, source frequency; bs, beam sampler; rb, rhomboid; PD_x, photodetector; m, mirror; nbs, neutral beam splitter; pbs, polarizing beam splitter; cc_x, cube corner reflector; and m', target mirror.

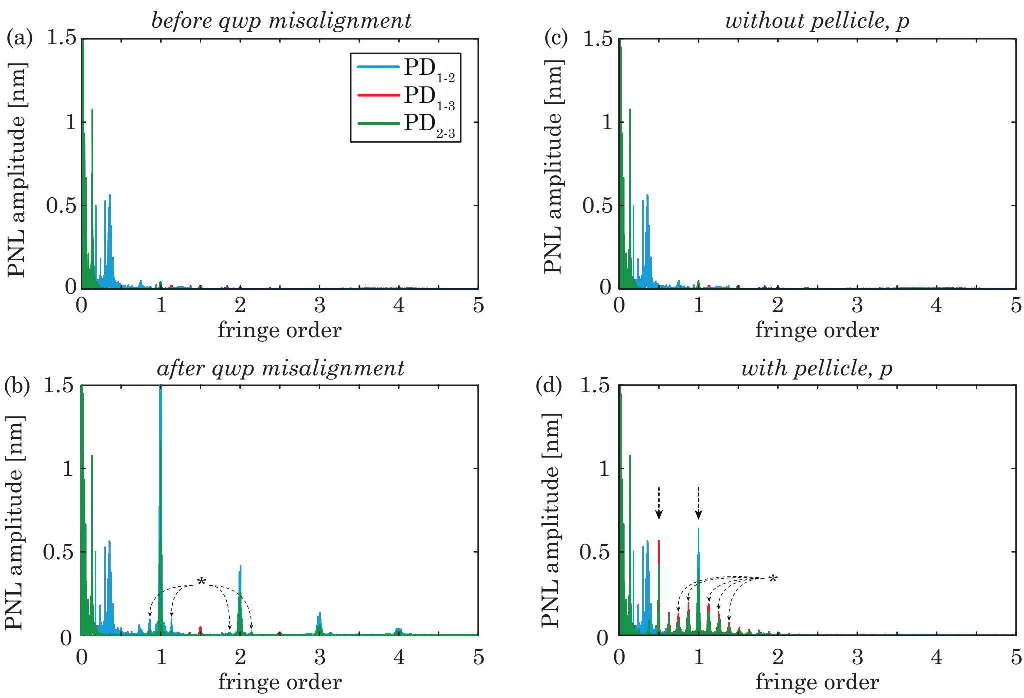

Figure 4.17: (a) Showing the result of three differential signals as measured with the setup in Fig.4.16 where the system had optimized alignment with respect to geometry and polarization. The results in (b) are with the setup from Fig.4.16a, with the qwp ~30° misaligned with respect to the polarization orientation of the measurement beams. (d) Shows results using the setup from Fig.4.16c, where a pellicle beam splitter was placed between the qwp and the target mirror. *The two * denote 'side lobes' which are the product of e.g. the measurement and data processing method, i.e. they could be the result from asymmetric sinusoid shapes (Fig.4.1) causing higher order frequency ouput from the FFT process.*

only visible with beam samplers present at locations A and B. The results presented in Fig.4.17d confirms PNL at primarily a half and a full fringe-order.

The sketched situation provides multiple opportunities where back-reflections caused by the pellicle constitute PNL at half and full fringe-order, which are indicated by the largest peaks at the respective fringe-order. Furthermore, frequency lobes are seen, which were studied to confirm that they were not caused by unknown optical effects in the interferometer that also can cause PNL. Measuring at a constant sampling frequency and moving the target at half and twice the velocity showed a proportional increase and decrease of the frequencies respectively. The change in frequency was opposite and proportional to the change in target velocity (i.e. twice the target velocity resulted in half the frequency spacing), which indicated that these peaks are not periodic with the wavelength and are therefore not part of the investigated PNL.

Concluding, with this interferometer layout it is possible to generate PNL via indirect ways, however, PNL was not present without the use of beam samplers at locations A and B, see Fig.4.16b and d.

Moreover, the presence of back-reflections can significantly be reduced by employing anti-reflection coatings at glass-to-environment interfaces, using optically monolithic structures (i.e. minimizing the refractive index differences upon propagation from one component to another), or even better, placing the optical components slightly angled with respect to the target mirror and input beams.

4.8.2 Potential leakage

Cube corner reflectors achieve reflection through either total internal reflection (i.e. TIR) or through the use of dielectric coatings applied on its surfaces (i.e. the black surfaces in Fig.4.20a). The reflecting surfaces of these reflectors are angled and known to influence the polarization of light [39–43]. If cube corner reflectors are used in conjunction with polarizing beam splitters, leakage might occur due to polarization rotation exerted by the reflector as sketched in Fig.4.18. *Note that the same leakage occurs for an imperfect operating polarizing beam splitter as well.*

For the interferometer shown in Fig.4.18b, this type of leakage did not affect measurement performance during tests, since such leakage was directed out of the interferometer, see Fig.4.18c; it only caused a decrease in optical efficiency.

However, for the designs showed in Fig.4.5 this type of leakage could potentially result in PNL, because leakage of e.g. reference signal f_2 could unwantedly end up

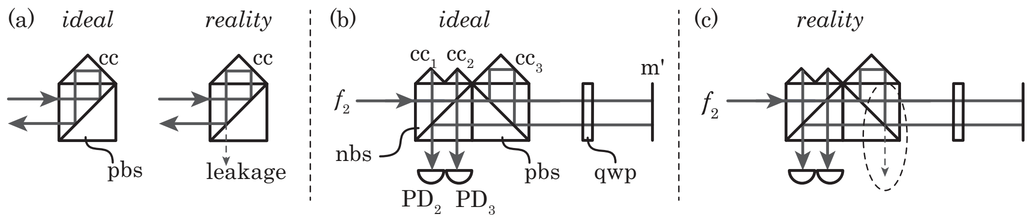

Figure 4.18: The sketch in (a) shows frequency leakage due to polarization rotation exerted by a cube corner reflector in combination with a polarizing beam splitter (pbs). The illustration in (b) shows the same situation for one frequency in a previously tested Delft interferometer.

at PD_b, as illustrated in Fig.4.20d-3; due to optical symmetry of the interferometer the leakage of only f_2 is demonstrated. Figure 4.20d-3 illustrates the only plausible case where leakage could potentially cause nonlinearity, all other cases are either not riskful or can be assumed to have negligible effect.

Decreasing the amount of polarization rotation by the cube corner reflector would reduce leakage via the polarizing beam splitter, which can be achieved by applying dielectric mirror surfaces for the cube corner reflectors instead of using total internal reflection [39–43]. This is done in a benchmark interferometer, it uses a dielectric coated cube corner reflector in conjunction with a polarizing beam splitter. In this setting a benchmark interferometer ensures low levels of PNL for even a coaxial system. This proves that using dielectric mirror surfaces for these reflectors is a viable solution for reducing the discussed type of leakage.

Further reduction of leakage can be achieved by employment of a polarizing beam splitter with a wedged double polarizing interface [44], see Fig.4.19a. This beam splitter does not eliminate leakage but rather ensures via induced walkoff and angle beam arrival upon detection (i.e. misalignment) that unwanted optical pathways will not reach detection, which thereby reduces this source of PNL, see Fig.4.19b.

Applying this concept to the Delft interferometer illustrated in Fig.4.5c, results in a fixed amount of beam walkoff. From this figure can also be seen that a single wedged interface (handling only the reference beams) already suffices for the depicted interferometer; still, a secondary wedged interface could be employed to reduce leakage from the measurement beams.

This secondary wedged interface will, however, lead to beam walkoff of the measurement beams in the opposing direction of the reference beam walkoff. The result of a double wedged interface thus enlarges the overall amount of static beam walkoff, which decreases the maximum obtainable AC-signal strength. This eventually decreases the signal-to-noise ratio and influences the measurement performance of the interferometer.

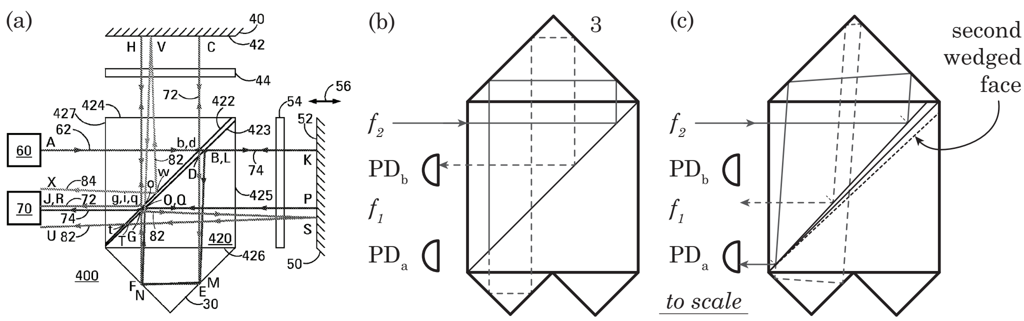

Figure 4.19: (a) Illustration that originates from patent *US 7,652,771 B2 (Agilent Technologies) [44]*, depicting how leakage can be withheld from entering the detector by means of a double polarizing beam splitter that contains a wedged splitting interface, where each face reflects either vertically or horizontally polarized light. Note that this patent aims on preventing interference due to both beam walkoff and angled beam arrival upon detection. (b) Showing the only potentially riskful case from Fig.4.20d-3. (c) Illustrating beam walkoff due to using a wedged polarizing face. *A secondary wedged face could be applied to also modify the optical pathways of the measurement beams.*

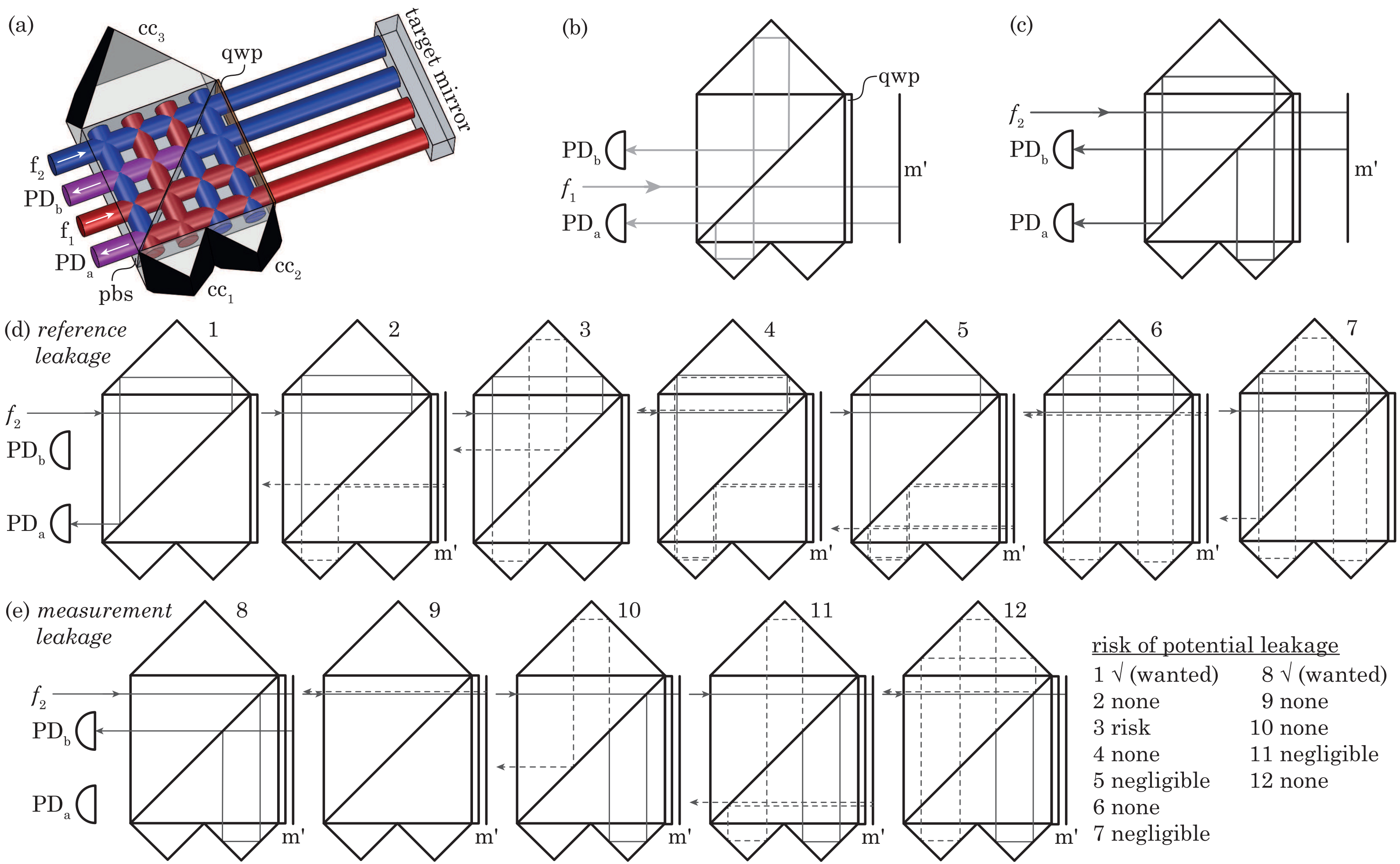

Figure 4.20: (a) 3D representation of the monolithic Delft interferometer used for studying polarization leakage. (b), (c) Illustrating the optical pathways of source frequency f_1, and f_2, respectively. (d), (e) Exemplifying for f_2 the unintended optical pathways of *reference leakage* and *measurement leakage*, respectively. These are the result of polarization manipulation of the cube corner reflectors in conjunction with the polarizing beam splitter.

4.9 Conclusions

This chapter introduced the Delft interferometer concept and an alternative heterodyne frequency source. The combination of these two was used for validating the measurement performance of the Delft interferometer. The results indicated that reduction of PNL was achieved, showing PNL amplitudes of only several picometers. Preventing PNL essentially consists of preventing the presence of frequencies other than the wanted *reference* and *measurement* frequency to show up in the system. Separation of the source beams proved a viable solution, achieving picometer level PNL without the disadvantages of e.g. implementing digital compensation that require calibration and make the measurements less real-time.
There are several different Delft interferometer configurations possible. All have in common that the source frequencies are delivered with separated optical beams, and that a reference signal is created at the interferometer itself, in contrast to a benchmark interferometer. For a lithography system where 30 measurement axes are monitored, a total of 36 photodetectors are required when using six 5-DoF Delft interferometers. In contrast the benchmark interferometer system uses 31 detectors (i.e. 30 axes + 1 common reference at the ROC, see Fig.3.3). Although generating a reference signal at each interferometer increases the amount of detectors, it does provide a major advantage, it enables the use of optical fibers (see next chapter), which is more valuable than a lower detector count.
An additional advantage of the presented Delft interferometer concept is the possibility of measuring at twice the resolution of the benchmark system, i.e. $\lambda/8$ instead of $\lambda/4$ (depending on the interferometer configuration).
For validation if the Delft interferometer concept achieved PNL reduction it was required to supply the interferometer with two inherently non-mixed source frequencies; something which could not be provided using the benchmark system's heterodyne source. Therefore, an alternative heterodyne frequency source was designed, using a two-mode HeNe laser, instead of a single-mode HeNe Zeeman laser as used in the benchmark system.
Experiments were performed with this alternative source, using two Delft interferometer types, which used either a cube corner reflector or a plane mirror as target. The experiments investigated the sensitivity relation of the two interferometers with respect to the presence of PNL and the orientation and state of the input polarizations. The results indicated that the Delft interferometers were insensitive for input polarization, whereas using the benchmark system showed nanometer level PNL in its measurement and eventually ceased operation.
Although the Delft interferometer concept substantially reduced the presence of PNL, deliberate re-injection of back-reflections and induced polarization related leakage did generate PNL. Furthermore, for a monolithic Delft interferometer configuration a potential source of PNL was found; concerning a polarizing beam splitter and a cube corner reflector. The benchmark interferometer has demonstrated that the influence from this combination can be reduced extensively, this same technique can also be applied to Delft interferometer concept. Moreover, this type of polarization leakage can be reduced using a double polarizing beam splitter with a wedged splitting interface [44].

To conclude, this research its first objective, *enhancing measurement linearity*, has been accomplished. PNL is reduced to below 0.1 nm as aimed for in the IOP project proposal: with a Delft $\lambda/8$ interferometer an average PNL of ~0.004 nm is achieved.

Chapter 5

Improving system modularity

The previous chapter dealt with enhancement of measurement linearity of a heterodyne displacement interferometer, which was one of this project's main aims. The second main research aim concerns the improvement of system modularity, which is addressed in this chapter.

In the first section, Section 5.1, the terms 'system modularity' and 'layout flexibility' are addressed, clarifying what modularity is and how a flexible layout can be obtained for an interferometer system. The next section, Section 5.2, discusses the different means of (e.g. optically) connecting subsystems in the benchmark system, together with the effort required for establishing these connections.
In Section 5.3 the separate delivery of the two source frequencies is investigated with the aim of determining whether this type of delivery is suitable for implementation of optical fibers. The following section, Section 5.4, discusses the differences between optical transport by means of free-space or optical fibers. The next section, Section 5.5, is in line with the previous one and discusses several commercially available types of optical fibers and their suitability for realizing fully fiber coupled heterodyne displacement interferometers. Section 5.6 follows with discussing suitable fiber connectors.
Section 5.7 presents results from a fully fiber coupled Delft interferometer that operated without showing detectable levels of PNL.

From the results presented in the several sections it can be concluded in the final section, Section 5.8, that optical fibers and their connective-properties provide a viable solution for achieving a modular heterodyne displacement interferometer system with a flexible system layout, based upon the Delft interferometer concept.

This chapter contains work from two publications by the author, both published in Optics Letters, titled: *Validation of separated source frequency delivery for a fiber-coupled heterodyne displacement interferometer* [6], and *Fiber-coupled displacement interferometry without periodic nonlinearity* [9].

5.1 System modularity and layout flexibility

In a lithography machine, precision placement of the wafer and mask are key to its operation. Overcoming the challenges of achieving sub-nm overlay errors at high process speed results in a highly complex and, therefore, expensive machine. The high purchase cost of such machines is compensated by continuous operation to maximize production volume. These machines will therefore benefit from fast module replacement upon malfunctioning (i.e. minimizing downtime), something which can be accomplished through implementation of *modularity*.

The term *modularity* has several definitions that depend on the context and the respective research area, a few examples are:

1. *Modular design,* the engineering discipline of complex device design using separately designed subsystems that can be calibrated and certified prior to installation.

2. *Modularity,* the degree to which a system's subsystems may be separated and recombined.

3. In ecology, *modularity* is considered a key factor in supporting resilience, which is the capacity of a system to respond to an environmental perturbation or disturbance by resisting damage and recovering quickly.

4. In architecture *modularity* refers to the construction of an object by joining together standardized units to form larger compositions, and/or to use a module as a standardized unit of measurement, interface, and proportion.

5. In industrial design *modularity* refers to an engineering technique to build larger systems by combining smaller subsystems that can be taken out and put in without the need for disassembling the whole system.

6. In the field of manufacturing *modularity* refers to the use of exchangeable parts or options in the fabrication of an object.

These different definitions have in common that a complex system is created from several less complex subsystems and that each subsystem has a specific task whose interaction relies on standardization and robustness. Robustness refers here to the interface between the sub-systems, which relates to its resistance for environmental disturbances; and additionally to the time required for achieving minimum connection efficiency for successful signal transfer. In this research *time* (i.e. effort) in relation to *connection efficiency* can be used as a performance indicator for the system's modularity with the goal to obtain a robust *plug-and-play* interferometer system.

Another key aspect is *layout flexibility*, which is an important factor during both the design process as well as during the realization of the lithography machine. During designing it is desired to have flexibility in the layout of sub-systems (e.g. the interferometers that are to be embedded), see Fig.5.1. The benchmark system only shows layout flexibility between the heterodyne frequency source and the remote optical combiner (ROC), which is achieved by the use of single-mode polarization-maintaining optical fibers, see Fig.5.1a. Less flexible are the free-space optical beams that exit the ROC and need to be delivered to the interferometers via mirrors and beam splitters. Once the free-space optical pathways and the locations of e.g. the mirrors are established it is difficult if not impossible to change this layout. This is in contrast to the use of optical fibers which almost do not require space reservation and easily allow for relocation, see Fig.5.1b.

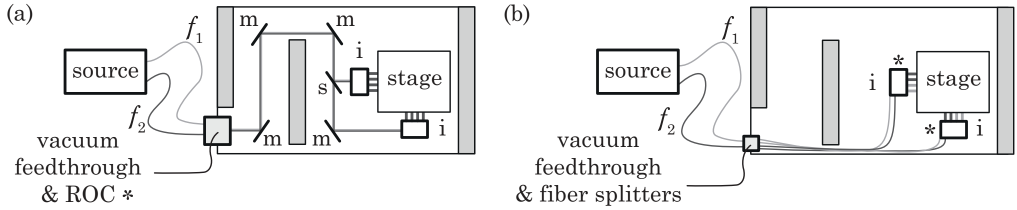

Figure 5.1: (a) Optical layout of the benchmark system using fiber optic delivery to a Remote Optical Combiner, ROC, which creates a free-space coaxial beam that transports the source frequencies using a non-flexible optical layout. (b) Fiber-coupled interferometers have a flexible optical layout and, thereby, ease host-system integration. The * denotes the generation of a reference signal. *The fiber optic transport of interference signals between the interferometers and phase measurement equipment is not shown.*

5.2 Subsystem interconnections

Dissection of the benchmark system into smaller systems reveals four distinct subsystems, constituting 6 interconnections, illustrated in Fig.5.2. These connections between the subsystems can be indexed, based upon the time/effort required for installation (i.e. establishing a connection that meets the minimum efficiency for signal transfer), from [**A**] (no time/effort required) to [**D**] (much time/effort required):

1. *environment* ⇢ *electrical connection* ⇢ *heterodyne frequency source*, [**A**]
The least sensitive transport concerns the electrical power for the heterodyne frequency source.

2. *heterodyne frequency source* ⇢ *SM fiber connection* ⇢ *ROC*, [**C**]
The optical fiber transport of the two source frequencies consists of two single-mode (i.e. SM) polarization-maintaining optical fibers. The optical efficiency of this connection is governed by the free-space-to-fiber in-coupling. Although this is a difficult coupling to realize, it is partially plug-and-play in the benchmark system, using designated optical fibers and factory pre-alignment.

3. *ROC* ⇢ *electrical connection* ⇢ *heterodyne frequency source*, [**A**]
Feedback from the ROC to the heterodyne frequency source takes place electrically and is used for irradiance-balancing between the two optical beams that carry the source frequencies. Establishing this connection merely consists of the effort of bridging the vacuum feedthrough.

4. *ROC* ⇢ *free-space optical connection* ⇢ *interferometers*, [**D**]
This optical connection concerns free-space coaxial beams that are guided via mirrors and beam splitters to each interferometer. This is the most demanding connection since misalignment (related to stability) of the free-space beam can both lead to optical efficiency loss and measurement error.

5. *interferometer*⇢ *MM fiber connection* ⇢ *phase measurement equipment*, [**B**]
This optical fiber transport concerns interference signals that are guided via multimode (i.e. MM) optical fibers, which require only little alignment effort.

6. *phase measurement equipment* ⇢ *electrical connection* ⇢ *environment*, [**A**]
The output of the phase measurement equipment consists of electrical signals that carry the displacement information. This connection only requires effort in ensuring the reliability of signal transfer, i.e. position feedback.

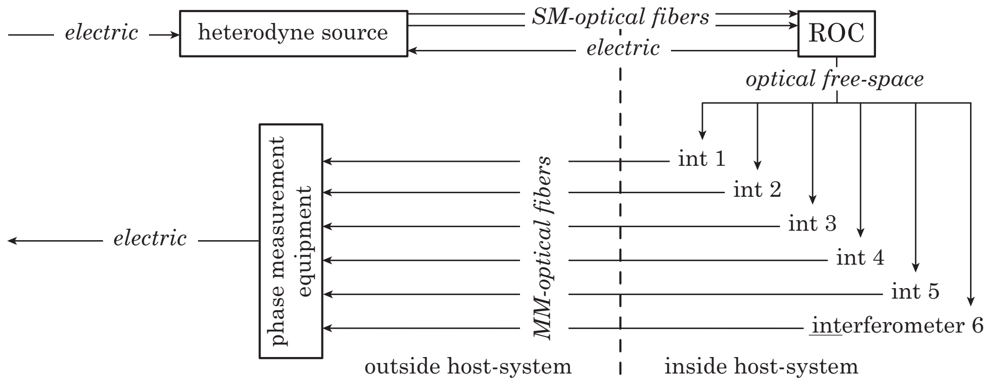

Figure 5.2: Overview showing four subsystems (the heterodyne source, the ROC, the six interferometers (i.e. each interferometer is a subsystem), and the phase measurement equipment) and their interconnections (electric, single-mode (i.e. SM) optical fibers, optical free-space, and multi-mode (i.e MM) optical fibers).

This analysis indicates that the signal transport between the four subsystems is either electrical or optical. The electrical connections are already at plug-and-play level, together with the multi-mode optical fibers that transport the interference signals. These connections are robust in the sense that they require little effort upon installation and can cope with environmental disturbances without showing a significant decrease in transmission efficiency.

The optical transport of the two source frequencies through the polarization-maintaining single-mode fibers is partially plug-and-play, i.e. at the input side of the fibers they allow for manual disconnection and reconnection; whereas the fiber outputs at the ROC are factory pre-aligned and fixed. However, with the use of nowadays manufacturing processes it is possible (though costly) to achieve geometric tolerances that enable for plug-and-play single-mode fiber optic connectors that provide a similar ease of connectivity as obtained when handling multi-mode fibers.
The fact that the fiber outputs are factory pre-aligned and fixed to the ROC is caused by the high level of alignment required for the coaxial output beam. This pre-aligned and fixed connection potentially requires significant alignment effort once a fiber needs replacement. Still, although the system is plug-and-play, component replacement of a single-mode fiber at the ROC results in difficulty due to the strict conditions required for the free-space coaxial beam.

The free-space optical transport of the source frequencies is the least robust of the three optical transport methods, the coaxial beam from the ROC is guided via mirrors and beam splitters that are all attached to the metrology frame (including the ROC), each presenting additional opportunities for disturbances to act on the free-space beams (e.g. inducing beam walkoff and optical wavefront deformations, see *Chapter 7*). Additionally, the free-space means of optical transport is highly inflexible and does not easily allow for rerouting once the host-system is designed.

The trend from this analysis shows that once the robustness to environmental influences decreases also the level of plug-and-play decreases, therefore, plug-and-play level connectivity is only ensured when the interconnection is robust with respect to environmental influences.

5.3 Validating separated source frequency delivery

In the previous chapter it was shown that a Delft interferometer is able to operate with separated source beams for delivery of the source frequencies. However, during those experiments, time variant influences of external disturbances acting on the free-space delivery were not analyzed extensively. The disturbances influencing the optical pathways were not predetermined or repeatable, two important prerequisites for validation of the concept's ability to operate with separately delivered source frequencies.

More extensive analysis is essential because separated frequency transport leads to optical pathlength differences and potentially causes measurement errors. The benefit of the Delft interferometer concept is that each interferometer has its own reference which makes it theoretically possible to account for phase differences due to pathlength inequalities.

With the experimental setup illustrated in Fig.5.3, a predetermined and repeatable disturbance source was used to characterize the Delft interferometer's ability to operate with separately delivered source frequencies. The experiment included two interferometers, one *classical* interferometer (using $PD_{1,2}$), and one *Delft* interferometer (using $PD_{3,4}$). The interferometers both received their source light from free-space beam delivery through a normal air environment. These source frequencies were provided by the alternative heterodyne source described in Section 4.5. The electro-optic modulator *(Thorlabs EO-phase modulator EO-PM-NR-C1)* modulated

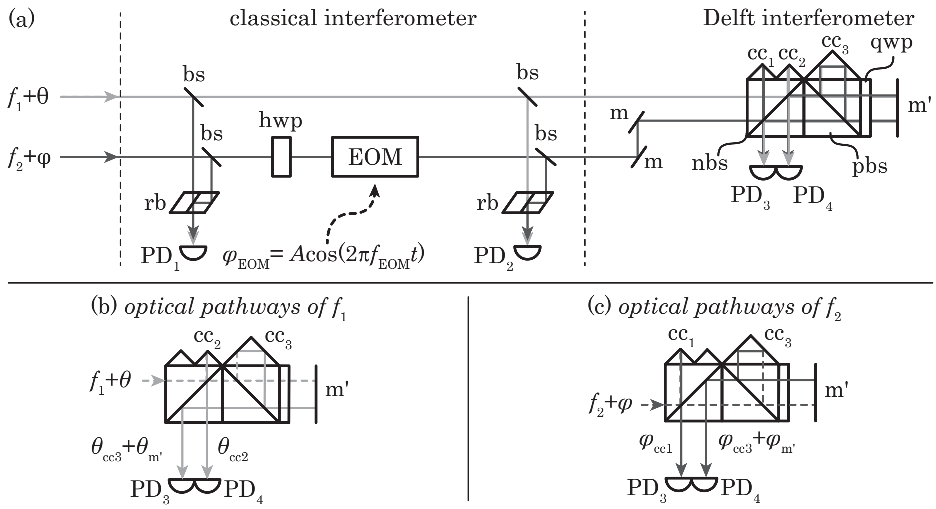

Figure 5.3: (a) Experimental setup for validating measurement operation with separated optical delivery of the source frequencies, where an EOM represents a repeatable error source that introduces a relative phase difference (φ_{eom}) between f_1 and f_2. (b), (c) Optical pathways of respectively f_1 and f_2 through the interferometer (dotted lines denote beams in the lower plane whereas solid lines are beams in the upper plane). *Note that the tested interferometer was not a monolithic structure as suggested by the illustration.* Legend: AOM_x, acousto-optic modulator; f_x, source frequency; bs, beam sampler; rb, rhomboid; PD_x, photodetector; m, mirror; nbs, neutral beam splitter; pbs, polarizing beam splitter; cc_x, cube corner reflector; qwp, quarter wave plate; and m´ , target mirror.

the phase of only source frequency f_2 (simulating e.g. air pressure fluctuations, temperature fluctuations, air turbulence, and fiber vibrations), which resulted in a time varying phase difference between f_1 and f_2.

The classical interferometer was used for monitoring EOM's phase modulation, since it interpreted the EOM's phase modulation as a displacement. Whereas the optical layout and the differential operation between $\mathrm{PD}_{3,4}$ of the Delft interferometer were expected exclude this phase disturbance, which is analyzed in this section.

The Delft interferometer's ability to reject disturbances encountered during optical delivery is first analyzed in theory. In this analysis two free-space linearly (vertically) polarized beams are provided to the interferometers (Fig.5.3a):

$$J_1 = E_1 \cdot \begin{bmatrix} 0 \\ 1 \end{bmatrix} e^{i(\omega_1 t+\theta)},\ J_2 = E_2 \cdot \begin{bmatrix} 0 \\ 1 \end{bmatrix} e^{i(\omega_2 t+\varphi)}, \tag{5.1}$$

where $\omega_{1,2} = 2\pi f_{1,2}$ (with $f_1 < f_2$) and θ and φ represent (unknown and uncontrollable) time varying phase components in f_1 and f_2, respectively, which are caused by the measurement environment. The use of rhomboids (see 'rb', Fig.5.3a) for beam overlap in the classical interferometer prevents frequency leakage of f_1 into f_2. Additionally, having both beams vertically polarized removes the need for an analyzer (i.e. a polarizer at 45°) in front of the PDs. At PD_1 the obtained interference signal is described by:

$$I_{\mathrm{PD}_1} \propto J_1^{\dagger} \cdot J_2, \tag{5.2}$$

$$I_{\mathrm{PD}_1} \propto E_1 E_2 \cdot e^{i(\{\omega_2-\omega_1\}t+\varphi-\theta)}. \tag{5.3}$$

Equation 5.3 shows the reference frequency for the classical interferometer, consisting of the frequency difference between f_1 and f_2 (i.e. ω_2 - ω_1). The EOM modulates the phase of f_2 according to:

$$\varphi_{\mathrm{EOM}} = A\cos\left(\omega_{\mathrm{EOM}} t\right), \tag{5.4}$$

where $\omega_{\mathrm{EOM}} = 2\pi f_{\mathrm{EOM}}$ describes the linear electric field that is applied to the EOM's electro-optic crystal, which gives rise to an electric-field dependent birefringence. The interference signals detected by the other PDs (Fig.5.3) are described by

$$I_{\mathrm{PD}_2} \propto E_1 E_2 \cdot e^{i(\{\omega_2-\omega_1\}t+\varphi+\varphi_{\mathrm{EOM}}-\theta)}, \tag{5.5}$$

$$I_{\mathrm{PD}_3} \propto E_1 E_2 \cdot e^{i(\{\omega_2-\omega_1\}t+\varphi+\varphi_{\mathrm{EOM}}+\varphi_{\mathrm{cc1}}-\theta-\theta_{\mathrm{cc3}}-\theta_{\mathrm{m}'})}, \tag{5.6}$$

$$I_{\mathrm{PD}_4} \propto E_1 E_2 \cdot e^{i(\{\omega_2-\omega_1\}t+\varphi+\varphi_{\mathrm{EOM}}+\varphi_{\mathrm{cc3}}+\varphi_{\mathrm{m}'}-\theta-\theta_{\mathrm{cc2}})}. \tag{5.7}$$

Vibrations of individual components had to be taken into account since the interferometer illustrated in Fig.5.3 was not monolithic, which explains the several additional phase terms. The signs of $\theta_{\mathrm{m}'}$ and $\varphi_{\mathrm{m}'}$ are opposite in Eqs.5.6 and 5.7, which is caused by an opposite shift of the beat frequency at the two detectors. To clarify, when target m´ displaces towards the interferometer, PD_3 encounters a decrease of the beat frequency, $f_{\mathrm{beat\,PD}_3} = f_2 - (f_1 + \theta_{\mathrm{m}'})$, whereas PD_4 encounters an increase of the beat frequency, $f_{\mathrm{beat\,PD}_4} = (f_2 + \varphi_{\mathrm{m}'}) - f_1$ (see also Section 4.4.2).

After performing a phase integration for each measured detector signal (similar to Section 3.3), a differential operation between $PD_{1,2}$ results in the measurement of φ_{EOM}, presenting itself as displacement s in the classical interferometer:

$$\theta_{\text{classical}} = \theta_{\text{PD}_2} - \theta_{\text{PD}_1} \Longrightarrow \theta_{\text{classical}} = \varphi_{\text{EOM}} \cdot 2\pi t, \tag{5.8}$$

$$s = \frac{\lambda_2 \cdot \theta_{\text{classical}}}{2\pi n}. \tag{5.9}$$

Equation 5.9 shows that the common noise terms θ and φ, and the frequencies $\omega_{1,2}$ cancel, resulting in the measurement of only φ_{EOM} (note that N is left out since it equals *one* for this interferometer). The same differential operation is performed for $PD_{3,4}$ of the Delft interferometer (analogous to Section 4.4.2):

$$\theta_{\text{Delft}} = \theta_{PD_4} - \theta_{\text{PD}_3} \Longrightarrow \theta_{\text{Delft}} = \varphi_{\text{cc3}} - \varphi_{\text{cc1}} - \theta_{\text{cc2}} + \theta_{\text{cc3}} + (\varphi_{\text{m}'} + \theta_{\text{m}'}) \cdot 2\pi t, \tag{5.10}$$

$$s = \frac{\lambda_1 \lambda_2 \cdot \theta_{\text{Delft}}}{2\pi N n \cdot (\lambda_1 + \lambda_2)}. \tag{5.11}$$

The absence of φ_{EOM} in Eq.5.10 shows that any phase difference between the two separately delivered source frequencies is mitigated. This is due to the interferometer's layout that delivers any fiber induced disturbance to both detectors, a differential operation between the detectors then cancels all common terms.

From Eq.5.10 can be seen that the phase due to target displacement, $\varphi_{\text{m}'} + \theta_{\text{m}'}$, is present twice, which indicates that the Delft interferometer consists of two interferometers that both have an optical resolution of λ/4; by means of the differential operation this eventually results in a displacement resolution of λ/8 (which is in agreement with Section 4.4.2).

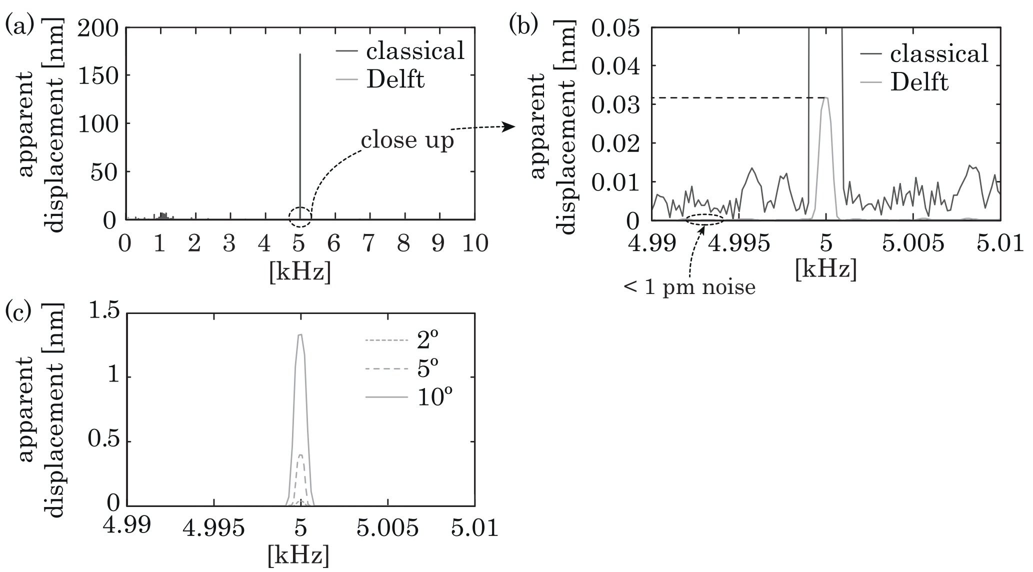

Figure 5.4: (a) The EOM's phase modulation is seen in the output of the classical interferometer with an amplitude of ~170 nm; and is reduced to ~0.03 nm the Delft interferometer's output (b). The 0.03 nm residual error is amongst others affected by polarization misalignment between f_2 and the EOM-crystal, causing an additional interference signal. (c) Additional interference was induced by 2°, 5° and 10° rotation of the hwp shown in Fig.5.3(a), resulting in an increase of the residual error.

These theoretical outcomes were experimentally verified using an EOM that applied a phase modulation at 5 kHz with a modulation depth of ~95° (at $\lambda = 633$ nm); leading to an apparent displacement of ~170 nm for the classical interferometer, indicated by the peak in Fig.5.4a. Data from both interferometers was obtained simultaneously and was processed using a Fast Fourier Transformation (FFT). The combination of the EOM operating at a fixed frequency and applying an FFT resulted in a noise level of less than a picometer for the Delft interferometer, see Fig.5.4b and c. The results from a stationary target and a moving target (0.5 mm/s, mounted on the *Aerotech* stage) showed similar results.

The influence of the EOM is clearly present in the classical interferometer's output, whereas it is not present in the output of the Delft interferometer, see Fig.5.4a and b. These results are in agreement with Eqs.5.8 and 5.10, and confirm that the disturbance from the EOM is canceled by the differential operation between $PD_{3,4}$.

However, a close up of Fig.5.4a, shown in Fig.5.4b, reveals a peak of ~0.03 nm and thereby indicates a phase disturbance suppression ratio of ~5700 (i.e. 170 nm / 0.03 nm), which suggests that the phase disturbance is not completely mitigated. For further robustness improvement of the interferometer concept it is essential to understand where this residual error originated from.

The error is the result of a differential operation between $PD_{3,4}$ and can therefore only consist of signal differences between these detectors, which could originate from a number of effects: the presence of additional interference signals, an unbalanced irradiance distribution between the detectors, or optical pathway asymmetry between the reference and measurement pathways (affecting the differential operation by a non-simultaneous arrival of a disturbance, see Section 7.3).

It is most likely that the residual error consisted of ghost-reflections (see also Section 4.8.1) that are caused by polarization leakage by the polarizing beam splitter due to imperfect quarter wave plate operation. The target's first reflection could partially be transmitted by the polarizing beam splitter and could then subsequently be re-injected by means of reflecting off the EOM-crystal's facet facing the interferometer, see Fig.5.3. The amount of irradiance required for explaining the residual error is already present even when good anti-reflection coatings are used [20].

Another source of additional interference signals is formed by the EOM itself. The EOM consists of a birefringent crystal that is modulated over one axis, which makes it sensitive to polarization misalignment. When the linear polarization orientation of f_2 mismatches with the birefringent index, the beam is only partially phase modulated. This results in a primary interference signal at 5 kHz between f_1 and f_2, (clearly visible with the classical interferometer in Fig.5.4a) together with a secondary interference signal from f_2 itself, also at 5 kHz. This additional source of interference was studied and verified by inducing polarization misalignment by means of insertion of a half wave plate (hwp) in front of the EOM, see Fig.5.3a. With the use of the hwp the polarization misalignment of f_2 was altered, which resulted in an nonlinear increase of the error, see Fig.5.4c.

Timing issues due to optical pathway asymmetry between the reference and the measurement pathway are present, but can be considered negligible in comparison to the influence from ghost-reflections.

A final source of error was comprised of irradiance modulation. Upon polarization misalignment between f_2 and the EOM crystal both an additional interference signal and an irradiance modulation (due to polarizing optics) at 5 kHz are obtained. When the EOM was operated (using equal settings as used for generating the results illustrated in Fig.5.4a and b), an irradiance modulation of less than 0.5% was measured, which represented no meaningful addition to the measurement error (see Section 7.4).

As can be seen, the residual error of 0.03 nm is comprised of multiple effects. However, some of them will not be encountered with an interferometer that operates under normal circumstances, and some can be reduced. This holds for partial phase modulation by the EOM when using single-mode optical fibers, and for ghost-reflections and optical-symmetry when employing monolithic optical structures.

With the presented demonstrator setup, phase disturbance reduction ratios in the order of 6000 were obtained using the Delft interferometer. These reduction ratios, however, were limited by the experimental setup itself and are expected to be exceeded under normal operating conditions.

The experimental setup thus confirmed that the Delft interferometer concept is robust and can operate with separately delivered source beams, which were delivered free-space but they could equally well be transported via optical fibers.

5.4 Optical fibers versus free-space transport

In Section 5.2 it was shown that for heterodyne displacement interferometry there are two methods used for optical transport: free-space propagation using mirrors and beam splitters, or optical fibers, see Fig.5.5.

The free-space transportation method relies on mirrors and non-polarizing beam splitters (i.e. neutral beam splitters) that are placed on specific locations on the metrology frame (i.e. temperature and vibration controlled) with a line of sight in between. Every mirror and beam splitter presents an error source because it can induce misalignment of the beam (i.e. via thermal changes and vibrations, leading to pointing instability), introduce wavefront deformations, and affect the polarization states of the source frequencies (inducing frequency leakage that causes PNL).

Another disadvantage of free-space optical transport is the rigidity of the optical network. The mirrors and beam splitters cannot be located just anywhere within the host-system, and they require a non-obstructed line of sight at all times. The specific location of those components poses difficulty when the host-system requires redesigning; for example, relocation of the beam splitter for interferometer I_5(Fig.5.5a), could also require relocation of the beams splitters for I_2 and I_6. The complexity of the host-system makes such a rearrangement of the optical layout even worse because many departments are involved with the host-system's design.

A more ideal situation would be to create the coaxial beams at the interferometer, realizing a fully fiber-coupled instrument. Unfortunately, this is costly and highly impractical with regard to space consumption and complexity. The solution is to combine the source frequencies into a coaxial beam only once, at the ROC, and branch off parts of the free-space beam to individual interferometers, see Fig.5.5a.

It is important to note that the free-space coaxial beams of the benchmark system cannot simply be replaced by optical fibers. Research indicated that fiber delivery of a coaxial beam with one polarization-maintaining single-mode fiber is possible, but increases PNL due to frequency mixing within the fiber [17]. This is the reason that there are two separate fibers used for source beam delivery to the ROC.

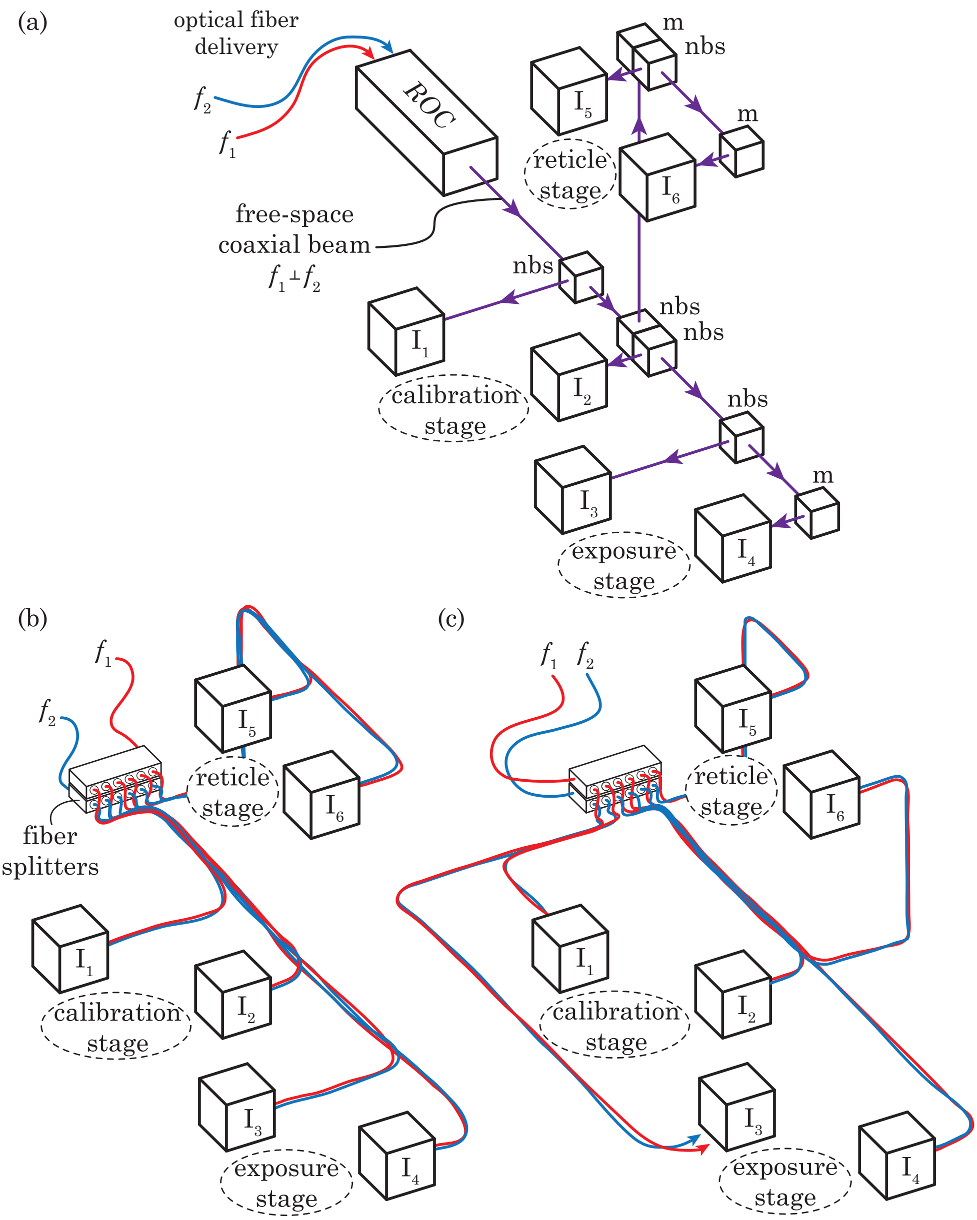

Figure 5.5: Indicating the difference in flexibility of optical system architecture. (a) In the benchmark system the two source frequencies (f_x) are transported with two separate single-mode optical fibers whose outputs are recombined at the ROC into a free-space coaxial beam that subsequently propagates to each interferometer (I_x) via beam splitters (nbs) and mirrors (m) attached to the metrology frame. (b), (c) Schematic representations of source beam delivery to Delft interferometers, demonstrating the flexibility in rerouting the optical fibers. *Note that the optical fibers for interference signal transport are not illustrated, see Fig.3.3.*

In contrast, optical fibers only require fixation of the fiber-ends, which removes the need for meeting many design constraints for the host-system. Figures 5.5b and c show source beam delivery via single-mode optical fibers which are divided each into six fibers (i.e. once for every interferometer). The major benefit of optical fibers is that they allow for reconfiguration of the optical pathways without affecting measurement performance, as long as the locations of the fiber-ends are determined, see Fig.5.5b and c.

The main advantage of the Delft interferometer is that it operates with separated source frequencies and that it has its reference at the interferometer. This concept allows for source frequency delivery through free-space and optical fibers as well; resulting in fully fiber-coupled heterodyne displacement interferometers.

5.5 Optical fiber types

The previous sections have indicated that the use of optical fibers is preferred over free-space optical transport due to the increased layout flexibility. Additionally, it was mentioned that the transport of interference signals via (multi-mode) optical fibers is already at plug-and-play level, in contrast to the use of single-mode fibers; this section shows why this is the case.

An optical fiber mainly consists of three parts, illustrated in the cross section in Fig.5.6. The size (with respect to the wavelength of the guided wave) and type of the core determine whether multiple or a single optical pathway exists, described by *multi-mode* (Fig.5.7a, b) or *single-mode* (Fig.5.7c) optical fiber respectively.

Figure 5.7 shows two types of multi-mode fibers, *step* index and *graded* index; the refractive index of a *step* index fiber is equal throughout the cross section of the fiber core, whereas the refractive index of a *graded index* fiber core decreases as the diameter increases. The number of optical pathways (i.e. *modes*) in multi-mode fibers increases as the core diameter increases, which can vary from 10 μm to more than 1000 μm (graded index fibers have on average core diameters below 100 μm), in comparison to the ~4 μm core diameter single-mode fibers used for this research.

There also exist two types of single-mode fibers, *polarization-maintaining* and *non polarization-maintaining*, see Fig.5.8. The core diameter of a single-mode fiber is many times smaller than that of a multi-mode fiber and is determined by both the refractive index of the core material, its core layout and on the wavelength of the transported light. Unfortunately, the core diameter of single-mode is only a few μm,

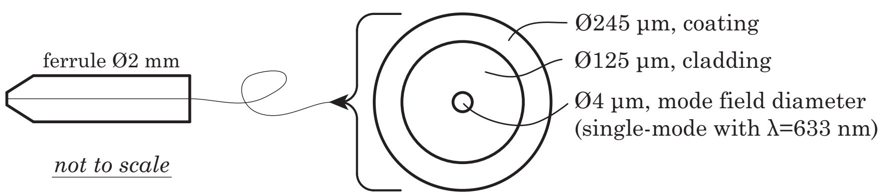

Figure 5.6: Example of an optical fiber, showing three layers in its cross section where the core is the only wave guiding medium.

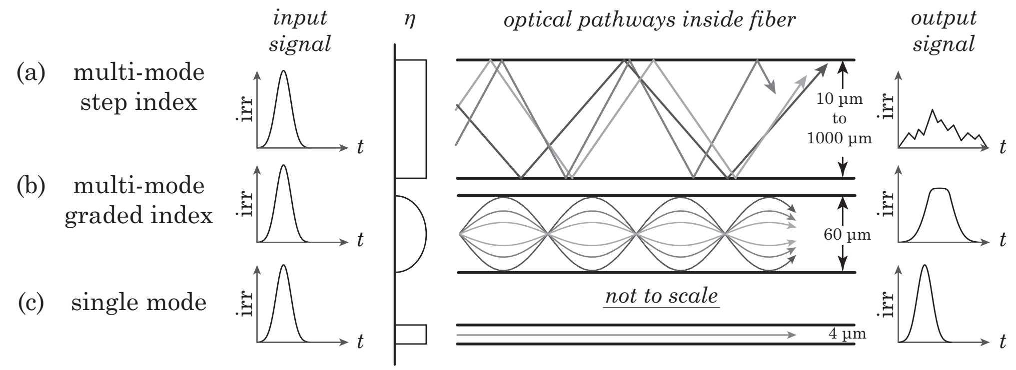

Figure 5.7: Three categories of optical fiber types. The figure illustrates that an input signal gets deformed during optical transport, which depend on the core size and refractive index (η) distribution.

for this research single-mode fibers with core diameters having a mode field diameter of about 4 μm (i.e. λ = 633 nm) have been used. There is no difference in core size between these two single-mode fiber types, only the structure of the cladding differs, as illustrated in Fig.5.8. The small core size of single-mode fibers (i.e. a few μm) poses difficulty with respect to obtaining optically efficient connections. The optical connection efficiency is related to the optical *mode-field-diameter* of the respective core. Moreover, polarization-maintaining fibers have due to their polarization preference an additional DoF affecting the optical in-coupling efficiency. The small core-surface area of single-mode fibers is the main reason that these fibers are not as plug-and-play as multi-mode fibers are.

Although multi-mode fibers can be connected at plug-and-play level due to their large core size, these large cores are unfortunately also the reason for the existence of many optical pathways, which are directly coupled to deformation of the fiber core (e.g. stretching, bending, clamping). These individual modes have varying exit angles that make it impossible to obtain a well focused or collimated output, therefore,

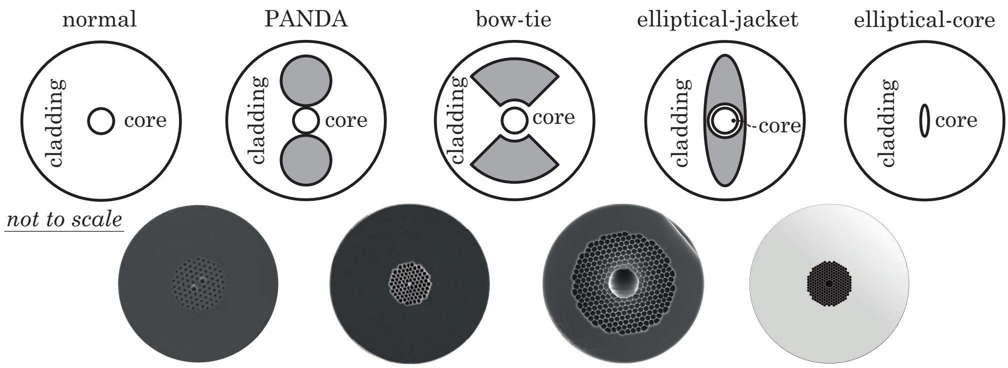

Figure 5.8: *Top row*, illustrating the cross sections of five single-mode optical fiber types of which only the 'normal' type, has no polarization preference (i.e. non polarization-maintaining). The dark gray areas represent material that induces anisotropic stress in the fiber core that makes the core birefringent and causes a polarization preference; these fibers are termed *stress-birefringent* fibers. The 'elliptical-core' fiber is an example of a form-birefringent fiber. During this research both 'normal' and PANDA type fibers have been used. *Bottom row*, cross sections of single-mode photonic-crystal fibers that e.g. have 2-3 times larger mode field diameters compare to the fibers from the top row. (modified from www.thorlabs.com).

applying these fibers for source frequency delivery would result e.g. in almost no irradiance upon detection. More importantly, their multi-mode operation results in individual optical pathways that each have their own phase. This is best visualized by observing *speckles* in the fiber output, see Fig.5.9. These speckles are locations where interference between modes takes place, indicating that each mode has its own phase. When these fibers are applied for source frequency delivery, these phase differences between individual modes cause measurement errors that prevent sub-nm measurement accuracy.

The presence of many optical modes presents no complication when transporting interference signals, provided that the light that is coupled into the multi-mode fiber already interferes (i.e. using a 45 degree rotated polarizer in front of the fiber). The detector at the fiber exit is located such that all light is captured, which removes the need to focus. Since all modes reach the detector the eventual measurement consists of a phase integral of the whole interference signal, mitigating the individual phase additions of the many optical modes.

To conclude, single-mode optical fibers provide the optical quality required for the source light delivery to ensure sub-nm measurement accuracy. However, due to the small core size of these fibers it is a challenge to achieve optically efficient connections on plug-and-play basis (a point of attention for further research). In contrast, multi-mode fibers have large cores that provide plug-and-play connections but cannot be used for source beam delivery due to the support of the many optical modes, which makes them only suitable at the detector side of the interferometer (i.e. for interference signal transport).

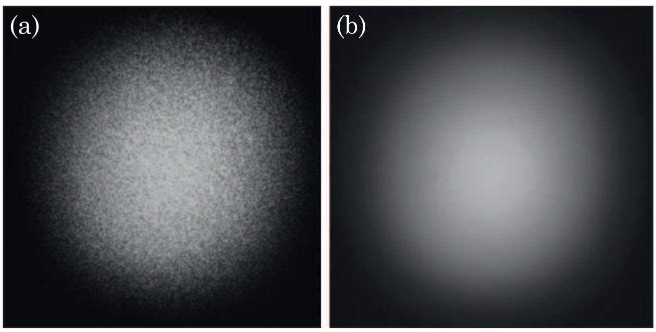

Figure 5.9: (a) Photo of a Gaussian distributed speckle pattern of a step-index multi-mode optical fiber, where each 'speckle' is comprised from interference between modes. (b) Photo of a Gaussian profile originating from a single-mode fiber, which inherently does not show speckles and is thereby much smoother than the profile of the multi-mode optical fiber.

5.6 Optical fiber connectors

There are several locations in the Delft interferometer system where fiber optic connectors are to be applied, where each location requires its own connector, illustrated in Fig.5.10a.

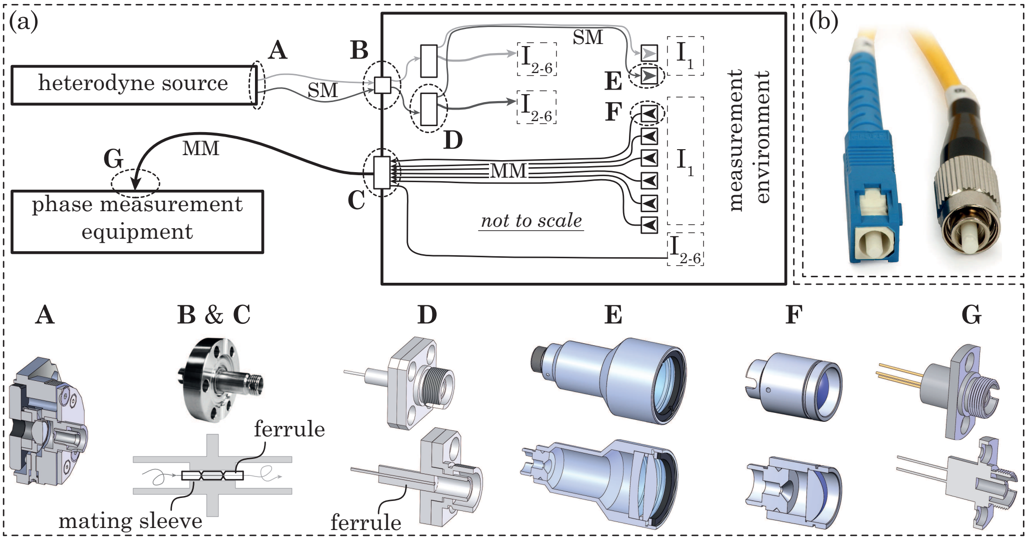

Figure 5.10: (a) Schematic overview depicting the several locations (**A** to **G**) and accompanying optical fiber connectors (**A** to **G**) in a Delft interferometer system. **A** fiber in-coupling; **B** & **C**, vacuum feedthrough; **D**, fiber-to-fiber coupling; **E**, fiber-to-free-space out-coupling; **F**, free-space-to-fiber in-coupling; and **G**, out-coupling with photodetector attached. (b) Photograph illustrating two examples of optical fiber end-connectors where the glass ferrule holding the fiber-end (white part) can be seen.

At location A, free-space light carrying the source frequencies is coupled into two polarization-maintaining single-mode optical fibers (each using a manually adjustable interface). These have already commercially proven to be *partially* plug-and-play, since each coupler is factory pre-aligned for an individual fiber and allows for reconnection of that specific fiber at the use of additional (minor) alignment effort [33]. The manufacturing tolerance of the location of the fiber's core with respect to the ferrule necessitates factory alignment; one or two micrometer misalignment between fiber core and the focal point of the in-coupling lens already leads to 50-80% efficiency loss. Due to manufacturing tolerances the optical efficiency can thus not be ensured when another fiber (equal type) is applied, therefore, *partially* plug-and-play.

Two examples of optical fiber end-connectors are shown in Fig.5.10b, the *FC/PC*-connector type, at the right, is used by the benchmark system at location A.

At location B, the source frequencies enter the (near) vacuum measurement environment via connectors that contain a fixed ferrule with a single-mode wave-guiding core. The ferrule acts as a vacuum seal and realizes a face-to-face coupling between two single-mode fibers. This connection is commercially available at plug-and-play level, however, frequent reconnection causes wear of both the fiber ferrule and mating sleeve, which affects fiber alignment and reduces the optical coupling efficiency. This necessitates connector replacement after a certain amount of reconnections.

Location D concerns two fiber splitters of which each divides the incoming optical power from one fiber (transporting one source frequency) over six fibers. These connectors have a fixed ferrule for a face-to-face connection, equal to B, and are equally subject to wear. Depending on design considerations a 'boxed solution' as shown in Fig.5.5b and c, or a (less volume consuming) fiber fan-out as shown in Fig.5.11a (which is expected to be more preferred for a lithography machine), can be chosen.

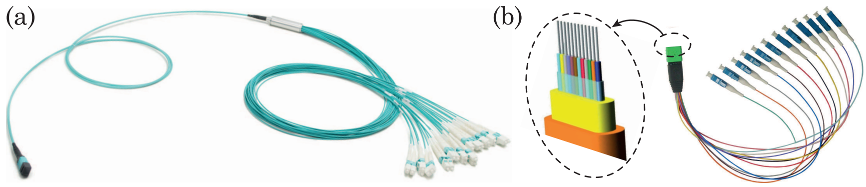

Figure 5.11: (a) Example for single-mode fiber delivery where one fiber's output is divided over several other single-mode fibers (i.e. a fiber *fan-out*). (b) Multiple multi-mode fibers can be combined into a *ribbon fiber* type, decreasing the amount of individual fibers throughout the system and reducing the amount of connections upon the vacuum feedthrough.

The optical fiber connections at location E (two per interferometer) are the most crucial fiber-connections in the interferometer system. To ensure sub-nm measurement uncertainty these require a high level of alignment and mechanical stability. At this location the fiber output is to be expanded from ~Ø4 µm to Ø9 mm and must be aligned such that (ideally) all beams emerge parallel from the interferometer. Both beam expansion and alignment are affected by the manufacturing accuracy of the fiber-core's location. Potentially a two stage subsystem might be required, consisting of two factory pre-aligned single-mode polarization-maintaining optical fibers, each with a beam expander at one fiber end, connected to an intermediate (short) optical fiber with a connector (e.g. D) at the other fiber end. This should lead to a plug-and-play interface that ensures a high level of alignment and mechanical stability.

Reception of the interference signals at location F takes place using free-space-to-fiber in-couplers, six per Delft interferometer. These connectors contain a lens (and a polarizer) for in-coupling of the free-space interference signals into multi-mode fibers with core diameters of ~Ø1 mm (i.e. optical fibers used during this research, *Agilent Technologies*). These large core diameters and the absence of polarization alignment results in plug-and-play connections that are not limited by wear.

At location *C*, the interference signals are transported with multi-mode fibers from the near-vacuum environment via the same type of connectors as applied at location B. These connections are plug-and-play without requiring careful attention or maintenance, which is significant seen the large number of connections (i.e. 36 interference signals). These fiber's large core diameter makes them suitable to be fabricated as *ribbon* fibers, see Fig.5.11b. From a practical point of view this ribbon fiber should include a number of spare fibers, such that malfunctioning of one fiber would not necessitate replacement of the ribbon fiber.

The photodetectors of the phase measurement equipment are housed within the connector shown in G. These connectors are equally easy to handle as the connectors at C and are readily available at plug-and-play level.

Concluding, the fiber connectors that handle multi-mode fibers are plug-and-play and have proven reliable operation in the benchmark system, whereas the connectors that handle single-mode fibers require more attention. The coupling efficiency of single-mode fibers is affected by wear, and by the manufacturing accuracy of both the connector as well as the location or the fiber core. The fiber-to-free-space out-coupling of the source light at the interferometer are the most critical fiber connections, factory alignment and installation of the fibers to the interferometer monolith must be considered. Although realizing plug-and-play connections for single-mode fibers presents quite a challenge, designing such connections is not impossible.

5.7 Validating a fully fiber coupled interferometer

The measurement performance of a fully fiber coupled Delft interferometer was investigated using the setup illustrated in Fig.5.12. The experiment was comprised of two tests, similar to Section 4.6. During the first test the source frequencies were free-space delivered, these results were used as a reference for the second test, concerning fiber optic delivery.

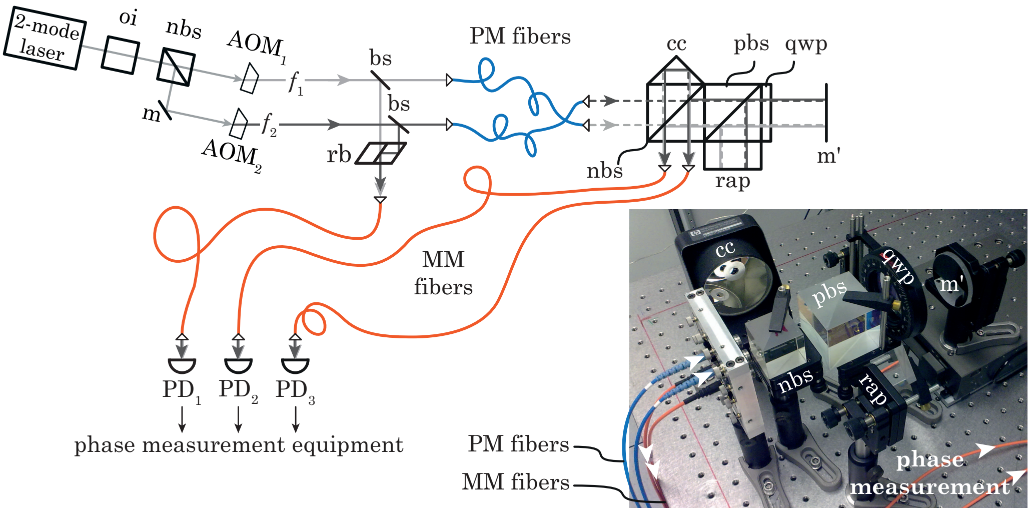

Figure 5.12: Overview of the experimental setup for validating fiber-coupled operation of a Delft interferometer using the alternative heterodyne source. Legend: oi, optical isolator; nbs, neutral beam splitter; m, mirror; AOM_x, acousto-optic modulator; f_x, optical frequency; bs, beam sampler; rb, rhomboid; PD_x, photodetector; PM, polarization-maintaining single-mode; MM, multi-mode; cc, cube corner reflector; rap, right-angle prism; qwp, quarter wave plate; pbs, polarizing beam splitter; and m', target mirror.

Figure 5.13 shows the differential results between photodetectors PD_1 and PD_2, and between PD_1 and PD_3. Both indicate fiber optic deformation of several µm [i.e. 8 µm error equals a phase phase shift of $2\pi N \cdot (8\ \mu\text{m} / \lambda) \approx 300$ rad (!)]. However, these deformations are not present in the output from the differential measurement between photodetectors $PD_{2,3}$. Additionally, PNL was visualized as described in Section 4.7.2 and showed equal to that section only a very limited presence of PNL.

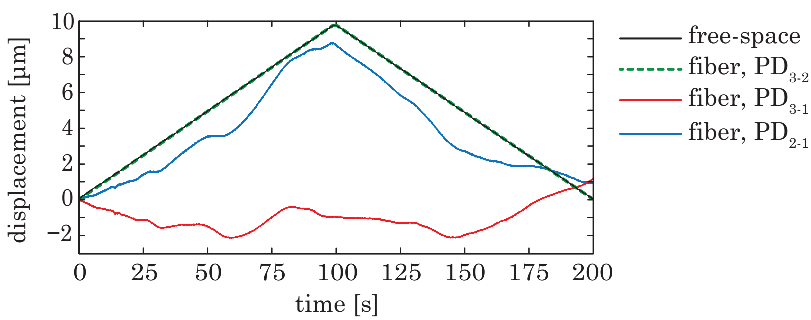

Figure 5.13: Linear displacement of 10 µm movement, forward and backward, using free-space and fiber-coupled delivery.

5.8 Conclusions

A system can be termed *modular* when its subsystems are comprised of *individual modules* that are *flexibly interconnected*, and can be taken out and placed back without the need for disassembling the host-system (i.e. the lithography machine).
With the Delft interferometer system all individual modules are optically connected (unlike the benchmark system which uses electrical feedback from the ROC). These optical connections can either consist of separated source light transport though free-space or via optical fibers, which was also validated by experiments using a fully fiber coupled Delft interferometer.
Free-space optical pathways prove an inflexible means of optical interconnection that is difficult if not impossible to reroute. In contrast, optical fibers only require strict positioning of their fiber ends, while allowing rerouting of the fiber in between.
Support of the fibers throughout the lithography machine can be done both at the metrology frame or at the base frame. The interferometers are attached to the metrology frame and require vibration isolation, therefore, near the interferometers the optical fibers require to be attached to the metrology frame. However, further away from the interferometers the fibers can also be connected to the base frame, via a low-stiffness loop to prevent vibration transmission. The benchmark system already showed successful operation with each interferometer connected to 5 multi-mode optical fibers, the Delft interferometer concept requires for the same amount of measurement axes only the addition of one multi-mode fiber plus two single-mode fibers (which are less stiff) per interferometer.
There are several commercially available fiber types of which only single-mode optical fibers (i.e. $\sim\text{Ø}_{core}$ 4 μm at λ = 633 nm) can be used for source light delivery. Multi-mode fibers are not suitable for delivery because their 'large' core diameter (i.e. up to ~Ø1000 μm) supports the existence of many individual optical pathways that all carry their own phase, which e.g. affect measurement accuracy when used for source light delivery. The effort required to achieve optically efficient connections with these fibers is dominated by the core dimension, which is the reason why multi-mode fibers can readily be handled on plug-and-play basis, while this is more difficult for single-mode fibers. However, the plug-and-play level of these fibers can be enhanced using photonic-crystal fibers, which provide enlarged mode-field diameters that ease the level of alignment and makes plug-and-play handling more feasible.
There are multiple locations within the Delft interferometer system where different types of optical fiber connectors have to be applied, many of them are already commercially available. The most critical fiber connection is located at the interferometer, and concerns the fiber-to-free-space connection. This connection requires a high level of mechanical stability and optical alignment, which are both directly coupled to the measurement accuracy of the interferometer.
Tests with a fully fiber coupled Delft interferometer (using single-mode polarization-maintaining optical fiber delivery and multi-mode optical fiber coupled external detection), confirmed performance equal to free-space delivery (using the same interferometer) and achieved sub-nm sized PNL.

Concluding, this chapter showed that the *system modularity* of a displacement interferometer system can be *improved* by means of the Delft interferometer concept, which enables fiber optic delivery. The following chapter illustrates what an interferometer system will look like when implementing the Delft interferometer concept into an EUV-lithography machine.

Chapter 6

The Delft interferometer system

The previous chapters dealt with redesigning a heterodyne displacement interferometer system, increasing its linearity by means of reducing PNL, and implementing modularity by means of using optical fibers for subsystem interconnection.
This chapter puts all elements together and illustrates how these constitute an improved heterodyne interferometer system.

In this chapter the overall layout of the Delft interferometer system is illustrated and the main differences between the Delft and the benchmark interferometer system are briefly clarified. How these differences affect the measurement accuracy is more thoroughly discussed in Chapter 7.

6.1 System architecture

Combining the findings from the previous chapters results in a heterodyne displacement interferometer system as illustrated in Fig.6.1. This interferometer system is designed to achieve "*a measurement range of 450 mm with sub-nm measurement uncertainty, while allowing for a modular system buildup that has a flexible optical layout and is robust enough for fast module replacement to reduce downtime*."

The measurement accuracy is improved by increasing the measurement linearity using an alternative heterodyne frequency generation method, Section 4.5, combined with separation of the source frequencies, Section 4.3.

System modularity is primarily enhanced by the replacement of the free-space source frequency delivery with optical fibers. Both source frequencies are delivered via a separate fiber to each interferometer, single-mode polarization-maintaining optical fibers, Section 5.7. These two fibers pass a vacuum feedthrough after which they are both split six times, once for every interferometer. Upon delivery at the interferometer the fiber-output is expanded and collimated into Ø9 mm free-space beams, which are subsequently divided over several measurement axes, enabling measurement of five DoFs per monolithic interferometer, see Section 4.4.3.

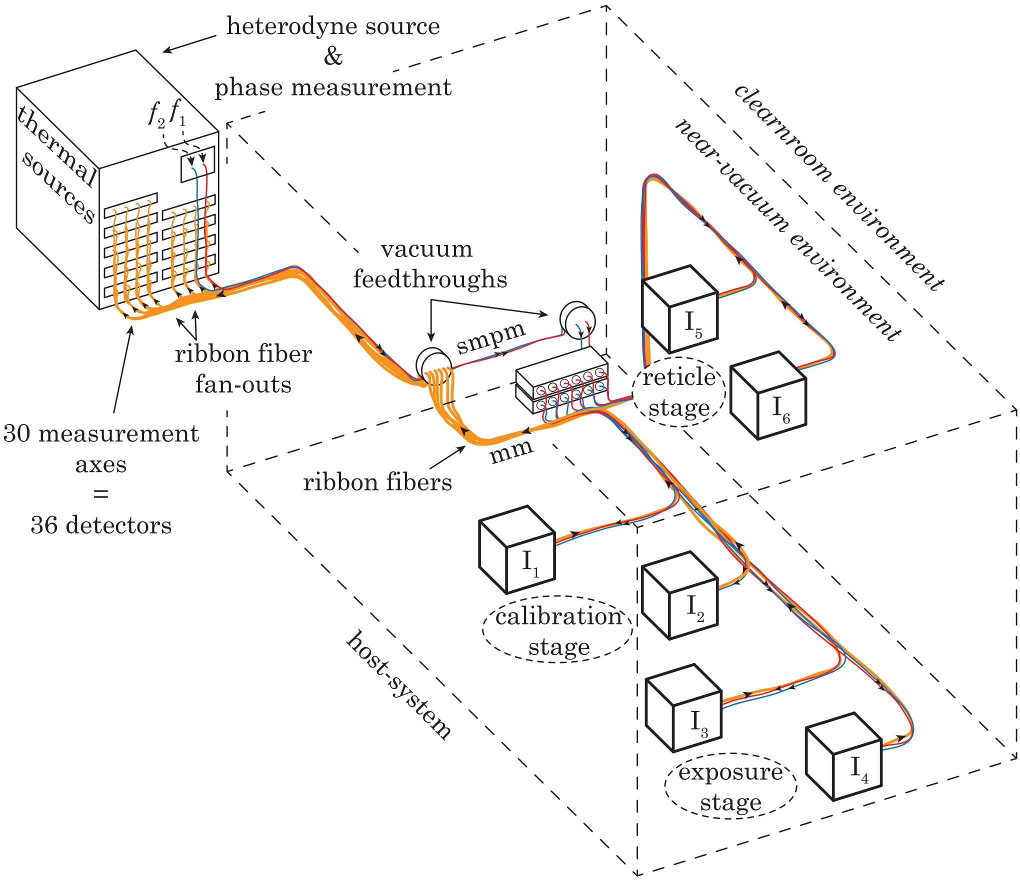

Figure 6.1: Illustration of a possible system architecture using Delft interferometers implemented into an EUV-lithography machine; using single-mode polarization-maintaining optical fibers (smpm) for source light delivery to the interferometers (I_x) and multi-mode optical fibers (mm) for interference signal transport to the external photodetectors.

Each interferometer measures 5-DoFs and generates six interference signals of which one signal is used as reference, due to this reference and the interferometer's optical layout, the interferometer can cope with disturbances that act on the optical fibers during source frequency delivery, Section 4.6 and 5.3. Each interference signal is coupled into a multi-mode optical fiber that transports the signal via a vacuum feedthrough to phase measurement equipment.

The host-system contains three planar stages of which each is monitored by two 5-DoF interferometers, which constitute a total amount of 36 interference signals for monitoring 30 measurement axes. In contrast, the benchmark system operates with 31 interference signals. This difference is caused by the fact that each Delft interferometer generates its own reference signal, whereas in the benchmark system all interferometers use a common reference signal from the ROC, addressed in Section 3.2 and 3.3.

6.2 Differences with the benchmark interferometer system

The main differences between the Delft and benchmark interferometer system are found in:

1. *Heterodyne source frequency generation*
The alternative heterodyne frequency source used for this research provides non-mixed source frequencies, unlike the benchmark system's heterodyne source.

2. *Individual reference per interferometer*
Each Delft interferometer generates its own reference, which enables amongst others the use of optical fibers.

3. *The use of optical fibers for source light delivery*
The benchmark system only employs optical fiber transport between the heterodyne source and the remote optical combiner (i.e. ROC). The ROC puts the two fiber outputs into two coaxial beams that continue free-space propagation to each interferometer. On the other hand, Delft interferometers can be fully fiber coupled; using single-mode polarization-maintaining optical fibers for delivery and multi-mode optical fibers for external readout. This gives the Delft interferometer system a more flexible optical layout that knows almost no limitations with respect to rerouting the locations of the optical fibers.

4. *Plug-and-play modularity*
The use of optical fibers enables the possibility to create flexible optical interconnections between subsystems (e.g. vacuum feedthroughs, interferometers) that can be connected on plug-and-play basis. This allows for easy (de)installation of e.g. the interferometers, compared to the use of free-space beams.

5. *Fully passive (optical) layout*
The benchmark system has an electrical interconnection between the ROC and the laser source for irradiance balancing, which is not required for a Delft interferometer (see Section 7.4).

Part III

Error source analysis: Delft versus benchmark

In the previous part the basis of the Delft interferometer and its system architecture have been addressed. This part continues with the obtained results and addresses both the measurement performance of this interferometer and its overall system layout. This is done by means of analyzing all relevant internal and external error sources, addressed in *Chapter 7* and *Chapter 8* respectively. *Except for PNL, which has already been investigated in Chapter 4, and error sources due to the heterodyne laser source, since e.g. wavelength stability affects both the benchmark and Delft interferometer system similarly.*

The internal error source analysis covers the influence from error sources that are related to the design of the interferometer itself, whereas the analysis concerning external error sources describes how changes in the measurement environment affect the measurement performance.

Performance comparisons between the outcomes of these analyzes and the benchmark system will eventually give insight in the achieved improvements.

This part shows a comprehensive error analysis which is in general applicable to any heterodyne displacement interferometry system.

Chapter 7

Analyzing internal error sources other than PNL

This chapter addresses all error sources, other than PNL (see Chapter 4), that are related to the design of the Delft interferometer and the overall interferometer system; and compares them to those of the benchmark system. However, measurement error due to the heterodyne frequency source is not discussed, since e.g. wavelength stability affects both the benchmark and Delft interferometer system similarly.
Section 7.1 briefly introduces the term 'internal' error source, followed by Section 7.2, which addresses measurement errors that are related to optical wavefront shapes and to their relative movement due to target rotation. This section also introduces a new method for assessing the optical wavefront shape of interference wavefronts.
Section 7.3 discusses the influence of data age and signal timing on measurement performance, which are both related to the interferometer system's architecture. The next section, Section 7.4 is related to system architecture and addresses the influence of variations in the irradiance distribution.

The concluding section, Section 7.5, summarizes the conclusions from the subsections, and states that the Delft system performs equally or better than the benchmark system regarding the addressed internal error sources.

This chapter contains work from a publication by the author, published in Optics Express, titled: *Relative optical wavefront measurement in displacement measuring interferometer systems with sub-nm precision* [10]; and a publication by the author, published in Optics Letters, titled: *Validation of separated source frequency delivery for a fiber-coupled heterodyne displacement interferometer* [6].

7.1 Internal error sources

In this work *internal error sources* refer to sources of error that are related to the optical layout and the used components that constitute the interferometer itself as well as the interferometer system in its entirety (including the overall optical fiber layout and the alternative heterodyne frequency source). By means of system design the overall impact of these internal error sources can be reduced.

7.2 Optical wavefront quality and beam walkoff

With heterodyne interferometry a photodetector receives two free-space optical beams, each carrying one source frequency. Throughout the cross section of each free-space beam phase differences can be present, which together shape the *optical wavefront* of that respective beam, see Fig.7.1a. If these relative phase differences are zero, the wavefront of that optical beam would be undeformed, i.e. it would have a 'flat' shape (compare the wavefront shape upon start and upon detection in Fig.7.1a).

One step further, an interference signal consists of the interaction between two frequencies whose individual wavefronts define the interference signal its wavefront, illustrated in Fig.7.1. Since the electromagnetic fields of the two wavefronts add, the shape of the interference wavefront corresponds to the phase *difference* between these two wavefronts (i.e. the wavefront of the interference signal is a differential wavefront).

The photo detector generates an electrical signal based upon the irradiance it receives. In this case the photocell actually integrates the incident irradiance that it receives over its two dimensional surface into a one dimensional electric current. The amount of irradiance varies over the cross section of the detector (directly related to the shape of the interference wavefront), which is determined by constructive and destructive interference (see Section 2.1.2).

A change in wavefront shape of e.g. one of the interfering wavefronts leads to a change in relative phase, which causes a differently shaped interference wavefront that subsequently results in a change in the phase-integration outcome. Since the outcome of that phase-integration represents target displacement information, a change in that outcome due to e.g. wavefront deformations results in a measurement error.

A Delft interferometer uses separated optical delivery of the source frequencies where each optical beam can be affected differently, resulting in two non-identical wavefronts. In contrast a benchmark interferometer uses a coaxial beam where the optical wavefronts of the two orthogonally polarized source beams will be identically shaped (since they have a common optical pathway) upon delivery at the interferometer. Understanding the implications of this difference requires insight how optical wavefront behavior can add to measurement uncertainty [45, 46].

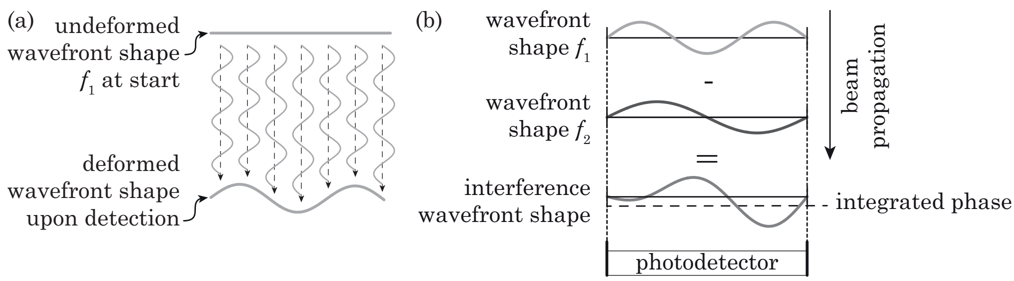

Figure 7.1: (a) Illustrating that an optical wavefront can be represented by multipe waves (throughout its cross section) with varying relative phase due to e.g. refractive index differences. (b) Illustration of two individually shaped wavefronts that together constitute the shape of the interference wavefront on the (phase) integrating photodetector.

There are several ways how the phase integration of the interference wavefront results in measurement error:

1. The amount of overlap between two non-flat wavefronts changes over time due to e.g. misalignment and target movement, or tilt of the target mirror (compare Fig.7.2a and b).

2. The wavefront(s) can have a time depended shape due to e.g. turbulence (compare Fig.7.2a and c).

Both situations lead to a different outcome of the phase-integration. Moreover, beam walkoff also leads to a change in strength of the interference signal, which eventually affects the measurement linearity through a lowered signal-to-noise ratio, see Section 7.4.

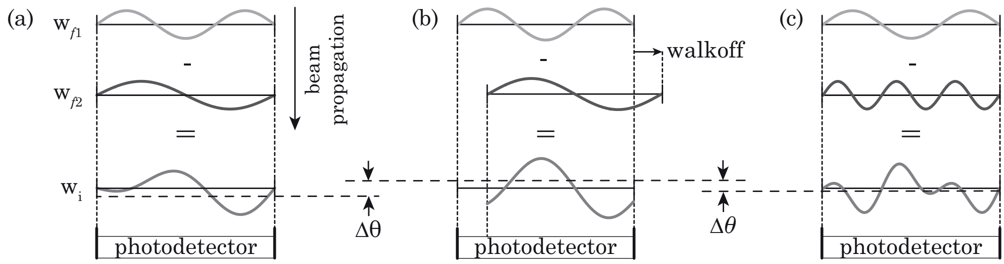

Figure 7.2: The outcome of the phase integration of the interference wavefront (dotted line) can vary, $\Delta\vartheta$, which is falsely interpreted as target displacement; caused by (b) beam walkoff of the measurement beam, or by (c) time varying wavefront shapes. Legend: w_{fx}, optical wavefront of source frequency f_x; and w_i, optical wavefront of the interference signal.

7.2.1 Optical wavefront deformation

The intention of the following brief analysis is merely to show the order of magnitude of wavefront deformations. The analysis deals with worst case scenarios which show that wavefronts can deviate several tens of nanometers. How large the deformations in reality are, is not relevant for this analysis.

The two biggest contributors to wavefront deformations are encountered upon refraction and reflection. Refraction based deformations are due to local refractive index variations that have multiple origins: turbulence in gaseous media during free-space transport, density inhomogeneity of optical components, and non-flat transmissive surface geometry. Deformations due to reflection have, on the other hand, only one origin: optical surface geometry (i.e. dealing with mirrors that reflect at the side that faces the incoming radiation), but are in general larger and thus more critical.

The magnitude of wavefront deformations due to turbulence can be several hundred nanometer, which makes it in normal air environments not possible to perform measurements over a long stroke with sub-nm measurement uncertainty. Fortunately, the near-vacuum environment of the benchmark system decreases this error source and re-enables long stroke measurements at high measurement accuracy.

Regarding wavefront deformations due to refractive index inhomogeneity of optical components, standard high grade optics have refractive index variations in the order of $\Delta\eta = \pm 0.5\text{e-}6$ [47]. When assuming an optical pathway of d = 100 mm through BK7 glass, η_{BK7} = 1.51, where this inhomogeneity is present over one beam diameter, this results in a wavefront deformation of

$$\text{deformation} = \frac{\triangle\eta}{\eta_{\mathrm{BK7}}} \cdot d \longrightarrow \text{deformation} \approx 33\,\mathrm{nm}. \tag{7.1}$$

Additionally, surface geometry causes wavefront deformations upon both transmission and reflection. In the case of transmission, assuming non-coated BK7 glass with a surface roughness of $\lambda/20$ across a Ø9 mm beam results in wavefront deformations in the order of

$$\text{deformation} = \left[\frac{\lambda/20}{c/\eta_{\mathrm{BK7}}} \cdot c\right] - \lambda/20 \longrightarrow \text{deformation} \approx 16\,\mathrm{nm}. \tag{7.2}$$

Whereas assuming the same surface roughness upon reflection results in deformations of twice the roughness, i.e. ~60 nm.

It can be understood quite straightforward that turbulent gaseous media causes time varying wavefront shapes, however, also wavefront deformations due to static geometry are dynamic, caused by the continuous movement (including target rotation, i.e. tip, tilt and yaw) of the target mirror. Therefore, all of these effects influence the phase integration outcome on a time variant basis.

7.2.2 Beam walkoff

As illustrated in Fig.7.2, a relative wavefront movement between the two interfering wavefronts causes a measurement error. There are two processes that drive this relative transverse movement, I) target rotation (i.e. tip, tilt and yaw) and II) pointing (in)stability of the two source frequencies. Target rotation only results in transverse movement of the measurement wavefront (i.e. beam walk off), whereas pointing instability of the source frequencies results in movement of the measurement wavefront as well as the reference wavefront, but with slightly smaller amplitude (due to shorter optical path length).

Relative wavefront movement in the situation sketched in Fig.7.3, leads to a change of the phase integration area, and therefore, to a change in strength of the interference signal; causing a change in the AC-DC ratio which lowers the signal-to-noise ratio.

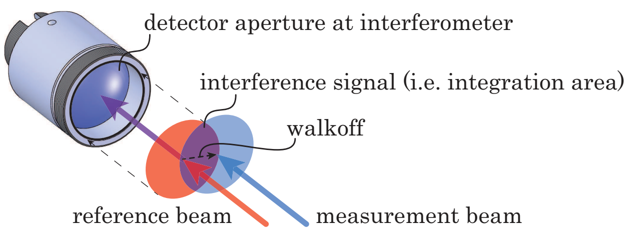

Figure 7.3: Illustrating 'beam walkoff', where the wavefront of the measurement beam 'walks' off the reference wavefront and the detector, due to e.g. target tilt. *(for simplicity the diameters of the wavefront and detector aperture are taken equal, which is not necessarily the case in reality)*

7.2.2.1 Target rotation

Transverse wavefront movement is comprised of target rotation and is proportional to the distance between the interferometer and the target, see Fig.7.4. Reduction of the effect of beam walkoff is amongst others achieved by employment of cube corner reflectors. These reflectors ensure that the measurement beams enter the detector parallel to the delivered reference beam, which means removing the effect of tilt in the measurement wavefront due to target rotation (i.e. tip, tilt, and yaw).

The amount of beam walkoff is mainly driven by the maximum distance between the interferometer and measurement target as shown by the following calculations.

Note that the following values (originating from Section 3.2*) are initial estimations determined in collaboration with ASML, which are meant for a future interferometric displacement system in a lithography machine, none of them refer to an actually realized system.*

1. size of pbs, A = 60 mm

2. deadpath, B = 500 mm

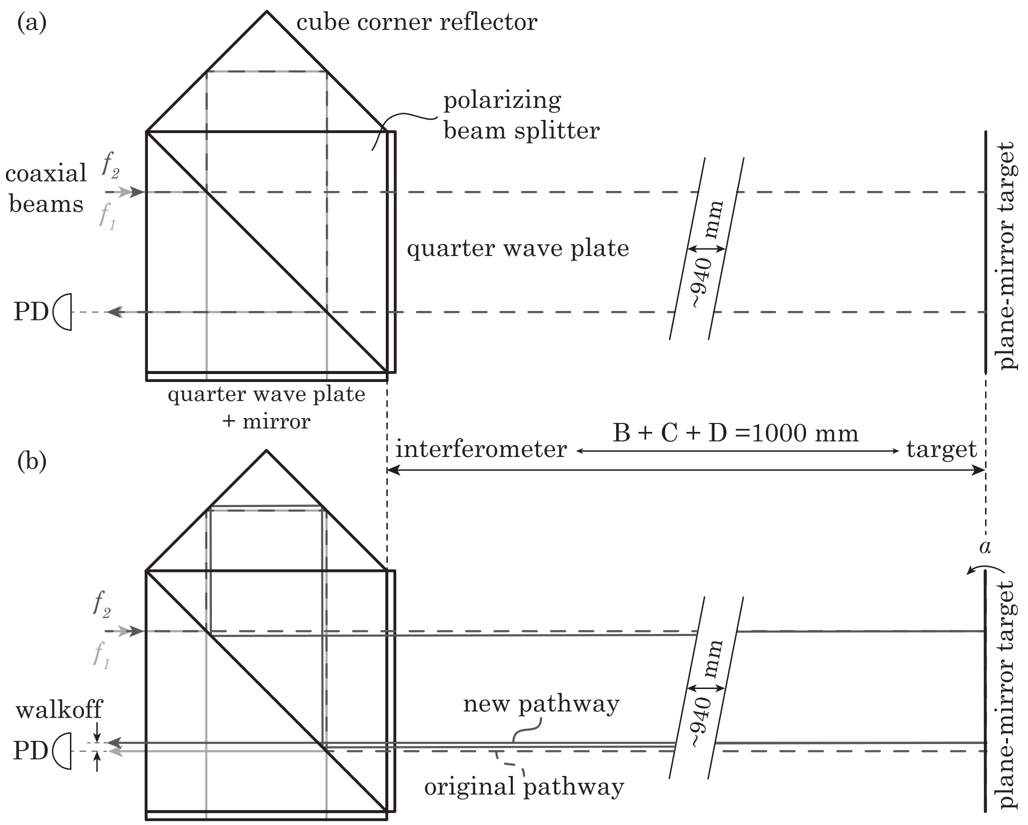

Figure 7.4: On scale representation of a single DoF benchmark interferometer with polarizing beam splitter of 60 mm, and an interferometer-to-target-distance = deadpath + measurement range + additional range = 1000 mm. (a) Without target rotation, (b) with target rotation. Due to the use of the cube corner reflector, the measurement beam arrives always parallel to the reference beam at the photodetector (PD).

3. operational measurement range, C = 450 mm (corresponding to a Ø450 mm wafer)

4. additional measurement range, D = 50 mm

5. N = 4, number of times the measurement beam traverses between the interferometer and the target mirror

6. α = 1 mrad target rotation, this includes both rotation at the start and during exposure.

7. initial separation, IS = 15 mm

8. beam diameter D = 9 mm

9. allowed walkoff is ±3 mm , corresponding to a 50% decrease in signal strength for a Ø9 mm beam (i.e. rule of thumb, *Agilent Technologies*)

The amount of walkoff (W) for this configuration is then determined by:

$$W = \frac{\sqrt{\left(2 \cdot \left\{\frac{IS}{2} - [(A+B+C+D) \cdot \tan(2\alpha)]\right\}^2\right)}}{\left(\cos\left\{\left(\frac{\pi}{4}\right) - (2 \cdot \alpha)\right\}\right)} \cdot \sin\left\{\left(\frac{\pi}{2}\right) - (4 \cdot \alpha)\right\}. \tag{7.3}$$

The overlap between the two beams is subsequently determined by calculating the overlap, $O_{walkoff}$, of two circles that are offset by W, as in

$$O_{\text{walkoff}} = 2 \cdot \left(\frac{D}{2}\right)^2 \cdot \cos\left(\frac{W}{D}\right) - \frac{W \cdot \sqrt{4 \cdot \left(\frac{D}{2}\right)^2 - W^2}}{2}. \tag{7.4}$$

Using the given parameters, the walkoff (W) amounts about ~4.3 mm. The decrease of the interference signal (i.e AC-signal) strength is subsequently obtained by calculation of the intersecting volume of two 3D Gaussian profiles (Fig.7.5), which results in an AC-signal strength decrease of ~70%. Furthermore, when taking into account that tip and yaw (or tilt an yaw) take place simultaneously, a decrease of ~90% is observed.

However, it is important to note that the in-plane rotation (i.e. yaw) of the wafer stage (to compensate for non-ideal wafer placement) will be larger than the out-of-plane rotations (i.e. tip and tilt). Therefore, stage rotation about e.g. yaw and tip and setting both rotations to equal 1 mrad represent a worst case scenario, but is in reality not expected to occur.

In an effort to reduce beam walkoff by interferometer design[1], one could decrease the size of the pbs (dimension A, depicted in Fig.7.4), though, this has little effect due to the small dimensions with respect to the long measurement pathway. The largest walkoff reduction is therefore achieved by decreasing the deadpath by e.g. a factor ten (from 500 mm to 50 mm). This results in a walkoff of only $W \approx 2.5$ mm when considering one DoF rotation, which decreases the wavefront overlap by $W \approx$ 35%, leading to a ~50% loss of AC-signal strength. The 2D case (i.e. yaw + tip, or yaw + tilt) leads subsequently to a loss of ~65%, which is more acceptable than the previously ~90% loss.

[1]A more efficient method is to improve the alignment accuracy (of the yaw DoF) during wafer placement on the stage, this reduces the mandatory compensation upon starting the exposure process, which is expected to be larger than the rotational adjustments required during exposure.

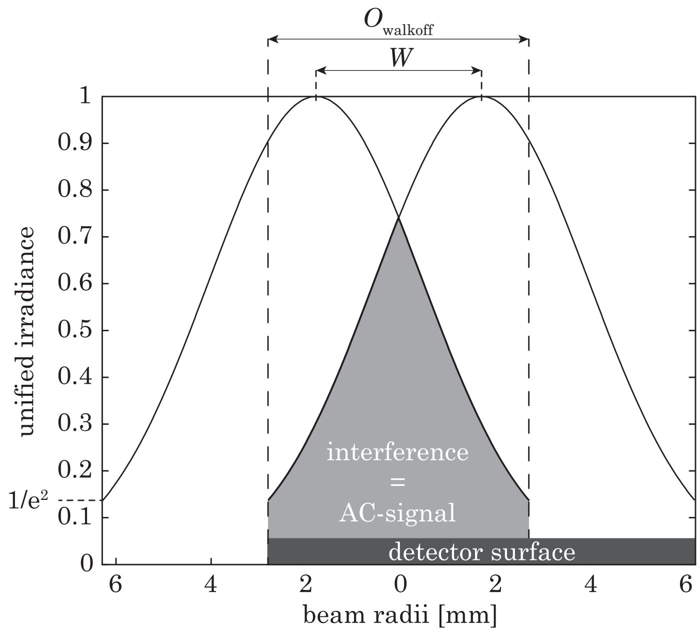

Figure 7.5: Beam walkoff with Gaussian irradiance distributions, having $1/e^2$ irradiance at the beam diameter. Note that the reference beam is fully received by the detector surface, whereas the measurement beam shows walkoff.

This analysis showed that the size of the measurement range and the amount of target rotation both result in substantial wavefront movement and substantially impact the AC-signal strength (which is the main reason for limiting the walkoff to ±3 mm). The benchmark system as well as the Delft interferometer system perform equal when it comes to beam walkoff.

There are optical solutions that counteract beam walkoff due to target rotation, however, these solutions result in a considerable size increase of the interferometer [48].

7.2.2.2 Pointing instability

The Ø9 mm free-space beams that originate from the source frequency delivery can show alignment instability, termed *pointing instability*. This pointing instability consists of time variant lateral and angular (i.e. yaw and tip) beam motion and affects the alignment of both the reference and measurement beams, see Fig.7.6. Examination of the benchmark system showed that pointing instability affects the system in several ways and takes place at several locations; pointing instability causes a time variant:

1. beam walkoff upon detection at the interferometer.

2. AC-signal strength upon detection at the interferometer (see Section 7.4).

3. in-coupling efficiency at the free-space to fiber in-coupling (see Section 7.4).

4. Cosine and Abbe error (see Section 8.3).

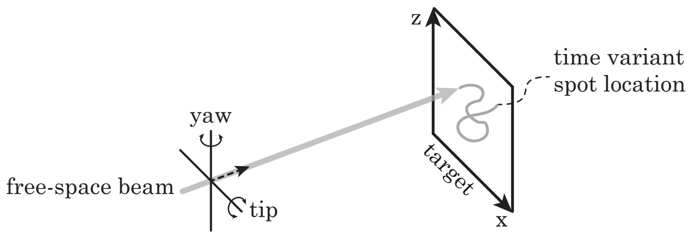

Figure 7.6: Illustrating how a time variant pointing location of a free-space beam results in both lateral (i.e. x, y) and angular misalignment with the target.

In the benchmark system the free-space coaxial beams are formed at the ROC, which presents a source of pointing instability determined by the thermal and mechanical stability of the supports of the fiber-ends, and the optical components involved in beam expansion and collimation. Although the ROC shows less pointing instability than the laser source, it cannot be neglected. Similar to the previous section, the result of pointing instability is mainly driven by the length of the free-space optical pathway, in case of the benchmark system this distance (between the ROC and the target) can amount up to several meters.

With the Delft interferometer also the thermal and mechanical stability of the free-space beam generation components determine the pointing instability, however, the Delft interferometer concept has the advantage that this process is located at the interferometer. This reduces the impact of pointing instability significantly since the free-space optical pathways are much shorter.

An additional aspect of pointing instability in the benchmark system consists of the beam splitters and mirrors that handle the free-space beams. Minimizing the pointing instability of these components requires both temperature and vibration control of these components, which is difficult, because not every location in the host-system allows for the desired level of control. In contrast, the Delft interferometer system only requires such control at the locations where the interferometers are located.

Concluding, a Delft interferometer has fewer sources of pointing instability whose measurement performance is, therefore, less impacted when exposed to equal thermal or mechanical disturbances as the benchmark interferometer system. However, each interferometer has two separated beams that show individual pointing, which present difficulty upon alignment.

7.2.3 Assessing interference wavefront topology

In the previous subsections it was shown that optical wavefronts affect measurement accuracy through time variant wavefront shapes and due to relative wavefront motion of deformed wavefronts. This section presents a method to confirm whether the indicated size of wavefront deformations estimated Section 7.2.1 are realistic.

There are several methods known for measuring the shape of optical wavefronts. The main group of wavefront sensors is based upon the 'Shack Hartmann' principle, where a micro lens array in combination with a CCD is used. This method is able to measure the absolute wavefront topology of the whole cross section of a beam in a single measurement, this method is also sensitive for tip/tilt alignment. With these sensors a trade-off is seen between phase-resolution versus spatial-resolution, which is limited by the size of the lenslet-array and the number of lenses. The phase resolution that can be obtained with this type of sensor ranges from λ/100 for a Ø6 mm beam diameter to λ/500 for Ø1 mm at λ = 633 nm [49].

Other research showed to obtain a phase measurement sensitivity up to λ/15500 at λ = 820 nm, though its spatial resolution was again limited by a lenslet array (30x30 lenslet-array over 12.5x12.5 mm, spatial resolution ≈ 400 x 400 μm per lens) [50]. Phase shifting interferometry is a different method which measures with the same order of phase resolution and beam diameters but offers a higher spatial resolution, which is limited by the CCD [51]. Another method worth mentioning [52] is based upon phase retrieval, in this method the wavefront is measured at different locations using a small moving sub-aperture while measuring irradiance distributions with a CCD. The use of a small movable sub-aperture for wavefront sampling shows similarities with the presented measurement method, depicted in Fig.7.7.

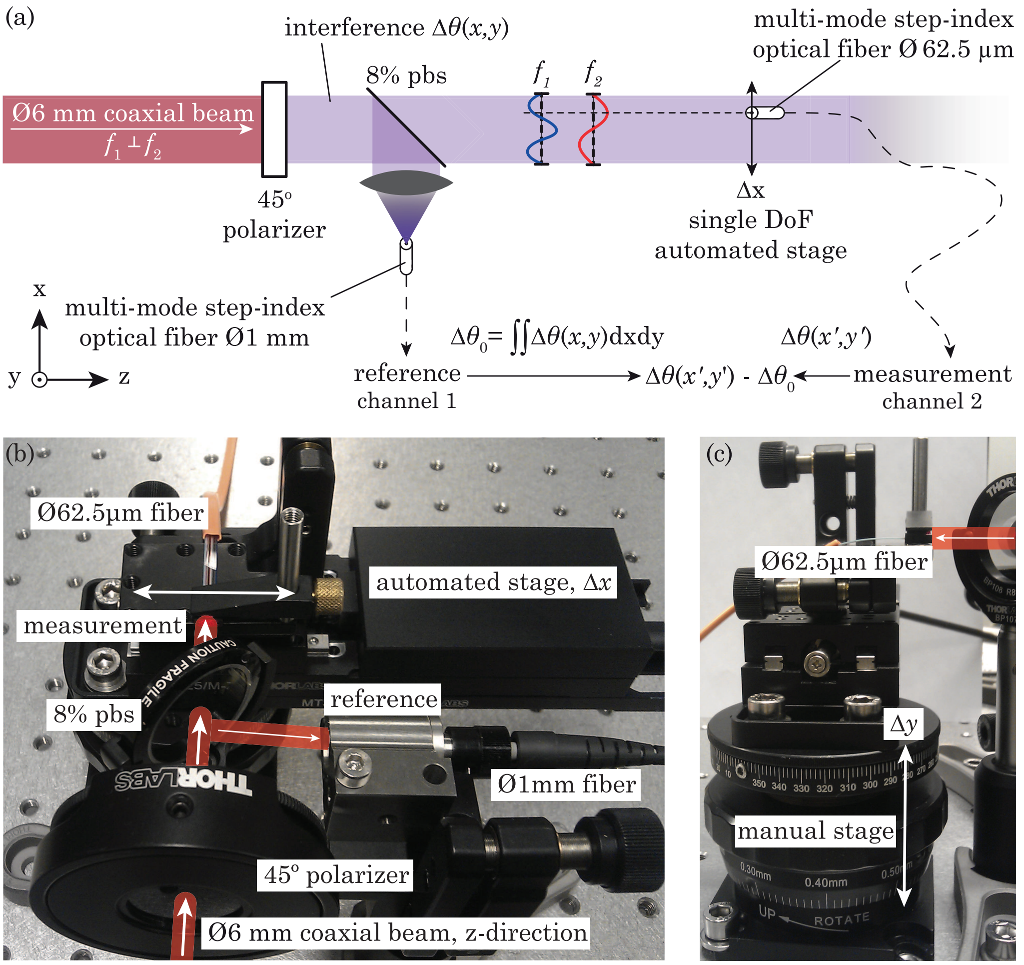

Figure 7.7: (a) Schematic overview of the experimental setup. (b), (c) Illustration of the realized setup, showing the automated x-stage and the manual y-stage for three dimensional reconstruction of an interference wavefront.

It is thus shown that the phase resolutions that can be obtained with commercial systems or other known measurement methods have an insufficient spatial resolution and phase resolution for investigating the shapes of interference wavefronts for this research. To gain a further understanding how the shape of individual optical wavefronts can lead to measurement errors via the interference wavefront required measurement at higher spatial and phase resolution, which promoted the development of a new measurement method.

The presented method examined the topology of the interference wavefronts that originated from two coaxial beam heterodyne laser sources. As the coaxial heterodyne beams entered the measurement system (Fig.7.7a), they passed a linear polarizer at 45°, creating interference between the two source frequencies. An 8% pellicle[2] beam sampler then sampled the entire interference wavefront (this signal contained the reference beat-frequency), which was subsequently coupled into a Ø1 mm step-index multi-mode fiber connected to channel 1 of the phase measurement board, here, the actual phase integration of the interference wavefront took place.

A second step-index multi-mode fiber (connected to channel 2 of the phase measurement equipment) with a core diameter of only Ø62.5 μm functioned as the aperture of the measurement probe that was transversely scanned through the beam. The light coupled into this measurement fiber was only a fraction of the total optical power (for the two tested laser sources these amounted ~0.4 nW using the *Agilent 5517D* and ~0.6 nW using the *Zygo Axiom 2/20*) and was only comprised of the collinear radiation that was in front of the fiber-facet; no light was coupled-in using lenses or any other aids. Therefore, the phase integration surface was equal to the fiber's core diameter. This resulted in a beat-frequency measurement of a small area. Next, the phase of this local beat-frequency was compared to the phase of the beat-frequency of the reference signal, by means of a differential operation as normally executed in heterodyne displacement interferometry. The differential outcome contained phase changes, $\Delta\vartheta$, over the cross section of the beam, representing the wavefront shape of the interference wavefront. With this method phase resolutions in the order of λ/25000 have been achieved, together with a spatial resolution of at least Ø60 μm, enabling detailed assessment of wavefront shapes for this research.

The Ø62.5 μm fiber was attached to a single DoF automated stage performing a continuous velocity displacement along the x-axis, see Fig.7.7b. The automated stage itself was located on top of a manually operated single DoF stage for displacement along the y-axis, see Fig.7.7c. These two stages enabled three dimensional reconstruction of the interference wavefront, see Fig.7.8.

The two illustrated interference wavefronts were measured at the exit of laser sources that provided coaxial heterodyne beams. In both cases they show that the interference wavefront can be deformed significantly. Deformations in the order of tens of nanometers are no exception. With such deformed wavefronts it would not be easy to obtain measurement uncertainty in the order of sub-nm.

Fortunately, wavefronts can be 'reset' by means of using a pinhole whose emerging light provides an ideally spherically shaped wavefront. In the benchmark system the source frequencies transported by the coaxial beam are separated after exiting the Zeeman laser source, the two separated beams subsequently propagate each through

[2] A pellicle type beam sampler was preferred because of its low amount of refraction due to its only 2 μm thick membrane.

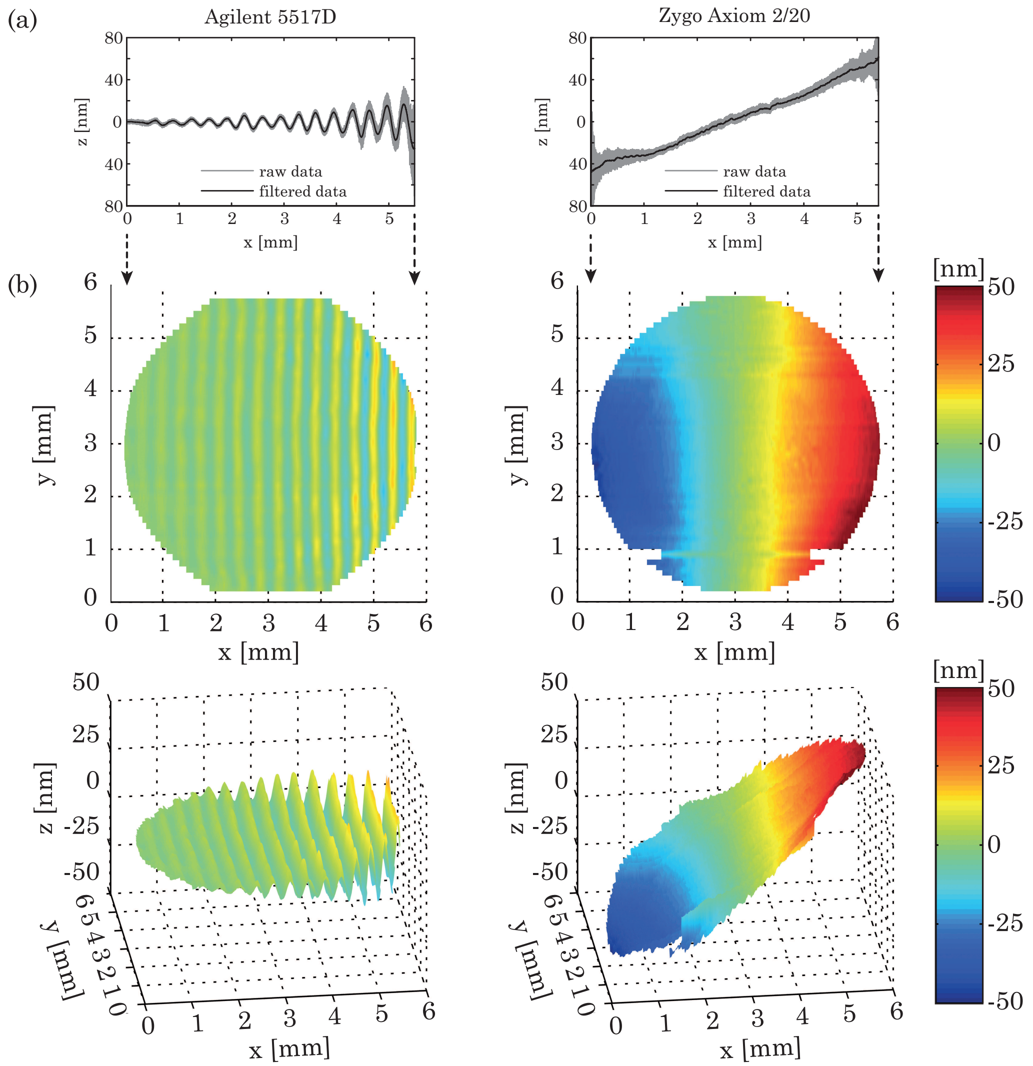

Figure 7.8: Illustration of two interference wavefronts from HeNe gas lasers, *Agilent 5517D* and *Zygo Axiom 2/20*. Both wavefronts were measured at the exit of the laser sources and originate from Ø6 mm coaxial heterodyne beams [10]. (a) Two line-scans showing the shape of the interference wavefronts along a single line, (b) 3D-wavefront reconstructions built from multiple line-scans. Although the interference wavefront of the *Zygo Axiom* laser is relatively flat, the tilt of the wavefront still results in several tens of nm measurement error upon beam walkoff. *During the research there was, unfortunately, no ROC available for wavefront shape assessment.*

an acousto-optic modulator and are finally coupled into two polarization-maintaining single-mode fibers (whose small core diameters act as a pinholes). At the ROC the free-space light from the fiber output is subsequently expanded, collimated, and put coaxial, in contrast to a Delft interferometer where the free-space light from a fiber only requires expansion and collimation.

Additionally, also an interference wavefront emerging from a single-mode non polarization-maintaining optical fiber was assessed, see Fig.7.9a and b. For this experiment the *Agilent 5517D* laser source was used.

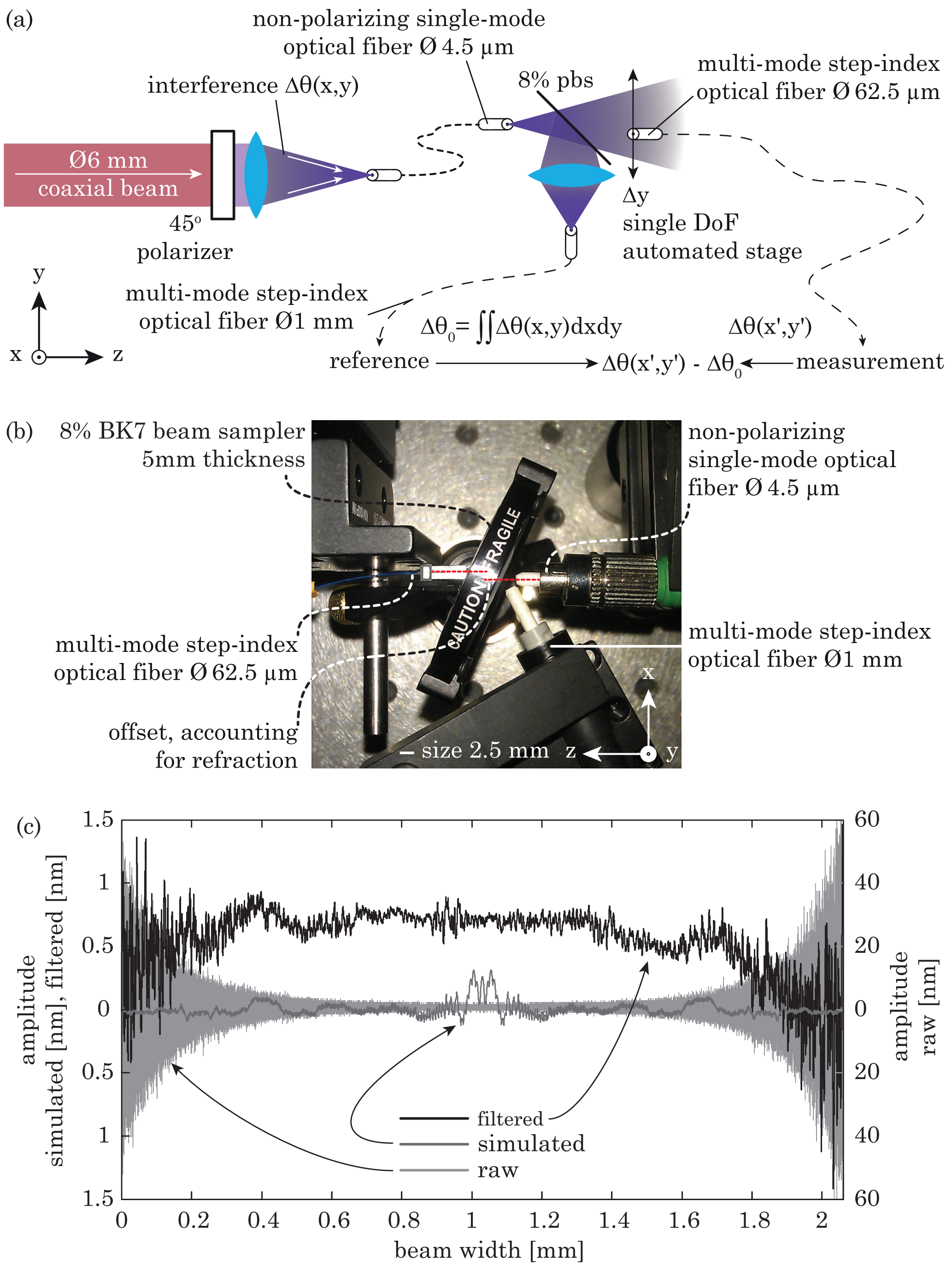

Figure 7.9: (a) Schematic overview of the measurement setup for measurement of an interference wavefront that is delivered by a single-mode optical fiber. For this experiment the *Agilent 5517D* HeNe laser source was used. (b) Close up of the measurement configuration. (c) Results of a *measured* and a *simulated* interference wavefront, both originating from a non polarization-maintaining single-mode fiber.

Comparing the line scan illustrated in Fig.7.9c with the line-scan from the *Agilent 5517D* laser source in Fig.7.8a confirms that a single-mode optical fiber (~Ø4 μm) is able to reset a deformed wavefront. The resulting wavefront from the single-mode fiber shows to be somewhat bulged but much less deformed, indicating a wavefront curvature of less than 2 nm, in contrast to the wavefronts of the coaxial beams that contained deformations in the order of ±20nm and ±50nm for the *Agilent* and *Zygo* laser, respectively.

In theory the single-mode optical fiber should act as a 'pinhole', which per definition delivers an ideally spherically shaped wavefront. To see if this was a realistic expectation the measurement was repeated in theory by means of simulation. The 2D-simulation featured a slit of which its size was equal to the optical fiber's core diameter, Ø4.5 μm. Through this slit, light with a center wavelength of 633 nm was passed and was comprised of two frequencies that were offset by 4 MHz (~equal to the split frequency of the *Agilent 5517D* laser source). The phase of the emerging light that was received by the fiber was subsequently integrated over a length equal to the core diameter of the Ø62.5 μm multi-mode step-index fiber. The eventual result is shown in dark gray in Fig.7.9c.

The simulated wavefront shows to be relatively 'flat' while the actual wavefront is slightly 'bulged', other than that, the two wavefronts show much resemblance. The absence of the bulging shape could be explained taking into account that the simulation integrated over a one dimensional line of 62.5 μm, instead of integrating over a 2D circular surface of 62.5 μm. It must be noted that the results consist of the phase differences between two individual wavefronts, therefore, the result does not represent the actual wavefront shape of the two individual wavefronts themselves.

It is known from theory that the wavefront that emerges from an ideal point source such as a pinhole is smooth and spherically shaped. Since the simulation shows much resemblance with the actual measured interference wavefront, it can indirectly be concluded that the wavefront emerging from a single-mode optical fiber in reality equals the ideal shaped wavefront from theory. This indicates that a single-mode optical fiber indeed approaches point source operation and enables delivery of optical wavefronts to an interferometer that are of higher quality (i.e. more flat) than provided by free-space coaxial beams.

7.2.4 Optical wavefronts in the benchmark system

The advantage of the benchmark system's coaxial beams is that both source frequencies are equally impacted by phase disturbances during the free-space optical transport. The common optical pathways of the beams ensure equal shaped wavefronts upon arrival at the interferometer, see Fig.7.10. This is solely useful when the wavefronts eventually overlap with the same relative orientation and positioning upon detection. Only under that condition, the equal shaped wavefronts result in a flat interference wavefront.

However, even under ideal circumstances, target rotation causes both lateral motion of the measurement beam, f_2 (i.e. beam walkoff) and an angled re-entry into the interferometer as illustrated in Fig.7.11, which leads to wavefront reshaping even under ideal circumstances, see Fig.7.12.

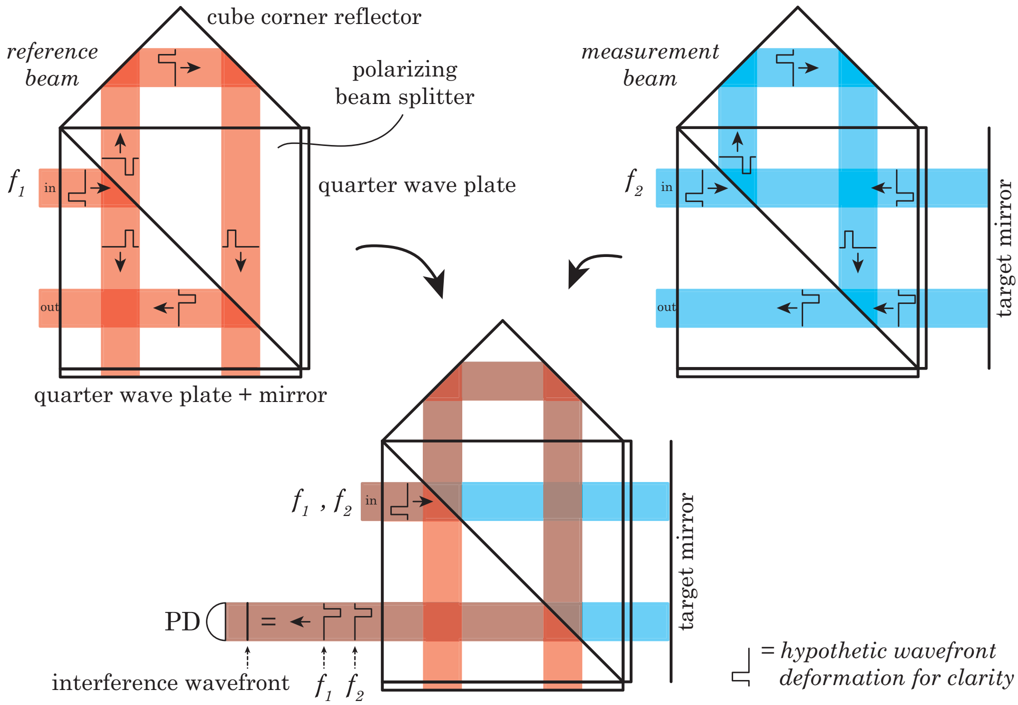

Figure 7.10: Illustration of a single DoF benchmark interferometer, showing beams with equal deformed wavefronts upon arrival (red and blue). Provided that no extra wavefront deformations are induced and assuming ideal alignment results in zero relative phase difference and leads to a 'flat' interference wavefront.

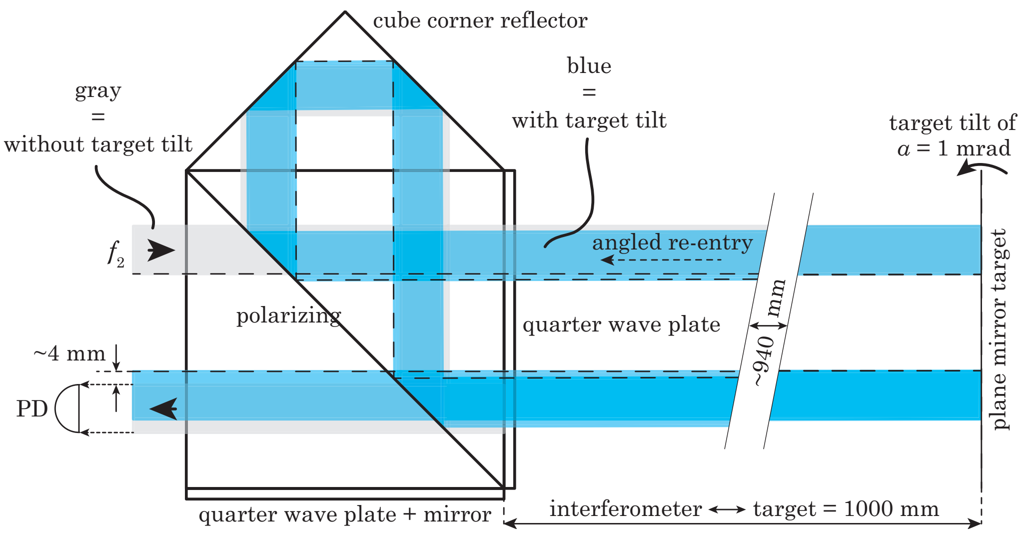

Figure 7.11: On scale overview of the measurement beam, indicating the optical pathway without (gray) and with (blue) target tilt.

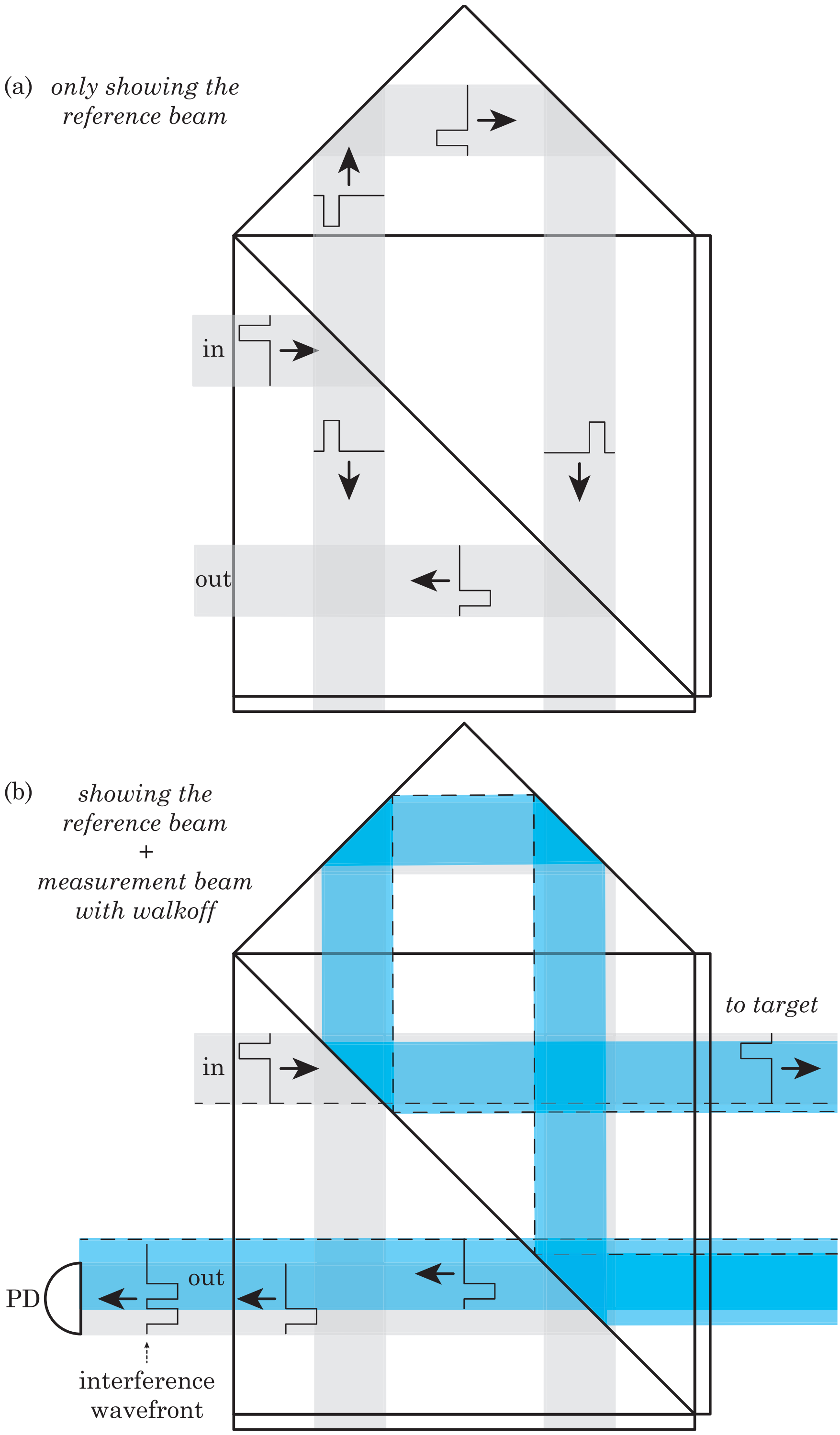

Figure 7.12: 1:1 Scale overview showing that having two identical wavefronts upon input (reference beam in a and measurement beam in b), combined with beam walkoff under ideal circumstances, leads to a non-flat interference wavefront. Therefore, beam walkoff alone already impairs the benefit of identical input wavefronts as provided by coaxial beams.

Figure 7.13a is used for explaining the effects when two transmissive surface bumps are located at the surface of the quarter wave plate. When assuming ideal alignment and no target tilt, these bumps reshape the wavefront twice at the same location. In contrast, Fig.7.13b illustrates the same interferometer with a tilted target, showing that walkoff causes the surface bumps to deform the wavefront at different locations, and with different impact due to the tilting angle, causing angled re-entry (equal to twice the target's tilt). In reality every surface has a certain geometry that reshapes any wavefront, which affects both the reference beam and measurement beam.

These figures show that the benefit of a coaxial beam (i.e. delivering equally deformed wavefronts to the interferometer) is negated at the moment the coaxial beam is split by the polarizing beam splitter. The two separated wavefronts are during their travel exposed to individual surface geometries and show a relative translation upon arrival at the detector, which removes any benefit of having equally shaped wavefronts upon entering the interferometer.

In other words, propagating with a beam along a partially common pathway and reflecting off a partially common mirror surface does not result in improved flatness of the interference wavefront. Based on this finding it can be stated that beam walkoff will have less impact if one provides an interferometer with two wavefronts that are unequal but have a flattened shape, instead of two identical wavefronts that are considerably deformed.

These findings lead to the conclusion that the use of coaxial beams does not result in a more flat interference wavefront (with the aim of reducing measurement error) compared to delivery of two separated wavefronts instead. The notion that: "using two separated source beams instead of a coaxial beam, leads to an induced measurement error", is thus a misconception.

Furthermore, the wavefronts delivered with free-space coaxial beams (in the benchmark system) are more prone to significant amounts of wavefront deformation than the wavefronts delivered with single-mode fibers[3] (in the Delft interferometer system). With a Delft interferometer, the free-space light delivered to the interferometer by the two single-mode fibers only requires propagation through a beam expander/-collimator before usage, which inherently results in more flat wavefronts compared to the benchmark system where the coaxial beams propagate several meters free through space and via several optical components.

7.2.5 Concluding optical wavefronts

The shape of an interference wavefront consists of the relative phase differences between the reference and measurement wavefront. A photodetector integrates the phase of the interference wavefront of which the outcome varies when the interference wavefront's shape is time variant, or when the integration area changes due to beam walkoff. A change in the phase integration is then subsequently falsely interpreted as target displacement and therefore results in measurement error.

[3]As a reminder, single-mode fiber delivery at each benchmark interferometer is not an option due to mixing of the orthogonally linearly polarized source frequencies within the fiber [17], as explained in Section 5.4.

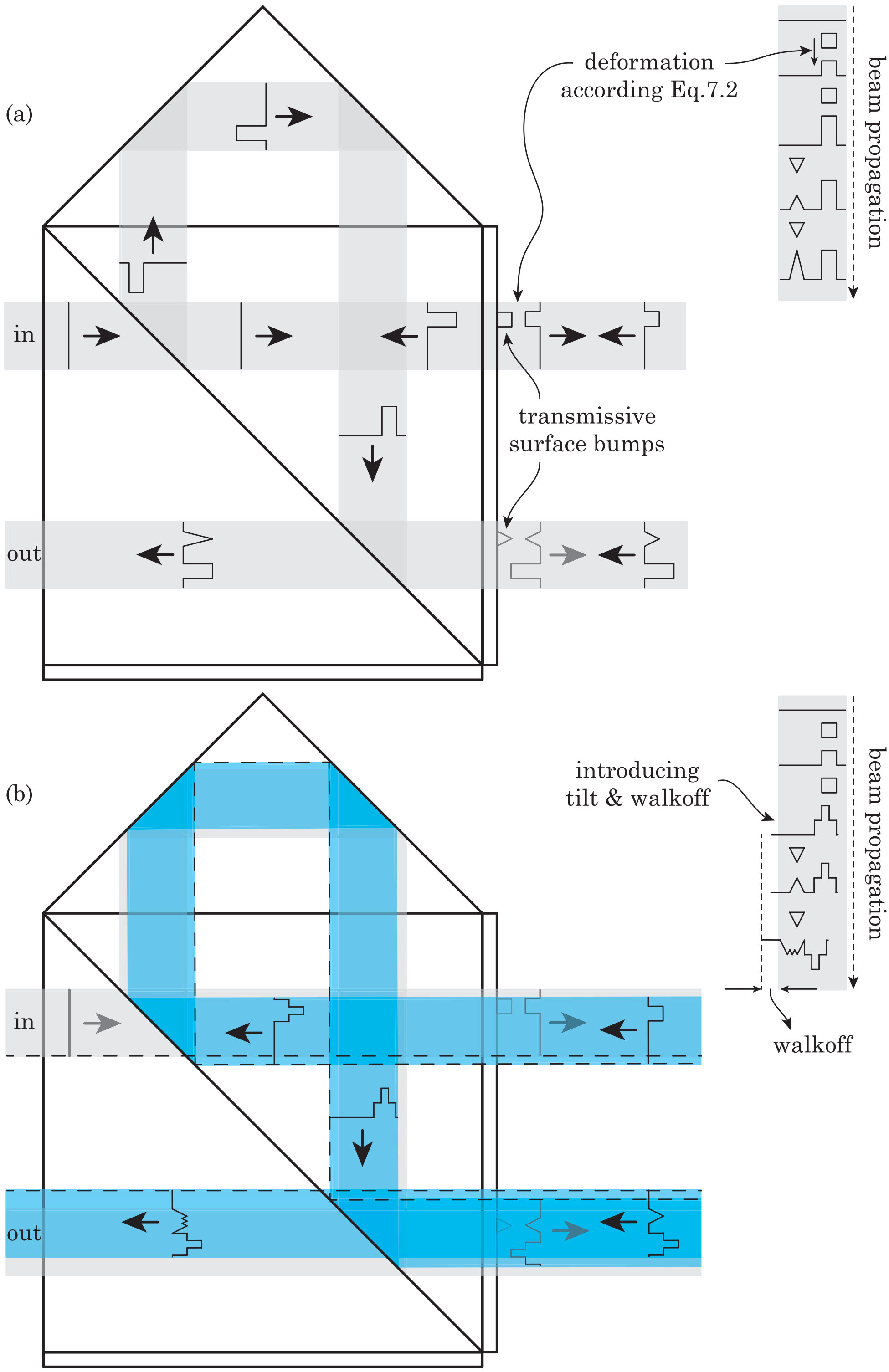

Figure 7.13: 1:1 Scale overview of wavefront deformations due to transmissive 'bumps' on the quarter wave plate. (a) Ideally aligned, (b) with target rotation. The illustration indicates that even with no walkoff (a), wavefront deformations due to surface geometry result in a non-flat wavefront. Walkoff (b) eventually makes the interference wavefront shape even more complex.

Wavefront deformations are incurred during both refraction and reflection. Refractive index variations affect a wavefront in different ways: during free-space propagation through (turbulent) gaseous media, density inhomogeneity of the optical components, and via non-flat or tilted optical surface geometries. Wavefront deformations due to reflection have, on the other hand, a single origin: optical surface geometry. The influence of turbulent gaseous media is minimized by operating in near-vacuum, however, the other sources of deformations remain and are especially present in combination with beam walkoff (i.e. transverse wavefront movement) of both the reference and measurement wavefronts.

There are two processes that drive the transverse movement between the reference and measurement wavefronts, target rotation (tip, tilt and yaw) and pointing (in)stability of the source beams. Target rotation affects only the measurement beam, whereas pointing instability of the source beams affects the alignment of both the reference and measurement beams. A Delft interferometer has fewer sources of pointing instability and shows less beam walkoff when exposed to equal thermal or mechanical disturbances as the benchmark interferometer system, which is mainly caused by the location of free-space beam generation (i.e. at the ROC in the benchmark system versus at each interferometer in the Delft system). The amount of beam walkoff due to target rotation is for the Delft and benchmark interferometer equal.

A new measurement method for assessing the optical wavefront shape of an interference signal showed that such a wavefront of free-space coaxial beams is already deformed significantly at the exit of the laser source. Interference wavefront deformations in the order of ±20nm and ±50nm were obtained for an *Agilent 5517D* and *Zygo Axiom 2/20* laser, respectively. Although the interference wavefront of the *Zygo Axiom* laser was relatively flat, the tilt of the wavefront still results in several tens of nm measurement error upon beam walkoff.
The interference wavefront emerging from a non-polarizing single-mode optical fiber was also assessed, it showed wavefront curvature in the order of less than 2 nm. Numerical simulation validated that the single-mode fiber acted as a point source and that wavefronts delivered by single-mode optical fibers are less deformed than the wavefronts delivered with free-space coaxial beams.

Additionally, a study regarding the potential advantage of coaxial beams and the interference wavefront shape upon detection concluded that: coaxially delivered source frequencies do not result in a more flat interference wavefront upon detection (with the aim of reducing measurement error), compared to delivery of two separated source frequencies. On the contrary, the measurement error due to beam walkoff is reduced when feeding an interferometer with two separated wavefronts that are unequal but more flattened (Delft interferometer), compared to providing an interferometer with two identical wavefronts that are considerably deformed (benchmark interferometer).

7.3 Data-age and signal timing

The limited propagation speed of light and electronic signals affects the measurement uncertainty of a displacement measuring interferometry system by two means: *data-age* and *signal timing*, both are explained in this section.

7.3.1 Data-age

The interferometer system in a lithography machine tracks the position of the stage carrying the wafer and delivers numerical values as input for the actuation system that handles the positioning of the wafer. This 'closed loop' but primarily 'feed forward controlled' system requires wafer placement to be accurate within 2 nm, while accelerating the wafer at 50-60 m/s^{2}and reaching velocities in the order of 1 to 2 m/s [53]. Such high positioning accuracy combined with these velocities puts heavy constraints on the 'age' of the data, i.e. how 'old' the data is from the moment of measurement.

Data-age is influenced by different domains, the 'electrical/digital' domain (i.e. signal conversion and mathematical operations), and the 'physical' domain (i.e. the optical layout of the interferometer system), see Fig.7.14. The digital-domain depends on the computer hardware of the phase measurement equipment, which generates data with a repeatable data-age [54].

The data-age caused by the physical domain is driven by the limited speed of light and describes the time required for target displacement-information to reach the phase measurement equipment. Part of this physical data-age is 'fixed', since the interferometer and detector have a fixed position and (i.e. their optical pathways do not vary in length over time, including deadpath), the 'variable' part consists of the distance between the interferometer and the displacing target.

This fixed amount of optical delay can be several nanoseconds and consists of both free-space propagation in a near-vacuum environment with (i.e. $\eta \approx 1$ for an optical pathway of e.g. 6 m gives $6 / c \approx 20$ ns), as well as optical propagation through optical fibers, which cause more delay per meter due to their increased refractive index (i.e. $\eta \approx 1.5$ for again an optical pathway of e.g. 6 m gives $6 / (c / 1.5) \approx 30$ ns).

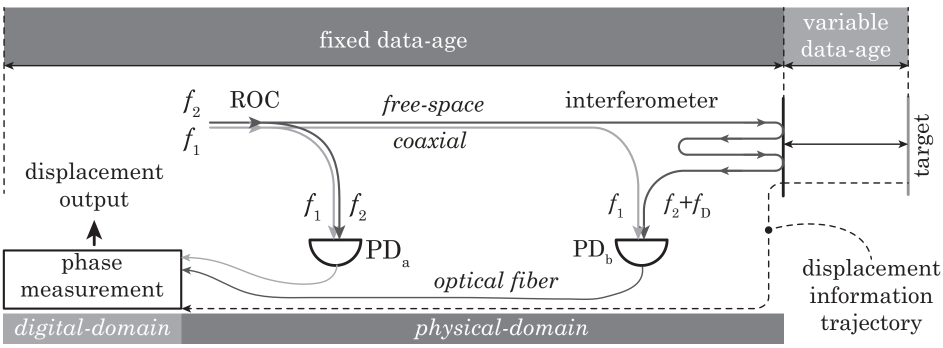

Figure 7.14: Schematic overview (using the benchmark system as example) indicating that the data-age of target displacement information is comprised of *digital* and *physical domain* related data-age. It is also shown that the data-age between the phase measurement equipment and PD$_{a,b}$ is fixed, whereas the data-age between the interferometer and the measurement target varies due to target displacement.

7.3.2 Signal delay

Analyzing signal timing in both interferometer systems requires to distinguish several cases where a phase disturbance in one of the source frequencies is assumed.

7.3.2.1 Benchmark interferometer system

An instant frequency increase (Δf) of source frequency f_1 combined with signal delay can cause measurement error. To indicate the problem that arises due to signal delay it is assumed that Δf starts at $t = 0$ and has a finite duration x, using the system as sketched in Fig.7.15a. The parameters that are considered are:

1. Stationary target

2. $\Delta f = 0.1$ MHz, a change in frequency that corresponds with a measurement error of ~0.4 nm (clarified at the following page).

3. x, duration of the source frequency deviation in seconds

4. $f_1 = c / \lambda_1$, where c is the speed of light in m/s, and λ_1 equals 633 nm.

5. $\lambda_2 = c / f_2$, where $f_2 = f_1 + f_s$, with split frequency f_s Hz.

6. $A = 3$ m, being the optical pathlength between PD_a and PD_b, deadpath $B = 0.5$ m, measurement range $C = 0.45$ m, and the additional measurement range $D = 0.05$ m.

7. $N = 4$, being the interferometer's fold factor.

At $t = 0$ the beat-frequency at both detectors is equal since the target is standing still, if a change in frequency is introduced, Δf, this will be measured by the two detectors

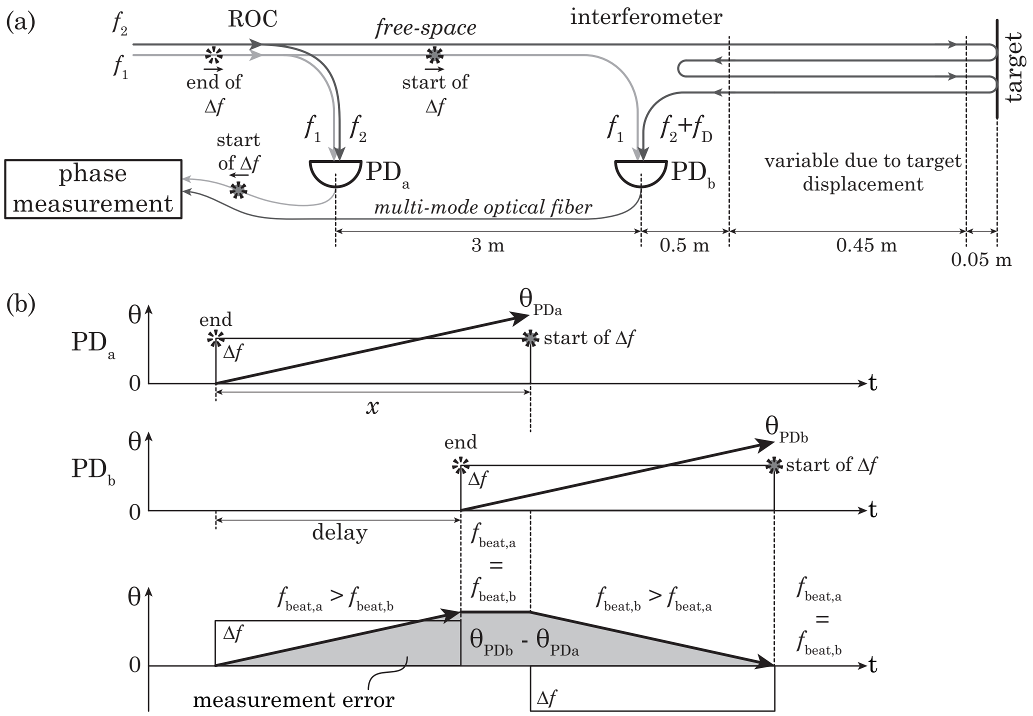

Figure 7.15: (a) Illustration indicating that the physical distance between the common reference, PD_a, and the detector at the interferometer, PD_b, results in measurement error due to a time delay. (b) As the beat-frequency of PD_a ($f_{beat,a}$) increases while $f_{beat,b}$ stays unaltered, phase accumulates and gives rise to measurement error via the differential operation until $f_{beat,b}$ equals $f_{beat,a}$, then the error stagnates and eventually reduces when $f_{beat,b} > f_{beat,a}$.

with a time delay (see Fig.7.15a) of ~25 ns (3 m free-space + 3 m optical fiber). During this delay the phase integration of PD_a accumulates until the beat-frequency at PD_b equals the beat frequency of PD_a, see Fig.7.15b.

A frequency increase of 100 kHz (i.e. 10^5 Hz) at PD_a leads to a phase accumulation of $10^5 \cdot 633$ nm per second, which results (after taking into account $N = 4$) in a measurement error of ~0.4 nm (i.e. $[(10^5 \cdot 633\ \text{nm})/N] \cdot 25$ ns) due to the optical delay; for a Δf in f_2 (3 m free-space + 4 m free-space + 3 m optical fiber $\approx$ 40 ns delay) this error could go up to 0.6 nm.

The use of the common reference at the ROC and the time delay caused by the physical distance between this reference and each individual interferometer results in a measurement error. Fortunately, the fixed delay can be accounted for by means of calibration (e.g. buffering the ROC's reference signal for a certain duration). However, the delay for a disturbance in f_2 can only be accounted for partially (only the fixed part, the variable part due to the moving target cannot be accounted for).

7.3.2.2 Delft interferometer system

Similar to the previous section also for the Delft interferometer system a phase disturbance in e.g. f_1 can be assumed. From Fig.7.16a can be seen that if detectors $PD_{a,b}$ both use f_1 for referencing and f_2 for measuring (and vice versa, both detectors using f_1 for measuring and f_2 for referencing), a differential operation between these detectors has no time-delay issues (i.e. no time delay between $PD_{a,c,e}$ and no time delay issues between $PD_{b,d,f}$, see page 35, Fig.4.8). Such detector pairs are used for several DoFs (see Section 4.4), and inherently inhibit measurement error due to timing issues.

In another case one can assume a phase disturbance in f_1 using the signal distribution as depicted in Fig.7.16b, here, PD_a uses f_1 for referencing while PD_b uses f_1 for measuring and f_2 for referencing. In that case the fixed delay consists of the optical pathway through the interferometer (i.e. only several tens of mm) and the variable delay is again proportional to the target displacement. Having the reference at the interferometer thus helps reducing the fixed time delay between detectors (and completely removes this error for a number of measurement axes with the Delft interferometer) and reduces the measurement error upon a frequency change (i.e. phase disturbance) in the source frequencies.

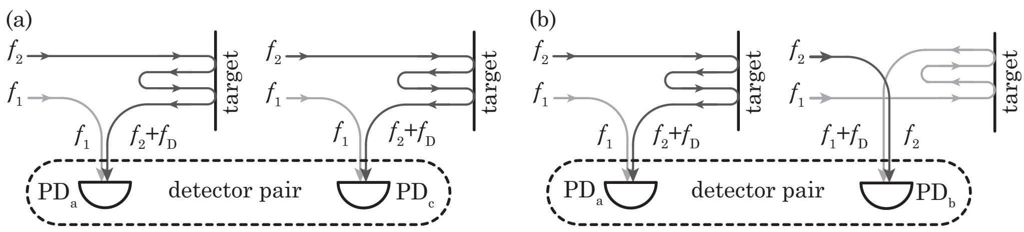

Figure 7.16: Timing related measurement errors are mitigated upon a phase disturbance in f_1 (a) and f_2 (b). *(Related to Fig.4.8.)*

7.3.3 Concluding data-age and signal delay

The data-age of target displacement is equal for both interferometer systems, provided that the same optical fibers (i.e. material and length) are used for interference signal transport, and that both interferometers have equal folding factors, which is the case.

Regarding signal delay the Delft interferometer system performs better than the benchmark system. In one case only the fixed time delay is solved, whereas in the other case both the fixed time delay and the variable time delay due to target motion are canceled, these two cases depend on which detectors are used for the differential measurement.

7.4 Irradiance distribution

The previous section showed that the result from a differential operation depends on the timing between the two signals (i.e. *phase*), however, the result of the differential operation also depends on the amplitude of the two signals (i.e. *irradiance*). A differential operation between to signals that are unequal in amplitude results in a residual error with an amplitude equal to the difference of the two primary signals, illustrated in Fig.7.17. Such unequal signal amplitudes come forth from fluctuations in the irradiance distribution, causing one interference signal to have a larger amplitude than the interference signal at another detector.

However, this does not need to result in measurement error since only the AC-component of the interference signal used, which is digitally normalized prior to the phase integration using the peak-to-peak values of the AC-signal. It is then after obtaining the integrated values (i.e. phase) of several detectors that the differential operation takes place. By means of this process no measurement error results from relative amplitude differences between individual interference signals. It is, nevertheless, important to realize that irradiance fluctuations must not take place at the beating frequency of the interference signal, since these fluctuations could be interpreted at the photodetector as being part of the interference signal's AC-component and, thereby, affect the phase interpolation; leading to measurement error.

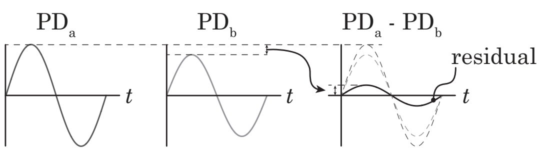

Figure 7.17: A differential operation between two unequal amplitude signals results in a residual signal. Something similar occurs when these signals have unequal phase.

7.4.1 Validating sensitivity to irradiance imbalance

There are several disturbance sources that affect the irradiance distribution within an interferometer system, such as vibrating optical components. The Delft interferometer system has one source of irradiance imbalance that differs from the benchmark system, which consists of the several fiber-optic connections that are employed for source light transport. Therefore, the effect of irradiance fluctuations (due to e.g. vibration) on the measurement performance of a Delft interferometer was experimentally investigated by means of optical irradiance modulation of one of the source beams. This was achieved by irradiance modulation of f_2 by means of amplitude modulation of the driver signal of AOM_2 (i.e. varying the power of the acoustic waves in the AOM crystal), see Fig.7.18.

The irradiance amplitude was varied around 50% of the maximum irradiance (i.e. ~7.5 μW AC-signal at detectors $PD_{1,2}$), with peak-to-peak modulation amplitudes of 10%, 20%, and 30%. The results are illustrated in Fig.7.19 and indicate a linear increase of the measurement error for irradiance variations up to 30%. From the results can be seen that although the amplitude of the irradiance fluctuations are quite large, their influence on the measurement error is modest. Since such large irradiance modulations are not expected during normal operation it can be concluded that the Delft interferometer concept is rather insensitive for irradiance fluctuations.

The AOM-drivers of the benchmark system did not provide the possibility to have their acoustic power varied, and other methods for varying the irradiance (e.g. using an EOM combined with a linear polarizer) would have resulted in secondary effects.

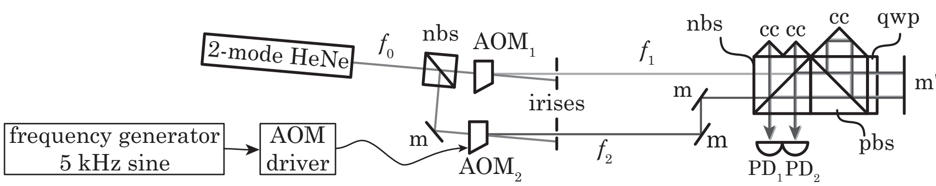

Figure 7.18: Schematic of the experimental setup where AOM_2 was used to modulate the irradiance of source frequency f_2 while the target mirror m´ was kept stationary. Legend: AOM_x, acousto-optic modulator; f_x, source frequency; PD_x, photodetector; m, mirror; nbs, neutral beam splitter; pbs, polarizing beam splitter; cc, cube corner reflector; and qwp, quarter wave plate.

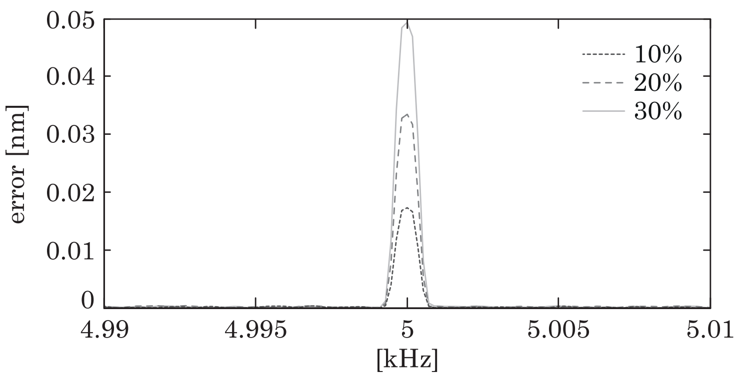

Figure 7.19: The figure illustrates the measurement error in the frequency domain due an irradiance modulation of source beam f_2, see Fig.7.18. The irradiance modulation was obtained by means of acoustic power modulation of AOM_2.

7.5 Conclusions internal error sources

A study regarding the potential advantage of coaxial beams and the interference wavefront shape upon detection concluded that coaxially delivered source frequencies do not result in a more flat interference wavefront upon detection, compared to delivery of two separated source frequencies. On the contrary, the measurement error due to beam walkoff is reduced when feeding an interferometer with two separated wavefronts that are unequal but more flattened (Delft interferometer), compared to providing and interferometer with two identical wavefronts that are considerably deformed (benchmark interferometer).

Regarding data-age both the benchmark and Delft interferometer system perform equal, provided that both interferometer systems have equal folding factors and use the same optical fibers for interference signal transport.

With respect to signal delay the Delft interferometer system performs better than the benchmark system. The Delft interferometer concept inhibits the delay related to the use of the common reference signal (i.e. at the ROC). It shows no timing related issues for several DoFs, and for the DoFs that do show timing issues, the Delft interferometer system performs better than the benchmark system.

The Delft interferometer system shows to have one source of irradiance imbalance that differs from the benchmark system: the optical fiber connections used for source light delivery. The sensitivity of the Delft interferometer concept for irradiance fluctuations (due to e.g. vibrations acting on fiber couplings) was analyzed experimentally. The experiment consisted of irradiance modulation of the source light carrying source frequency f_2, by means of amplitude modulation of an AOM, and was carried out at 5 kHz. The modulation amounted 10%, 20%, and 30% and resulted in a maximum error of less than 50 pm, indicating that the Delft interferometer system is robust regarding time varying irradiance of the source frequencies.
This also indicates that it is not necessarily required to use *polarization-maintaining* single-mode optical fibers. 'Normal' single-mode fibers are more favorable regarding modularity, since each fiber ending only requires four DoF alignment instead of five.

Chapter 8

Analyzing external error sources

In contrast to the previous chapter, this chapter deals with error sources that are not induced by the interferometer design itself but are caused by the measurement environment and the installation process.

The first section, Section 8.1, briefly clarifies what the term 'external error sources' means for this work. In the next section, Section 8.2, environmental error sources are addressed. These error sources include thermal effects, discussed in Section 8.2.1, followed by a subsection about mechanical vibrations and stability of the interferometer mount, Section 8.2.2. Furthermore, refractive index in combination with deadpath are addressed in Section 8.2.3, followed by the last subsection, Section 8.2.4, which briefly deals with target mirror uniformity.

The second part of this chapter discusses error sources that are related to 'installation' of the interferometer system. This part only consists of one section, Section 8.3, which in short reviews the Abbe and Cosine error in relation to the Delft interferometer.

The last section of this chapter, Section 8.4 summarizes that the Delft and benchmark interferometer show equal sensitivity for homogenous heating, however, the Delft interferometer is more sensitive for inhomogeneous heating. Moreover, the Delft interferometer offers compensation for deadpath or for interferometer motion in the x-direction, without the need for an additional detector. A Delft interferometer also has improved surface roughness averaging for the x-axis, which reduces the impact of surface inequalities. Final, Abbe and Cosine errors are potentially smaller for a Delft interferometer due to its increased system modularity that eases system installation and alignment.

8.1 External error sources

In this work *external error sources* refer to sources of error that are related to both the measurement environment where the measurement is performed (e.g. temperature variations), as well as to the installation process during which the interferometer system is installed in the host-system (e.g. misalignment).

8.2 Environmental error sources

The environmental error sources influence the measurement performance at the locations where the interferometer system interacts with or connects to its environment, examples are: the temperature variations of the environment, mechanical stability of the interferometer-support, time variant refractive index fluctuations in the free-space medium, or target mirror uniformity.

Variations in the environment of the heterodyne frequency source also affect the measurement performance of the interferometer system, but to a lesser degree than variations in the environment where the measurement takes place. Therefore, the environment of the heterodyne frequency source is not taken into account.

8.2.1 Thermal drift

Thermal sensitivity of an interferometer is given by the measurement error that is caused by thermal expansion of the interferometer optics. Expansion of the optics could result in an unequal change in optical pathlength between a reference and a measurement optical pathway, which is falsely interpreted as target displacement, and therefore, represents a measurement error.

Changes in environmental temperature influence the state of the interferometer optics via three distinct processes, conduction (via mounting), convection (through gaseous flow) or radiation. The level of impact (i.e. component deformation) depends on the duration of the thermal variation, its magnitude (i.e. temperature difference) and the process of interaction.

the measurement environment consists of a near-vacuum environment (see Section 3.1) where the gas-mixture and temperature are both controlled. The temperature inside this near-vacuum chamber is controlled by means of temperature control of the supplied gas mixture, achieving temperature stability between 50-100 mK.

The temporal stability required depends on the maximum duration of the wafer calibration or exposure process. This temporal stability is thus driven by the throughput of the lithography machine. Since each wafer carries its own calibration marks, the temporal stability of the interferometer only requires to have sub-nm accuracy within the time frame of the start of the calibration process till the end of the exposure process. Assuming similar process speeds as ASML's NXT platform, then this time equals approximately 15 seconds with 230 wafers/hour exposure. With an increase in surface area of a 300 mm wafer to a 450 mm wafer (i.e. a factor 2.25), the processing time would be ~35s.

8.2.1.1 Homogeneous heating

First, an example is presented to clarify the relation between thermal expansion and the decrease in measurement accuracy. The materials that are usually applied for interferometer optics (e.g. BK7 glass and fused silica), show a positive material expansion and a negative change in refractive index upon a temperature increase. Figure 8.1 shows a Michelson interferometer where a temperature difference exists

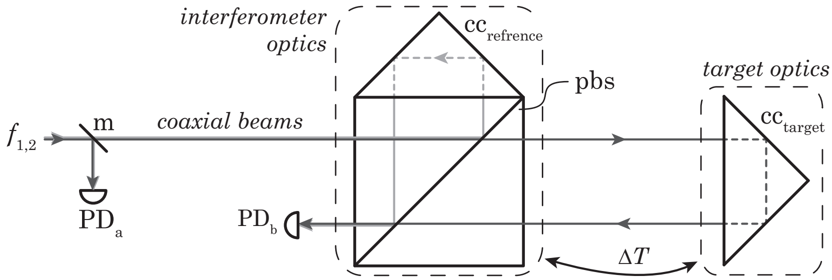

Figure 8.1: A temperature difference (ΔT) incurred during the measurement between the interferometer optics and the target optic results in measurement error. When the interferometer optics and the target optics are at equal temperature, the dotted lines are equal in length. When a change in temperature occurs, the length of the reference pathway through $cc_{reference}$ will differ from cc_{target}, which is falsely interpreted as target displacement.

between the interferometer optics and the target optic, affecting the optical pathlength equality between f_1 and f_2. The relation between a temperature increase of ΔT, and the increase of the optical pathlength, Δs_α, is given by

$$\triangle s_\alpha = s \cdot \alpha_{\mathrm{BK7}} \cdot \triangle T, \tag{8.1}$$

where the initial pathlength is represented by, s, and the thermal expansion coefficient is given by α_{BK7} (e.g. α_{BK7} = 7.1e-6 [m/K]).

As the material heats up and expands, its refractive index, η_{BK7} (i.e. η_{BK7} = 1.51) changes according the thermal coefficient of the refractive index, e_{BK7} (e.g. e_{BK7} = -3e-6 [η/K]). The change in refractive index alters the physical length of the optical pathway and partially compensates for the increase in pathlength due to material expansion (through Snell's law).

The change in optical pathlength due to a change in environmental temperature is given by

$$\triangle s = \frac{\triangle s_\alpha}{\eta + (e_{\mathrm{BK7}} \cdot \triangle T)}. \tag{8.2}$$

Taking into account an initial optical pathway s = 20 mm (using one of the small cc's from Fig.8.2b), and a temperature change of 50 mK, this results in an optical pathlength increase of ~4 nm, which shows up in the setup of Fig.8.1 as result of the differential phase measurement between PD_a and PD_b and will be interpreted as target displacement[1]. Thermal expansion of the interferometer optics thus results in 'drift', a time varying measurement error.

When reviewing the benchmark system (Fig.8.2a), it is shown that the optical pathways of both the reference pathway and the measurement related pathway part inside the interferometer are equally long. Therefore, when this interferometer is manufactured ideally it will show no thermal drift upon an overall thermal expansion.

Figure 8.2b illustrates the optical pathways of the Delft interferometer from Fig.4.7 and shows that the pathlength-ratio between the reference and measurement beams

[1]Dispersive effects can be neglected due to their small impact, i.e. ~10^{-15} m.

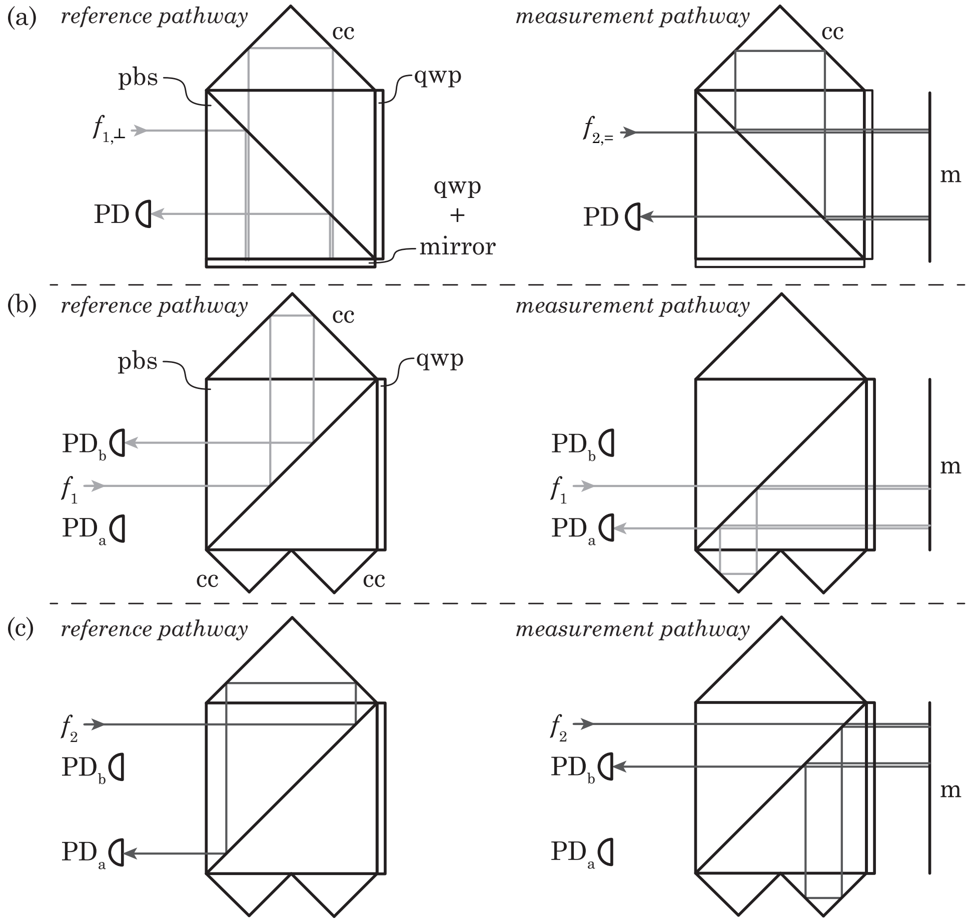

Figure 8.2: Illustration of the reference (left) and measurement (right) optical pathways of (a) a single DoF benchmark interferometer, and (b), (c), a Delft interferometer. The illustration shows in (a) that the optical pathways for the reference and measurement beam are equally long inside the optical monolithic structure, which leads (when ideally manufactured) to no measurement error upon thermal expansion. The Delft interferometer mitigates homogeneous thermal expansion differently, it does this by optical symmetry between the two detectors; this removes the need for pathway balancing as applied with the benchmark interferometer.

amounts 1.5, which is not as balances as seen in a benchmark interferometer. Fortunately, the Delft interferometer is designed symmetric, making this ratio equal for both f_1 and f_2. This optical symmetry results in equal presence of the thermal expansion in both detectors signals, which is canceled after the differential operation between PD_a and PD_b.

To conclude, homogeneous thermal expansion results in global expansion of the interferometer optics, which has long time constants. For this type of expansion the Delft interferometer concept does not require optical pathlength balancing between reference and measurement pathways, as required for a benchmark interferometer, because thermal expansion is compensated by optical symmetry between e.g. PD_a and PD_b.

8.2.1.2 Inhomogeneous heating

Inhomogeneous thermal expansion concerns local expansion of the interferometer optics, which is driven by thermal gradients that arise due to unevenly distributed heat loads. Such heat loads are critical when causing significant optical pathlength variations within the time required to process a single wafer. Thermal processes that have larger time constants than the time required for processing a single wafer are less critical because an interferometer performs relative measurements.

The most crucial locations regarding inhomogeneous heating of the optically monolithic structure are the edges, corners, and surfaces that are exposed to the measurement environment. This indicates that the cube corner reflectors are the interferometer's most sensitive parts with regard to thermal expansion.

Figure 8.3a illustrates that the optical pathway of f_1 is situated towards the 'tip' of the large cube corner reflector, while the pathway of f_2 is located more at the base of this cube corner (see also Fig.8.2b). Due to the shape of the reflector (surface versus volume) there is less thermal mass at the tip to than at the bottom, when impacted by a heat load this causes the material at the reflector's tip to expand more than than the material at the bottom. This leads to pathway lengthening of f_1 while f_2 is less (or not) affected, this results in measurement error.
Something similar can take place between the two smaller cube corner reflectors at the bottom in Fig.8.3b, which can be impacted unequally by a thermal load.

Three examples of solutions that could increase thermal robustness are:

1. Coating on cube corner reflectors
A solution that reduces the unequal material expansion illustrated in Fig.8.3a consists of applying a coating on the cube corner's outer surface that has varying properties regarding radiation absorption, and/or thermal conductivity. By means of these varying material properties a thermal absorption/distribution profile can be achieved that accounts for the shape of the cube corner reflector and results in a more uniform material expansion.

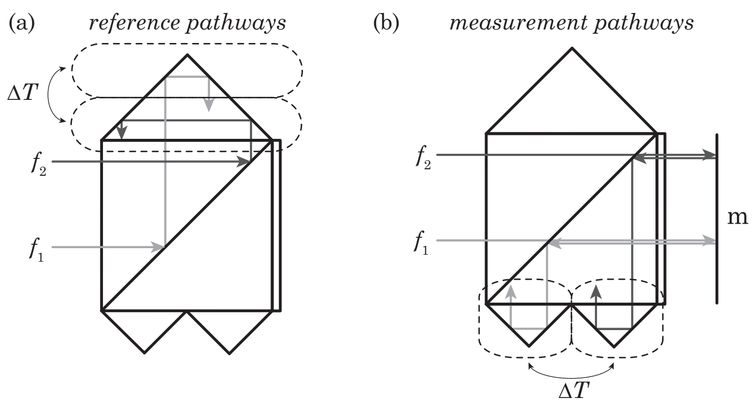

Figure 8.3: Illustrating inhomogeneous heating of (a) one large cube corner reflector, and (b) two smaller ones. Both situations result in optical pathlength differences between the optical pathways of f_1 and f_2.

2. Adding thermal mass
Adding thermal mass to a cube corner reflector as illustrated in Fig.8.4a increases the component's thermal time constant and reduces thermal gradients. Adding thermal mass is an easy and passive solution, however, encapsulating a cc in this manner requires complicated manufacturing methods and leads to increased cost. An easier method would be to add thermal isolation around the reflector, blocking fast thermal influences; also this method is passive and presents a more feasible solution (see below).

3. Thermal shielding
Figure 8.4b shows an example of a passive thermal shield that encloses the interferometer optics and shields the cube corners from heating up unequally. Still, the holes in the shield (required for the free-space beams) allow for unwanted passages to the interferometer optics, these holes can be closed by using nitrocellulose membranes, being only a few micrometer thick (i.e. ~2 µm in general). The shield has to act as an interface between the interferometer and the measurement environment that has to absorb 'fast' (i.e. time to process one wafer) local heat loads and release them over time over an enlarged surface. A shield from thermally conductive material such as aluminum should achieve this.

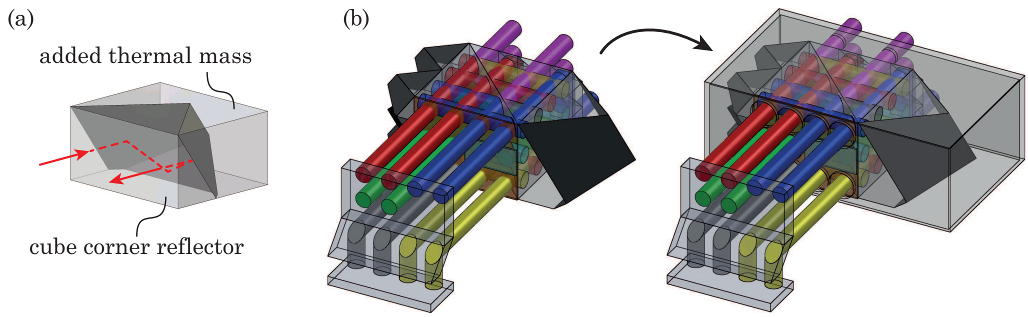

Figure 8.4: (a) Adding thermal mass to a cube corner reflector reduces the impact from 'fast' localized heat loads, which could consist of BK7 glass as illustrated, or a plastic. (b) Applying a shield of thermally conductive material helps distributing local heat loads, and spreads heat loads over time (i.e. damping).

8.2.1.3 Concluding thermal drift

When dealing with homogeneous temperature changes, both the Delft and the benchmark interferometers show no change in measurement accuracy. Regarding inhomogeneous temperature variations, the Delft interferometer is more sensitive to thermal variations than the benchmark system. This is mainly caused by the thermal sensitivity of the cube corner reflectors and the several individual optical pathways.

A potentially effective and easy to implement solution to protect the optics from fast (i.e. driven by the process time per wafer) thermal fluctuations is to use a passive shield that encloses the interferometer optics with a thermally conductive material (e.g. aluminium).

8.2.2 Mechanical stability interferometer mount

The interferometers described in this work measure relative displacement between the interferometer and the measurement target, which means that the measurement includes both target displacement and displacement of the interferometer optics. Measuring target displacement with sub-nm accuracy thus requires the interferometer to measure from a stable position. This position, however, is affected by mechanical vibrations or thermal expansion of the interferometer mount, which is therefore attached to the metrology frame to ensure positional stability.

The reference mirror as proposed in Section 4.4.1, and shown for a 3-DoF interferometer in Fig.8.5, determines the interferometer's reference position, whose position is determined by datum pins on the metrology frame.

The reference mirror of the Delft interferometer does not lead to an improved measurement performance over a benchmark interferometer, both are equally affected by mechanical motion of the interferometer mount.

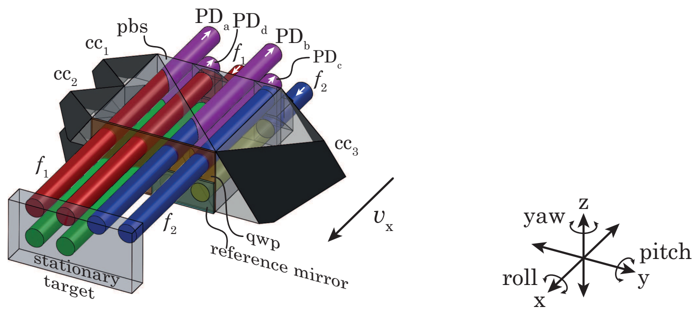

Figure 8.5: Illustrating movement of a 3-DoF Delft interferometer over the x-axis caused by mounting instability of the interferometer optics, while measuring a stationary target.

8.2.3 Refractive index and deadpath

Changes in the refractive index of a free-space medium affect the physical length of optical pathways (referring here to global changes in optical pathlength and not to spatial wavefront deformation, see Section 7.2) and result in measurement errors. By obtaining environmental information, such as gas pressure, gas purity, temperature, and humidity (which is not of importance when operating at near-vacuum conditions), the measurement error due to refractive index variations can partially be accounted for by means of using the modified Edlen equations (e.g. using Birch and Downs [55]).

In the benchmark system the measurement performance is not affected by refractive index changes of the medium where the free-space coaxial beam propagates through, due to the common optical pathways of the (linearly orthogonally polarized) source beams. With regard to refractive index changes that affect the free-space beams between the interferometer and the measurement target, the benchmark and Delft interferometer are equally affected.

However, without the use of additional detectors the Delft interferometer concept can reduce deadpath related measurement errors (Fig.8.6a) by means of using a 'ref-

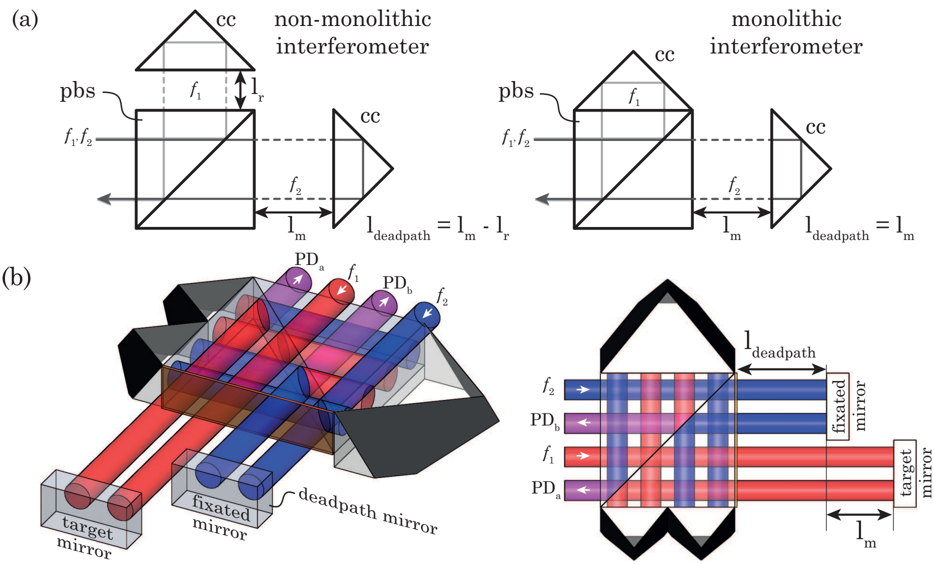

Figure 8.6: (a) The deadpath consists of the difference in physical pathlength of free space beams, between the reference and measurement pathways. A change in refractive index result in a relative difference of the physical optical pathways. (b) Without the need for an additional detector a Delft interferometer can compensate for deadpath by locating a mirror at the end of the deadpath.

erence' mirror located at the end of the deadpath, see Fig.8.6b. Taking into account that the interferometer and the deadpath mirror are both held by the metrology frame (i.e. vibration isolated), and assuming that the refractive index fluctuations are on average the same for all beams, then the deadpath related error can be compensated without the need for an additional measurement channel.

The mirror at the end of the deadpath will function as a reference mirror, any differential measurement is subsequently performed with respect to this mirror. Refractive index changes that occur along the deadpath are assumed to equally affect all measurement beams (i.e. f_2, blue and f_1, red, Fig.8.6b) and thereby do not add to a measurement error.

The feasibility of this concept depends on the system architecture of the lithography machine, a possible location for such a deadpath mirror (that still ensures full mobility of the wafer stages) is in between the wafer stages and the planar surface where the two stages are levitating above.

8.2.4 Target mirror uniformity and optical footprint

The target mirror uniformity refers to the surface geometry of the target's reflecting surface. As was shown in Section 7.2, surface inequalities result in wavefront deformations that result in measurement errors.

The amount of optical beams that traverse back and forth between the interferometer and the target mirror are equal for both the benchmark and Delft interferometer, both 5-DoF interferometers use 10 free-space beams (see page 23, Fig.3.4, and page 35, Fig.4.8), which results in similar sized optical footprints at the target mirror.

However, with the Delft interferometer concept the x-axis (for example) is measured using four Ø9 mm spots divided over two spots per measurement/detector (see page 34, Fig.4.7), whereas with a benchmark interferometer this DoF is measured with only a single measurement using two Ø9 mm spots. The optical surface integration area per measurement is thus not increased, but, now two (uncorrelated) measurements are used for determining the position of the target surface. This reduces the impact from surface non-uniformities (i.e. noise), and leads to an improvement of the signal to noise ratio compared to a benchmark interferometer.

Nevertheless, when aiming for sub-nm measurement uncertainty both the Delft and benchmark interferometer require calibration to cope with target mirror non-uniformity (i.e. mapping the mirror surface and generating a digital look-up table).

8.3 Installation error sources

Upon misalignment of the measurement axes the measurement performance of the benchmark and Delft interferometer is equally influenced by the Abbe and Cosine error, Fig.8.7, with one difference, the modularity and optical layout of the Delft interferometer aids alignment optimization. Although there are two individual supply beams that need alignment with respect to the Cosine error, and relative to each other as well. The relative alignment can be factory aligned and calibrated prior to installation into the EUV-lithography machine.

In the benchmark system the Abbe and Cosine related alignment already starts at the free-space coaxial beam generation at the ROC, whose alignment is directly coupled to the alignment of the measurement beams. The alignment optimization of these measurement beams is difficult when taking into account that the coaxial beams are guided via mirrors and beam splitters, which are sources of misalignment.

An extra complication of the free-space coaxial beam delivery is that all interferometers use the same coaxial beam that originates from the ROC, which adds complexity or even prohibits alignment optimization of individual interferometers. In contrast, for a Delft interferometer the free-space optical beams are generated *at* the interferometer. When taking also into account the modularity provided through the use of optical fibers, the Delft interferometer concept allows for individual alignment of each interferometer, which supports further alignment optimization compared to a benchmark interferometer as well. Therefore, the measurement errors related to installation are reduced when using the Delft interferometer concept.

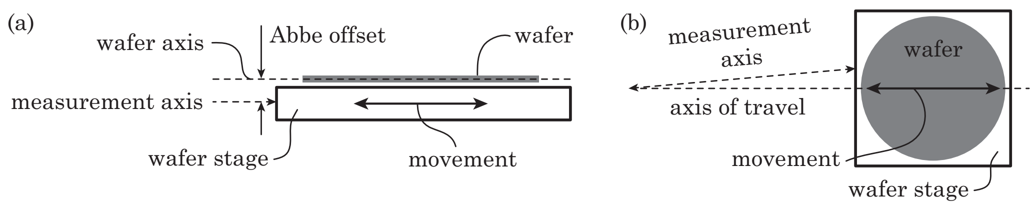

Figure 8.7: (a) Abbe offset error results from a lateral offset between the desired axis of measurement and the actual axis of measurement. (b) Cosine error results from angular misalignment between the measurement axis and the target's travel axis.

8.4 Conclusions external error sources

The Delft interferometer is equally sensitive for homogeneous heating as the benchmark interferometer, but it is more sensitive for inhomogeneous heating. However, the influence of inhomogeneous temperature changes are only crucial when impacting the interferometer within the processing time of a wafer (i.e. ~35 s). A feasible solution that protects the interferometer from direct influence of heat loads could consists of a passive shield from thermally conductive material (e.g. aluminium). Such a shield absorbs thermal energy and release it over time (i.e. damping thermal impact and increasing the thermal time constant) over an enlarged surface of the interferometer optics.

The benchmark and Delft interferometer systems are both equally sensitive to mechanical motion of the interferometer mount, and to refractive index variations in the free-space medium between the interferometer and the target. However, without the cost of an additional measurement channel a Delft interferometer can compensate for deadpath related error by placing (i.e. relocating) the reference mirror at the end of the deadpath.

The optical footprint of both the benchmark and Delft interferometer are equal, but the measurement surface used for determining one DoF displacement is twice as large with the Delft interferometer compared to a benchmark interferometer. This improves determination of the surface average of the target mirror by ~35%, which thereby reduces measurement error due to target mirror surface inequalities.

Moreover, compared to the benchmark system, the modularity of the Delft interferometer (i.e. employment of optical fibers) achieves in combination with the generation of the the free-space beams (which can be factory aligned) at the interferometer a reduction of alignment related errors source such as the Abbe and Cosine error.

Part IV

Industrial implementation

***Chapter 9*, treats the implementation of the Delft interferometer system into industry. In this chapter two $\lambda/8$ Delft interferometer configurations are illustrated, which can measurement up to five DoFs. The chapter also describes how to gradually implement the Delft interferometer concept into industry.**

Chapter 9

Proposed Delft interferometer system implementation

All preceding chapters have dealt with system design and analyzing the performance of the benchmark and Delft interferometer system. This chapter describes how the Delft interferometer system can be realized in industry.

The chapter consists of only two sections, Section 9.1, illustrates two 5-DoF interferometer configurations together with a number of configurations for fiber out and in-coupling at the interferometer.

The second section, Section 9.2 addresses how the Delft interferometer system can be introduced best into industry, distinguishing between full implementation of the system as shown in Chapter 6 or gradual introduction into existing host-systems.

The final section, Section 9.3 states that short-term industrial implementation of the Delft interferometer concept is feasible, and that it is beneficial to use the benchmark system's heterodyne frequency source upon introduction to industry.

9.1 Monolithic five-DoF configurations

The benchmark system, sketched in *Chapter 3,* uses 5-DoF interferometers similar to the one illustrated in Fig.9.1a, with next to it two 5-DoF configurations of the Delft interferometer. Although the number of optical pathways inside the Delft interferometer optics is larger, the size of the optical monolith is of the same order.

9.1.1 Size of the interferometer monolith

Besides taking into account beam walkoff, it is important to realize that the size of the interferometer optics is also related to the Abbe error. During wafer exposure in a

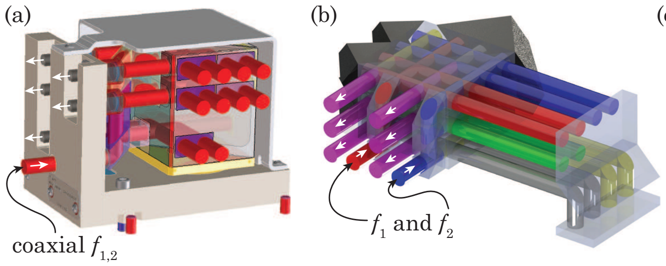

Figure 9.1: 3D Representation of five-DoF monolithic interferometers. (a) 'right-turn' benchmark interferometer (*Agilent Z4420B*) shown with interferometer mount and optical pickup but without plane target mirror, (b) 'right-turn' Delft interferometer, (c) 'straight' Delft interferometer. The illustrations are to scale and all accommodate Ø9 mm beams.

lithography machine, the location of exposure forms the 'point of interest', location A, see Fig.9.2. Unfortunately, it is not possible to measure always in line with location A (which would be ideal, see also page 823 of [15]), since the wafer can tilt around the y-axis and move along the z-axis (in the sketched situation), while the optical beams of the interferometer are stationary. Because in-line measurement does not take place, a second measurement beam is required to also take into account angular motion, which enables compensation of the effect of the Abbe offset.

When doing so, measurement errors in the x direction along the interferometer's measurement axes a and b, lead to position errors of A along the x and z-axis, which can be larger than the initial measurement errors in beams a and b.

In the sketched situation, Fig.9.2, the position related error comes forth from a combination of the Abbe offset, the relative beam separation c and the distance e. When assuming a positive and a negative measurement error of 0.1 nm for a and b respectively, this leads for location A to a measurement error of ~0.3 nm in the x-direction and ~3 nm in the z-direction. Both measurement errors are much larger than the initial displacement measurement error of the two interferometer axes.

Smart placement of the measurement axes and their separation play an important role in reduction of the Abbe error. For example, when c is enlarged, the angle determination suffers less from the measurement error in a and b, leading to a reduced Abbe error. This, however, increases the size of the interferometer optics.

To give a fair size comparison of the Delft interferometer with respect to the benchmark interferometer, a number of design parameters (such as those assumed in

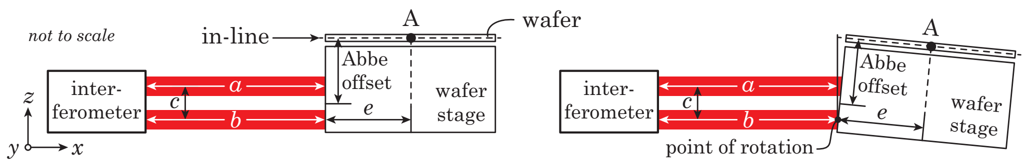

Figure 9.2: 2D example showing how a measurement error in a and b in the x direction lead to increased measurement errors in the x and z direction for point A, due to the Abbe offset. If a includes an error of +0.1 nm and b includes an error of -0.1 nm, then the Abbe error for A in the x direction amounts ~0.3 nm and in the z direction ~3 nm; for c = 15 mm, e = 225 mm, and Abbe offset = 15 mm. When e.g. increasing c and keeping the 'point of rotation' at the same location, these Abbe errors can be reduced.

Fig.9.2) must be known; amongst which are the eventual measurement accuracy of both the Delft and benchmark interferometer, together with information about the dimensions of the benchmark interferometer and its target mirror configuration. Because this information was not available a more realistic estimation than what's already described could not be made.

The size of the Delft monoliths, depicted in Fig.9.1, are determined upon the allowed amount of beam walkoff; which leads to a minimum interferometer size. Depending on the configuration of the measurement axes it could be required that the separation between measurement axes needs to increase. However, the Delft interferometer has an improved measurement uncertainty compared to the benchmark interferometer, which decreases the effect of the Abbe offset via angular measurement (when c is kept constant). The improved measurement uncertainty of the Delft interferometer concept could thus potentially result in a size decrease of the interferometer optics.

Another aspect concerns manufacturing imperfections of e.g. anti reflection coatings, which take place near the edges of the optical surfaces. Because of these imperfections the optical beams may not approach edges too closely, which causes a size increase of several mm of the optical monolith. Detailed information about these level of imperfections and further implications was unavailable.

Concluding, the size of the Delft interferometer optics shown in Fig.9.1, and the optical beam layout, both approach reality. However, a size increase, and a reconfiguration of the beam layout are still at hand. Due to the unavailability of the many design variables it was not possible to determine the eventual size for a 5-DoF Delft interferometer; it can be slightly larger than depicted in Fig.9.1a and b, but it could also be smaller than a benchmark interferometer due to the improvements in measurement accuracy.

9.1.2 Free-space beam generation and optical pickup

Each Delft interferometer requires two fiber-to-free-space out-couplings, which expand and collimate the fiber output. Expansion and collimation can be achieved with lenses (Fig.9.3a) or using a parabolic mirror, Fig.9.3b. The need for this free-space beam generation at the interferometer slightly increases the interferometer's space consumption compared to the benchmark system. Nevertheless, depending on the size and volume available in the host-system, one can position the free-space beam generation in several configurations. Two important characteristics of these beam expanders are mechanical stability (related to optical alignment) and wavefront quality. The influence of the collimators on polarization state is less of importance, see Section 4.7. Whether these collimators can be off-the-shelf or that they need to be designed and which of the collimators is most suitable needs to be determined during a research-followup.

The optical pickup of the interferometer signals can also be configured in multiple ways, similar to the fiber-to-free-space beam generation, see Fig.9.3d. However, these collimators do not require to be manufactured at the same strict tolerances. The fiber optic pickup contains a linear polarizer behind (only) one lens that couples the free-space light into a multi-mode optical fiber, which can be the same as those used in the benchmark interferometer system.

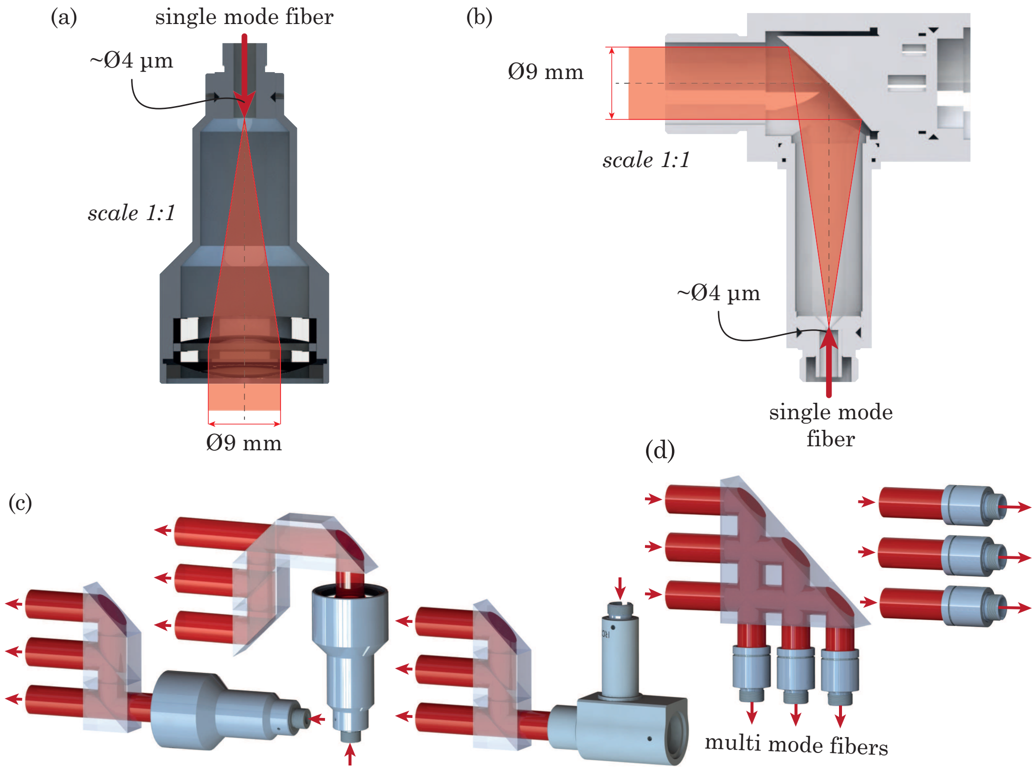

Figure 9.3: Fiber-to-free-space beam expansion and collimation using an (a) air spaced doubled collimator *(Thorlabs, F810-FC-635)*, and a (b) parabolic mirror collimator *(Thorlabs, RC08FC-P01)*. (c) The fiber-to-free-space collimators can be positioned in different configurations. (d) Two optical configurations of optical pickup at the interferometer, using off-the-shelf components from the benchmark system.

9.2 Implementation upon commercial introduction

Commercial introduction of the Delft interferometer system in its total setting, as shown in Fig.6.1, including the alternative heterodyne source, will be a challenge since the alternative heterodyne source has not yet commercially proven itself. In contrast, the risks of an intermediate (hybrid) system that consists of both the benchmark system and Delft system are expected to be small enough to justify the change of the measurement system that is currently applied.

9.2.1 Gradual introduction

The system architecture of the Delft interferometer concept allows for a gradual stepwise introduction into industry, which can be realized by the following steps:

1. *Benchmark heterodyne source and free-space beam delivered Delft interferometers.* For this option, at the location of the ROC, the fiber outputs only require to be expanded and collimated (instead of putting these outputs also coaxial as currently done by the ROC). The source frequencies are then transported by two separated free-space beams via mirrors and beam splitters attached to the metrology frame, similar as currently done.

2. *Benchmark heterodyne source and fiber coupled Delft interferometers.*
After industrial validation of the system proposed at *step 1*, the next step is to employ fiber-coupled delivery to the Delft interferometers, still using the benchmark system's heterodyne source.

3. *An alternative heterodyne source and fiber coupled Delft interferometers.*
There are many types of alternative heterodyne frequency sources possible, such as the frequency stabilized 2-mode HeNe source from this research, a frequency stabilized 3-mode HeNe laser [56], or a solid state laser source. The main improvements of a new heterodyne source should focus on an optical design that inherently provides non-mixed source frequencies, accompanied by an increase of optical output power (to reduce measurement error due to detector nonlinearity upon detection of low levels of irradiance).

During this research the benchmark system's phase measurement equipment has demonstrated successful operation (this included the free-space-to-fiber collimators, Ø1 mm multi-mode optical fibers, and the *Agilent Technologies* N1225A 4 channel phase measurement board). When implementing the Delft interferometers into an existing industrial application only the number of measurement channels needs to be increased from 31 channels to 36.

9.2.2 Validation of a hybrid interferometer system

As mentioned in the previous subsection, the Delft interferometers can be provided with source light that originates from the benchmark system's heterodyne frequency source. Measurement operation of this combination has been experimentally validated using the setup shown in Fig.9.4a.

The benchmark system's heterodyne source is initially more preferred than the alternative source from this research upon industrial introduction, which is mainly due to its commercial maturity (i.e. its proven frequency and irradiance stability). Although the alternative heterodyne source from Section 4.5 ensures non-mixed source frequencies and higher optical power, the benchmark system's heterodyne source is still very well usable in combination with the Delft interferometer.

Test results obtained with the depicted experimental setup (Fig.9.4b) show first and second fringe-order PNL that are caused by frequency-mixing at the heterodyne source. It must be noted that this heterodyne source was aged and was possibly (internally) optically less well aligned (due to e.g. transport) than an equal source that would have been applied in a commercial lithography machine. It is therefore expected that a well aligned benchmark source can result in picometer level PNL similar as achieved when the Delft interferometer was supplied by the alternative heterodyne source (see Section 4.7).

Although digital PNL compensation is unwanted due to e.g. a required calibrations stroke (see *Chapter 4*) it does significantly reduce the amount of PNL, compare Fig.9.4b and c (these results are only for indicative purposes to indicate the capability of current digital PNL reduction).

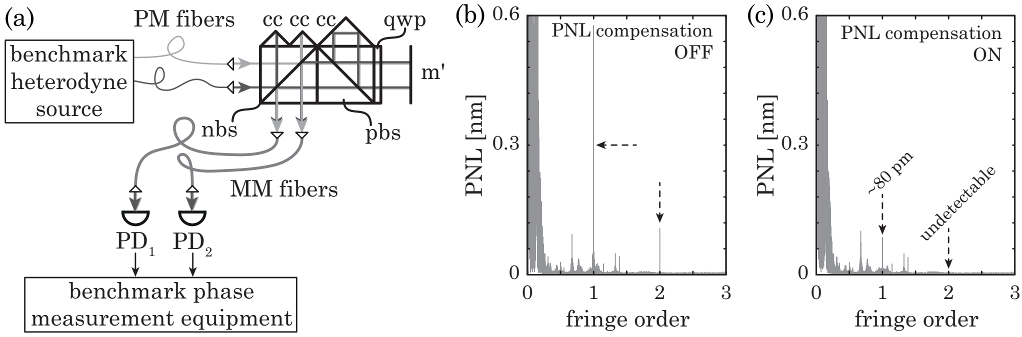

Figure 9.4: (a) Experimental setup for validating Delft interferometer operation using the fiber coupled laser and phase measurement equipment from the benchmark system. (b) Results from a moving stage show PNL at the first and second fringe-order, caused by source frequency mixing at the benchmark system's heterodyne source. (c) Reduction of PNL by means of digital compensation.

9.3 Conclusions Delft interferometer system implementation

The monolithic interferometers of the Delft system are of the same order of size as the benchmark system. Nevertheless, the fiber to free-space beam generation potentially results in a slightly larger space consumption compared to a benchmark interferometer. The fiber-to-free-space, and free-space-to-fiber collimators know several configurations that can be adapted, depending on the size and shape of the available installation volume within the lithography machine.

The system architecture of the Delft interferometer concept allows for a gradual and stepwise introduction into industry. The first step is to deliver the two source frequencies by means of separate free-space optical beams that are guided via mirrors and beam splitters to the individual Delft interferometers, similar to the benchmark system.
After validation of that system the free-space delivery can be replaced by optical fibers. A final step would be to enhance the heterodyne frequency source by aiming for an optical design that inherently provides non-mixed source frequencies, accompanied by an increase of optical output power (to reduce measurement error due to detector nonlinearity upon detection of low irradiance levels).

Experimental validation showed that a Delft interferometer is able to operate fully fiber coupled using the benchmark system's heterodyne source. The results indicated the presence of first and second fringe-order PNL, which are, however, expected to be resolved when using a benchmark heterodyne source that is less aged and internally better aligned.

Part V

Closing

The last part, covering *Chapter 10*, summarizes the most important results and implications of the described research, together with recommendations covering potential improvements or aspects that could be further investigated.

Chapter 10

Conclusions and recommendations

10.1 Conclusions

This thesis has presented a "*compact heterodyne displacement interferometer for a measurement range of 450 mm that achieves sub-nm measurement uncertainty, while allowing for a modular system buildup that has a flexible optical layout and is robust enough for fast module replacement to reduce downtime*", the 'Delft interferometer system'. The improvements that led to this new heterodyne interferometer system focused on enhancement of measurement linearity and system modularity.

This aim was split into several aspects that were theoretically analyzed and followed up by experimental validation when deemed fundamental to the interferometer concept. The outcomes were compared to the performance of a heterodyne interferometer system from *Agilent Technologies*, which used free-space coaxial beams for source frequency delivery and optical fiber pickup for signal detection. This system was set to operate within an EUV-lithography machine and acted as a benchmark system throughout this research.

The initial starting point of the research was comprised of a heterodyne interferometer design from the research done by Dr. Ki-Nam Joo and Dr. Jonathan Ellis [3, 4]. This displacement interferometer primarily achieved improved measurement linearity by removing one source of periodic nonlinearity (PNL) from the interferometer system through eliminating the need for the polarization based frequency separation; as used in traditional heterodyne interferometer systems. The interferometer design from that research was updated during this research and has resulted in a number of new compact optical layouts that are to a high degree comparable to the benchmark interferometer. This interferometer design focused on the displacement measurement of a plane mirror target since the benchmark system also concerned a plane mirror system.
Furthermore, a theoretical design of a monolithic five-DoF interferometer has been presented, having a similar compactness and manufacturability as the benchmark system's monolithic interferometers. Theoretically this design is able to account for deadpath error, without addition of extra measurement detectors.

The heterodyne source used for Dr. Joo's research [4] was (due to practical reasons) replaced by a frequency stabilized two-mode HeNe laser *(Thorlabs HRS015)*. This source proved more reliable due to the absence of mode-hopping and irradiance drift. It was validated that this heterodyne source provided in combination with two acousto-optic modulators *(ISOMET, AOM 1141-T40-2, with drivers 531C-L, operating at 39 and 41 MHz)*, two separated and non-mixed frequencies. This source's non-mixed frequencies were essential for this research since measurement nonlinearity due to frequency mixing of the interferometer itself was under investigation.

During the previous research [4] a piëzo-electric stage was used for target motion, consisting of a *Thorlabs MAX311* stage with a 20 μm stroke. For this research a new stage was implemented, comprising of a linear stage *Aerotech ABL10100LT*, which had air-bearing support and a stroke of 100 mm. For this research target mirrors were mounted on top of the stage, which was programmed to displace at constant velocity. Each measurement was started after the stage reached constant velocity and was stopped before the end of the displacement, thereby excluding starting and stopping effects from the measurements. Stage motion was analyzed for nonlinear displacement behavior and stage vibrations, by means of a capacitive probe, which has a low noise level and is inherently free of PNL *(probe 2805MSE A9089 and electronic readout using MicroSence, LLC, model 4810)*. For the measurements where PNL was investigated it was confirmed that the stage did not show PNL or stage vibrations at the fringe-order locations [5].

The first experiment analyzed the Delft interferometer's robustness for input polarization of the source frequencies with respect to the presence of PNL. For comparison both the Delft interferometer and the benchmark interferometer were subjected to equal polarization manipulation of the free-space delivered source frequencies. The polarization orientation of the linearly polarized source frequencies were manipulated using half-wave plates (hwps), while quarter wave plates (qwps) were used to alter their polarization state.
Results showed for the benchmark interferometer up to eight PNL-orders of which the first fringe-order exceeded 10 nm when exposed to approximately ±15° hwp rotation or ±20° qwp rotation; at these limits the nonlinearity became too large for the electronics to continue measuring. Under normal circumstances the benchmark interferometer was able to digitally compensate for PNL and typically ensured PNL well below one nm, however, this required periodic calibration, a minimum displacement per time frame, and additional calculation time compared to uncompensated systems.
In contrast, the Delft interferometer concept continued operation regardless of any polarization manipulation without digital compensation, while the measurements only showed a first fringe-order error with an average of less than four pm. This confirmed that the Delft interferometer is insensitive for input polarization, while the traditional coaxial interferometer showed high sensitivity and even seized operation [5]. Moreover, the results also imply that the new interferometer concept is more real-time, and that it also can be used for quasi-static measurement targets. This is the first indication of the new interferometer's robustness and its opportunity to comprise a modular system.

Delivering the source frequencies with separated optical beams resulted in relative phase differences between the frequencies when the beams are unequally disturbed during delivery, which potentially affects measurement performance. This presents

itself not with coaxial beams, since these beams share the same optical pathway and are therefore equally disturbed (dispersion not taken into account). Theoretical analysis showed that such phase differences can be accounted for by creating a reference signal at the interferometer itself, instead of externally as done in the benchmark system (i.e. at the ROC).
This concept was experimentally validated using an electro-optical phase modulator that introduced a phase disturbance of ~170 nm at 5 kHz in one of the two source frequencies. Results indicated that this disturbance was reduced by a factor of ~6000, which was limited by secondary effects that were caused by the experimental setup itself; under normal operating conditions this factor is therefore expected to be exceeded [6]. This outcome is a second indication of the ability of the new interferometer system to withstand external influences.

Having a reference at the interferometer itself required one extra detector per five-DoF interferometer. It, however, enabled the use of optical fiber delivered source frequencies as measurements with a single DoF demonstrator have indicated. With optical fibers a flexible and modular system layout can be achieved, since the layout flexibility and modularity of an interferometer system are determined by the optical interconnections between the several subsystems. Most importantly, optical fibers can be bent and relocated as long as the location of the fiber ends is determined.
A fiber coupled Delft interferometer has been realized to validate that a fully fiber coupled heterodyne interferometer system is feasible. The setup used single-mode polarization-maintaining optical fibers for source frequency delivery and demonstrated an operational system without PNL [9]. This proves that the interferometer concept is robust enough for sub-nm displacement measurement, that its separated source frequencies can be transported with optical fibers and that a modular system buildup is feasible.

Theoretical analysis illustrated that irradiance imbalances between the reference and measurement detector always exists. Therefore, irradiance fluctuations are a cause of measurement error in both the benchmark and the Delft interferometer. The analysis also indicated that the level of irradiance imbalance in the benchmark system is larger than in the Delft system. This is mainly caused by the use of an external reference in combination with free-space beams that are handled with mirrors and beam splitters, whereas the Delft system has fewer sources of imbalance thanks to referencing at the interferometer.
The influence of irradiance fluctuations on the Delft interferometer's measurement performance was tested by means of irradiance modulation of one source frequency using an amplitude modulated acousto-optic modulator. During the experiment the irradiance was modulated up to ±2.5μW around ~7.5μW (AC-signal at detector), which resulted in a linear measurement error of less than 50 pm, while using a non-monolithic interferometer (i.e. signal timing between the reference and measurement detectors also presents a source of irradiance imbalance) [6].
It can be concluded that irradiance fluctuations have little influence on the measurement performance of the Delft interferometer, which is again an indicator of its robustness for external influences.

Inhomogeneous heating of a monolithic interferometer is an aspect where the Delft interferometer shows enlarged sensitivity compared to a benchmark interferometer; this outcome originates from a theoretical analysis where the five-DoF monolithic interferometer designs of both systems were compared. It also indicated that homogeneous heating equally affects both the Delft and the benchmark interferometers equally. Inhomogeneous heating in combination with the thermal sensitivity of the cube corner reflectors and the individuality of the optical pathways inside the interferometer, affects the relative phase between reference and measurement frequency, which results in measurement error. The eventual size of this error depends on the corner cube(s) affected, the temperature difference, the time over which the temperature variation takes place, and between which measurement channels the differential measurement is performed. A realistic error-estimation required more knowledge of an EUV lithography machine than was available during the research. With respect to drawing false conclusions it was not possible to give an estimation.

At final, the influence of wavefront deformations in combination with beam walkoff was analyzed. Ideally a flat interference wavefront is obtained upon detection, causing only the fringe contrast to change upon beam walkoff. A new wavefront measurement method designed during this research showed that the interference wavefront can already be deformed several nanometers at the exit of a coaxial laser source; up to ±20nm for an *Agilent Technologies 5517D* HeNe laser, and ±50nm for a *Zygo Axiom 2/20* HeNe laser [10]. From experiments it was shown that the source beams delivered with single-mode fibers resulted in wavefronts that were deformed relatively smooth and contained deformations of less than 2 nm.
Further analysis illustrated that the identical wavefronts of coaxial beams result in a flat wavefront if, and only if, there is no beam walkoff, and having the wavefronts arriving at the detector with the same shape as they had before they were split; both requirements are not realistic. The interferometer and target optics, and the measurement environment inherently alter the shapes of the wavefronts via surface reflections or refractive index variations; both are in the order of several tens of nanometers. Also beam walkoff is inherently present, either due to misalignment or due to need for target rotation during wafer exposure.
It is therefore expected that the increased optical wavefront quality of single-mode fiber delivery, in contrast to free-space coaxial beams, leads to less deformed interference wavefronts upon detection, and therefore result in better measurement performance. Also for this case a realistic performance improvement is not given, due to the many variables involved and the required complexity of the model. However, the main goal of this analysis was to falsify the argument that using two separately delivered source frequencies leads to a decrease in measurement performance.
This outcome emphasizes that optical fiber delivery not only enhances modularity, it also potentially improves measurement linearity upon beam walkoff; indicating once more improved measurement performance over the benchmark system.

To conclude, this research has modeled and validated an improved heterodyne displacement interferometer system. The presented plane mirror Delft interferometer ensures sub-nm measurement uncertainty for a measurement range of 450 mm, while using off the shelf components. With the use of optical fibers a flexible optical layout is achieved with fully fiber coupled interferometers. The fibers help reducing installation related errors and ease the integration into complex host-systems such as lithography machines. In addition, the plug-and-play nature of optical fibers leads to a modular system buildup that potentially allows for fast component replacement.

10.2 Recommendations

The recommendations below are listed based on priority regarding aspects that require attention upon commercial implementation.

Experiments with a prototype monolithic Delft interferometer are expected to show improved measurement performance with respect to e.g. thermal stability and optical symmetry. It is therefore recommended that the experiments described in this work are extended with a monolithic interferometer made from optics of comparable quality as used for a benchmark interferometer, preferably using the 5-DoF interferometer configuration from *Chapters 4* and *9*, with the main aim to validate the expected improvements.

The thermal sensitivity of a Delft interferometer is theoretically higher than that of a benchmark interferometer. Since thermal expansion potentially presents the largest measurement error for the Delft interferometer concept it is recommended to study the use of a passive thermal shield made from thermally conductive material that encloses the (monolithic) interferometer. It is expected that such a shield absorbs thermal energy and release it over time (i.e. reducing thermal impact and increasing the thermal time constant) over an enlarged surface of the interferometer optics.

Optical fiber connectors aid fiber alignment by reducing manual alignment upon installation. During the research much effort was spent analyzing and validating the operational interferometer concept, less time was spend on studying what the most favorable connectors would be. A closer analysis into fiber connectors would be beneficial for the system's ability to be handled plug-and-play, and it will help increasing the measurement linearity due to ensuring stable optical coupling efficiencies. Additionally, a critical fiber connection that requires attention is the fiber-to-free-space out-coupling at the interferometer. This connection should have high mechanical stability.

Appendices

Appendix A

Additional research: Heterodyne frequency generation

For heterodyne displacement interferometry there are in general only two commercial methods used for generating two offset frequencies with sufficient frequency stability. These are, however, rather limited when it comes to bandwidth or controllability of the modulation. In this chapter an alternative optical frequency modulation method is presented that is based on a rotating wave plate, which has the potential to replace the current used methods.

The first section, Section A.1 briefly introduces a few methods that can modulate optical frequencies, amongst which is the use of rotating wave plates. The next section, Section A.2, addresses the use of electro-optic materials for achieving an electrically controllable wave plate, followed by Section A.3 where the mathematical operation behind rotating wave plates and frequency modulation is explained.
In Section A.4 the operation of a realized electro-optic wave plate is demonstrate and validated. Section A.5 *discusses the employment of the electro-optic wave plate in both the heterodyne source of the benchmark system and in the alternative heterodyne source.*
Section A.6 shows by experiment that the electro-optic wave plate can also be used for generating frequency combs.

The final section, Section A.7, concludes that this additional research has resulted in a new means of frequency modulation that can replace the AOMs in both the benchmark and alternative heterodyne frequency source. The modulator has no moving parts, it can be controlled electrically, it can be fiber coupled, and it achieves a larger bandwidth than provided by AOMs or Zeeman-split lasers.

** This 'additional research' started with a search for a means of heterodyne frequency generation other than using a Zeeman-split laser source or acousto-optic modulators. This search resulted in the finding that optical wave plates can be used for frequency modulation. This spinoff research has been continued based upon promising initial findings and out of research interest.*

A.1 Methods of heterodyne frequency generation

A frequency modulator for heterodyne displacement interferometry requires amongst others, a single sideband suppressed carrier (SSB-SC) modulation to ensure spectral purity of the output. The term 'single sideband' refers to having a single frequency in the output while the original carrier frequency is fully suppressed, which is required to prevent PNL. Furthermore, a with a bandwidth of several MHz is ought to be achieved (driven by the maximum target velocity, see Section 3.3), together with an operating frequency stability of less then than one Hz.

The current most applied methods that are able to produce SSB-SC frequency modulation at a fixed frequency (with high stability of <10 Hz) concern either acousto-optic modulators (AOMs), or Zeeman-split laser sources (addressed in Section 4.5).

Acousto-optic modulators have the disadvantage of a small bandwidth and decreased optical efficiency due to a distribution of optical power over the several output modes (i.e. frequencies), instead of all optical power confined in the used mode (generally the ±1st order mode). The utilization of the Zeeman effect also has drawbacks, mainly the decrease of optical power when the Zeeman frequency-split is increased.

There are also other methods that are capable of optical frequency modulation, such as mechanically rotated phase gratings [57, 58]. Due to its mechanical nature this method tends to wear (e.g. losing alignment), and it suffers from vibrations and inertia (limiting the controllability), and is therefore not preferred in high precision systems. Furthermore, also optical fibers exposed to acoustic waves [59, 60] can be employed, which generally suffer from low acousto-optic coupling and a limited bandwidth.

The angular Doppler effect

Another type of optical frequency modulation is based upon the interaction between optical wave plates and photons, an interaction that takes place via the 'spin' momentum of a photon, which describes the photon's polarization state [61–63]. The interaction between circularly polarized light and rotating wave plates became known as the *rotational* or *angular* Doppler effect [64], where an increase in rotational momentum can be treated similarly as a change in linear momentum with the *linear* Doppler effect. In other words, when circularly polarized light propagates through a wave plate that is rotating about its optical axis, one observes a frequency increase or decrease (depending on the direction of rotation) of the light exiting the wave plate.

Jones Calculus [65–71] and experiments [72] show that the rotational Doppler effect is optimal when using a wave plate that applies (a relative) half wavelength phase retardation[1] between electric field components E_x and E_y.

The physical interaction between a rotating hwp plate in conjunction with a specifically polarized wave has been known for a while [65–71] but has not been used extensively. Several publications discuss mechanical wave plate rotation and all tend to maximize the frequency manipulation range (i.e. bandwidth). Some propose extending the range by increasing the rotational velocity of the wave plate up to several hundred kHz [69], while others propose (i.e. more feasible) multiple rotating

[1]A half wave wave plate generates for a specific wavelength a relative phase retardation of 180° between its ordinary and extraordinary axis (i.e. birefringence), it's also called a 'λ/2 plate'

hwps in series [70], or multi-pass solutions [71]. Any of these solutions suffer from the typical mechanically related error sources (e.g. vibration and wear), which limit the frequency stability, controllability, and bandwidth.

Bandwidth is an important parameter for heterodyne displacement interferometry, since the maximum target velocity is limited by the split frequency of the source frequencies (see Section 3.3), which already requires to be several hundred kHz for slow moving targets[2]. Obtaining such a frequency shift through mechanical rotation of a hwp would be unpractical or even impossible when taking into account the stringent conditions for displacement interferometry as mentioned in this work (e.g. mechanical vibrations, optical wavefront quality (see Section *7.2*), and frequency stability of both the base frequency (i.e. determined by the geometrical stability of the laser cavity) and the split frequency (i.e. Zeeman-split or AOM related).

Therefore, practical implementation of frequency manipulation at high frequencies requires circumvention of mechanical rotation, which can be achieved by creating a wave plate from electro-optic material.

A.2 Electro-optic wave plate

Electro-optic materials show under the influence of e.g. an electric field a change of the material's optical properties, in most cases this concerns birefringent materials [73]. With such materials an electro-optic wave plate can be achieved, whose phase retardation can be controlled electrically, which is found in electro-optic modulators such as e.g. a Pockels cell (Fig.A.1).

The next step is to create a rotating wave plate, which requires to rotate the birefringent index of the crystal. Electro-optic material that is part of the 3m crystal class is especially suitable for this purpose, since it exhibits a three-fold rotation symmetry about its 'c-axis' [74, 75]. When using the c-axis of the crystal as the optical axis, applying an electric field along either the x or y-axis results in an identical amount of birefringence, see Fig.A.2a.

By means of applying an alternating electric potential over both the crystal's axes (Fig.A.2b) the birefringent index can be rotated. This results in a wave plate whose phase retardation and rotational rate are controlled electrically. Such wave plates are proposed in a number of publications [65, 66, 72, 76], which are primarily relate to frequency modulation for telecommunication purposes.

[2]A heterodyne interferometer with a fold factor of 4, combined with a target moving at 0.5 m/s, already generates a beat-frequency of >3 MHz (at λ = 633 nm).

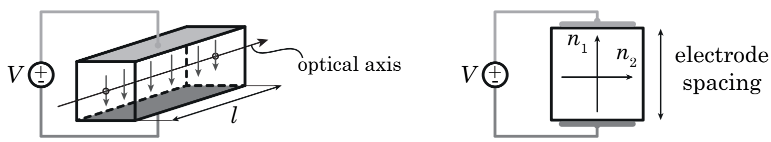

Figure A.1: A transverse Pockels Cell as used in commercial electro-optic modulators (i.e. EOM). An electric potential between two electrodes creates an electric field that induces birefringence (i.e. at V = 0 Volt $\rightarrow n_1 = n_2$, at $V \neq 0$ Volt $\rightarrow n_1 \neq n_2$). The phase retardation between depends on the material's electro-optic coefficient, crystal length l, electrode spacing a, and the applied electric potential V.

Besides having symmetry about the opto-mechanical axis, the electro-optic material preferably also has a high electro-optic constant (i.e. electric potential versus the amount of birefringence). Lithium niobate ($LiNbO_3$) is a material that has these properties and is readily commercially available [74, 75].

The most advanced attempt to create an optical frequency modulator using an electro-optic rotating half wave plate is described by [72]. This research concluded that the modulator could not keep up with the fast frequency manipulation required for high data-rates in the telecommunication industry (i.e. fast switching between operating frequencies introduced higher order spectral content due to e.g. crystal resonance). However, such fast switching between operating frequencies is not required for heterodyne displacement interferometry. On the contrary, for displacement interferometry the operating frequency is preferably fixed without variation.

Moreover, several researches used bar shaped lithium niobate crystals [65, 66, 72] and have indicated that better SSB-SC ratios can be obtained by utilizing rod-shaped crystals instead of the traditional bar-shape. Due to the shortcomings of fabrication methods (1960 ~ 1970) to produce small (i.e. a diameter of a mm) rod-shaped crystals, no crystal geometries other than bar-shapes have been investigated thus far. Fortunately, current fabrication methods allow for small (i.e. minimized electrode spacing for achieving for large E-field at low Voltage) high tolerance rod-shaped crystals.

This additional research used the work from [72] as a starting point. With the use of multi-physics finite element analysis (i.e. *COMSOL*) the electro-optic crystal geometry and the amount of electrodes was investigated. The use of two electrode pairs as shown in Fig.A.2 resulted in the best birefringent index homogeneity, which was made visible via the relation of birefringence with internal stress. The outcome of the finite element analysis was used for custom manufacture of three crystals of Ø1x20 mm (i.e. rod-shaped) and three crystals of 1x1x20 mm (i.e. bar-shaped).

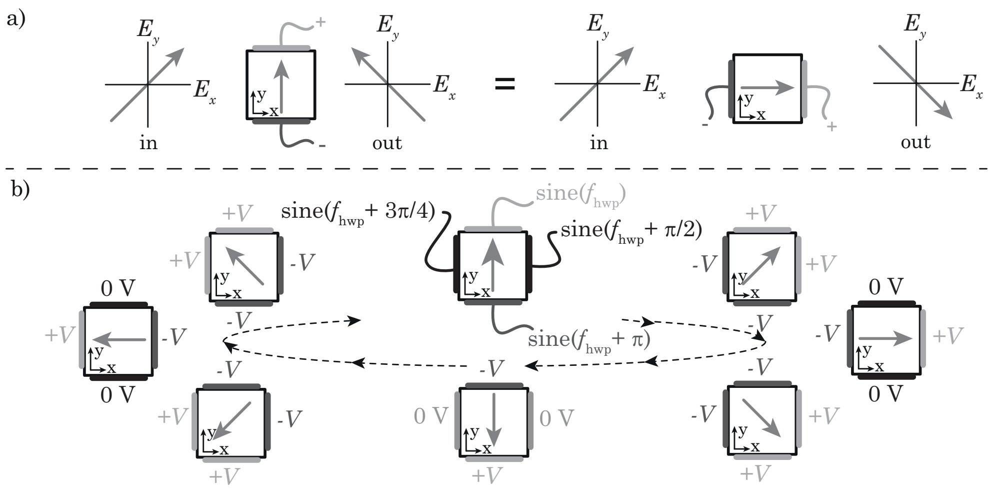

Figure A.2: cross sectional view of electrode placement on a bar-shaped electro-optic crystal. (a) Due to the rotational symmetry of the crystal structure it does not matter how the electric field is applied, both lead to equal birefringence at equal electric potential. (b) Applying electric fields using four electrodes in a sinusoidal fashion, results in rotation of the birefringent index, at frequency f_{hwp}.

A.3 Mathematical rationale using Jones Calculus

A brief mathematical analysis using Jones Calculus explains the idea behind the optical frequency manipulation of a polarized wave propagating through a rotating half wave plate. Assume a right handed circularly polarized (rcp) wave at the input:

$$J_{\mathrm{rcp}} = \frac{1}{\sqrt{2}} \begin{bmatrix} 1 \\ i \end{bmatrix} e^{i\omega_0 t}, \tag{A.1}$$

with $\omega_0 = 2\pi f_0 t$, where $f_0 = c / \lambda_0$. This circularly polarized wave propagates through a rotating halve wave plate (hwp). Here a stationary hwp is represented by J_{hwp}, whereas J_{R} represents a rotation matrix,

$$J_{\mathrm{hwp}} = \begin{bmatrix} 1 & 0 \\ 0 & -1 \end{bmatrix}, \tag{A.2}$$

$$J_{\mathrm{R}} = \begin{bmatrix} \cos\omega_{\mathrm{hwp}} & \sin\omega_{\mathrm{hwp}} \\ -\sin\omega_{\mathrm{hwp}} & \cos\omega_{\mathrm{hwp}} \end{bmatrix}, \tag{A.3}$$

where ω_{hwp} describes continuous hwp rotation as in $\omega_{\mathrm{hwp}} = 2\pi f_{\mathrm{hwp}} t$, having f_{hwp} as the hwp's rotational frequency. In this case, ω_{hwp} is positive and corresponds to a clockwise rotating wave plate, as in:

$$J_{\text{rotating hwp}} = J_{\mathrm{hwp}} \cdot J_{\mathrm{R}}, \tag{A.4}$$

$$J_{\text{rotating hwp}} = i \begin{bmatrix} \cos(2 \cdot \omega_{\mathrm{hwp}}) & \sin(2 \cdot \omega_{\mathrm{hwp}}) \\ \sin(2 \cdot \omega_{\mathrm{hwp}}) & -\cos(2 \cdot \omega_{\mathrm{hwp}}) \end{bmatrix}. \tag{A.5}$$

Upon propagation of the rcp-wave through the rotating hwp, one obtains:

$$J_{\text{rotating hwp}} = (J_{\mathrm{hwp}} \cdot J_{\mathrm{R}}) \cdot J_{\mathrm{rcp}}, \tag{A.6}$$

$$J_{\text{rotating hwp}} = \frac{1}{\sqrt{2}} \begin{bmatrix} 1 \\ -i \end{bmatrix} e^{i(\omega_0 + 2\cdot\omega_{\mathrm{hwp}})t}. \tag{A.7}$$

Equation A.7 shows that the wave that exits the hwp has become a left handed circularly polarized (lcp, i.e. polarization reversal), and it obtained a frequency increase that equals two times the rotational frequency of the hwp. The eventual sign of the frequency shift results from the combination between the polarization state of the input wave (i.e. rcp or lcp), and the direction of hwp rotation (clockwise or counter-clockwise).

In the shown example a single circular input polarization was used, when a linear polarization would have been used, one would observe both right and left circular polarization states in the output, since linear polarization is a superposition of the two circular states. Therefore, using a single linear input polarization results in a right circularly polarized wave that is up-shifted by $2{\cdot}f_{\mathrm{hwp}}$, together with a left circularly polarized wave that is down-shifted by $2{\cdot}f_{\mathrm{hwp}}$(i.e. showing a relative frequency offset of $4{\cdot}f_{\mathrm{hwp}}$). This also indicates that the limited alignment and polarization quality obtained in reality always result to a certain level of frequency mixing.

A.4 Validating electro-optic frequency modulation

The experimental setup used for validating electro-optic frequency modulation by means of an electro-optic rotating half-wave plate is illustrated in Fig.A.3. The used frequency generator *(Variable phase function generator Model 203A, Hewlett Packard)* provided two coupled outputs that could be offset in phase, from 0 to 2π. For the experiment a phase offset of 90° between the two electrode pairs was used (i.e. $e_{1,3}$ and $e_{2,4}$, see insert bottom right Fig.A.3).

The two outputs from the frequency generator were supplied to a pre-amplifier *(non-commercial equipment, built for this research)*, which provided manual adjustment of the gain and DC-offset of each individual channel, and it allowed for inversion of the input signal, e.g. creating a negative sine (i.e. 'sine + π') from a 'sine'. The pre-amplifier's four output signals were delivered to a four channel high-voltage amplifier *(non-commercial equipment)*, whose outputs were connected to the four electrodes at the crystal (see insert Fig.A.3, and Fig.A.4).

Previous research, [72] amongst others, reported residual stress induced birefringence due to the method of crystal fixation. This was due to curing the electro-optic crystal to a rigid base electrode that also provided support and a means of cooling for the crystal. Curing the crystal to a metal (i.e. stiffer) base electrode at elevated temperature resulted in internal stress at room temperature, leading to unwanted stress induced birefringence (i.e. which negatively affects the SSB-SC ratio). Additionally, internal stress could also originate from the production process. Adjustment of the DC-level of each electric channel could compensate for this and was, therefore, built into the pre-amplifier. Moreover, although the operation of the crystal is analogous to the rotation of a half wave plate, the magnitude of the frequency shift exerted by the crystal is equal to the rotation of the electric field (rather than twice) [72].

Examination of internal stress related birefringence was examined by means of a circular polariscope. It was shown that none of the tested crystals showed significant internal stress. The polariscope also proved a helpful tool to visualize the electric-field induced birefringence once operating the crystal.

A solution that provided support but prevented internal stress was found in suspending the crystal in between four tensioned electrodes, see Fig.A.4.

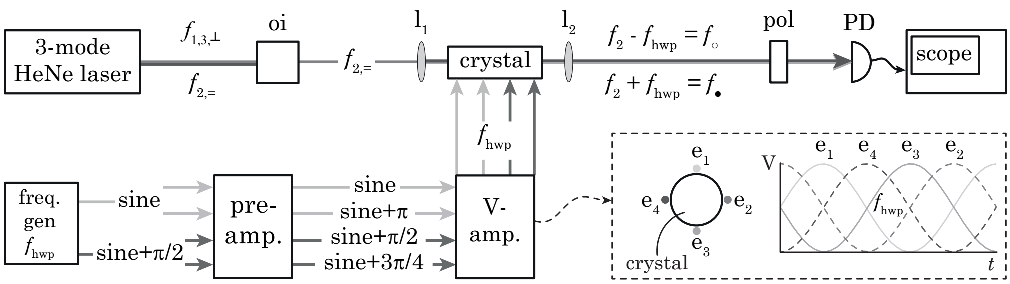

Figure A.3: Experimental setup for demonstrating electro-optic frequency modulation. Linearly polarized input light from a non-stabilized 3-mode HeNe laser resulted in a coaxial beam containing two counter rotating circularly polarized waves. Legend: f_x, optical frequency; l_x, lens; oi, optical isolator; pol, polarizer; PD, photodetector; scope, oscilloscope; freq. gen, frequency generator; pre-amp., pre-amplifier; V-amp., Voltage-amplifier; ●, left handed circular polarization; ○, right handed circular polarization; ⊥, vertical linear polarization; and =, horizontal linear polarization.

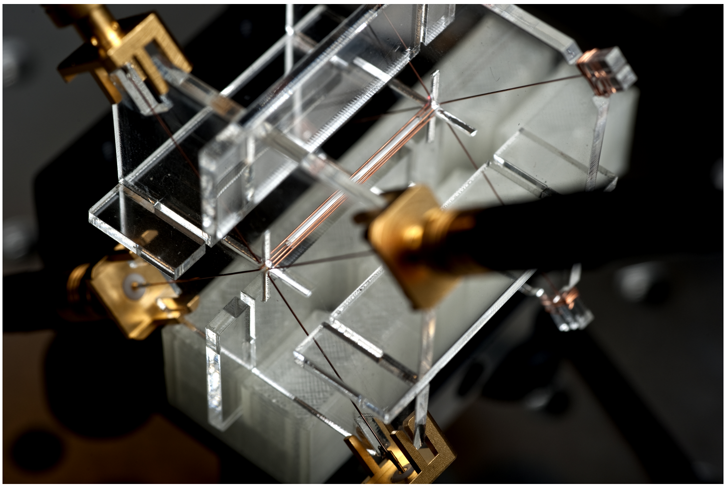

Figure A.4: Photograph of the realized electro-optic frequency modulator, showing a lithium niobate rod of Ø1 x 20 mm, supported by four tensioned electrodes.

In Fig.A.5 three measured beat-frequencies are shown that were obtained with the setup from Fig.A.3. The plotted beat-frequencies consisted of the interference between a left circularly polarized beam that was frequency down-shifted and a right circularly polarized beam that was frequency up-shifted. By means of manual adjustment of the frequency generator the device achieved frequency modulation between 0 Hz and several tens of kHz (with an upper limit of 60 kHz, limited by the bandwidth of the frequency generator).

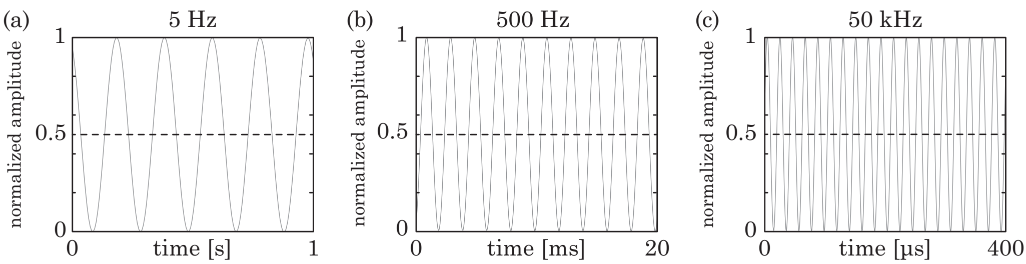

Figure A.5: Data logged with an oscilloscope visualized in the time domain, showing three beat-frequencies generated with the setup shown in Fig.A.3.

A.5 Implementing the electro-optic wave plate

The method of frequency shifting as discussed in the previous section can be implemented in several ways, either in combination with the Zeeman laser from the benchmark system, or in combination with the 2-mode laser as used in the alternative heterodyne frequency source from Section 4.5, or any other optical source radiating that wavelengths between 350 and 5200 nm

A.5.1 Zeeman-split HeNe laser source

The benchmark's heterodyne frequency source generates two source frequencies using a Zeeman-split HeNe laser source supported by two acousto-optic modulators. The reason that this laser source is assisted by two acousto-optic modulators (Fig.A.6a) is related to the decrease of optical power upon an increase of the Zeeman split-frequency. The AOMs are used to enlarge the split-frequency from the Zeeman effect such that the frequency offset is large enough to allow for target speed up to a few m/s (see Section 3.3), while the Zeeman split is kept minimal to provide sufficient optical power for 30 measurement axes.

Implementation of the electro-optic wave plate replaces the two AOMs, shown in Fig.A.6b. Here, the wave plate amplifies the Zeeman split-frequency offset, using the two counter rotating circular polarizations that originate from the Zeeman effect (as shown with the Jones Calculus analysis). Upon proper electro-optic wave plate operation and alignment, the coaxial beam that emerges from the crystal should show equal polarization quality compared to the output of a Zeeman-split laser source.

Implementation of the wave plate results in the cancellation of one potential source for frequency instability, it improves the optical efficiency (i.e. no optical losses in unused optical modes), and allows for a much wider frequency bandwidth (if required).

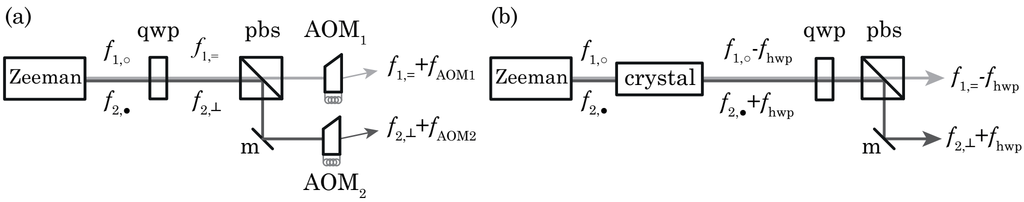

Figure A.6: (a) Sketch of a Zeeman laser whose split-frequency is increased using two AOMs. (b) The discussed electro-optic wave plate can also amplify the Zeeman split frequency and could replace the two AOMs from (a). Legend: AOM_x, acousto-optic modulator; f_x, optical frequency; pbs, polarizing beam splitter; qwp, quarter wave plate; m, mirror; ●, left handed circular polarization; ○, right handed circular polarization; ⊥, vertical linear polarization; and =, horizontal linear polarization.

A.5.2 2/3-Mode HeNe laser source

The electro-optic wave plate can also replace the two AOMs of the alternative heterodyne frequency source (see Section 4.5). There are two different configurations possible: I) generating a coaxial beam from a linearly polarized beam (Fig.A.7a), or II) frequency manipulation of a single circularly polarized beam (Fig.A.7b).

The benefit of a linearly polarized input beam is that it contains both circular polarization states[3], which results in an up as well as a down-shift simultaneously, which leads to a relative frequency offset equaling two times the rotational rate of the crystal's refractive index (i.e. f_{hwp}), whereas the configuration in Fig.A.7b achieves a frequency offset that equals only one time the rotational rate of the crystal's birefringent index .

[3]A linear polarization state consists of the superposition of two counter rotating circular polarization states.

However, the major advantage of the configuration from Fig.A.7b, is that it inherently provides non-mixed source frequencies, unlike the configuration of Fig.A.7a which uses a coaxial beam. Therefore, the configuration sketched in Fig.A.7b is advised for heterodyne displacement interferometry with sub-nm measurement uncertainty.

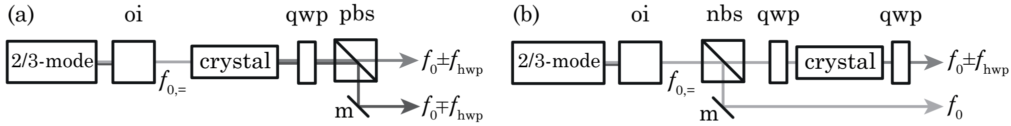

Figure A.7: Sketch of two systems that use a two or three-mode laser of which one of the frequencies is transmitted by the optical isolator (oi). (a) Split frequency generation of two times, and (b) a single time the rotational frequency of the crystal's birefringent index (f_{crystal}). Legend: f_{x}, optical frequency; oi, optical isolator; pbs, polarizing beam splitter; nbs, neutral beam splitter; qwp, quarter wave plate; m, mirror; and =, horizontal linear polarization.

A.6 Demonstrating frequency comb generation

A final set of experiments demonstrated that the electro-optic wave plate was also capable of generating a 'frequency comb', can be defined as *'a light source whose spectrum consists of a series of discrete, equally spaced elements'*. Such a source was made by inserting the electro-optic wave plate into an optical cavity as shown in Fig.A.8, where to 50% reflective mirrors enabled multiple optical passes through the wave plate. Upon each optical pass through the wave plate the optical wave undergoes a discrete frequency shift.

The setup from Fig.A.8a showed with the qwp inserted either frequencies that were all up-shifted or down-shifted – hence single sided (i.e. asymmetric) frequency comb –, of which only the 'odd-numbered modes' were detected. The 'odd-numbered modes' refer to the fact that only the 1st, 3rd, 5th, and so on, modes (i.e. the uneven numbered optical passings) were detected with the detector, FigA.9a and b. When the qwp was removed from that setup the frequency comb became double sided (i.e. symmetric).

In a similar fashion a frequency comb was generated using two neutral beam splitters that created an optical feedback loop, see Fig.A.8b. The optical loop resulted in the measurement of both even and odd-numbered modes. Additionally, by leaving the qwp out of the setup, a linearly polarized polarization was provided to the wave plate, which resulted in the generation of a double sided frequency comb, FigA.9c.

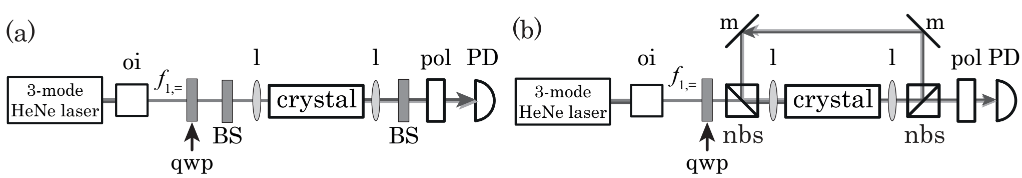

Figure A.8: Two experimental setups that generated (a) single sided frequency comb of which only the odd-numbered modes reach the detector, and (b) single sided frequency comb where both even and odd-numbered modes reach detection. Legend: oi, optical isolator; =, horizontal linear polarization; qwp, quarter wave plate; BS, 50% reflective mirror; l, lens; PD, photodetector; nbs, neutral beam splitter; and m, mirror.

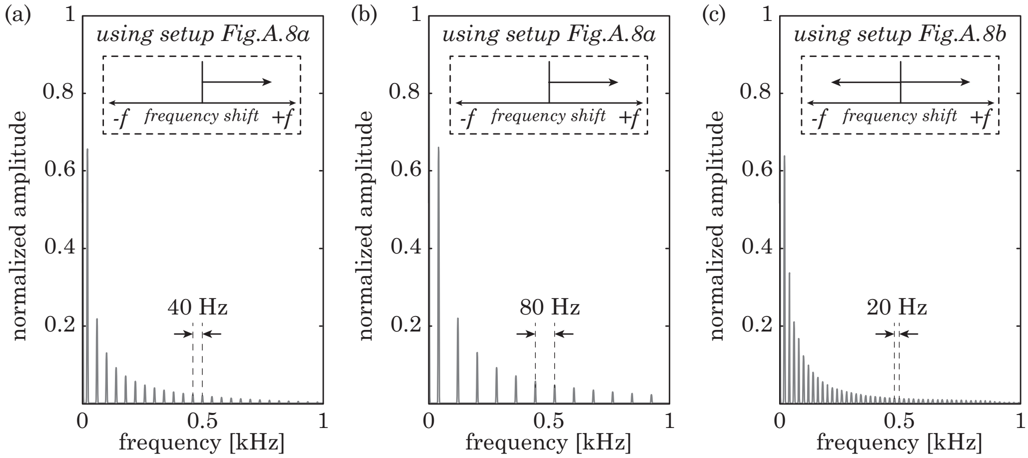

Figure A.9: Measurement data logged with an oscilloscope and visualized in the frequency domain. (a) Frequency comb generated with the setup from Fig.A.8a, showing the beat-frequencies from odd-numbered modes that were 40 Hz apart. (b) Equal setup as (a), with the crystal's birefringent index rotating twice as fast. (c) Results from using the same operating frequency as used for (a), showing both even and odd-numbered modes. *Note that the decrease in amplitude is caused by the optical loss upon each passing.*

In the scientific fields where frequency combs are used (e.g. spectroscopy) a frequency comb requires to be octave spanning (i.e. the highest frequency must be twice the lowest frequency). This could be achieved by e.g. implementation of the electro-optic wave plate in a pumped fiber laser. However, the frequency combs generated in this research have not demonstrated octave spanning frequency combs.

A.7 Conclusions additional research

This additional research was concentrated on development of a new method for heterodyne frequency generation, and has resulted in the development of an electro-optically controllable wave plate. The birefringent index of this wave plate was controlled in magnitude and orientation. The resulting electro-optical wave plate acted equally to a normal wave plate that rotated around its optical axis, with the difference that the phase retardation and the rate of rotation were not fixed and were controlled electrically, which resulted in a device with no moving parts.
Experiments demonstrated that the birefringent index's rotational rate was proportional to the magnitude of the frequency shift, and that the rotational direction of the index determined the direction of the frequency shift.
Other experiments, where the device was placed in an optical cavity, demonstrated that also single and double-sided frequency combs could be generated.

This optical frequency modulation method possesses much potential for the field of metrology, and allows for new measurement approaches in e.g. heterodyne displacement interferometry, such as closed-loop phase forward displacement measurement. However, there are several error sources that affect ideal operation, which require further analysis before this frequency modulation concept can be introduced to industry.

References

[1] K. Ergenzinger, T. Schuldt, P. Berlioz, C. Braxmaier, and U. Johann. Dual absolute and relative high precision laser metrology. In *International Conference on Space Optics*, volume 4, page 8, October 2010.

[2] B. Calvel, I. Cabeza, A. Cabral, E. Manske, J. Rebordao, R. Sesselmann, Z. Sodnik, and A. Verlaan. High precision optical metrology for Darwin: design and performance. In *5th International Conference on Space Optics*, volume 554, page 501, April 2004.

[3] K-N. Joo, J.D. Ellis, J.W. Spronck, P.J.M. van Kan, and R.H. Munnig Schmidt. Simple heterodyne laser interferometer with subnanometer periodic errors. *Optics Letters*, 34(3):386, February 2009.

[4] K-N. Joo, J.D. Ellis, E.S. Buice, J.W. Spronck, and R.H. Munnig Schmidt. High resolution heterodyne interferometer without detectable periodic nonlinearity. *Optics Express*, 18(2):1159, January 2010.

[5] A.J.H. Meskers, J.W. Spronck, and R.H. Munnig Schmidt. Heterodyne displacement interferometer, insensitive for input polarization. *Optics Letters*, 39(7):1949, March 2014.

[6] A.J.H. Meskers, J.W. Spronck, and R.H. Munnig Schmidt. Validation of separated source frequency delivery for a fiber-coupled heterodyne displacement interferometer. *Optics Letters*, 39(15):4603, July 2014.

[7] A.J.H. Meskers, J.D. Ellis, J.W. Spronck, and R.H. Munnig Schmidt. Displacement interferometry with fiber-coupled delivery. In *10th International Measurement Confederation symposium*, September 2011.

[8] A.J.H. Meskers, J.D. Ellis, J.W. Spronck, and R.H. Munnig Schmidt. Fiber coupled sub nanometer displacement interferometry without periodic nonlinearity. In *10th International Symposium on Measurement Technology and Intelligent Instruments*, June 2011.

[9] J.D. Ellis, A.J. H. Meskers, J.W. Spronck, and R.H. Munnig Schmidt. Fiber-coupled displacement interferometry without periodic nonlinearity. *Optics Letters*, 36(18):3584, September 2011.

[10] A.J.H. Meskers, D. Voigt, and J.W. Spronck. Relative optical wavefront measurement in displacement measuring interferometer systems with sub-nm precision. *Optics Express*, 21(15):17920, July 2013.

[11] A.J.H. Meskers, J.W. Spronck, and R.H. Munnig Schmidt. Measuring wavefronts of displacement interferometer systems with sub-nm uncertainty. In *American Society of Precision Engineering, Spring Topical Meeting*, April 2013.

[12] T. Castenmiller, F. van de Mast, T. de Kort, C. van de Vin, M. de Wit, R. Stegen, and S. van Cleef. ASML, Towards ultimate optical lithography with NXT:1950i dual stage immersion platform. In *Optical Microlithography XXIII*, volume 7640, page 76401N, March 2010.

[13] ASML 2013 Fourth Quarter and Annual Financial Results, December 2013.

[14] R. Schuurhuis, M. Coogans, and J. Lammerts. ASML's customer magazine: Images, New TWINSCAN NXT:1960Bi starts shipping, February 2013.

[15] R.H. Munnig Schmidt, G.R. Schitter, A. Rankers, and J. Van Eijk. *The Design of High Performance Mechatronics - 2nd Revised Edition*. Published by IOS Press under the imprint of Delft University Press, 2nd edition, July 2014.

[16] A. Srivastava, S. Pereira, and T. Gaffney. Sub-atmospheric gas purification for EUVL vacuum environment control. In *SPIE 8322, Extreme Ultraviolet (EUV) Lithography III*, volume 8322, page 83222U, March 2012.

[17] B.A.W.H. Knarren, S.J.A.G. Cosijns, H. Haitjema, and P.H.J. Schellekens. Validation of a single fibre-fed heterodyne laser interferometer with nanometre uncertainty. *Precision Engineering*, 29(2):229, April 2005.

[18] P.L.M. Heydemann. Determination and correction of quadrature fringe measurement errors in interferometers. *Applied Optics*, 20(19):3382, October 1981.

[19] S.J.A.G. Cosijns, H. Haitjema, and P.H.J. Schellekens. Modeling and verifying non-linearities in heterodyne displacement interferometry. *Precision engineering*, 26(4):448, October 2002.

[20] C-M. Wu. Periodic nonlinearity resulting from ghost reflections in heterodyne interferometry. *Optics Communications*, 215:17, January 2003.

[21] G.V. Fedotova. Analysis of the measurement error of the parameters of mechanical vibrations. *Measurement Techniques*, 23(7):577, July 1980.

[22] R.C. Quenelle. Nonlinearity in interferometer measurements. *Hewlett Packard Journal*, 34(4):3, April 1983.

[23] C.M. Sutton. Non-linearity in length measurement using heterodyne laser Michelson interferometry. *Journal of Physics E: Scientific Instruments*, 20(10):1290, October 1987.

[24] W. Hou and G. Wilkening. Investigation and compensation of the nonlinearity of heterodyne interferometers. *Precision Engineering*, 14(2):91, April 1992.

[25] C-M. Wu and R.D. Deslattes. Analytical Modeling of the Periodic Nonlinearity in Heterodyne Interferometry. *Applied Optics*, 37(28):6696, October 1998.

[26] W. Hou. Optical parts and the nonlinearity in heterodyne interferometers. *Precision Engineering*, 30(3):337, July 2006.

[27] M. Tanaka, T. Yamagami, and K. Nakayama. Linear interpolation of periodic error in a heterodyne laser interferometer at subnanometer levels. *IEEE Transactions on Instrumentation and Measurement*, 38(2):552, April 1989.

[28] C-M. Wu, J. Lawall, and R.D. Deslattes. Heterodyne Interferometer with Subatomic Periodic Nonlinearity. *Applied Optics*, 38(19):4089, July 1999.

[29] T.L. Schmitz and J.F. Beckwith. Acousto-optic displacement-measuring interferometer: a new heterodyne interferometer with Angstrom-level periodic error. *Journal of Modern Optics*, 49(13):2105, November 2002.

[30] C. Weichert, P. Kochert, R. Koning, J. Flugge, B. Andreas, U. Kuetgens, and A. Yacoot. A heterodyne interferometer with periodic nonlinearities smaller than 10pm. *Measurement Science and Technology*, 23(9):094005, July 2012.

[31] J. Lawall and E. Kessler. Michelson interferometry with 10 pm accuracy. *Review of Scientific Instruments*, 71(7):2669, July 2000.

[32] A.B. Ray. Monolithic displacement measuring interferometer with spatially separated but substantially equivalent optical pathways and optional dual beam outputs, Agilent Technologies Inc., Patent US 7,705,994 B2, November 2007.

[33] Agilent Technologies Inc., 5301 Stevens Creek Boulevard, Santa Clara, California 95052-8059. *Agilent N1211A and N1212A/B AOM Laser and Remote Optical Combiner, N1211-90003*, 1st edition, p. 48, October 2011.

[34] Interferometer E1826G, frequency stabilized laser source 5517D, and phase measurement board N1225A, Agilent Technologies Inc., Santa Clara, CA (US).

[35] V.G. Badami and S.R. Patterson. A frequency domain method for the measurement of nonlinearity in heterodyne interferometry. *Precision Engineering*, 24(1):41, January 2000.

[36] T.L. Schmitz, D. Chu, and L. Houck III. First-order periodic error correction: validation for constant and non-constant velocities with variable error magnitudes. *Measurement Science and Technology*, 17(12):3195, November 2006.

[37] C. Schluchter, V. Ganguly, D. Chu, and T.L. Schmitz. Low velocity compensation for first order periodic error caused by beam shear. *Precision Engineering*, 35(2):241, April 2011.

[38] Capacitive probe 2805MSE A9089, readout using MicroSense, LLC, model 4810.

[39] E.R. Peck. Polarization Properties of Corner Reflectors and Cavities. *Journal of the Optical Society of America*, 52(3):253, March 1962.

[40] J. Liu and R.M.A. Azzam. Polarization properties of corner-cube retroreflectors: theory and experiment. *Applied Optics*, 36(7):1553, March 1997.

[41] C-H. An and J.W. Morris. Polarization properties of nonsymmetric retroreflectors. In *SPIE 1317, Polarimetry: Radar, Infrared, Visible, Ultraviolet, and X-Ray*, volume 1317, page 333, October 1990.

[42] Z. Guo, L. Yan, W. Pan, B. Luo, K. Wen, and X.S. Yao. Design of polarization-maintaining retro-reflector for folded-path applications. *Chinese Optics Letters*, 9(10):100601, July 2011.

[43] M.A. Player. Polarization Properties of a Cube-corner Reflector. *Journal of Modern Optics*, 35(11):1813–1820, November 1988.

[44] G. Felix. Interferometer with double polarizing beam splitter, Agilent Technologies Inc., CA (US), Patent US 7,652,771 B2, October 2007.

[45] K. Dorenwendt and G. Bonsch. Eber den EinfluB der Beugung auf die interferentielle Langenmessung. *Metrologia*, 12(2):57, April 1976.

[46] G. Mana. Diffraction effects in optical interferometers illuminated by laser sources. *Metrologia*, 26(2):87, November 1989.

[47] Schott. TIE-26: Homogeneity of optical glass. Technical report, 2004.

[48] E.S. Johnstone, J.J. Bockman, A.B. Ray, and K.B. Bagwell. Interferometer using beam re-tracing to eliminate beam walk-off, Agilent Technologies Inc., CA (US), Patent US 6,897,962 B2, May 2005.

[49] A. Chernyshov, U. Sterr, F. Riehle, J. Helmcke, and J. Pfund. Calibration of a Shack-Hartmann sensor for absolute measurements of wavefronts. *Applied Optics*, 44(30):6419, October 2005.

[50] A.F. Brooks, T-L. Kelly, P.J. Veitch, and J. Munch. Ultra-sensitive wavefront measurement using a Hartmann sensor. *Optics Express*, 15(16):10370, August 2007.

[51] H. Medecki, E. Tejnil, K.A. Goldberg, and J. Bokor. Phase-shifting point diffraction interferometer. *Optics Letters*, 21(19):1526, October 1996.

[52] G.R. Brady, M. Guizar-Sicairos, and J.R. Fienup. Optical wavefront measurement using phase retrieval with transverse translation diversity. *Optics Express*, 17(2):624, Januari 2009.

[53] R. Peeters. ASML's NXE platform performance and volume introduction. In *Presentation, SPIE 2013, Advanced Lithography*, 2013.

[54] Agilent Technologies Inc., 5301 Stevens Creek Boulevard, Santa Clara, California 95052-8059. *Agilent N1225A Four-Channel High Resolution Laser Axis Board for VME User's guide*, 3rd edition, Manual Part No.: N1225-90012, May 2008.

[55] K.P. Birch and M.J. Downs. An Updated Edlen Equation for the Refractive Index of Air. *Metrologia*, 30(3):155, February 1993.

[56] J.D. Ellis, K-N. Joo, E.S. Buice, and J.W. Spronck. Frequency stabilized three mode HeNe laser using nonlinear optical phenomena. *Optics Express*, 18(2):1373, January 2010.

[57] W.H. Stevenson. Optical Frequency Shifting by Means of a Rotating Diffraction Grating. *Applied Optics*, 9(3):649, March 1970.

[58] T. Maekawa, T. Minami, K. Makino, S. Tanaka, S. Kubo, and M. Iguchi. Frequency shift of 1.45 MHz for 337 HCN laser beam with a super rotating grating. *Review of Scientific Instruments*, 62(2):304, February 1991.

[59] M. Berwick and D.A. Jackson. Coaxial optical-fiber frequency shifter. *Optics Letters*, 17(4):270, February 1992.

[60] B.Y. Kim, H.E. Engan, H.J. Shaw, and J.N. Blake. All-fiber acousto-optic frequency shifter. *Optics Letters*, 11(6):389, June 1986.

[61] R.A. Beth. Direct Detection of the Angular Momentum of Light. *Physical Review*, 48(5):471, September 1935.

[62] R.A. Beth. Mechanical Detection and Measurement of the Angular Momentum of Light. *Physical Review*, 50(2):115, July 1936.

[63] P.J. Allen. A Radiation Torque Experiment. *American Journal of Physics*, 34(12):1185, May 1966.

[64] B.A. Garetz. Angular Doppler effect. *Journal of the Optical Society of America*, 71(5):609, May 1981.

[65] C.F. Buhrer, D.H. Baird, and E.M. Conwell. Optical Frequency Shifting by Electro-Optic Effect. *Applied Physics Letters*, 1(2):46, October 1962.

[66] C.F. Buhrer, L.R. Bloom, and D.H. Baird. Electro-Optic Light Modulation with Cubic Crystals. *Applied Optics*, 2(8):839, August 1963.

[67] G.E. Sommargren. Up/down frequency shifter for optical heterodyne interferometry. *Journal of the Optical Society of America*, 65(8):960, August 1975.

[68] R.N. Shagam and J.C. Wyant. Optical frequency shifter for heterodyne interferometers using multiple rotating polarization retarders. *Applied Optics*, 17(19):3034, October 1978.

[69] B.A. Garetz and S. Arnold. Variable frequency shifting of circularly polarized laser radiation via a rotating half-wave retardation plate. *Optics Communications*, 31(1):1, October 1979.

[70] M.P. Kothiyal and C. Delisle. Optical frequency shifter for heterodyne interferometry using counterrotating wave plates. *Optics Letters*, 9(8):319, August 1984.

[71] Y. Li and G. Eichmann. Multipass counterrotating wave-plate frequency shifters for heterodyne interferometry. *Optics Letters*, 11(11):718, November 1986.

[72] J. Campbell and W. Steier. Rotating-waveplate optical-frequency shifting in lithium niobate. *IEEE Journal of Quantum Electronics*, 7(9):450, September 1971.

[73] I.P. Kaminow and E.H. Turner. Electrooptic light modulators. *Proceedings of the IEEE*, 54(10):1374, October 1966.

[74] R.S. Weis and T.K. Gaylord. Lithium niobate: Summary of physical properties and crystal structure. *Applied Physics A: Materials Science & Processing*, 37(4):191, August 1985.

[75] K-K. Wong. *Properties of lithium niobate*. The Institution of Electrical Engineers, ISBN 0-85296-799-3, January 2002.

[76] H. Shimizu and K. Kaede. Endless polarisation controller using electro-optic waveplates. *Electronics Letters*, 24(7):412, March 1988.

Preface

(English transcript of the Dutch 'Voorwoord')

During my time at TU Delft I've done and learned many things, in terms of knowledge acquisition as well as personal development. My most interesting period of study began with the start of my Mechanical Engineering Masters in Mechatronic System Design (MSD) when I finally had the opportunity to follow the courses that truly interested me. During that period I met Rob and Jo, who at that time were still Prof. Munnig Schmidt and Prof. Spronck to me. The courses were taught the 'Delft' way, which made following the lectures very pleasant and supported my decision to start another masters in parallel, the Biomedical masters in Tissue Biomechanics and Implants (TBI).
Instead of a literature assignment for TBI, in 2009 I obtained, with the help of Rob, a position with the Precision Engineering Research Group at the Massachusetts Institute of Technology (MIT) led by Prof. Alexander Slocum; that was a great experience. Rob, I'm still very grateful to you for this opportunity! Alex, thank you for this magnificent experience and this memorable period, you are an incredible, enthusiastic and motivating professor. I also would like to thank Nevan Hanumara for making my stay at the MIT even more memorable. Nevan, since that period we have met several times, either in the United States or here in Delft, it's always a pleasure meeting and I hope we can help each other out many more times through our network of connections. After that period at MIT, I was convinced that I was going to pursue a PhD at that university, and no other, until I met Jo...

While performing my graduation research for the TBI master, Rob suggested that I contact Jo for an interesting graduation assignment for my MSD master. During that conversation, Jo asked me if I wanted to start a PhD under his supervision. Lit by Jo's enthusiasm, I soon agreed to this request, not knowing how vast and complex the topic would turn out to be.
Less than four years after that moment, I can look back on a very enjoyable, educational, and busy period that passed by quickly. It was a period during which my way of thinking changed significantly and I developed personally; becoming more relaxed and less rushed when discussing and refuting ideas proved to be a special challenge. Meeting with Jo and Rob and the semi-annual meetings with the user committee were good exercises. Learning when to be less rushed and when to take a step back is an insight I benefit from every day.
I have never doubted if PhD research was the right thing to do, despite the many challenges, which I gladly took up and found fulfilling. Writing publications was an exciting process, which again and again posed a challenge, primarily since these were intensive and time consuming undertakings. I learned a lot from designing

and executing well defined experiments that were needed to scientifically validate specific research aspects. It gave me great satisfaction when my results were recognized, after critical analysis by experienced researchers, and were made available to the community of fellow scientists. However, as probably many graduated PhD holders will agree with me, writing a thesis is a challenge of a different magnitude. This thesis has demanded determination, but at no time during this period did I stand alone.

Rob, Jo, thank you for this great period; your leadership of the group of 'mechatronici' created a rich educational environment, with a broad range of knowledge.
Rob, thank you for your effort and for the conversations we've had about research, your working experience from your time at ASML, and your view on how things are done in industry. During my studies at the TU Delft you wrote a great book with much educational value, and only now (after writing this work) do I fully appreciate how much time and energy it must have cost you to write it. Although we haven't had weekly meetings, our interactions always made me wiser; I've learned a lot from you, thank you.
Jo, it always amazes me how admirably sharp you are in your thinking, day in and day out. I gratefully made use of your background in physics, which was very welcome during this research. Your creative and multidisciplinary character, together with your commitment to all of your masters and PhD-students, have had a major and positive impact on me, thank you.
Something for which I wish to thank you both for, was the freedom you gave me to do things not directly related to my research, such as participation in the Alpbach and Post-Alpbach Summerschools, and letting me to start my own independent research project (the electro-optic wave plate). You have always given me your approval, provided that the rationale behind my choices was sound; I'm well aware that this freedom was exceptional. I have also come to realize that cooperating and communicating on the same level with each other as we did, was a rarity that isn't experienced by every PhD-candidate. Your open character, dedication and advice has truly given me a solid foundation for a successful scientific career.

Another person who I wish to thank is Jonathan Ellis. Jon, thank you for helping me getting up to speed (i.e. high speed) at the start of the project. During your last four months in the Netherlands you were an unlimited source of information about optical interferometry; thank you for answering every question I had. With your help, I had the opportunity to give presentations at two conferences and to publish, together with you, my first journal publication, all in the first year of my PhD.

I also want to thank my user committee[4], including Han Haitjema (*Mitutoyo*), Dirk Voigt (*VSL*), Arthur van Nes (*VSL*), Rob Bergmans (*VSL*), Bert van der Pasch (*ASML*), Suzanne Cosijns (*ASML*), Kees Bos (*Keysight*, previously known as *Agilent Technologies*), Lex Uittenbogaard (*Keysight*), Ad Verlaan (*TNO*), Machteld de Kroon (*TNO*), Henny Spaan (*IBS Precision engineering*), Guido Florussen (*IBS Precision engineering*), Pleun Dona (*FEI Company*), Annette Steggerda (*Rijksdienst voor Ondernemend Nederland, previously known as Agent-schap NL*) and Eddy Schippers (*Rijksdienst voor Ondernemend Nederland*). Many of you took the effort to visit the university every half year and to provide advice about the research, thank you.

[4]When reading this work not everyone will know who I mean when I only mention first names, therefore, I opted to use both first name and surname so that no ambiguity can exist who helped me during this PhD research.

Han, your detailed research criticism during the meetings gradually acquired my appreciation. When I thought I had a well-defined piece of research you could always identify a few points that I needed to take another look into. Especially at the beginning of the project, these meetings were a good exercise for me and made me less rushed while giving counterarguments. Han, your insights led to better results and offered an extra incentive to place my mindset under the microscope, thank you.
Kees and Lex, the meetings with you were always pleasant and informative. Your knowledge about the interferometry systems of *Agilent Technologies* and your help in providing measurement equipment from *Agilent Technologies* were of great value for the research, thank you. I also would like to thank two other people from *Keysight*, Larry Zurbrick and Greg Felix. Larry and Greg, thank you for your willingness to visit the university, and for your interest in the research. Your viewpoints and advice regarding the Delft interferometry concept were much appreciated. During the research I became acquainted with your company's high-end interferometric measurement systems/equipment and after completing my work I fully appreciate the challenges that are involved in reaching sub-nm measurement uncertainty. Therefore, I find it astonishing and a great accomplishment what's already commercially achieved. With this research, I hope that I have contributed to a further reduction of measurement uncertainty for these magnificent optical measurement tools that your company realizes.
Suzanne, thank you for your visits to the TU Delft and for the informative discussions we had at *ASML*; your practical view on many error sources resulted in research that stands close to reality. I also would like to thank Bert van der Pasch, Robbert van Leeuwen and Hans Vermeulen from *ASML* for receiving Jo and me at *ASML*, for their interest in the research and for giving advice. Bert, thank you for taking the time for completely reading my work and giving comments, they have raised the quality of the thesis.
From the *Van Swinden Laboratorium (VSL, the Dutch National Metrology Institute)* I would like to thank Arthur, Dirk and Rob, for providing me with advice with a deeper understanding of physics and for the use of equipment from *VSL*. Furthermore, Dirk, I really enjoyed our email correspondence about fundamental optics and appreciated your time spent reviewing my publications. You helped me to understand new aspects of optics and I very much liked writing a joint publication with you, thank you.
Ad, you are a much more experienced scientist that I am, though, during our conversations you always treated me as a colleague, which I greatly appreciated. I also liked it that you involved me during my second year in the preparations of the 'HPOM-2' [1,2] thermal vacuum tests in the cleanrooms of *TNO*, which was an instructive experience. Related to these tests, I would also like to thank Thilo Schuldt (*University of Konstanz*) and Dmitry Ityaksov (*TNO*) for their time and enthusiasm in teaching me new aspects of frequency stabilization and laser operation.

Physics has always fascinated me, however, due to my mechanical engineering background a number of fundamental gaps related to optics remained after my studies. Fortunately, I filled these with the help of the Optics Department of Applied Sciences. The courses 'optical waveguiding' and 'theoretical optics' taught by Paul Urbach, Jaap Caro and Omar El Gawhary are among the most interesting courses I've followed. Paul, Jaap and Omar, thank you for answering many questions that sometimes might have been quite straightforward for a physicist. I would also like to thank two other members of the optics group: Nandini Bhattacharya and Jeffrey

Meisner. Nandini, thank you for your interest in the electro-optic wave plate, and for our discussions about the design of a new instrument for measuring magnetic fields of space-based plasmas using radio waves (related to the Post-Alpbach summerschool). Jeff, your experience with radio waves helped a lot during the elaboration of the fundamentals of this instrument and gave me a new perspective on electromagnetic waves, thank you.

Of course I must not forget my fellow PhD-candidates, Oscar van de Ven, Johan Vogel, Ruijun Deng, Phuc (Foppe) Vuong, Patrice Lambert, Teun Hoevenaars, Rudolf Saathof, Takeshi Morishima, Guido Delhaes, Jan Shutte, Jasper Wesselingh, Jeroen van Schieveen, Chris Valentin and Pablo Estevez Castillo. Thank you for the many brainstorming sessions, informative coffee breaks and lunches. Johan, Oscar and Rudolf, thanks for the many reflections we've had regarding Fourier transforms. Johan, thank you for your help with the numerical simulation of an interference wavefront that originated from a single-mode optical fiber.
In addition to PhD-students, the MSD group also included master students, Bart Festen, Luuk Ursem, Martijn Wansink, Max Café, Simon van Veen, Charlie van der Schoor, Gihin Mok, Paul Ouwehand, Arnold Zondervan, Stefan van der Kleij, Jeroen Karregat and Rens Berkhof. It was a pleasure to see your projects gradually take shape. Arnold, thanks for your help with the electro-optic wave plate.
Furthermore, I would like to thank the TU staff who helped me during the research, Patrick van Holst, Harry Jansen, and Rob Luttjeboer. Thank you for your advice when things had to be built and for your willingness and fast response to help out whenever possible, I greatly valued this.
I would also like to thank Corinne du Burck, Birgit Rademakers, Marli Guffens, Gaby Offermans and Marianne Stolker for processing a ream of paperwork and making arrangements: without you PhD-candidates would have had much less time to spend on their research.

No matter how much I appreciate the ones who I've already mentioned, my greatest appreciation goes out to my parents. I have much respect for the way that you've raised and supported my brother and me; your commitment and advice regarding the many choices in life has led to the fact that your two children have become mechanical engineers, of which one even has become an aviator, and the other has obtained a PhD in science. And we must not forget that you accomplished this while establishing and working in your own company, growing flowers in greenhouses. Sander, my 'big brother', you too have contributed to making me who I am today, thank you for your technical enthusiasm, enterprising spirit, and your will to face challenges. You three were my role-models of perseverance.

I've waited until the end to thank the most important person: Dear Janneke, thank you for your support and your joyful companionship throughout my PhD. I know very well that it hasn't always been easy for you to live with someone who was always busy, and not just with his PhD research; a minor downside of someone who likes nearly everything that is technical/scientific. While the past year was mainly devoted to completing my research, and less to doing things together, undertaking things together with you is what I like the most! Therefore, I hope that we can have many more adventures together, during which I promise to learn what the term 'having vacation' really means.

Arjan Meskers
Delft, September 2014

Samenvatting

Lithografische apparatuur voor de vervaardiging van onder andere computer chips vergt steeds nauwkeurigere positie meetsystemen. Momenteel wordt de nauwkeurigheid hiervan gedreven door de opkomst van extreem ultraviolet licht voor lithografie doeleinden (EUV-lithografie). Dit proefschrift beschrijft een interferometrisch meetsysteem voor het meten van verplaatsingen dat de benodigde meetnauwkeurigheid voor EUV-lithografie tot ver in deze eeuw veilig stelt. Niet alleen de meetnauwkeurigheid van deze lithografie machines is veeleisend, ook de vergroting van de silicium substraten van 300 mm diameter naar 450 mm diameter vormt een uitdaging. De continue vooruitgang van deze twee aspecten bevordert de vooruitgang of ontwikkeling van nieuwe meetinstrumenten voor lithografische doeleinden.

De doelstelling van dit onderzoek was het ontwerpen van een "*compacte heterodyne verplaatsingsinterferometer voor een meetbereik van 450 mm met subnanometer meetonzekerheid, terwijl deze een modulaire systeemopbouw toestaat met een flexibele optische lay-out en een robuustheid die groot genoeg is om modules snel te kunnen vervangen en zo downtime te reduceren*".

Dit werk was een voortzetting van het onderzoek van Dr. Ki-Nam Joo (die met Dr. Jonathan Ellis heeft samengewerkt), waarbij een interferometer concept werd toegepast dat zijn oorsprong heeft in de astronomie. Dat onderzoek beschreef hoe de meetlineariteit van een heterodyne verplaatsingsinterferometer verhoogt kon worden door het reduceren van een aanzienlijke periodieke en niet-lineaire foutenbron. Dit werd bewerkstelligd door het scheiden en gescheiden houden van de twee optische bundels (waarvan ieder een bronfrequentie draagt) tot het moment van detectie [3, 4].
Het doel van dit onderzoek betrof meer dan alleen verbeteringen op componentniveau, er zijn ook verbeteringen op systeemniveau bereikt, waarbij gefocust werd op de verbetering van de meetlineariteit en systeem modulariteit. Deze twee aspecten waren onderverdeelt in meerdere afzonderlijke sub onderwerpen waarvan elk theoretisch geanalyseerd is en indien nodig ook experimenteel gevalideerd. Elk resultaat is vervolgens vergeleken met de prestaties van een referentie meetsysteem. Dit referentie meetsysteem (ook wel benchmarksysteem) betrof het huidige meest geavanceerde heterodyne interferometrisch verplaatsingsmeetsysteem, welke afkomstig was van *Agilent Technologies*. Dit systeem maakte gebruikt van coaxiale optische bundels die vrij in de ruimte propageerden voor de aanlevering van de bronfrequenties aan de interferometers, welke vervolgens via optische fibers aan externe detectieapparatuur (fase-meetapparatuur) gekoppeld waren. Dit meetsysteem was voor dit proefschrift vervolgens geschetst te opereren in een EUV-lithografiemachine, welke een compartiment bevatte waarbinnen bijna-vacuüm condities heersten. Bin-

nen dit compartiment bevonden zich zes interferometers en drie ’stages’, één ’reticle-stage’ en twee ’wafer-stages’, waarbij elke stage in zes graden van vrijheid werd gevolgd door twee interferometers die elk vijf graden van vrijheid maten; resulterend in 30 meetassen). Door op deze manier te meten werd een stuk meetzekerheid gewaarborgd.

Bij het meten in een vacuüm (of bijna-vacuüm) omgeving is periodieke niet-lineariteit (PNL) de belangrijkste foutenbron die de meetlineariteit limiteert van een heterodyne interferometer welke wordt voorzien van bronfrequenties middels een coaxiale optische bundel. Een coaxiale bundel bevat twee lineair gepolariseerde optische frequenties die orthogonaal zijn georiënteerd. Wanneer deze twee frequenties gescheiden worden op basis van hun polarisatie kan er een fenomeen optreden dat ’frequentielekkage’ wordt genoemd, dit resulteert in het mengen van de twee frequenties. Wanneer dergelijke gemende frequenties worden gebruikt voor het meten van verplaatsing leidt dit tot niet-lineaire fouten bovenop de meetresultaten, welke zich iedere fractie van een golflengte (λ = 633 nm) verplaatsing herhalen, vandaar de term ’periodieke niet-lineariteit’. Er is aangetoond dat wanneer er geen polarisatie gebaseerde frequentie splitsing wordt toegepast, dit een significante bron van PNL wegneemt en de weg vrij maakt voor verdere toename van meetlineariteit [3,4].
Het onderzoek beschreven in dit proefschrift heeft de interferometer lay-out van Dr. Joo’s onderzoek als uitgangspunt gebruikt voor metingen met twee interferometers, beiden gebaseerd op het gebruik van twee optische gescheiden bundels die elk een eigen bronfrequentie bevatten. De ene interferometer gebruikte een retroreflector als meet-’spiegel’ en de andere gebruikte een vlakke meetspiegel. In dit proefschrift ligt de nadruk op de laatstgenoemde, omdat het referentie meetsysteem ook een vlakke meetspiegel gebruikte. De laserbron van Dr. Joo’s onderzoek [4] was om praktische redenen vervangen door een 2-mode frequentie gestabiliseerde helium neon (HeNe) laser. Experimenten en frequentiedomein-analyses bevestigden dat deze ’alternatieve’ heterodyne bron (welke een samenstelling was van de 2-mode laser en twee acousto-optische modulatoren) in staat was om de voor dit onderzoek benodigde output te leveren: twee gescheiden en ongemengde bronfrequenties (met een frequentie offset van ~2 MHz). Een aangepaste en verbeterde interferometer lay-out vormde samen met de alternatieve bron de demonstratie opstelling van het ’Delftse interferometrie systeem’.
Omdat coaxiale interferometers verhoogde aanwezigheid van PNL vertonen bij suboptimale polarisatie uitlijning en polarisatie onvolkomenheden, betrof één van de eerste metingen een onderzoek naar de invloed van bronfrequentie-polarisatie op de aanwezigheid van PNL. Experimenten lieten zien dat de meetresultaten van het Delftse systeem enkel PNL van de 1^e ’fringe-orde’[1] vertoonden, met een gemiddelde grootte van minder dan 4 pm, ongeacht de polarisatie manipulatie. Het benchmarksysteem vertoonde echter bij gelijke polarisatie manipulatie PNL tot wel de 8^e fringe-orde, waarbij de grootst gemeten 1^e fringe-orde groter was dan 10 nm waarna het systeem uiteindelijk ophield met meten door-dat de niet lineariteiten té groot werden. De resultaten van dit onderzoek zijn gepubliceerd en demonstreerden de ongevoeligheid (robuustheid) op de meetnauwkeurigheid van het Delft interferometrieconcept met betrekking tot de polarisatie van de aangeleverde bronfrequenties, in tegenstelling tot het benchmarksysteem [5].

[1]Een ’fringe-orde’ wordt bepaald door $(N \cdot d)/\lambda_{HeNe}$, waarbij d = verplaatsing, N = interferometer ’vouw’-factor (het aantal keer dat het licht tussen de interferometer en meetspiegel heen en weer reist), en λ_{HeNe}= 633 nm

De Delftse interferometer behaalde sterk gereduceerde waarden van PNL (enkel nog pm grootte) welk echter nog steeds duidden op de aanwezigheid van ongewilde frequenties in de interferentie signalen; een proces waaraan PNL ten grondslag ligt. Eén waargenomen bron van zulke ongewilde frequenties bestond uit ongewilde reflecties (ghosting) en één potentiële bron werd gevormd door polarisatiedraaiing door een retroreflector in combinatie met een gepolariseerde bundelsplitser. Anders dan deze twee bronnen van PNL zijn er niet waargenomen of er wordt niet van verwacht dat zij enige invloed hebben op de meetprestaties van de interferometer.
Vervolgexperimenten onderzochten het optisch gescheiden vervoer van de twee bronfrequenties naar de interferometer omdat de scheiding van optische bundels zorgt voor optische weglengte verschillen die mogelijk van invloed zijn op de meetprestaties. Het voordeel van het Delftse interferometer concept is dat elke interferometer zijn eigen referentie heeft en het theoretisch mogelijk maakt om rekening te houden met faseverschillen door toedoen van optische weglengte ongelijkheid. Dit werd bevestigd door experimenten welke aantoonden dat faseverstoringen een factor 6000 werden gereduceerd. Deze reductiefactor werd echter gelimiteerd door de experimentele opstelling zelf en zal naar verwachting onder normale bedrijfsomstandigheden worden overschreden [6]. Met behulp van deze resultaten is aangetoond dat het Delftse interferometrie concept overweg kan met gescheiden aanvoer van de bronfrequenties met behoud van de meetlineariteit.
Een klein minpunt van het hebben van een referentie op elke interferometer voor de genoemde 30 gemeten assen is dat dit resulteert in vijf extra detectorkanalen opzichte van de benchmark systeem. Dit wordt echter ruimschoots gecompenseerd doordat deze referenties aanvoer van de bronfrequenties via licht geleidende fibers (glasvezels) ondersteunen. Het toepassen van fibers voor het aanvoeren van de bronfrequenties verbeterd zowel de flexibiliteit van de optische lay-out, alsmede de modulariteit van het systeem. Dit komt doordat enkel de positionering van de uiteinden van een fiber aandacht vereist, in tegenstelling tot de vrij te houden zichtlijn van een optische bundel die door de ruimte propageert. Daarnaast bieden fibers tevens de mogelijkheid om plug-and-play verbindingen tussen modules te realiseren.
Theoretische en experimentele analyses met betrekking tot multi-mode fibers gaven aan dat dit type fiber niet geschikt is voor het aanleveren van de bronfrequenties doordat dit type fiber meerdere (afzonderlijke) optische lichtwegen ondersteund, ook wel 'modes' genoemd. Deze modi voorkomen goede collimatie van het aangevoerde licht over het beoogde meetbereik wat resulteert in een té lage lichtsterkte bij detectie. Veel belangrijker, de fase van elke mode is individueel beïnvloedbaar en bleek zeer gevoelig voor omgevingsinvloeden, wat leidde tot een afname van de meetlineariteit [7]. Ondanks de vele typen fibers blijken alleen single-mode fibers de gewenste optische eigenschappen te hebben die benodigd zijn voor het bereiken van de beoogde meetprestaties.
Met gebruik van single-mode polarisatie behoudende fibers is een volledig fiber gekoppelde Delft-interferometer gerealiseerd. Deze opstelling demonstreerde de haalbaarheid van het gebruik van optische fibers voor de bouw van een optisch flexibel interferometersysteem met niet-detecteerbare niveaus van PNL. De behaalde resultaten met deze opstelling zijn gepresenteerd op een conferentie en gepubliceerd in een journal [8, 9]. Gerelateerd werk demonstreerde tevens dat het Delftse interferometer concept aanzienlijk ongevoelig is voor optische intensiteitsschommelingen, wat aangeeft dat ook niet polarisatiebehoudende fibers een optie zijn en dat mechanische trillingen op de fiberverbindingen potentieel niet kritisch zijn [6].

In een andere analyse was de invloed van optische golffronten op meetlineariteit bestudeerd. In 'traditionele' interferometersystemen worden de bronfrequenties aangevoerd middels een optische coaxiale bundel, welke als voordeel heeft dat beide bronfrequenties een gemeenschappelijk optisch pad delen waardoor zij identiek beïnvloed worden door verstoringen zoals brekingsindexverschillen. Het gemeenschappelijke optische pad voorkomt faseverschillen tussen de bronfrequenties onderling en leidt tot de twee identiek gevormde optische golffronten. In tegenstelling, twee gescheiden bundels (waarbij ieder één bronfrequentie draagt) hebben geen gemeenschappelijk optisch pad waardoor zij individueel verstoord kunnen worden en dus verschillende optische golffronten kunnen hebben. Interferentie tussen de golffronten van de twee bronfrequenties creëert een 'interferentie golffront', waarvan de vorm uit de relatieve faseverschillen tussen de interfererende golffronten bestaat. Rotatie en translatie van de meetspiegel zorgen ervoor dat de overlap tussen de twee interfererende golffronten veranderd (ook wel 'beam walkoff' genoemd) waardoor de sterkte en de golffrontvorm van het interferentie signaal veranderen, beide beïnvloeden de meetlineariteit.
Een nieuwe meetmethode was ontworpen voor het onderzoeken van de vorm van interferentie golffronten. De methode maakte het mogelijk om de vorm van het wavefront inzichtelijk te maken met sub-nm nauwkeurigheid - zelfs in openlucht - en toonde aan dat reeds bij de uitgang van een laserbron het interferentie golffront vele nanometers was vervormd, ±20 tot ±50 nm. In tegenstelling tot een golffront dat voortgebracht wordt door een single-mode fiber, hiervan werd indirect aangetoond dat deze bolvormig is en aanzienlijk minder gedeformeerd, metingen lieten een overall vervorming zien van minder dan 2 nm. Deze nieuwe meetmethode en de bevindingen die hieruit voort kwamen zijn zowel op een conferentie gepresenteerd als in een journal gepubliceerd [10, 11].
Nadere analyse met betrekking tot de invloed van optische golffront deformatie in combinatie met beam walkoff heeft aangegeven dat de Delftse interferometer mogelijk minder wordt beïnvloed door beam walkoff dan de benchmarksysteem. De analyse toonde aan dat wanneer beam walkoff plaatsvindt het beter is om twee individueel vervormde maar relatief vlakke (en niet gekantelde) golffronten aan een interferometer aan te leveren, in plaats van twee identieke maar significant vervormde golffronten (door propagatie vrij in de ruimte); wat het geval is bij het benchmarksysteem.
Verder zijn middels theoretische analyses ook een aantal andere aspecten bestudeerd, zoals data-age en thermische invloed; welke respectievelijk voorbeelden zijn van *interne* en *externe* foutenbronnen. *Interne* foutenbronnen hadden betrekking op meetfouten die voortkwamen uit het ontwerp van de interferometer. In deze categorie presteerde de Delftse interferometer gelijk aan of beter dan de benchmark interferometer. *Externe* foutenbronnen bestonden uit meetfouten die ontstaan onder invloed van de meetomgeving en de installatie van het interferometer systeem. Ook in deze categorie vertoonde de Delftse interferometer gelijke prestaties, behalve voor thermische invloeden. Het gebruik van afzonderlijke lichtwegen in combinatie met retroreflectoren maakt de Delftse interferometer gevoeliger voor inhomogene opwarming dan de benchmark interferometer, waarvan wordt verwacht dat dit de interferometer zijn belangrijkste foutenbron zal zijn.
Additioneel onderzoek dat betrekking had op heterodyne frequentie generatie methoden heeft geleid tot de ontwikkeling van een elektro-optische faseplaat als zijnde een nieuwe methode voor heterodyne frequentie generatie. Experimenten toonden

aan dat de draairichting van de dubbele refractieve index van de faseplaat de richting van de frequentie verschuiving bepaalde en dat de rotationele snelheid van deze index proportioneel was aan de frequentieverschuiving. Andere experimenten, waarbij de faseplaat bijvoorbeeld tussen twee half doorlatende spiegels werd gezet, toonden aan dat het met deze elektro-optische faseplaat ook mogelijk was om zogenaamde ’frequentie-kammen’ te maken.
Deze methode om optische frequenties te moduleren bezit veel potentie om toegepast te worden op het gebied van metrologie en maakt voor bijvoorbeeld heterodyne verplaatsingsinterferometrie nieuwe meetmethodieken mogelijk, zoals fase gekoppelde verplaatsingsmeting.

Het in dit proefschrift beschreven onderzoek heeft geresulteerd in vier peer-reviewed journal publicaties, één niet-journal publicatie, drie conferentie presentaties met bijbehorende publicaties, nieuwe methoden voor optische golffront detectie en heterodyne frequentie generatie, en een uitgebreide foutenanalyse voor heterodyne verplaatsingsinterferometers. Tezamen hebben deze werken een nieuw heterodyne interferometer concept gepresenteerd, welke verbeterde meetlineariteit vertoon ten opzichte van een state-of-the-art benchmark interferometersysteem. Het initiële interferometer ontwerp van Dr. Joo is verbeterd met betrekking tot uitlijnbaarheid en heeft vervolgens middels een verbetering van de optische lay-out een compactheid verkregen die vergelijkbaar is met een benchmark interferometer. De Delftse interferometer waarborgt sub-nm meetonzekerheid over een meetbereik van 450 mm, terwijl deze een optisch flexibele lay-out heeft tussen de heterodyne bron, de interferometers en de fasemeetapparatuur. Het gebruik van optische fibers helpt bij de integratie van dit meetsysteem in een host-systeem en biedt een modulaire systeemopbouw waarbij de modules kunnen worden aangesloten op een plug-and-play basis, waardoor zowel de tijd voor inbedrijfsstelling als downtime gereduceerd worden.

Om het gepresenteerde interferometer concept commercieel toepasbaar te maken zou in toekomstig onderzoek geëxperimenteerd moeten worden met een vijf graden van vrijheid metende interferometer zoals beschreven in *Hoofdstukken 4* en *9*, inclusief tests met een thermisch passieve afscherming van de interferometer optica. Indien een daadwerkelijk plug-and-play systeem is beoogt is het wenselijk om een studie naar fiber-connectoren uit te voeren, waarbij verhoogde aandacht gegeven moet worden aan de mechanische stabiliteit en golffront kwaliteit van de fiber uitkoppeling op de interferometer.

Publications and conferences

Publications

2014 *Validation of separated source frequency delivery for a fiber-coupled heterodyne displacement interferometer*, A.J.H. Meskers, J.W. Spronck, and R.H. Munnig Schmidt, Optics Letters 39(15), 4603.

2014 *Heterodyne displacement interferometer, insensitive for input polarization*, A.J.H. Meskers, J.W. Spronck, and R.H. Munnig Schmidt, Optics Letters 39(8), 1.

2013 *Relative optical wavefront measurement in displacement measuring interferometer systems with sub-nm precision*, A.J.H. Meskers, D. Voigt, J.W. Spronck, Optics Express, 21, 17920.

2012 *Sub-nanometer accurate fiber-fed heterodyne interferometer*, A.J.H. Meskers, Mikroniek (a quarterly magazine for professionals in the field of precision engineering), 52(2), 5.

2011 *Fiber-coupled displacement interferometry without periodic nonlinearity*, J.D. Ellis, A.J.H. Meskers, J.W. Spronck, and R.H. Munnig Schmidt, Optics Letters, 36, 3584.

Conferences

2013 ASPE, Spring Topical Meeting, MIT, Boston, United States, oral presentation.
Measuring optical wavefronts in displacement measuring interferometer systems with sub-nm uncertainty, A.J.H. Meskers, J.W. Spronck, and R.H. Munnig Schmidt, American Society for Precision Engineering.

2011 IMEKO, Braunschweig, Germany, oral presentation.
Displacement interferometry with fiber-coupled delivery, A.J.H. Meskers, J.D. Ellis, J.W. Spronck, and R.H. Munnig Schmidt, 10th IMEKO symposium.

2011 ISMTII, KAIST, Daejeon, South Korea, oral presentation.
Fiber coupled sub nanometer displacement interferometry without periodic nonlinearity, A.J.H. Meskers, J.D. Ellis, J.W. Spronck, and R.H. Munnig Schmidt, 10th ISMTII symposium.

Extracurricular

2014 (publication)
A Space weather information service based upon remote and in-situ measurement of coronal mass ejections heading for Earth (A concept mission consisting of six spacecraft in a heliocentric orbit at 0.72 AU), B. Ritter, A.J.H. Meskers, O. Miles, M. Ruβwurm, S. Scully, A. Roldán, O. Hartkorn, P. Jüstel, V. Réville, S.S. Lupu, and A. Ruffenach, Journal of Space Weather and Space Climate, (manuscript accepted for publication).

2014 (publication)
Voorspellen van ruimteweer door zonneuitbarstingen, A.J.H. Meskers, Ruimtevaart (Nederlandse Vereniging voor Ruimtevaart, i.e. Dutch society for aerospace, quarterly magazine), 3, 3.

2013 (summerschool)
Post-Alpbach, Graz, Austria. Organized by: ESA, FFG-Austria The winning mission from the Alpbach Summerschol was further developed by a selected group of 15 participants from the summerschool.

2013 (conference)
European Space Weather Week, Antwerp, Belgium.
Selected from participants of the Alpbach Summerschool to present the winning concept mission from the Alpbach Summerschool.

2013 (summerschool)
Alpbach Summerschool, Alpbach, Austria. Organized by: ESA, FFG-Austria, only selected Dutch participant and team leader of the winning team.

2012 (publication)
CT-Compatible Medical Drilling Stylet, C.J. Walsh, A.J.H. Meskers, A.H. Slocum, and R. Gupta, Journal of Medical Devices, ASME, 6, 041001-8.

Curriculum Vitae

Arjan Meskers was born on February 20th, 1985 in Voorhout, The Netherlands. After finishing his secondary education at the Fioretti College in Lisse in 2002, he started at the HTS Haarlem. He obtained his Mechanical Engineering (ME) propaedeutics degree in one year and left the HTS Haarlem to join the TH Rijswijk. In 2006 he graduated *cum laude* (*summa cum laude* according US-definition) voor his ME BSc. degree, and started at the Delft University of Technology with a masters in ME, *Mechatronic System Design*, and a masters in Biomedical Engineering (BE), *Tissue Biomechanics and Implants*.

In 2009 he performed research at the Massachusetts Institute of Technology with the Precision Engineering Research Group, as part of his BE masters. His BE graduation research was on the design of a micro-actuation system for a flapping wing micro aerial vehicle. In collaboration with the department of Chemical Engineering of the TU Delft he designed a micro-sized chemical converter to convert chemically stored energy (hydrogen peroxide) into mechanical motion. The graduation work was titled: *High Energy Density Micro-actuation based on Gas Generation by means of Catalysis of Liquid Chemical Energy* *(see www.library.tudelft.nl)*.

After obtaining his BE MSc. degree in 2010 he was invited for a PhD-candidate position within the ME department of Precision and Microsystems Engineering, in the field of *optical heterodyne displacement interferometry*. He was given the opportunity to graduate for his ME masters in parallel to his PhD-research and received his ME MSc. degree in 2011 with the work: *Fiber Coupled Sub-Nanometer Heterodyne Displacement Interferometry* *(see www.library.tudelft.nl)*.

In 2014 he obtained his PhD-degree with the research presented in this thesis.

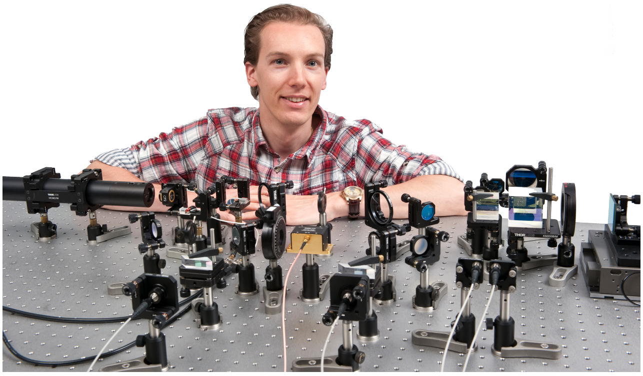

Showing the experimental setup for validating the separated source frequency delivery concept (with its enclosure removed), as addressed in Section 5.3.

reduced periodic nonlinearity

sub-nanometer measurement uncertainty

extreme ultraviolet lithography

NEAR-VACUUM MEASUREMENT ENVIRONMENT

heterodyne displacement interferometry

single-mode optical fiber delivery

flexible optical layout

fiber-coupled interferometer

modular buildup

plug-and-play

fast module replacement

ABOUT THE COVER

FRONT PAGE: a picture showing the basic optical setup of a non-monolithic Delft interferometer for displacement measurement with $\lambda/8$ resolution of a plane target mirror, see also page 32, Fig.4.4.

BACKGROUND: simulation of interference between waves that originate from two separated point sources, located at the upper left and lower right, see also page 13, Fig.2.4.

ISBN 978-94-6203-674-1